UNIVERSITEIT VAN PRETORIA
UNIVERSITY OF PRETORIA
YUNIBESITHI YA PRETORIA

Delta ferrite in modified 9Cr–1Mo steel weld metal

By

Sibusiso Samuel Mahlalela

A thesis submitted in fulfilment of the requirements for the degree of

PHILOSOPHIAE DOCTOR (METALLURGY)

In the

Department of Materials Science and Metallurgical Engineering
Faculty of Engineering Built Environment and Information Technology,
University of Pretoria, SOUTH AFRICA

Supervisor: Prof. P.G.H. Pistorius

October 2024

Abstract

Modified 9Cr−1Mo steel (P91) steel has attractive properties, such as high creep-rupture strength, good resistance to stress corrosion cracking, low thermal expansion coefficient, and high thermal conductivity. For adequate performance of P91 steels, the alloy design and thermo-mechanical processes during manufacturing should be such that a fully martensitic microstructure is achieved that is free from delta (δ) ferrite. Production of P91 base metal always includes austenitisation at temperatures of 1040−1150°C to dissolve any delta ferrite, followed by air cooling and tempering. P91 weld microstructure sometimes exhibits delta ferrite, which is detrimental to mechanical properties and performance. During the fabrication of P91 components, austenitisation is not a feasible post-weld heat treatment (PWHT), so delta ferrite formed in the weld and heat-affected zone may persist. The two main contributing factors that influence the presence of delta ferrite in the P91 as-welded microstructure are chemical composition and cooling rate.

This research focused on examining the role of chemical composition on the presence of delta ferrite in the weld metal. Empirical formulae are extensively applied to evaluate their accuracy in predicting the P91 as-welded microstructure. An important objective was also to determine if delta ferrite can be observed in as-welded microstructures of P91 weld metal that fully complies with the chemical composition requirements of the American Welding Society (AWS) A5.28/A5.28M:2020 (ER90S-B9) and International Standards Organisation (ISO) 21952:2007 (CrMo91) standards. The use of preheating during welding, PWHT, and experimental techniques like dilatometry and Gleeble simulation were applied in this research to examine the effect of thermal treatment on the presence of delta ferrite in the weld structure.

To meet the objectives of the current study, a total of twenty-eight gas–metal arc (GMA) welds that had varying compositions were deposited on a P91 steel pipe. Six of the twenty-eight welds were deposited with 250°C preheating and the rest of the welds were done without preheating. Five welds that contained delta ferrite were selected for PWHT at 760°C, 795°C, and 815°C. A further five delta ferrite-containing welds were selected for Gleeble thermal treatment to peak temperatures of 900°C, 1100°C, and 1350°C to simulate the thermal cycle experienced by a weld bead when a subsequent bead is deposited in a multiple bead weld. Dilatometry was performed on a P91 base metal by cooling at rates varying from 1−200°C/s from a 1350°C peak temperature.

Hardness testing was conducted on all specimens, including the as-welded beads, Gleeble, PWHT, and dilatometry specimens, to give an indication of the effect of chemical composition and thermal treatment on mechanical properties of P91 weld metal.

Direct laser deposition was applied as an alloying technique to alter the composition of GMAW beads. The applied alloying technique was satisfactory in achieving the desired compositional changes. The nature of the laser deposition process limits this alloying technique to single-bead welds. The composition was fairly uniform along the bead lengths of five analysed welds except for one which showed the most inconsistency in all three added alloying elements (Cr, Mo, and Si). Inhomogeneity observed along the weld bead length was attributed to the laser deposition process and not the alloying technique. By optimising the laser parameters and ensuring better control of the powder particle size, reliability in altering the weld composition can be accomplished with the alloying technique.

In evaluating the effect of composition on the observed amount of delta ferrite, metallography of the as-welded beads showed that eighteen of the twenty-eight welds contained delta ferrite. Thirteen of the twenty welds that complied with the composition specification contained delta ferrite. The amount of delta ferrite in martensite ranged from 0.3% to 6.2%. The morphology of the observed delta ferrite was a mixture of small to large polygonal delta ferrite grains and, in some welds, fine elongated delta ferrite grains. The addition of austenite-forming elements in the weld was effective in limiting delta ferrite. Delta ferrite was observed to increase with the chromium equivalent (Cr_{eq}), which is based on ferrite-forming elements like Cr, Si, and Mo. Empirical formulae that reflect the balance between austenite- and ferrite-forming elements showed that 64% of the weld microstructures were correctly predicted. These results show that empirical formulae cannot exclusively be relied upon to accurately predict weld microstructures with the currently recommended limits, especially where small amounts of delta ferrite are probable.

These results clearly demonstrate that compliance of weld metal chemical composition to the AWS A5.28/A5.28 M:2020 (ER90S-B9) and EN ISO 21952-A (CrMo91) specification ranges does not ensure a fully martensitic as-welded microstructure. It is recommended that these specification limits be revised to ensure a fully martensitic microstructure. Mo and Si are ferrite formers, so it is proposed that the range be revised to 0.7–1.0 mass% Mo and 0.15–0.35 mass% Si. Mn and Ni are austenite formers/stabilisers, so it is proposed that these limits should be specified as 0.6–1.2 mass% Mn and 0.4–0.8mass% Ni.

Phase-transformation temperatures were calculated using Thermo-Calc software. A larger ($Ae_4 - Ae_3$) temperature range, which is the region where only austenite is stable, allows more time for delta ferrite to transform to austenite during cooling. An ($Ae_4 - Ae_3$) temperature range above 415°C for welds that were not preheated seems to be necessary to suppress delta ferrite in the as-welded microstructure. The required ($Ae_4 - Ae_3$) temperature range decreased to 385°C when 250°C preheating was applied. These results indicate that both the chemical composition, which determines the ($Ae_4 - Ae_3$) temperature range, and the cooling rate through this temperature range are important in suppressing delta ferrite in the final as-welded microstructure.

In evaluating the role of thermal treatment on residual delta ferrite, the following were observed:

- The applied PWHT did not change the amount of delta ferrite observed, even for PWHT temperatures that exceeded the weld Ae_1 temperature.
- The Gleeble results indicated that significant reduction in delta ferrite was observed in specimens treated at 900°C and 1100°C. Specimens treated at 1350°C peak temperature were fully martensitic. This means that the amount of delta ferrite can be reduced by applying a subsequent bead or temper bead.
- The dilatometry experiment observations during cooling were twofold: above the Ae_4 temperature, delta ferrite decreased with faster cooling rate; below the Ae_4 temperature, slower cooling rate resulted in decreased delta ferrite.

A general observation was that higher peak temperatures during thermal treatment and slower cooling rate during welding will limit the amount of delta ferrite in P91 weld metal.

Publications

Based on the current research, the following papers have been published:

1. Mahlalela, S.S. and Pistorius, P.G.H., 2022. Investigation of δ-ferrite content in weld metal of modified 9Cr–1Mo electrodes using thermodynamic modelling and quenching experiments. *Welding in the World*, *66*(6), pp. 1191–1198.
2. Mahlalela, S.S. and Pistorius, P.G.H., 2023. Influence of alloying elements and cooling rate on the presence of delta ferrite in modified 9Cr–1Mo as-welded microstructure produced by gas–metal arc welding. *Welding in the World*, *67*(5), pp. 1169–1180.

Acknowledgements

Psalm 115 vs 14-16

May the Lord richly bless both you and your children. May you be blessed by the Lord, who made heaven and earth. The heavens belong to the Lord, but he has given the earth to all man.

This research work has taken many years of conducting experiments, writing papers and writing this dissertation, and many people have supported me along the way. There were many times when I thought I would not reach this point, at times feeling hopeless and frustrated. However, with persistence and taking one step at a time, it is finally complete. I would first like to give thanks to the Lord, to you goes all the glory.

Thank you to everyone who has contributed ideas, knowledge, assistance, encouragement, and prayers. This research work is a product of many people who have supported me, without which this would never have been completed.

I wish to thank my wife, Malebo and our two daughters, Uthando and Lethubuhle, for the support, understanding as I worked in the evenings and on some weekends. This milestone is equally yours.

I would like to extend my gratitude to my excellent supervisor, Prof. Pieter Pistorius for the guidance, sacrifice and your belief in me. Your invaluable expertise, professional network and going an extra mile for me, have made it possible for me to complete this work. SAIW Centre for Welding Engineering at the Department of Material Science and Metallurgical Engineering provided financial support.

I am grateful to Kabelo Matea for your assistance with laboratory work, Ms Gabi Ngema of Department of Material Science and Metallurgical Engineering for always being available to assist, Edwin Mohale of Mechanical Engineering Department for your great help. I am grateful to Prof. Kathy Sole for editorial assistance and guide on this manuscript.

Thank you to Dr. Corney van Rooyen and Ms Maritha Theron of the National Laser Centre at South African Council for Scientific and Industrial Research (CSIR) for advice, assistance with the laser metal deposition and providing some of the alloying elements; SecMet for providing the P91 base material; Steinmüller Africa for donating the welding consumable.

I am truly grateful and pray that you and your families will be blessed for your generosity.

Table of Contents

List of Figures

List of Tables

Nomenclature and Abbreviations

Ae_1	Temperature at which austenite begins to form on heating
Ae_3	Temperature at which a fully austenitic phase is achieved on heating
Ae_4	Temperature at which delta ferrite-to-austenite transformation begins on heating
Ae_5	Temperature at which austenite-to-delta ferrite transformation is completed on heating
AM	Additive manufacturing
ASME	American Society of Mechanical Engineers
ASTM	American Society for Testing and Materials
AWS	American Welding Society
CCT	Continuous-cooling transformation temperature
Cr_{eq}	Chromium equivalent
CGHAZ	Coarse-grained heat-affected zone
CI	Confidence interval
CNB	Chromium–nickel balance
DBTT	Ductile-to-brittle transition temperature
DLD	Direct laser deposition
DOE	Department of Energy (USA)
EDS	Energy-dispersive X-ray spectroscopy
EN	European Standard
FGHAZ	Fine-grained heat-affected zone
FF	Ferrite factor
FN	Ferrite number
GMAW	Gas–metal arc welding
GTAW	Gas–tungsten arc welding
HAZ	Heat-affected zone
HI	Heat input
Hv/VHN	Vickers hardness number
IC-HAZ	Inter-critical heat-affected zone
ISO	International Organisation for Standardisation
KFF	Kaltenhauser ferrite factor

L×H×W	Length × height × width
LMR	Liquid metal reactor
LMFBR	Liquid metal fast breeder reactor
M_s	Martensite start temperature
M_f	Martensite finish temperature
Ni_{eq}	Nickel equivalent
OES	Optical emission spectrograph
ORNL	Oak Ridge National Laboratory
OM	Over-tempered martensite
PAGB	Prior austenite grain boundaries
PWHT	Post-weld heat treatment
PDS	Powder delivery system
R^2	Coefficient of determination
RAFM	Reduced-activation ferritic martensitic (steel)
RT	Room temperature
SEM	Scanning electron microscope
SMAW	Shielded-metal arc welding
T_m	Melting temperature
T_o	Temperature of the base metal prior to welding (preheating temperature)
T_p	Peak temperature
TEM	Transmission electron microscopy
UTS	Ultimate tensile strength
XRD	X-ray diffraction
YS	Yield strength

Introduction

Introduction

Modified 9Cr−1Mo steel, also known as P91, is a ferritic–martensitic steel in the 9%−12%Cr steel family. P91 steel has attractive properties, such as high creep-rupture strength, good resistance to stress corrosion cracking, low thermal expansion coefficient, and high thermal conductivity [1, 2]. P91 steel provides excellent properties for long-term high-temperature applications, such as coal-fired power plant boilers, high-pressure steam piping, headers, and tubing [3, 4].

For adequate performance of P91 steels, the alloy design and thermo-mechanical processes during manufacturing should be such that a fully martensitic microstructure is achieved that is free from delta ferrite. Production of P91 base metal always includes austenitisation at temperatures of 1040−1150°C to dissolve any delta ferrite, followed by air cooling and tempering [5]. P91 final weld microstructure sometimes contains delta ferrite, which is detrimental to mechanical properties and service performance [6]. During the fabrication of P91 components, austenitisation is not a feasible post-weld heat treatment (PWHT), so delta ferrite formed in the weld and heat-affected zone (HAZ) will remain in the welded joint.

The two main factors that influence the presence of delta ferrite in the P91 as-welded microstructure are composition and cooling rate. A strict balance between austenite- and ferrite-forming elements in P91 is necessary to ensure that no delta ferrite is present in the weld metal [7]. In this study, five alloying elements (Cr, Ni, Mn, Si, and Mo) were varied in the weld metal. The roles of these elements (individually and collectively) were examined for their influence on the morphology and delta ferrite amount in a weld microstructure. The use of preheating during welding and other experimental techniques like dilatometry and Gleeble thermal treatments were applied to examine the effect of cooling rate on the formation of delta ferrite.

Objectives

I. Determine the relationship between weld composition and delta ferrite.
   - Determine if delta ferrite can be observed in as-welded microstructures of weld metal that fully complies with the composition requirements of the AWS A5.28/A5.28M:2020 (ER90S-B9) and EN ISO 21952:2007 (CrMo91) standards.
   - Determine the contribution of selected elements (Cr, Ni, Mn, Si, and Mo) on the presence delta ferrite in the final as-welded microstructure.
   - Evaluate the accuracy of empirical formulae in predicting the P91 final microstructure.
   - Evaluate the significance of the ($Ae_4 - Ae_3$) temperature range in limiting the presence of delta ferrite.

II. Study the role of cooling rate on the amount of delta ferrite.

III. Establish the reliability of the direct laser deposition (DLD) alloying technique in altering the P91 weld metal composition.

Section I

Literature Review

Chapter 1

History of P91

1.1 Background

Before the 1970s, the main materials of construction for liquid metal reactor (LMR) components, such as pressure vessels, cladding, ducts, hot-leg and cold-leg piping, were 304 and 316 stainless steels. Steam generators utilised 2.25Cr−1Mo alloy, and the Inconel 718 was used for special applications. There were some issues that necessitated the development of new materials.

Some of these problems were [8]:

(i) Austenitic stainless steels have a high coefficient of thermal expansion which results in high thermal stresses during operation;
(ii) Grades 304 and 316 stainless steels are sensitive to stress corrosion cracking;
(iii) The allowable compositional specification ranges of 304 and 316 stainless steels results in wide variability in their properties;
(iv) Difficulties with in-service inspection of austenitic stainless-steel weld joints;
(v) 2.25Cr−lMo steel suffers atmospheric corrosion;
(vi) Low design stress is allowable for 2.25Cr−lMo steel;
(vii) Difficulties with ferritic-to-austenitic weld transition joints.

In 1974, a task force at Oak Ridge National Laboratory was authorized by the U.S. Department of Energy to perform research that would lead to the recommendation of alternative materials for liquid metal reactor applications. The study was divided into three phases, directed at:

(i) evaluating the deficiencies in Grades 304 and 316 stainless steels for LMR applications;
(i) selecting candidate alloys with potential for improved performance;
(ii) A strategy for acquiring the data base required to use the alloys in a future LMR should be developed.

After consideration of several ferritic alloy compositions based on creep strength and microstructural characteristics, the modified 9Cr−1Mo steel was selected for further development [8].

1.2 Development of P91 Steel

Modified 9Cr−1Mo (P91 or T91) is a creep strength-enhanced ferritic steel that belongs to the 9%−12% Cr steel family. Modified 9Cr−1Mo steel was first developed under the designation P9 for tubing and piping of steam power plants [9]. The development route is shown in Fig. 1.1. The improved P/T9 steel was developed by ORNL based on the 9Cr−1Mo steel used in petrochemical plants since the 1950s [10]. The 9Cr−1Mo steel was modified by the addition of carbo-nitride-forming elements, a specified range of 0.06%–0.1% Nb and 0.18%−0.25% V, and a limited amount (0.05%) of N [1]. The Nb and V

contents in P9 steel were optimised in the early 1980s and the alloy was standardised as T91/P91 in ASTM 213/ASTM A335, respectively. Both Nb and V improve the elevated-temperature strength properties. For simplicity, the modified 9Cr−1Mo (P91/T91) steel is referred to as P91 steel in the rest of this document.

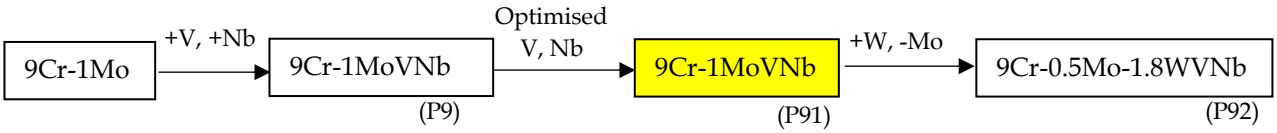

Fig. 1.1 Development of modified 9Cr−1Mo (P91) steels, including P92 steel.

Improved creep strength and hot tensile properties of P91 were attractive to designers because of the prospects of reducing pipe-wall thicknesses. Additionally, thinner walls improved reliability and minimised thermal stresses in a plant during service [11].

Nippon Steel in 1993 developed a 9Cr-0.5Mo−1.8W−Nb−V steel, named NF616, by the addition of W and a reduction of the amount of Mo in the P91 composition. This grade was standardised as P92 steel by the ASTM. The P92 steel grade showed higher creep resistance compared with P91, as shown in Fig. 1.2 [12, 13]. P91 and P92 steels are both extensively applied in modern power plants.

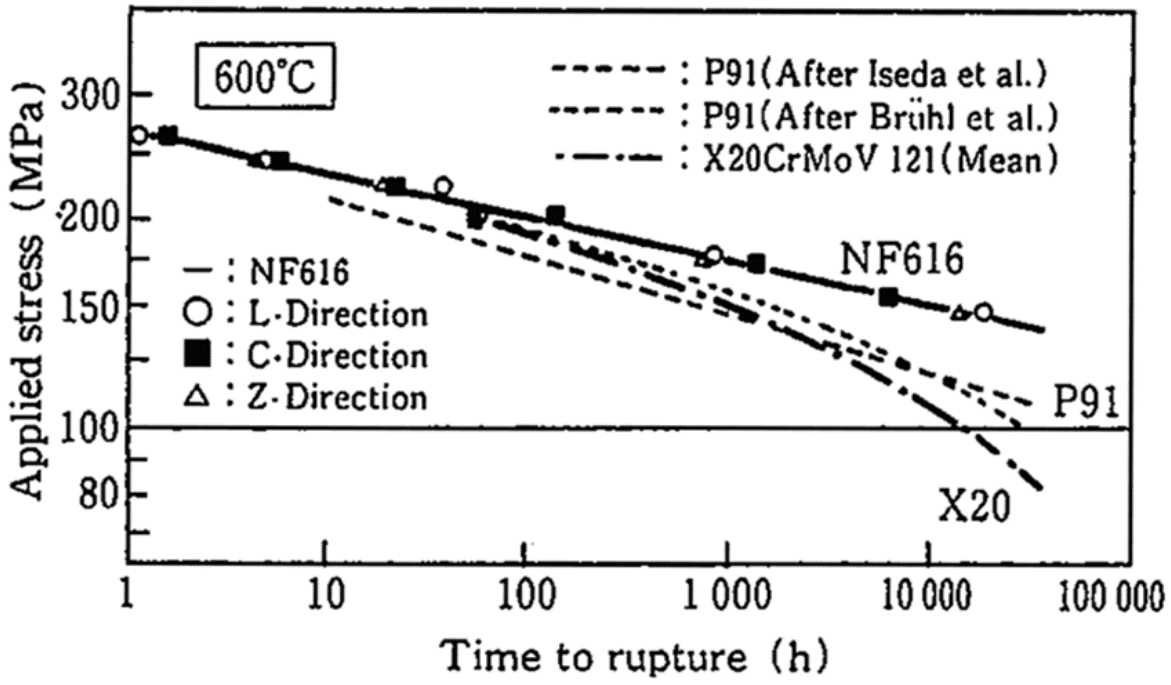

Fig. 1.2 Applied stress to rupture time curves of NF616 and P91 [13].

1.3 Application of P91 steel

Initially, P91 steel was mainly used for liquid metal fast breeder reactor (LMFBR) applications at a service temperature of about 550°C [8]. In 1980, P91 steel used on trial bases in U.S. power boilers, and in 1983, the steel was approved under the rules of the ASME Boiler and Pressure Vessel Code for use in boiler tubing construction. Currently, P91 steel finds broad application in modern thermal power plants, petrochemical

industries, and nuclear applications [9]. P91 steel enables higher operating parameters such as pressure and temperature to improve power plant efficiency. By increasing the thermal efficiency of a generating plant, less fuel is needed for a given power output and emissions are reduced [2]. Typical subcritical power plants are capable of achieving an efficiency of 40% at a steam temperature of 600°C and a pressure of 22 MPa. A supercritical plant can achieve 45% efficiency by using high pressure (30MPa). In ultra-supercritical conditions, efficiencies of 50% are possible if steam temperature is also increased [14].

In conventional coal-fired power-plant boilers, P91 steel finds application in steam piping, headers, and tubing components shown in **Fig. 1.3**. Steam pipes transport high pressure steam from the boiler to the turbine. Headers are pipes, except they contain numerous tube penetrations that bring in or carry out steam from the header. In addition, the pipes and headers are heavy section components, which are subject to fatigue induced by thermal stresses. P91 steel is therefore preferred because of its higher thermal conductivity and lower coefficient of thermal expansion [3, 4]. The creep-rupture strength at 600°C and 10^5 h of P91 steel is better to that of the previously applied 2.25Cr–1Mo alloy and 410 stainless steel. The creep-rupture strength at 600°C and 10^5 h regarded as the most important mechanical property for power-plant steels [13].

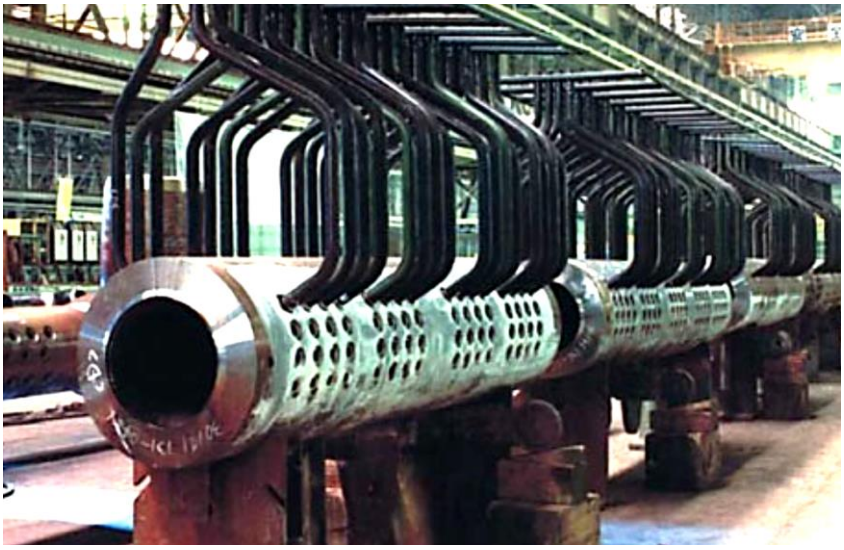

Fig. 1.3 Header consisting of thick walled pipe penetrated by a number of tubes [15].

In the petrochemical and chemical processing industries, P91 steel is used to manufacture components for hydrogen desulfurization and combustion of oil and for containment of chemical products. It is also used for furnace tubes in petrochemical plants [4].

In recent years, interest in the use of P91 steel for fast breeder reactors (FBR), sodium-cooled FBR, fusion reactors, and Gen IV reactors has increased due to resistance to irradiation-induced void swelling and resistance to thermal load and fatigue compared with austenitic steels [16].

Chapter 2

Metallurgy of P91 Steel

2.1 Introduction

P91 steel contains about 9% Cr and 1% Mo as the main alloying elements. C, N, Nb, and V are added to form carbides, nitrides, and carbonitrides. Table 2.1 lists the chemical composition requirements of P91 steel and weld metal as per the applicable specification standard. Solid-solution strengthening from Cr and Mo and the presence of precipitates results in high creep-rupture strength, good resistance to stress corrosion cracking, low thermal-expansion coefficient, and high thermal conductivity [1]. For adequate performance of P91 steels, the thermo-mechanical processes during manufacturing should be such that a fully martensitic microstructure is achieved. P91 steel is recommended for use in the normalised and tempered condition (1040°C for 1 h normalise, air cooled to room temperature, followed by 760°C for 1 h temper) [17].

Table 2.1 *Chemical composition requirements of P91 steel grade and weld metal.*

Element	***P91 steel (%)***		***P91 weld metal (%)***					
	ASTM A335/A335M−21		*AWS A5.28/A5.28M:2020 (E90S-B9)*		*AWS A5.5/A5.5M:2014 (E9015-B91)*		*ISO 21952:2007 (CrMo91)*	
	Min	*Max*	*Min*	*Max*	*Min*	*Max*	*Min*	*Max*
C	0.08	0.12	0.07	0.13	0.08	0.13	0.07	0.15
Mn	0.30	0.60	−	1.20	−	1.20	0.40	1.50
Cr	8.00	9.50	8.00	10.50	8.00	10.50	8.00	10.50
Si	0.20	0.50	0.15	0.50	−	0.30	−	0.60
Mo	0.85	1.05	0.85	1.20	0.85	1.20	0.80	1.20
V	0.18	0.25	0.15	0.30	0.15	0.30	0.15	0.30
Nb	0.06	0.10	0.02	0.10	0.02	0.10	0.03	0.10
N	0.03	0.07	0.03	0.07	0.02	0.07	0.02	0.07
Ni	−	0.40	−	0.80	−	0.80	0.40	1.00
Al	−	0.02	−	0.04	−	0.04	−	

2.2 Phase composition as a function of chemical composition and temperature

Delta ferrite is the primary phase that forms from liquid at the start of solidification, as shown in the P91 compositional equilibrium pseudo-phase diagram constructed using Thermo-Calc software (Fig. 2.1(a) and (b)) [18]. The reference composition used for constructing the pseudo-phase diagrams in Fig. 2.1 is based on the AWS A5.28/A5.28M:2020 (ER90S-B9) mid-points of the elements' ranges and are as follows: 0.1% C, 0.9% Mn, 9.0% Cr, 0.25% Si, 1.0% Mo, 0.2% V, 0.07% Nb, 0.04% N, and 0.7% Ni. The broken red line indicates the average Cr and C contents in P91 steels.

The equilibrium transformation temperatures are defined as follows (on heating) [18]:

- Ae_1: onset of austenite formation;
- Ae_3: fully austenitic phase is achieved;
- Ae_4: onset of delta ferrite formation from austenite;
- Ae_5: completion of austenite-to-delta ferrite transformation

The phase-transformation sequence can take two slightly different routes during cooling, depending on the balance between austenite- and ferrite-forming elements in the composition of the P91 steel:

$$\text{Liquid} \rightarrow \text{liquid} + \delta \rightarrow \delta \rightarrow \delta + \gamma \rightarrow \gamma \quad (2.1)$$

$$\text{Liquid} \rightarrow \text{liquid} + \delta \rightarrow \delta + \gamma \rightarrow \gamma \quad (2.2)$$

In the first transformation sequence, the liquid transforms to 100% delta ferrite phase during cooling. With further cooling below the Ae_5 temperature, austenite phase will begin to transform from delta ferrite. In the second transformation sequence, austenite begins forming before solidification is completed and is referred to as a peritectic transition [19, 20]. There are two components to the peritectic transition, according to Kerr et al. [21]: the peritectic reaction and the peritectic transformation. The peritectic reaction occurs where the liquid and delta-ferrite phases react to form austenite where a thin film of austenite grows along the liquid/delta ferrite interface. Peritectic transformation then occurs with further growth of austenite from both the liquid and delta ferrite phase [22].

Cr is a strong ferrite former and the equilibrium pseudo-phase diagram (Fig. 2.1(a)) with increasing Cr content demonstrates the influence of Cr on transformation temperatures and on restricting the austenite phase field. C is a strong austenite former and Fig. 2.1(b) shows how increasing C concentration enlarges the ($Ae_4 - Ae_3$) temperature range, which are the boundaries within which only the austenite phase is stable [18].

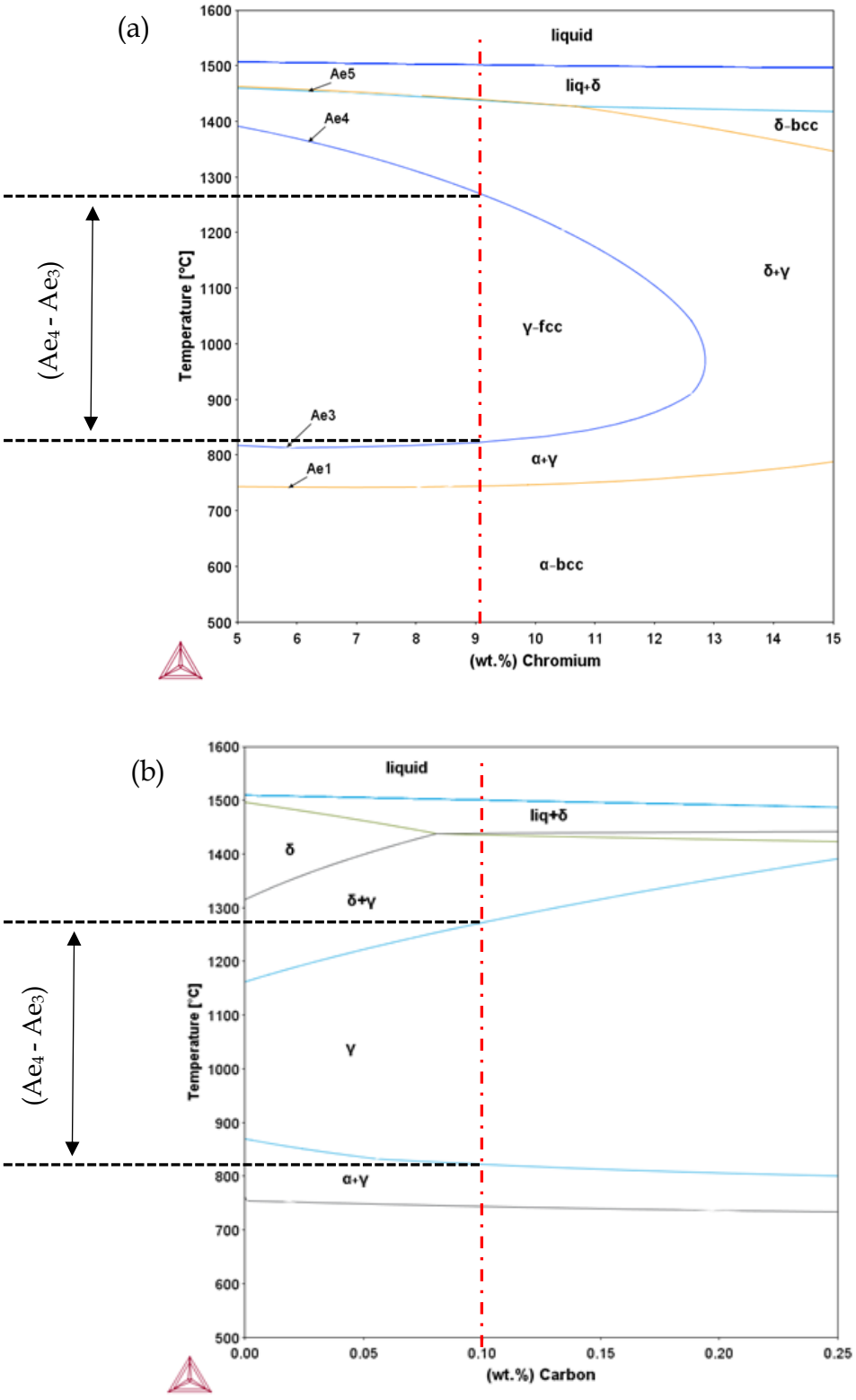

Fig. 2.1 P91 compositional pseudo-phase diagrams with (a) 5 to 15 mass% Cr range and (b) 0 to 0.25 mass% C range showing the (Ae_4 − Ae_3) region. The reference composition contains 9.0% Cr and 0.1% C; full details are given in the text.

The ($Ae_4 - Ae_3$) temperature range in Fig. 2.1 is the region where only austenite phase is stable under equilibrium conditions. Under non-equilibrium conditions, austenite transforms to martensite on subsequent cooling.

Mayr et al. [23] reported the critical transformation temperatures (CTT) shown in Table 2.2, which were calculated using Matcalc software and from X-ray diffraction with the P91 composition: 0.17% C, 0.22% Mn, 8.85% Cr, 0.23% Si, 1.54% Mo, 0.29% V, 0.06% Nb, 0.016% N, and 0.18% Ni. Included in Table 2.2 are non-equilibrium transformation temperatures as stated by Mayr et al. [23] and Pandey et al. [1].

Table 2.2 *P91 critical transformation temperatures calculated using Matcalc software and from experimental data.*

	Critical transformation temperatures (°C)		
	Matcalc (Mayr et al.) [23]	*In-situ XRD* [23] (on heating)*	*(Pandey et al.) [1, 5]*
M_s	–	403 ± 5	390–400
M_f	–	–	200–230
Ac_1	840	880 ± 15	810–825
Ac_3	895	1032 ± 15	912–930
Ac_4	1224	1210 ± 15	–

*Heating rate of 10°C/s to 1300°C

The given temperatures varied due to the specific composition of P91 being analysed. Mayr et al. [20] applied a heating rate of 10°C/s to a peak temperature of 1300°C and subsequent cooling to room temperature at the same rate. The Ac_3 temperature reported from the in-situ XRD was recorded when 99% of the transformation had occurred, and was at least 100°C higher than expected. Mayr et al. [20] explained that the difference between the measured and calculated values was as a result of the strong kinetic influence of the heating and cooling rates on phase transformations.

2.3 Precipitates

Mechanical properties, especially creep-rupture strength, is dependent on precipitates that are developed through normalising and tempering heat-treatment processes. During normalising treatment of P91, complete dissolution of $M_{23}C_6$ occurs. MX precipitates (20–80 nm) that are V nitrides and/or Nb carbonitrides ((Nb,V)(C,N)) are stable and remain undissolved during normalising. Pandey et al. [24] observed no $M_{23}C_6$ carbide precipitates along prior austenite grain boundaries (PAGB), lath boundaries, and within the matrix of P91 steel in normalised-only condition. $M_{23}C_6$ precipitates only develop after tempering. The main precipitation of carbides, nitrides, or carbonitrides occurs during tempering heat treatment on PAGB, ferrite subgrain boundaries, and on dislocations inside subgrains, as demonstrated in Fig. 2.2 [25, 26]. Precipitation hardening through pinning of dislocations and subgrain boundaries is reported as the most significant strengthening mechanism in P91 steels. Hald [25] also reported that the microstructure stability of these steels under creep load depends on the stability of the precipitates. During operation at elevated temperatures, further

particles that are thermodynamically unstable at the tempering temperature may precipitate, like Laves and Z-phases. The main precipitates observed in P91 steel are discussed below.

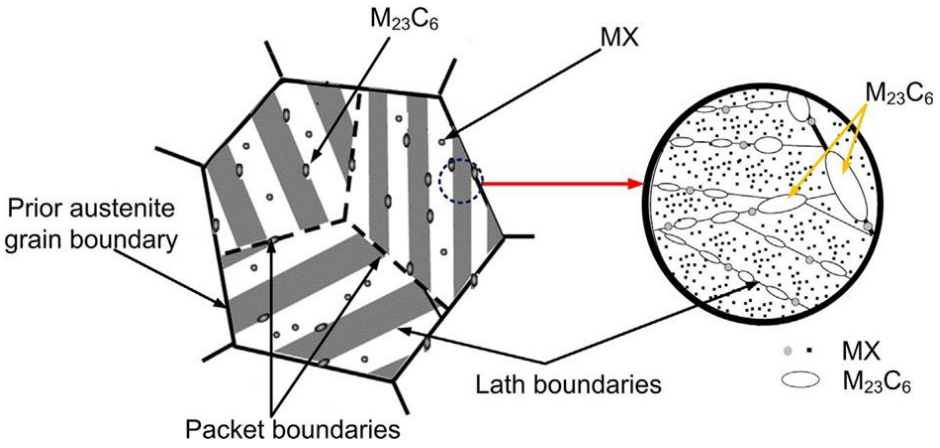

Fig. 2.2 Schematic drawing of $M_{23}C_6$ and MX precipitates in P91 steel [26].

M_3C *(precipitate during normalising)*: M_3C (Fe_3C) precipitates, shown in Fig. 2.3, are formed during the auto-tempering process, which occurs as the P91 steel cools down from the normalising treatment [27]. M_3C that precipitated after auto-tempering dissolves as the more stable carbides or nitrides of Cr, Mo, Nb, and V form during tempering [28].

Fig. 2.3 Needle-like M_3C carbides on a martensite lath of a normalised-only high-Cr (P92) steel [10].

$M_{23}C_6$ *(precipitate during tempering)*: $M_{23}C_6$ ($(Cr,Fe,Mo,Mn)_{23}C_6$) are the more abundant and large (60−150 nm) precipitates in P91 steel that form on PAGB, on subgrain boundaries, and within the martensite laths [29]. The $M_{23}C_6$ are face-centred cubic Cr-rich carbides. P91 steel exposure to elevated temperature causes coarsening of the $M_{23}C_6$ precipitates, which allows the martensite laths to transform to more equiaxed subgrains after about 30 000 h at 600°C. The dissolution of $M_{23}C_6$ precipitates on heating begins at temperatures above Ac_1 and is completed before the Ac_3 temperature.

MX *(precipitate during solidification and during tempering)*: MX are fine face-centred cubic precipitates (20–80 nm) that are V nitrides and/or Nb carbonitrides ((Nb,V)(C,N)) [29]. The MX precipitates have different morphologies. The first type is coarse primary Nb(C,N), which shows higher thermal stability compared with other MX phases and remains undissolved after typical austenitising treatment. The other type is secondary finer platelet V(C,N) and spherical Nb(C,N)-type precipitates, which are formed during the tempering treatment and show higher stability during creep [1]. The fine MX precipitates are uniformly distributed inside the lath. This restricts grain growth and produces a refined prior austenite grain size in the P91 microstructure [29]. MX particles do experience coarsening but at a much slower rate than $M_{23}C_6$ when exposed to elevated temperatures [30]. A schematic presentation of $M_{23}C_6$ and MX along the PAGB, lath boundaries, packet boundaries, and inside the intra-lath region is shown in Fig. 2.2.

Laves phase *(precipitate during creep exposure)*: The intermetallic Laves phase ($(Fe,Cr)_2(Mo)$) shown in Fig. 2.4 forms a hexagonal crystal structure and precipitates at temperatures around 600–650°C [25]. Laves phase is not observed after heat treatment, but appears on grain boundaries and sub-boundaries after less than 4000 h of creep exposure and experiences a significant growth rate up to 10 000 h [31]. Laves phase precipitates surround the $M_{23}C_6$ carbides by nucleating and growing on them and form a cluster on the PAGB [1]. This results in the loss of the pinning effect of $M_{23}C_6$ and other precipitates in the PAGB but, in the short-term, Laves formation enhances creep strength due to precipitation hardening. In long-term creep exposure, precipitation of Laves phase reduces the creep strength because of a higher coarsening rate [26]. Laves phase formation is detrimental to P91 properties because it decreases the Mo dissolved in the matrix, reducing solid-solution strengthening.

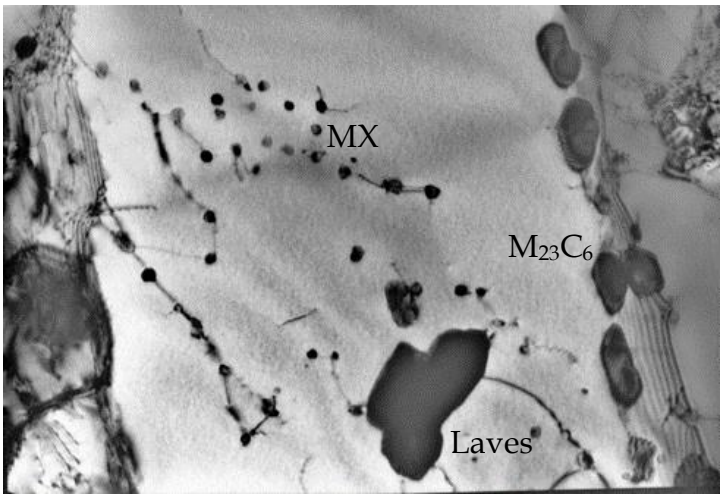

Fig. 2.4 Transmission electron micrograph showing Laves, $M_{23}C_6$, and MX precipitates after 6500 h creep exposure at 650°C [10].

Modified Z−phase *(precipitate after prolonged creep exposure)*: Modified Z−phase has a tetragonal crystal structure and is a complex nitride Cr(V,Nb)N, the precipitation of which leads to an almost complete dissolution of MX nitrides in P91 steel [25]. The original Z−phase (CrNbN), which contained no V, was discovered in 1950 in a Nb-

containing austenitic steel [32]. Modified Z−phase precipitation in creep-resistant martensitic steels is observed after long-term creep exposure, reported to begin after 34 100 h at 600°C, under a load of 100 MPa in P91 steel [31].

2.4 Heat treatment of P91 steel and welded joints

P91 steel is produced through various material processing routes, such as casting, forging, hot rolling, and extrusion. These processes lead to a non-homogeneous microstructure and non-uniform mechanical properties. Therefore, hardenable P91 components are subjected to a normalise-and-temper heat treatment to produce a tempered martensite structure, strengthened by solid solution, stable precipitates, and high dislocation density [33].

2.4.1 Normalising

A normalising treatment consists of austenitisation, which dissolves any delta ferrite, performed at temperatures between 1040 and 1080°C, as recommended by the ASTM A335/A335M−21 standard [34]. Coarse primary NbX precipitates remain undissolved after austenitisation [30]. The amount of NbX precipitates is found to decrease with increase in normalising temperature while the size of NbX precipitates increases [1]. Sikka et al. [35] examined the increase in austenite grain size of P91 as a function of the normalising temperature and time. Grain coarsening only occurred when the normalising temperature was increased by about 100°C or more above the specified 1040°C normalising temperature [17, 35]. Air cooling after normalising is associated with autotempering, due to reduced cooling rate [33]. The normalising treatment produces a fully martensitic structure with high dislocation density and some M_3C (M = Fe and Cr) precipitates. Increased cooling rate will produce finer martensite laths, with some evidence of transformation twinning and a higher dislocation density adjacent to the lath interfaces [33].

2.4.2 Martensite formation

The M_s (martensite start) temperature of P91 steel is observed at 390 to 400°C, whilst the M_f (martensite finish) temperature is between 200 and 230°C [1]. Haarmann et al. [4] stated that the M_f temperature is dependent on the prior austenite grain size and can be just above 100°C [4]. Zhou et al. [36] reported that for modified ferritic heat-resistant steel, the critical cooling rate for martensitic transformation is about 0.167°C/s when cooling from temperatures above the Ac_3. Di Gianfrancesco et al. [37] reported that for P91, the martensitic microstructure was achieved by cooling at > 0.2°C/s from the normalising temperature.

Figure 2.5 shows the CCT diagram of P91 steel [4]. The CCT diagram contains two critical cooling rate values: the first value indicates the maximum cooling rate (0.01°C/s) to achieve a fully ferritic microstructure; the second value indicates the minimum cooling rate (0.06°C/s) to have a fully martensitic microstructure. A mixture of alpha ferrite and martensite will be observed for cooling rates between these two values [38]. The critical cooling rates are sensitive to the chemical composition and the austenitic grain size through the austenite-only region [38].

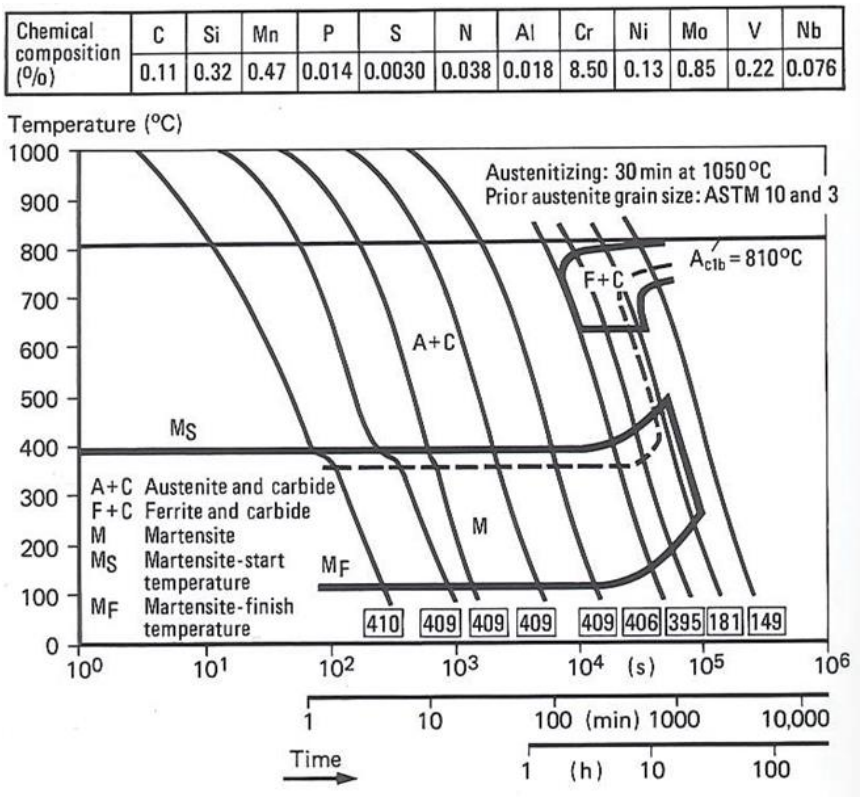

Fig. 2.5 P91 steel continuous cooling transformation diagram, including the alloy chemical composition, Vickers hardness values, and different cooling curves [4].

2.4.3 Tempering

The tempering process is typically done below the Ae_1 temperature at 650 to 780°C for 1 to 2 h and is followed by air cooling [30]. The ASTM A335/A335M−21 [34] standard recommends that the temperature for tempering should be at least 50°C above the application temperature but stipulates a tempering temperature between 730 and 800°C. Bush et al. [39] recommended a temperature of 760°C for optimal combination of strength, creep resistance, and impact toughness. It is essential for tempering to be performed at temperatures below the Ae_1 to avoid re-austenitisation and the formation of fresh martensite. The microstructural changes that occur with various tempering temperatures are as follows [40]:

< 350°C: fine dispersions of M_3C (Fe_3C) precipitates form and grow on the martensite laths. With time, the Fe_3C precipitates become enriched with Cr, increasing the possibility of in situ formation of M_7C_3.

450–550°C: the needle-like precipitates of M_2X (mainly $Cr_2(CN)$) primarily nucleate on dislocations in the martensite laths. At temperatures above 500°C, where effective diffusion of Cr occurs [33], M_7C_3 and M_2X will begin to coarsen.

> 550°C: The Cr-rich $M_{23}C_6$ forms on the martensite lath and PAGB replacing the M_7C_3 and M_2X precipitates. Annihilation of dislocation occurs, leading to a decrease in their

density when compared to "as−quenched" martensite. Effective diffusion of Mo, Mn, and V in the matrix occurs above 550°C to form MX and $M_{23}C_6$ precipitates.

> 650°C: $M_{23}C_6$ carbides continue to form. This results in further reduction in the amount of dislocations and in the formation of pronounced sub-grains across the martensite laths.

> 750°C: Lath martensite structure is replaced by a fairly equiaxed sub-grain structure. Coarsening of $M_{23}C_6$ precipitates continues.

2.5 Mechanical Properties of P91 steel

2.5.1 Creep

The 10^5 h creep-rupture strength at the operating temperature is often considered to be an important measure of creep resistance in power plants. The 10^5 h creep-rupture strength refers to the stress at which failure occurs at 10^5 h. The aim for the 10^5 h creep-rupture strength for producing new steels is typically 100 MPa at the working temperature [41].

Di Gianfrancesco et al. [37] published 700 creep test results performed in the temperature range of 500−700°C generated over 20 years from tubes and pipes from more than 30 different heats. The plotted creep-rupture curves are displayed in Fig. 2.6 for important selected test temperatures. The used stresses varied from 35 to 400 MPa. To date, the longest creep test has a time to rupture of 110 301 h at 550°C with 150 MPa stress [37].

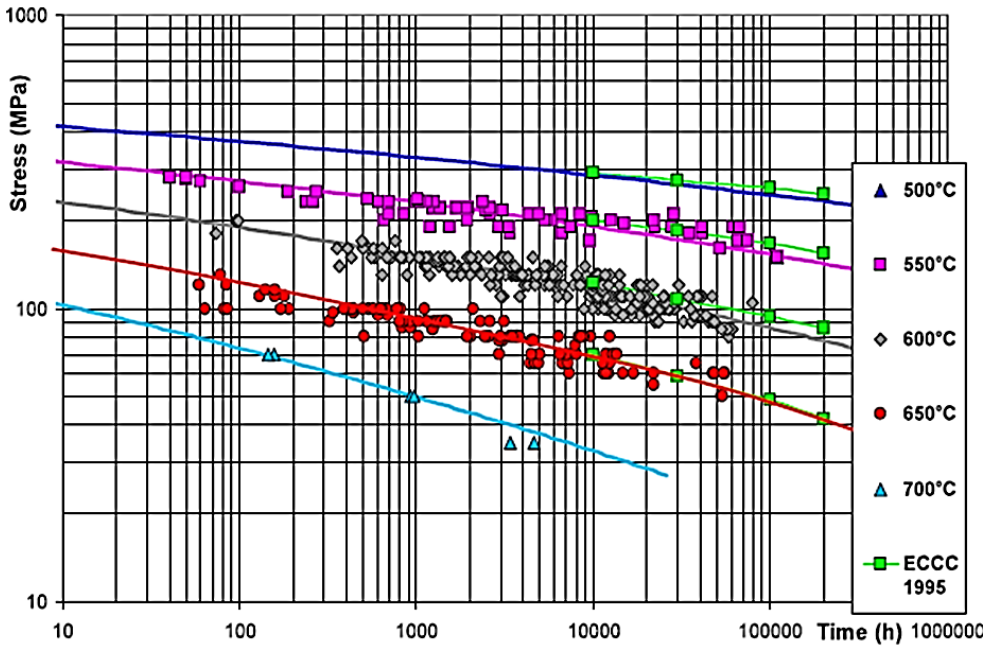

Fig. 2.6 P91 steel calculated creep-rupture curves [37].

2.5.2 Hardness

Arivazhagen et al. [42] performed a hardness test with a Vickers 10 kg load across four welds that varied slightly in composition. The hardness value of the P91 martensitic

alloy in the as-welded condition ranged between 452 to 507 Hv_{10}; after PWHT, the hardness was reduced to 274 Hv_{10}. Di Gianfrancesco et al. [37] reported hardness values of 405–460 Hv for the untempered base metal. Merchant [43] reported the influence of PWHT temperature on the hardness, as presented in Fig. 2.7. The hardness was observed to marginally decrease with PWHT temperature.

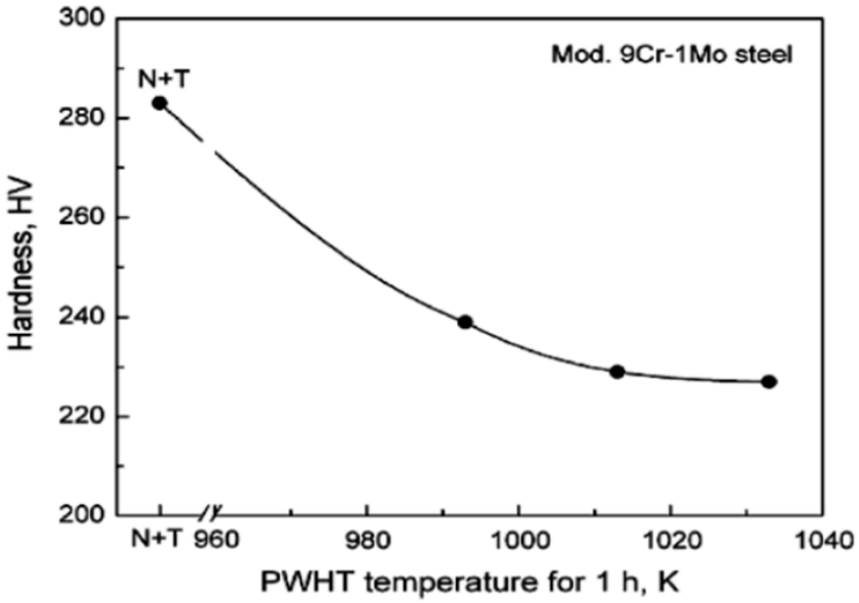

Fig. 2.7 Influence of post-weld heat treatment temperature on P91 steel hardness [43].

Abson et al. [11] reported that for an appropriately heat-treated P91 parent steel, the hardness values should be between 200−270 Hv. For an appropriately heat-treated P91 weld metal, the hardness is 200−295 Hv, which is very comparable to the base metal hardness. El-Azim et al. [44] reported hardness results for a P91 normalised and tempered base metal and a PWHT (760°C for 2 h) weld of 225 $Hv_{0.1}$ and 240 $Hv_{0.1}$, respectively.

2.5.3 Tensile properties

Table 2.3 presents tensile properties of P91 base metal and weldment [37, 45]. The base metal results reported by Di Gianfrancesco et al. [34] and Sireesha et al. [42] in Table 2.3 are both in normalised and tempered condition but show significant differences. Di Gianfrancesco et al. [34] summarised results of tests performed over two decades and the specific chemical compositions were not reported. The tensile strength and yield strength of as-welded P91 are superior to those of the base metal but the elongation was lower. This was a result of the untempered martensitic weld structure.

Table 2.3 *P91 base metal and weld metal tensile properties [37, 45].*

Material	*Yield strength (MPa)*	*UTS (MPa)*	*Elongation (%)*	*Reduction in area (%)*
Base metal	723	843	12.5	64
Base metal [37]	525	707	23	34
As-welded	1199	1451	8.9	34
PWHT 730 C/ 2h	873	960	8.2	52
PWHT 760 C/ 6h	673	786	11.2	51

2.5.4 Toughness

P91 steels are intended for application at temperatures of 500−600°C, which raised the argument of the relevance of specifying toughness requirements, especially in the weld metal. However, there are situations during construction or testing where parts may be structurally loaded or pressurised at room temperatures [46]. Toughness of weldments is an important required during hydro-testing of components welded from P91 steel to prevent failure [6].

The AWS standard does not stipulate impact requirements for P91 weld metal but EN 1599: 1997 specifies a minimum average of 47 J at 20°C [46]. Zhang et al. [46] also stated that the toughness requirements for weld metal after a prescribed PWHT is applied are in the range of 35−50 J when tested at ambient temperature.

Application of PWHT at 760°C for 3 h can optimise toughness to values similar to that of the base metal. Figure 2.8 shows the toughness of weld metal after various temperatures and hold times of PWHT. Improved toughness is observed with high temperatures and increased hold time [4].

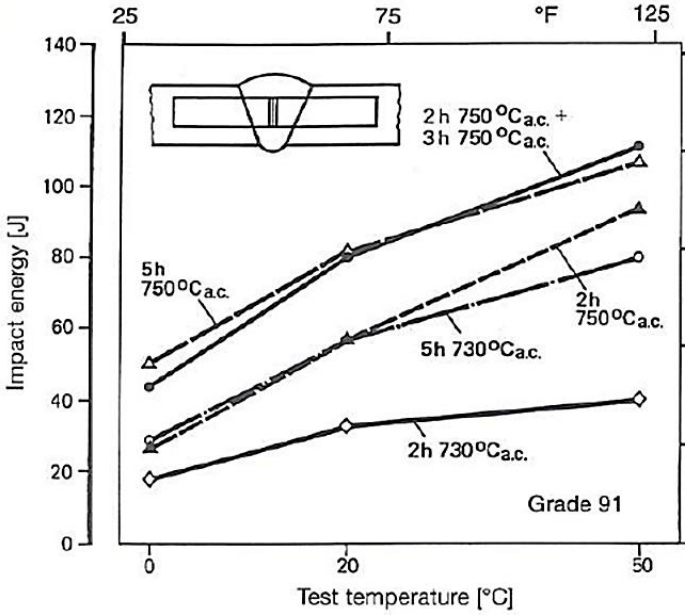

Fig. 2.8 P91 weld metal toughness after post-weld heat treatment [4].

2.6 Role of alloying elements in P91 steel

In this study, five alloying elements (Cr, Ni, Mn, Si, and Mo) were varied in the weld metal. The roles of these elements in P91 steel are considered below.

Chromium (Cr) is the main alloying element in P91 steels. Cr is a ferrite-stabiliser and has a strong influence on the ferrite factor (FF) and in suppressing the delta ferrite–austenite transformation temperature (Ae_4). Increasing the Cr content reduces the "austenite-only" region ($Ae_4 - Ae_3$), which increases the potential for delta ferrite presence in the final microstructure [7]. Anderko et al. [47] reported that delta ferrite increased to between 0% to 25% phase fraction with a Cr increase of 9% to 14% in six melts of martensitic high-Cr steel. The mean chemical composition of the six melts was: 0.13% C, 0.34% Si, 0.63% Mn, 9%−14% Cr, 0.65% Ni, 0.60% Mo, 0.27% V, 0.18% Nb. The influence of Cr between 10% to 13% on the performance of high Cr steels was investigated by Liu et al. [48] and about 2% delta ferrite was observed when Cr increased to 13 mass%. Cr reacts with C and N present in modified 9Cr-1Mo steels to form mainly $Cr_{23}C_6$ carbide and Cr_2N nitride precipitates. Cr carbonitrides play a significant role in increasing creep strength for elevated-temperature application [29, 48]. The peak creep strength of modified 9Cr–1Mo steels was obtained at about 9.5 mass% Cr [49]. Abe [41], in Fig. 2.9, showed the influence of Cr on the ductile-to-brittle transition temperature (DBTT) and creep-rupture strength at 600°C after 1000 h in (2–15)Cr-2W-0.1(mass%)C steels. An addition of Cr from 2% to 5% to 9% where the steels contains tempered martensite or tempered bainite significantly increased the creep-rupture strength but the increase in DBTT was muted. At Cr concentrations above 10%, the steel contained dual phases of martensite and delta ferrite. Abe [38] reported that an increase to 15% Cr increased the amount of delta ferrite, which pushed up the DBTT and lowered the creep strength.

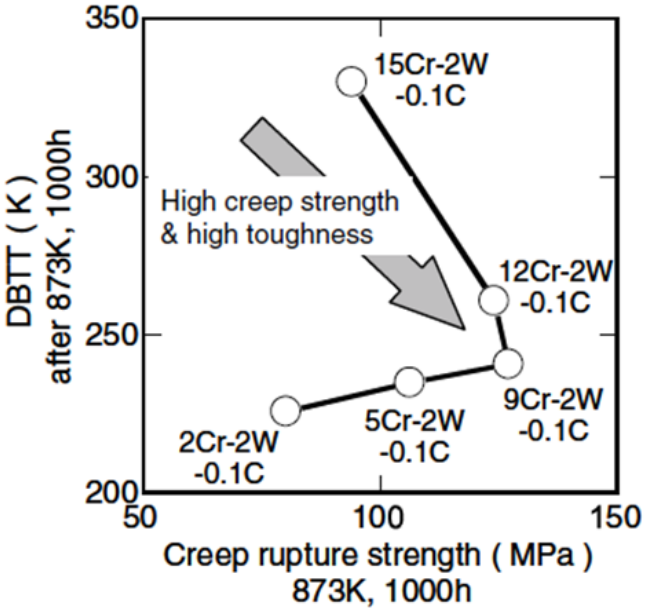

Fig. 2.9 Influence of Cr on the correlation between ductile-to-brittle transition temperature and creep-rupture strength at 600°C after 1000 h [41].

Cr improves resistance to oxidation and corrosion, and has important effects on toughness and elevated-temperature strength. To achieve sufficient oxidation and corrosion resistance in pressure steam turbine rotors, which operate at 650°C, Cr is required to be at least 9 mass% [48].

Nickel (Ni) is a strong austenite former. An increase of Ni in P91 steel widens the ($Ae_4 - Ae_3$) temperature range and lowers the Ae_1 temperature. These factors ensure complete austenitic transformation, which translates to a fully martensitic final microstructure [50]. The addition of Ni to P91 steel improves toughness of the weld metal [50]. Ni addition depresses the Ae_1 temperature, bringing it closer to the PWHT temperature. Thus, care must be taken to ensure that Ae_1 is not so low that PWHT causes some austenite to form, which upon cooling will transform to fresh martensite [46]. Excess amounts of Ni can also adversely affect the creep properties of P91 steel because it promotes the formation of unwanted $M_6(C,N)$, which exhibits a high coarsening rate at elevated temperatures that destabilizes $M_{23}C_6$ precipitates during service [29]. Kimura et al. [51] reported the impact of Ni on the creep-rupture strength (Fig. 2.10) and creep rate with time (Fig. 2.11) at 600°C. Kimura et al. [48] observed that long-term creep-rupture strength in P91 steel decreased and there was a rapid increase in creep rate with increase in Ni content [51]. Kimura et al. [48] attributed the negative effect of Ni on creep properties to the instability of MX carbonitride precipitates through creep. Reduction in phase transformation temperature of Ae_1 with increase in Ni may lower stability of the precipitates at higher temperatures [51].

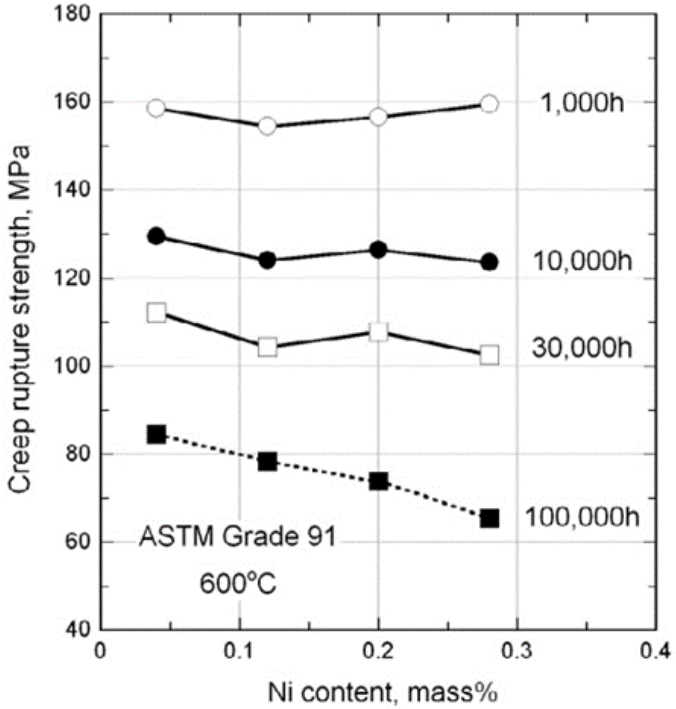

Fig. 2.10 Influence of Ni in creep-rupture strength of P91 steel at 600°C [51].

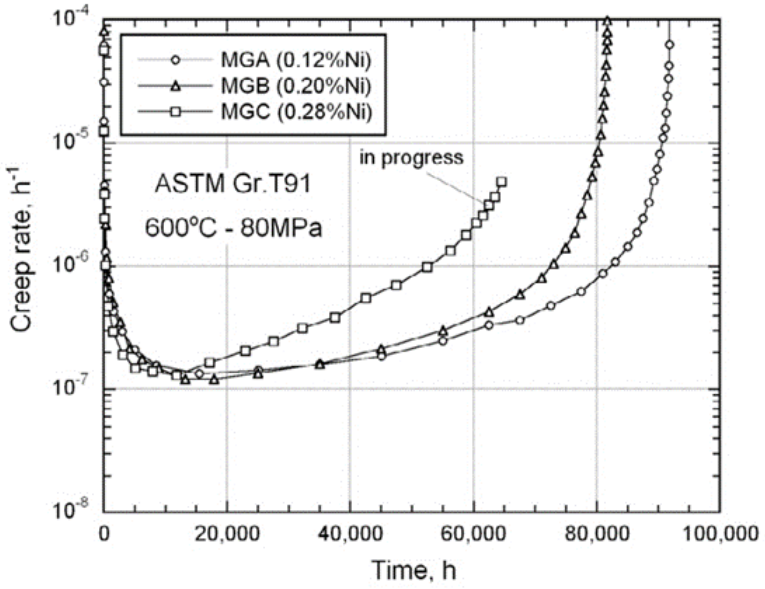

Fig. 2.11 Creep rate in relation to time for P91 steels with varying Ni content [51].

Manganese (Mn) is a austenite stabiliser and, as with Ni, lowers the Ae_1 temperature and M_s and M_f temperatures [13]. Mn and Ni are very effective in preventing the retention of delta ferrite, but their total amount (Mn + Ni) in the weld metal is limited to 1.5% maximum as a safeguard against austenite reformation during PWHT [46]. Swindeman et al. [5] reported that retained austenite of up to 20% was observed in modified 9Cr–1Mo steels when (Ni + Mn) reached 1.4%. This was because, at these high levels of (Ni + Mn), the Ae_1 lowers to 780°C, the M_s lowers to below 350°C, and the M_f drops to lower than the preheat temperature of 200°C.

Mn is an effective deoxidant and is added in the P91 weld metal at concentrations above that of the base metal to ensure a sound weld metal [46]. To allow sufficient Mn in weld consumables for effective oxidation, the Ni is limited, which compromises toughness of the weld. Mn has little effect on mechanical properties but does appear to provide minimal solid-solution strengthening [52].

Silicon (Si) is a ferrite stabilizer. Increasing its content in P91 weld metal will result in a higher volume fraction of delta ferrite in the microstructure [50]. Si is a strong deoxidant, so its controlled addition to weld consumables is beneficial. Si, to a lesser degree than Cr, contributes to oxidation resistance but negatively affects toughness [46]. Chen et al. [53] reported the influence of Si on the reduced-activation ferritic/martensitic alloy. The prior austenite grain size was observed to reduce with larger Si concentration. Because Si is not a carbide-forming element, the grain refinement was attributed to the increase of Ae_3 temperature with the increase of Si. Chen et al. [53] further reported that increasing Si encouraged the precipitation of Laves phases by reducing the solubility of Mo and W in the 9Cr−2Si ferritic/martensitic structure.

Si is limited in P91 steel because it is known to form several iron silicides (FeSi, Fe_2Si, Fe_3Si, Fe_5Si_3) and a Cr_3Si intermetallic, all of which tend to embrittle the structure and

lower toughness. Si is also known to segregate during solidification, resulting in the nucleation of low-melting phases, especially with Ni [52].

Molybdenum (Mo) is a ferrite stabiliser and must thus be limited to avoid delta ferrite presence in the final weld microstructure. Mo increases the upper and lower critical temperatures (Ae_3 and Ae_1, respectively), which reduces the austenite-only region. Mo lowers the M_s temperature [26]. Mo is a strong ($M_{23}C_6$) carbide former [13] and also contributes significant solid–solution strengthening, and is thus the most important element that determines high-temperature strength in heat-resistant steel [54]. Excessive Mo can be detrimental in long-term creep strength owing to the formation of Fe_2Mo Laves phase that depletes the Mo in solution [29, 55]. Fe_2Mo has been shown not to be effective in blocking dislocation motion during creep. In short-term creep, Mo extends the primary creep stage and enhances the creep strength by retarding the coarsening rate of $M_{23}C_6$ [1]. Hald et al. [25] concluded that at elevated temperatures, solid-solution strengthening from Mo had negligible influence on long-term microstructure stability of 9%−12% Cr steels. Precipitation hardening by pinning of dislocations and subgrain boundaries must be considered as an important strengthening mechanism in 9%−12% Cr steels under creep load. Golanski [56] reported that Mo elevates the recrystallization temperature and counteracts temper embrittlement.

Chapter 3
Welding Metallurgy of P91 Steel

3.1 Introduction

P91 steels have good weldability if the specified welding requirements, such as preheating and PWHT to temper the martensitic weld, are applied. Incorrect welding practice can result in defects, such as delayed cracking, reheat and hot cracking, and sensitization [57]. P91 steel has high hardenability and, consequently, is considered as more challenging to fabricate than austenitic stainless steel. The main reason for failure of P91 welds are the presence of delta ferrite, segregation of impurity elements, over-coarsening of austenite near the fusion line, and formation of an inter-critical region. In specific conditions, such as inadequate PWHT, sensitization has also been observed which could lead to intergranular corrosion [57].

3.2 Fusion Zone

The fusion zone is the region in the weldment that is melted and re-solidifies upon cooling. When a filler material is used, the fusion zone comprises of a admixture of the filler material and base material [58]. The performance of P91 weldments primarily depends on the appropriate chemical composition of the weld; therefore, the filler metal used and dilution are important parameters.

During welding of P91 alloy, the primary phase during solidification is delta ferrite, which, upon further cooling, transforms to austenite [23]. At temperatures below M_s, austenite transforms to martensite [59]. The as-welded fusion zone microstructure consists of martensitic lath packets that form inside the PAGB with orientation in uniform direction. The untempered martensitic microstructure of the weld metal results in increased strength and hardness, poor toughness, and susceptibility to cracking. In as-welded condition, no precipitates are observed in the weld fusion zone except for M_3C particles [16]. The microstructure of P91 weld bead after PWHT is tempered martensite with Cr-rich $M_{23}C_6$ and MX precipitates preferentially formed along the PAGB [60, 61]. Arivazhagan et al. [57] reported on P91 weld microstructure after PWHT at 760°C for 2 h and 5 h. The weld metal PWHT for 2 h contained extensive $M_{23}C_6$ precipitates in a martensitic matrix. Delta ferrite phase of less than 2% was observed in the form of islands in the matrix. Carbonitride precipitates occurred in the grain interior and along the PAGB. At high magnification, the weld showed Cr-rich precipitates along the martensite lath boundaries. The morphology of Cr-rich precipitates varied from spherical to elongated, and promoted ductile fracture [60]. After 5 h, sub-grain formation was well defined and there was an elevated amount of V and Nb contents in the precipitates [60]. Sireesha et al. [62] observed a dense dislocation structure within the martensite laths of P91 weld that was tempered at 750°C for 1 h. This implied that the applied tempering was not adequate for recovery to be complete [62].

Chakrabort et al. [63] conducted a study to evaluate the effect of cooling rate on delta ferrite volume fraction and morphology of a P91 autogenous weld partially melted zone. Gleeble thermal simulator was used to vary cooling rates between 1 and 40°C/s from 1450°C peak temperature. The varying cooling rate did not change the volume fraction of the observed delta ferrite but its morphology changed from polygonal structure to a grain boundary plane with decrease in cooling rate [63]. Chakrabort et al. [60] also stated that the delta ferrite present in the fusion zone was retained from the primary phase that developed during solidification. The morphology and amount of the delta ferrite retained from the solidification of the liquid metal are dependent on the composition of the weld metal and cooling rate experienced during welding [63]. The presence of delta ferrite, even in small quantities, in the final microstructure has a detrimental effect on mechanical properties [7], especially creep-rupture strength in long-term high-temperature applications [48]. Production of P91 base metal always includes austenitisation at temperatures of 1040−1150°C to dissolve any delta ferrite, followed by air cooling and tempering [5]. During fabrication, austenitisation is not a feasible PWHT [18].

The presence of austenite in the weld metal has recently been reported during the characterisation and modelling of non-equilibrium transformation during solidification of P91 alloy [56]. C and other austenite stabilizers have poor solubility in delta ferrite, which results in the reduction of these elements in the ferrite phase. This leads to regions with significant segregation, resulting in incomplete transformation of austenite to martensite and the formation of retained austenite or delta ferrite [59]. Austenite was observed in the interdendritic zone of the weldment [59, 61].

3.3 Heat-affected zone in as-welded condition

P91 steel weldments experience different peak temperatures during welding. Regions in the base metal that experience thermal cycle from temper temperatures below the Ac_1 to just below the melting temperature (T_m) form different structures, referred to as the heat-affected zone (HAZ) [64]. A section of a simulated equilibrium pseudo-phase diagram for P91 and how dissimilar parts of the phase diagram approximately correlate to dissimilar microstructural regions of the HAZ are shown in Fig. 3.1.

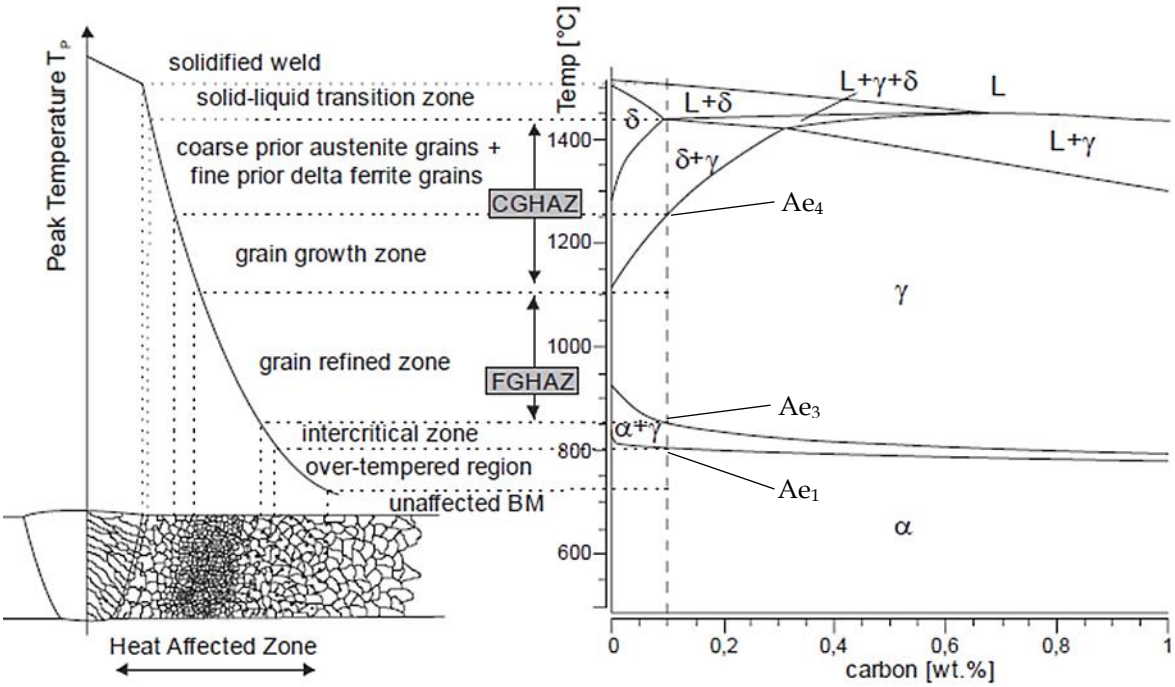

Fig. 3.1 Schematic representation of regions of the heat-affected zone (HAZ) corresponding to the equilibrium phase diagram of P91 steel [11].

The microstructure of the HAZ is primarily depends on the heating and cooling rates during the welding, peak temperature (T_p), the duration at peak temperature, number of welding runs, and succeeding post-weld heating (PWH) and PWHT [59]. Increased heating rates during the welding causes lifting of the transformation temperature, recrystallizing temperature, and solution temperature to higher values [59].

The P91 HAZ is divided into the following sub-zones, as presented in Fig. 3.1.

Coarse-grained heat-affected zone (CGHAZ): This sub-zone is adjacent to the fusion line and experiences the highest temperature during welding (above the Ae_3), which results in the base material transforming to austenite (Ɣ) and austenite phase grain growth. Delta ferrite forms above the Ae_4 temperature and, upon cooling, transforms to austenite but some delta ferrite may often be observed at room temperature in this sub-zone. Owing to the high temperatures, full dissolution of precipitates occurs, which increases the presence of C and N in the matrix and results in high hardness and reduced toughness compared with other HAZ regions [16]. The CGHAZ has no grain boundary precipitates. The dissolution of precipitates also results in reduction of the pinning effect of the precipitates, which results in increased grain growth rate [16].

Fine-grained heat-affected zone (FGHAZ): The temperature in the FGHAZ sub-zone is slightly above the Ae_3 transformation temperature. In this region, the base metal tempered martensite transforms into austenite. Smaller quantities of precipitates are reported in the FGHAZ as a result of their partial dissolution. Undissolved precipitates obstruct the growth of austenite grain through pinning resulting in a finer grain structure [61]. The undissolved precipitates are found at the lath boundaries and PAGB.

The FGHAZ has moderate toughness with low hardness and is regarded as the weakest region in HAZ for elevated temperature applications [16].

Inter-critical heat-affected zone (IC-HAZ): In this zone, incomplete transformation of martensite to austenite happens because the peak temperature is between the Ae_1 and Ae_3 temperatures. Formation of austenite grains occurs at preferred positions like PAGB or martensitic boundaries [16]. In the IC-HAZ, incomplete dissolution of precipitates and coarsening of existing $M_{23}C_6$ precipitates occur. The carbonitrides change in shape from needles to spheres. The microstructure in this region consists of fresh untempered martensite (from the newly formed austenite) and over-tempered martensite [59]. The IC-HAZ is also characterised by low hardness and moderate toughness, and is susceptible to type IV cracking in service [16]. The FGHAZ and IC-HAZ found in P91 welds demonstrate a higher susceptibility to type IV cracking and restricts the lifespan of component [26] shown in Fig. 3. 2 [11] .

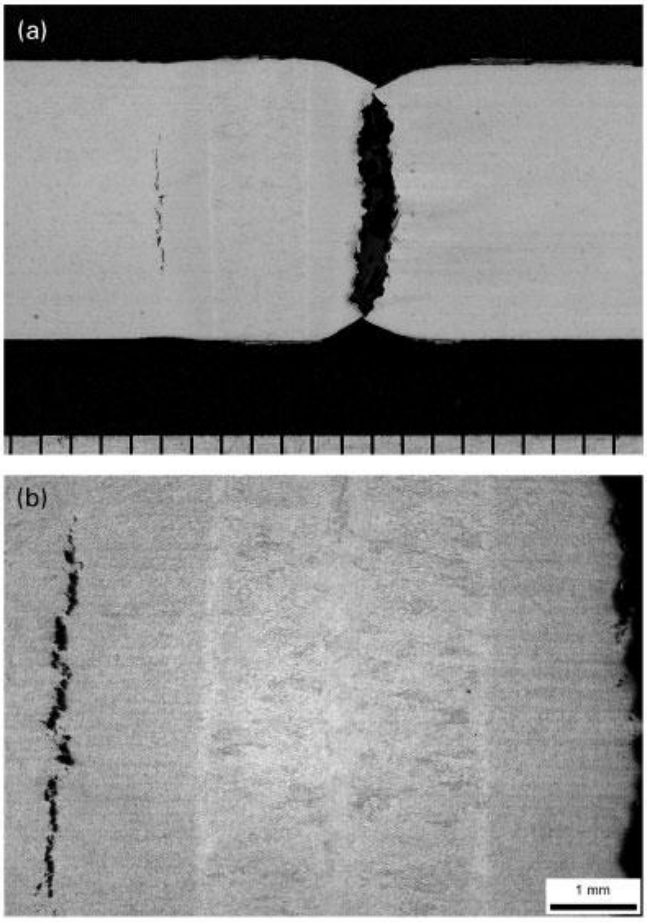

Fig. 3. 2 Type IV cracking in electron beam welded P91 steel [11]

A summary of the transformation reactions at specific temperatures found in the P91 HAZ regions, final structure, and properties are shown in Table 3.1 [1].

Table 3.1 *Heat-affected zone regions, transformation reactions at specific temperatures, and final structure and properties [1].*

Sub-zone	*Temperature*	*Transformation reaction on cooling*	*Microstructure characterisation*	*Mechanical properties (after PWHT)*
CGHAZ	$T_m > T_p > Ae_4$	$\Upsilon + \delta \rightarrow M + \delta$	Untempered martensite, delta ferrite, undissolved NbX, dissolved $M_{23}C_6$	Poor toughness and high strength
	$Ae_4 > T_p > Ae_3$	Coarse $\Upsilon \rightarrow M$	Untempered martensite, undissolved NbX, dissolved $M_{23}C_6$	Poor toughness and high strength
FGHAZ	$T_{\Upsilon\delta} > T_p > Ae_3$	Fine $\Upsilon \rightarrow M$	Untempered martensite, dissolved fine $M_{23}C_6$, undissolved MX and coarse $M_{23}C_6$	Adequate toughness and strength
IC-HAZ	$Ae_3 > T_p > Ae_3$	$\Upsilon \rightarrow M + OM$	Untempered martensite, tempered martensite, dissolved very fine $M_{23}C_6$, undissolved MX, and coarse $M_{23}C_6$	High toughness and poor strength
Over-tempered base zone	$T_p > Ae_1$	OM	Tempered martensite, undissolved MX and coarse $M_{23}C_6$	High toughness and poor strength

T_p = peak temperature experienced during welding; T_m = melting point of steel; Ae_4 = temperature at which Y-to-δ transformation is completed during heating; Ae_3 = upper critical temperature at which a-to-Y transformation is completed on heating; Ae_1 = lower critical temperature at which a-to-Y transformation starts on heating; Y = austenite; δ = ferrite; M = martensite; OM = overtempered martensite.

3.4 Influence of delta ferrite on behaviour and properties of P91 steel

The influence of delta ferrite presence on mechanical properties of P91 steel is generally viewed as detrimental but, in some cases, the reported effect has been inconsistent [65]. Schafer [62] attributed the contradictory results to the presence or absence of dendritic carbides that often envelop the delta ferrite. The dendritic carbides increase in volume fraction with increasing delta ferrite content [65].

3.4.1 Impact properties

In 1991, Anderko et al. [47] studied the influence of delta ferrite on impact properties of martensitic Cr steels. Six samples were produced with Cr contents of 9% to 14%, which resulted in 0% to 25% delta ferrite content. Figure 3.3(a) shows impact energy in relation to the testing temperature and Fig. 3.3(b) displays the DBTT plotted against the amount of delta ferrite. The DBTT was determined from the midpoint between the upper and lower shelf energies. Figure 3.3(b) shows the DBTT results of (2–15)Cr–2W–0.1C martensitic steel against % delta ferrite published by Abe et al. [66, 67], which linearly increases with the amount of delta ferrite. The lower DBTT between the (2–15)Cr–2W–0.1C and (9–14)Cr steels was attributed to the Fe_2W precipitates in the delta ferrite phase.

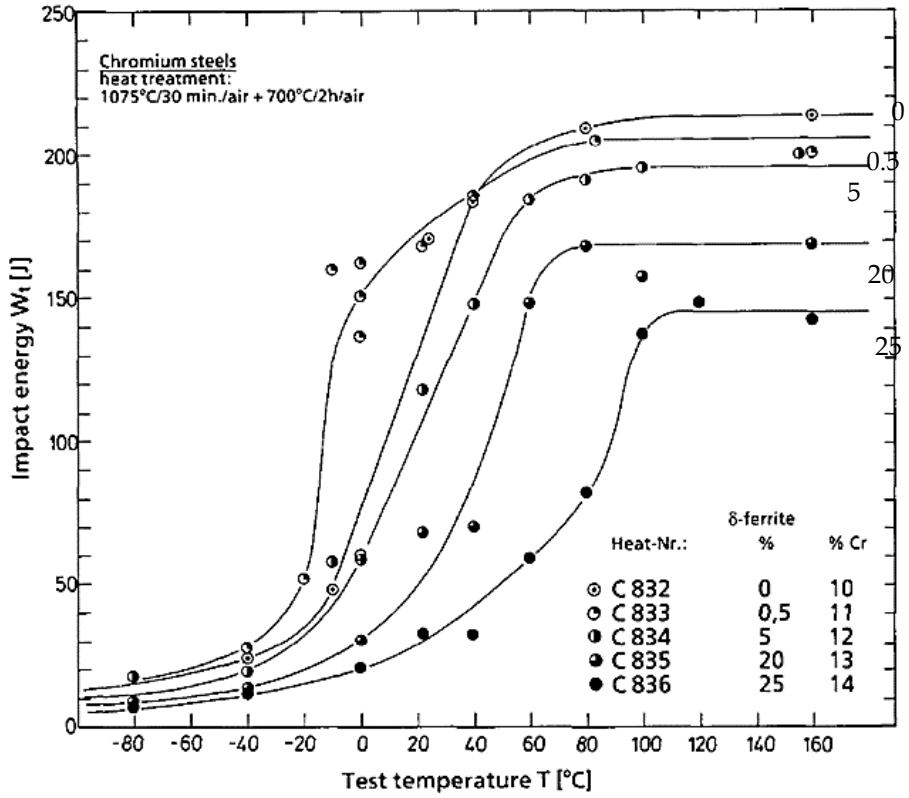

Fig. 3.3 (a) Impact energy in relation to the test temperature. The influence of delta ferrite on ductile-to-brittle transition temperature and upper shelf energy is also observed [47].

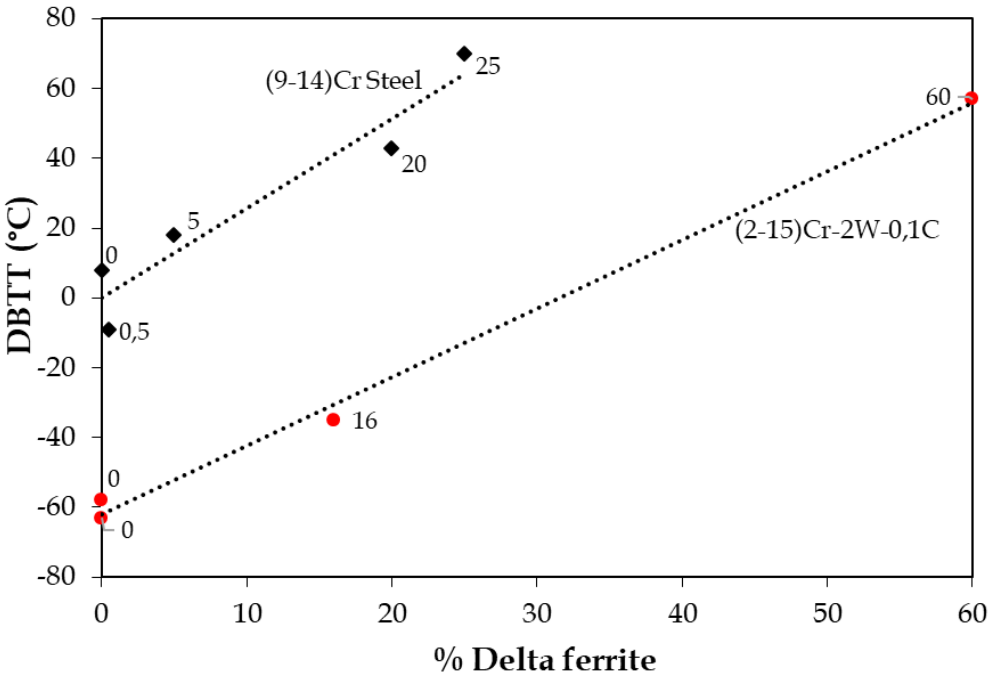

Fig. 3.3 (b) Ductile-to-brittle transition temperature (DBTT) plotted against delta ferrite. The graphs are reconstructed from results published by Anderko et al. [47] and Abe at al. [66].

The reported results shown in Fig. 3.3(a,b) indicate that an increase in delta ferrite fraction led to a reduced upper shelf energy and higher DBTT. A Cr-rich carbide ($M_{23}C_6$) layer that occupied the phase boundary between the martensitic matrix and delta ferrite was observed to increase with delta ferrite volume fraction. This carbide layer was not present at contents below 5% delta ferrite, which is the reason for lower DBTT and greater upper shelf life at 0.5% delta ferrite when compared with a fully martensitic specimen [68].

Anderko et al. [47] concluded that delta ferrite content below 2%−3% can be tolerated in martensitic steels because this improves ductility. Arivazhagan et al. [60] reported that delta ferrite less than 2% with isolated island morphology in the martensitic matrix had no effect on the toughness of P91 weldment. Carrouge et al. [69] also stated that the DBTT of martensitic stainless steel containing 2% delta ferrite was comparable with that of a fully tempered martensitic matrix. An increase of the DBTT by 50°C was observed when the material contained 14% delta ferrite.

The effect of delta ferrite on impact properties was studied by Wang [70], where high-temperature anneal was performed in 13Cr−4Ni martensitic stainless steel to achieve different delta ferrite contents. The existence of delta ferrite decreased both the crack initiation and propagation energies through the impact progress, and altered the fracture mode from dimple to quasi-cleavage as the delta ferrite amount increased. The results also showed that the presence of delta ferrite decreased the impact energy in the transition temperature range (Fig. 3.4) and increased the DBTT of the material.

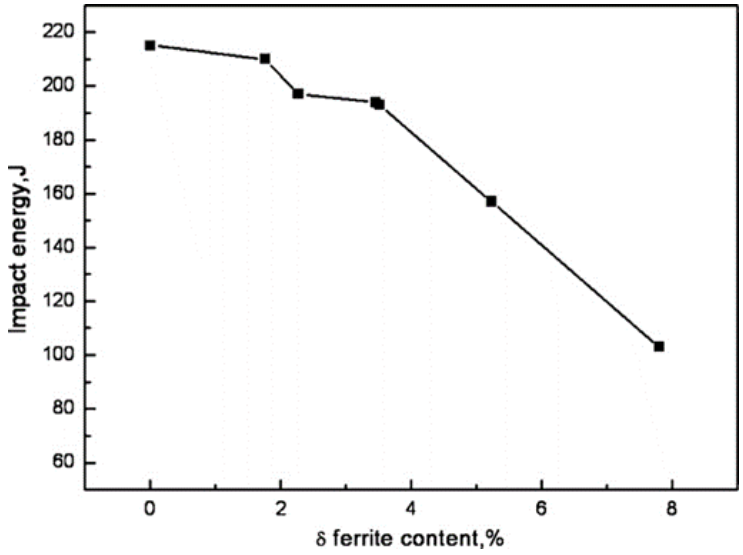

Fig. 3.4 Changes in impact energy with delta ferrite fraction, tested at 0°C [70].

Schafer [65] performed an austenitisation and temper heat treatment on martensitic Cr steel with the intention of evaluating the influence of delta ferrite on impact properties without the influence of dendritic carbides that often encapsulate the delta ferrite grains. Delta ferrite without dendritic carbide precipitates ($M_{23}C_6$) increased both ductility and toughness of the martensitic steel, while the strength was negatively affected. With a different heat treatment, which resulted in increasing dendritic carbides

around an increasing amount of the delta ferrite, all impact properties (ductility, maximum force, and impact energy) decreased [65].

3.4.2 Creep rupture properties and low cycle fatigue

The impact by delta ferrite on creep-rupture properties of high-Cr ferritic steel was reported by Liu et al. [45] in 1989. Three samples were prepared with Cr contents of 10%, 11.5%, and 13%. The samples were austenitised at 1020°C and cooled in air before tempering at 700°C for 2 h. The creep-rupture test was performed at 650 and 700°C. The sample with 13% Cr contained 2% delta ferrite, whereas the other samples were fully martensitic. The increase of Cr from 10% to 11.5% lead to an increased creep-rupture strength. This agrees with the understanding that increasing the Cr content will increase both solution and precipitation strengthening, and thus increase creep-rupture strength. However, the sample with 13% Cr showed a decrease in creep strength, which was attributed to the presence of delta ferrite. Liu et al. [48] concluded that delta ferrite, even at quantities as low as 2%, is detrimental to the long-term creep-rupture strength; the negative effect is accelerated with test temperature.

Sawada et al. [71] analysed two steel samples of the same P91 steel grade, where one sample showed a fully martensitic microstructure and the other showed a microstructure consisting of about 5% volume fraction of delta ferrite in martensitic matrix due to slightly higher Cr content. The short-term creep-rupture strength of both steels was comparable; however, the long-term creep-rupture strength of the steel containing delta ferrite was inferior to that of the fully martensitic steel. The microstructure containing delta-ferrite demonstrated a sudden decrease in creep strength at extended time, attributed to faster growth of precipitates at the delta ferrite/martensite boundary [11, 71]. The decline in creep strength was assumed to be brought about by enhanced coarsening of precipitates and recovery of tempered martensite along the delta ferrite/martensite grain boundaries [72]. Yoshizawa and Igarashi [73] further explained that at increased stress level, no significant difference observed in the deformation characteristics between the fully martensitic steel and the dual phase containing delta ferrite. At reduced stress level, the metal containing delta ferrite exhibited a decrease in creep strength. It was found that the reduction in fine MX precipitates and uneven distribution of MX in the delta ferrite phase resulted in the loss of strength [73].

Kobayashi [71] studied the relation between the presence of delta ferrite in P91 steel and creep strength. Two heats were prepared (MgB and MgC) with similar composition but MgB samples were normalised at 1050°C for 10 min and MgC samples were normalised at 1060°C for 90 min. MgB microstructure contained delta ferrite; MgC was fully martensitic [74]. Figure 3.5 displays the creep stress against time to rupture for both samples tested at temperatures between 500°C and 650°C under stress levels between 30 MPa and 320 MPa. The time to rupture of MgB samples was lower for all test ranges when compared with MgC. The lower creep strength in MgB was as due the presence of delta ferrite in its microstructure [51, 74].

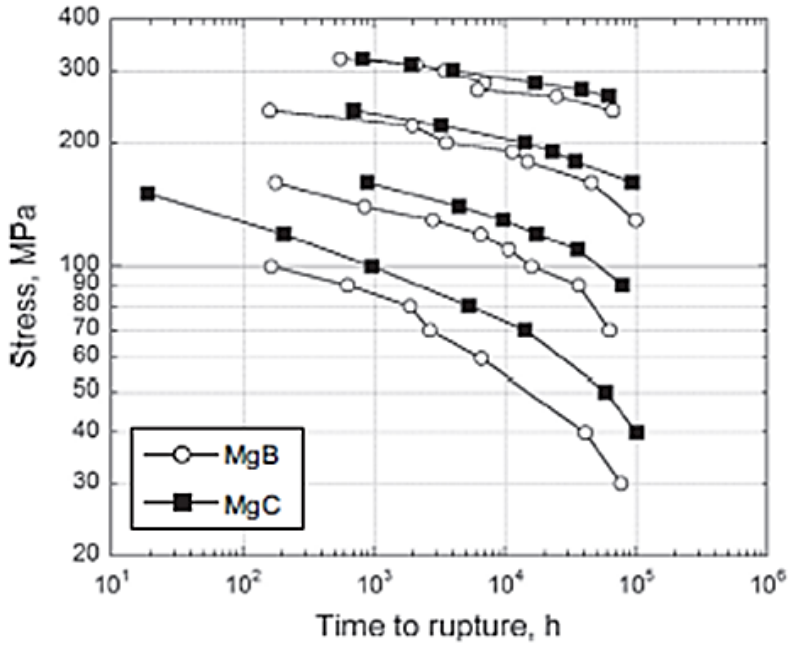

Fig. 3.5 Evaluation of creep stress against rupture time of two P91 steels tested at temperatures between 500°C and 650°C. MgB and MgC are two P91 heats with similar composition but different heat treatments. MgB microstructure contained delta ferrite; MgC was fully martensitic [74].

Abe et al. [64] investigated the increase of creep strength in ferritic steel through the addition of W. The creep-rupture strength linearly increased with increasing W content up to 2% W, where the microstructure was fully martensitic [67]. Above 2% W, the microstructure contained delta ferrite and the creep-rupture strength plateaued.

3.4.3 Tensile properties and hardness

Laha et al. [75] investigated hot tensile properties in P91 weldments and observed that the presence of delta ferrite restricted grain growth, increased strength, and decreased ductility. Liu et al. [48] conducted room-temperature tensile tests on ferritic heat-resistant base metal steels containing Cr in the range of 10% to 13 %. The results indicated that small amounts of delta ferrite have no significant effect on strength [48].

Chandravathi [76] studied the influence of soaking temperature from the range below Ae_1 to above Ae_4 (500−1350°C) on hardness and tensile properties of P91 base metal. At soaking temperatures above 1230°C, the delta ferrite formed along the austenite grain boundaries was retained in the microstructure on quenching. The delta ferrite restricted grain growth [72, 76, 77], therefore the grain size decreased with higher soaking temperatures because of increased amount of delta ferrite. The presence of delta ferrite had a stronger effect than the decrease in grain size on the decrease of hardness of specimens soaked above 1230°C. The tensile strength was reported to slightly increase with the presence of limited delta ferrite due to its effect on grain refinement [76]. Elongation of the P91 steel was improved by the presence of delta ferrite.

Delta ferrite formation in P91 steel metals and welds might improve solidification cracking resistance but could reduce toughness due to notch sensitivity of the delta ferrite phase, and decrease creep ductility at elevated temperature [78].

3.5 Empirical relationships to predict weld microstructure

3.5.1 Historical Background

In the early 1900s, during the development of the austenitic and duplex stainless steels, the quantities and morphology of the ferrite phase present in the weld microstructure were important considerations. This stimulated research on methods to predict weld metal microstructures. Equilibrium phase diagrams are not directly applicable in predicting weld microstructures because they are developed with two or three elements under equilibrium conditions. Empirical relationships to predict weld microstructures based on the alloy chemical composition were developed for cooling rates typical of weld thermal cycles [79].

The first diagram published to predict microstructure was probably that of Strauss and Maurer in 1920 based on wrought materials [76]. The modified Strauss diagram presented in Fig. 3.6 displays the actual Cr and Ni contents on the axes and illustrates the effect of each element [79].

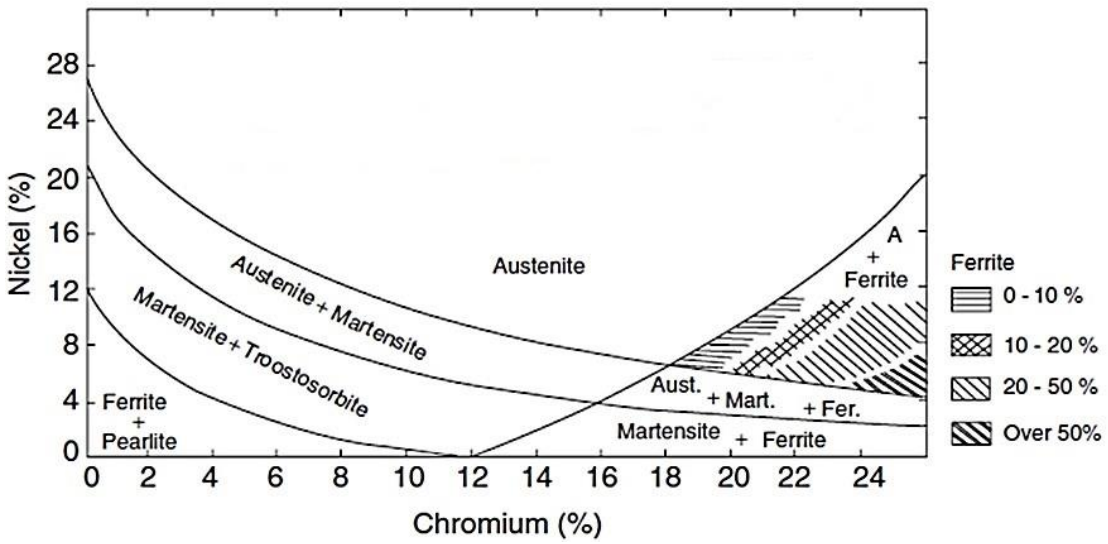

Fig. 3.6 Modified Strauss and Maurer Ni–Cr diagram that allowed prediction of microstructure, developed based on wrought materials [79].

In 1938, Newel and Fleischmann [80] presented an equation to define the region of austenite stability in the Strauss diagram, which was also based on analyses of wrought materials. Newel and Fleischmann's significant contribution was the inclusion of the effect of elements other than Cr and Ni, as seen in Equation (3.1):

$$\mathrm{Ni} = \frac{(Cr+2Mo-16)^2}{12} - \frac{Mn}{2} + 30(0.10 - C) + 8 \qquad (3.1)$$

Ni defined the region of austenite stability in modified the Strauss and Maurer Ni–Cr diagram.

The need for austenitic stainless-steel welds with good ductility and strength in the fabrication of armour materials just prior to and during World War II provided motivation for further improvements in the prediction equations. Feild, Bloom, and Linnert [81, 82] in 1943 presented a modification of the Newell–Fleischmann equation [77], which gave better prediction of austenitic weld metal by moving the austenite-promoting elements to the left side and changing the constant from 8 to 14, as shown in Equation (3.2). This was after they had applied the Newell–Fleischmann equation and found that it did not accurately predict the austenitic weld microstructures [82].

$$\mathrm{Ni} + 0.5\mathrm{Mn} + 30\mathrm{C} = \frac{(\mathrm{Cr}+2\mathrm{Mo}-16)^2}{12} + 14 \qquad (3.2)$$

A significant development in the prediction of weld metal microstructure was the publishing of the 1949 Schaeffler diagram (Fig. 3.7). Schaeffler [79] proposed a diagram with the vertical and horizontal axes given as the Ni-equivalent of (Ni + 0.5Mn + 30C) and Cr-equivalent of (Cr + Mo + 1.5Si + 0.5Cb), respectively. Over the years, the Schaeffler diagram has been shown to be wrong in the application of Mn. The diagram also overlooks the significant influence of N in encouraging the formation of austenite at the detriment of ferrite. Mn does not promote the formation of ferrite to austenite at elevated temperature but does stabilize austenite at lower temperatures [83].

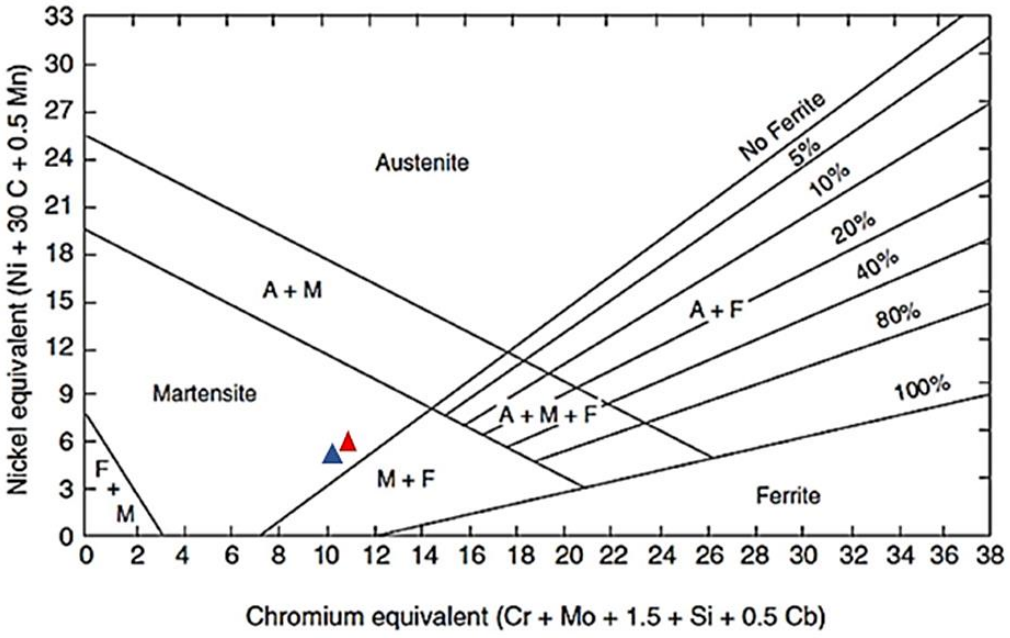

Fig. 3.7 The 1949 Schaeffler prediction diagram [79].The red and blue triangles represent the average P91 compositions of base and weld metals, respectively.

Schneider in 1960 [79] developed a predictive diagram (Fig. 3.8) for cast microstructures based on the Schaeffler diagram but introduced Co and V to the Ni and Cr equivalents, respectively.

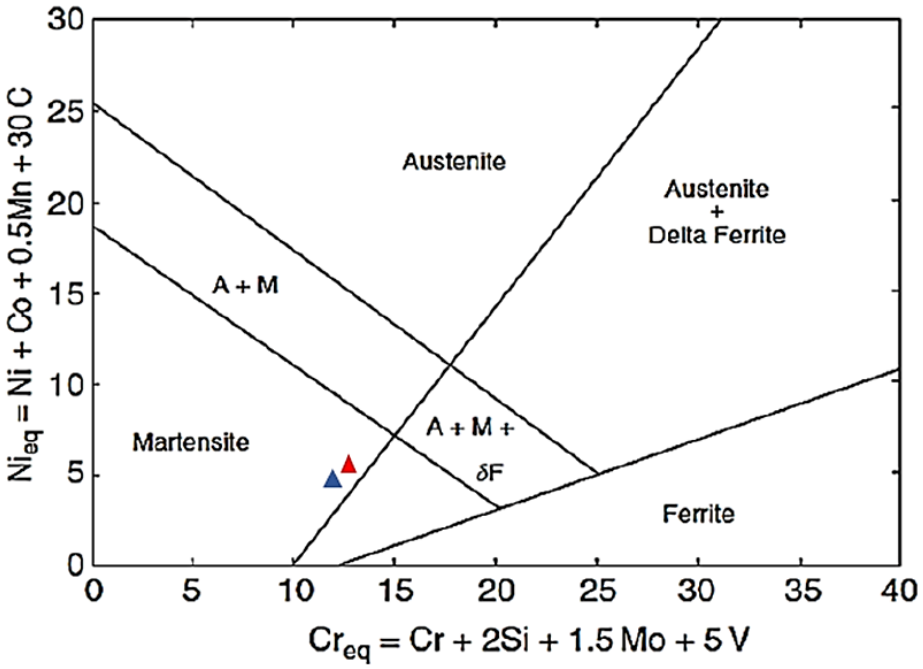

Fig. 3.8 The Schneider diagram developed for cast materials. The red and blue triangles represent the average P91 compositions of base and weld metals, respectively.

In 1973, Long and DeLong [76] proposed a predictive diagram that was based on an investigation to refine the portion of the Schaeffler diagram that contains major austenitic stainless-steel weld compositions. Figure 3.9 shows the Long–Delong diagram, which allowed for quantitative and reproducible prediction of the delta ferrite content [79]. Note that the P91 composition is outside borders of the Long–Delong diagram.

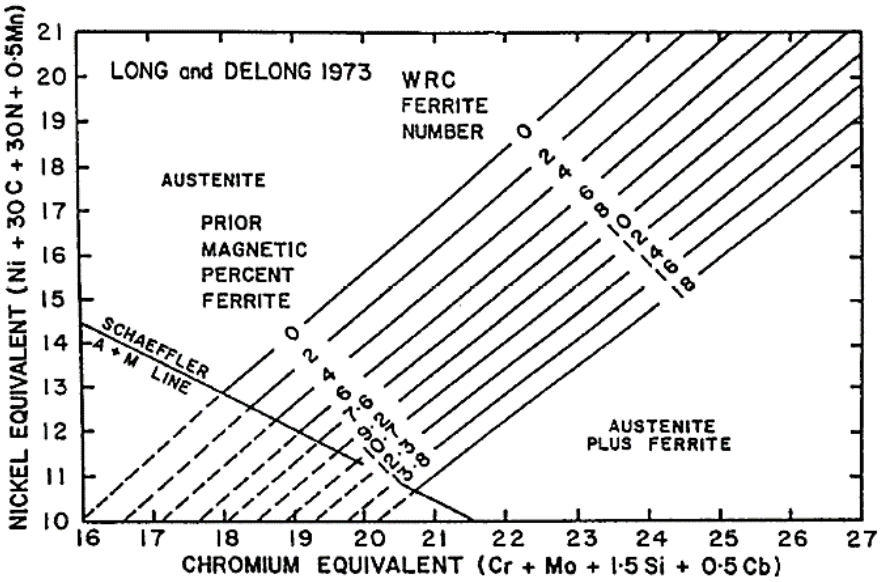

Fig. 3.9 The 1973 Long and DeLong prediction diagram with improved accuracy and introduction of the ferrite number scale.

DeLong and Reid [49] found that N had the same influence as C in stabilising austenite, which led to the modification of the Ni equivalent, as shown in Equation (3.3):

$$Ni_{eq} = Ni + 0.5Mn + 30C + 30N \quad (3.3)$$

The difficulty of quantitatively measuring the ferrite content led to Long and DeLong's inclusion of the ferrite number (FN) scale to the diagram [52]. The FN was adopted in 1973 by the Welding Research Council Subcommittee for quantifying ferrite and the diagram was known as the DeLong–WRC diagram.

In 1988, Siewert et al. [84] proposed a new diagram (Fig. 3.10), known as the WRC–1988 diagram, which included the solidification mode boundaries and included an increased range of compositions, from 0 to 100 FN.

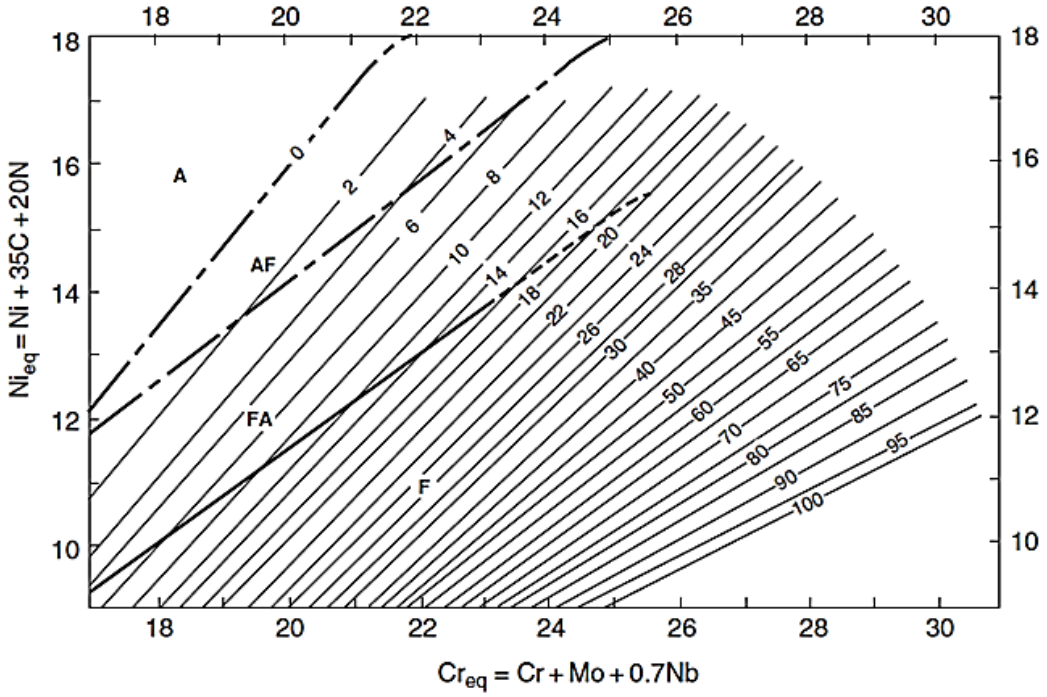

Fig. 3.10 WRC–1988 diagram that contains solidification mode boundaries.

Balmforth and Lippold (1998) [85] demonstrated that although the Schaeffler diagram had been used extensively for many years, it was not sufficient for accurately predicting weld metal microstructure in the ferrite–martensite region. Balmforth and Lippold [85] plotted data for percentage volume fraction of ferrite in martensitic alloys on the Schaeffler diagram presented in Fig. 3.11. The results showed that the martensitic alloys predicted to contain some ferrite were actually fully martensitic. The data in Fig. 3.11 indicate that the ferrite–martensite region of the Schaeffler diagram is not sufficient to accurately predict the weld metal constituents [85].

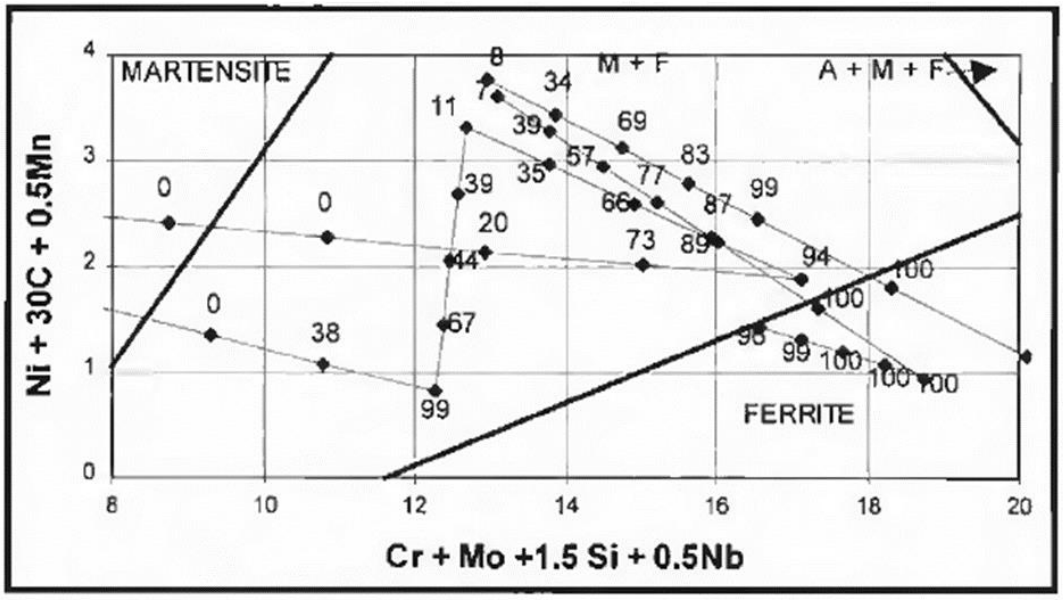

Fig. 3.11 Schaeffler diagram with % volume fraction of ferrite [85].

3.5.2 Prediction of delta ferrite in P91 steel weld

The two most relevant empirical relationships according to Faulkner et al. [86, 87] for P91 steel welds are the Schaeffler modified equations (3.4 and 3.5):

$$Cr_{eq} = Cr + 1.5Si + Mo + 0.5Nb + 0.75W \quad (3.4)$$

$$Ni_{eq} = Ni + 0.5Mn + 30C + 30N + 0.3Cu + Co \quad (3.5)$$

and the Schneider equations (3.6 and 3.7):

$$Cr_{eq} = Cr + 2Si + 1.5Mo + 5V + 1.75Nb + 0.75W \quad (3.6)$$

$$Ni_{eq} = Ni + 0.5Mn + 30C + 25N + 0.3Cu \quad (3.7)$$

A convenient method was to utilise the ferrite factor (FF) ($Cr_{eq} - Ni_{eq}$), defined as the measure of the balance between ferrite and austenite-stabilising elements [88].

Faulkner et al. [86] reported on a series of shielded-metal arc welds (SMAW) from the 9CrMoV alloy but contained Cu and Co and W instead of Mo. Falkner et al. [86] observed that an increase in the Cr and Cr_{eq} values lead to an increase in the delta ferrite quantities of various Cr–Mo alloy systems, shown in Fig. 3.12. The results were observed from the final bead deposited in the weld, which was not influenced by subsequent beads. The graph shows the average ferrite level as a function of Cr_{eq}, defined using the original Schaeffler relationship.

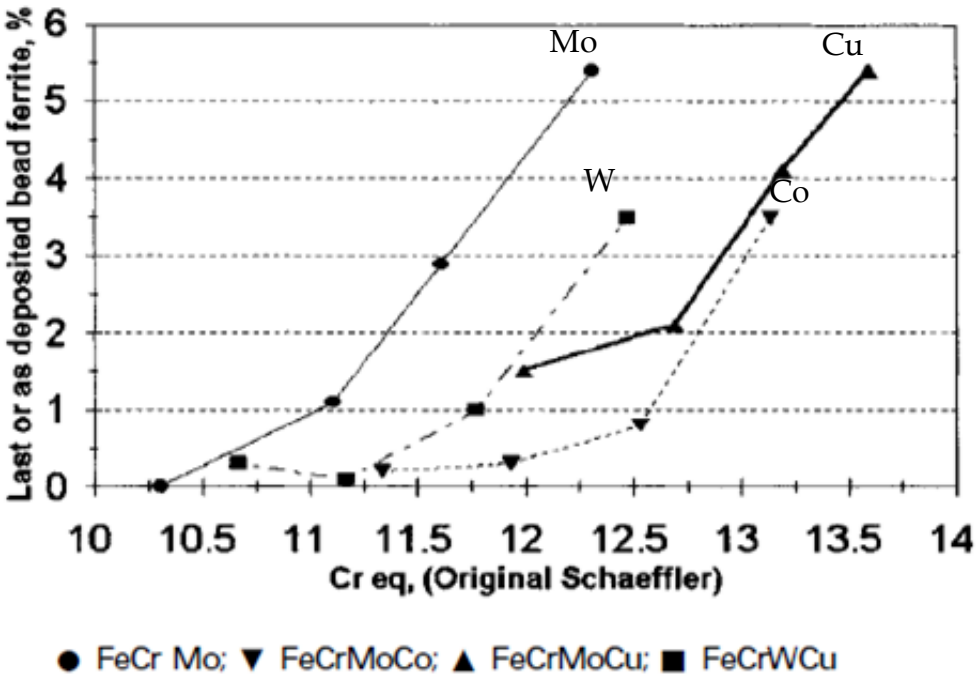

Fig. 3.12 Influence of Cr equivalent on ferrite in deposited weld metal [86].

The compositions of the reported FeCrMo welds stated in Table 3.2 complied with AWS A5.28 requirements [86]. Faulkner et al. [80] concluded from their experimental results that for a weld metal to be fully martensitic, the Cr_{eq} and FF should not exceed 13 and 8.0, respectively, based on the Schneider relationships, and 12.5 and 6.0 using the modified Schaeffler relationship.

Table 3.2 *Weld metal compositions used to plot the data in Fig. 3.12*

Weld metal (Fe+)	Cr	C	Si	Mn	Mo	Ni	Co	Cu	B	N	Nb	V	W
Cr+Mo	8·4	0·129	0·22	0·50	1·55	0·43	0·02	0·02	0·012	0·02	0·057	0·25	0·02
	9·2	0·129	0·22	0·50	1·55	0·43	0·02	0·02	0·012	0·02	0·057	0·25	0·02
	9·7	0·129	0·22	0·50	1·55	0·43	0·02	0·02	0·012	0·02	0·057	0·25	0·02
	10·4	0·129	0·22	0·50	1·55	0·43	0·02	0·02	0·012	0·02	0·057	0·25	0·02
Cr+Mo+Co	9·4	0·134	0·23	0·52	1·56	0·42	1·17	0·02	0·012	0·02	0·055	0·25	0·02
	10	0·134	0·23	0·52	1·56	0·42	1·17	0·02	0·012	0·02	0·055	0·25	0·02
	10·6	0·134	0·23	0·52	1·56	0·42	1·17	0·02	0·012	0·02	0·055	0·25	0·02
	11·2	0·134	0·23	0·52	1·56	0·42	1·17	0·02	0·012	0·02	0·055	0·25	0·02
Cr+Mo+Cu	10·1	0·128	0·23	0·52	1·52	0·48	0·02	1·11	0·012	0·02	0·053	0·24	0·02
	10·8	0·128	0·23	0·52	1·52	0·48	0·02	1·11	0·012	0·02	0·053	0·24	0·02
	11·3	0·128	0·23	0·52	1·52	0·48	0·02	1·11	0·012	0·02	0·053	0·24	0·02
	11·7	0·128	0·23	0·52	1·52	0·48	0·02	1·11	0·012	0·02	0·053	0·24	0·02
Cr+W+Cu	10·3	0·123	0·21	0·49	0·03	0·48	0·02	1·11	0·010	0·02	0·044	0·23	1·42
	10·8	0·123	0·21	0·49	0·03	0·48	0·02	1·11	0·010	0·02	0·044	0·23	1·42
	11·4	0·123	0·21	0·49	0·03	0·48	0·02	1·11	0·010	0·02	0·044	0·23	1·42
	12·1	0·123	0·21	0·49	0·03	0·48	0·02	1·11	0·010	0·02	0·044	0·23	1·42

Onoro [89] reported that a Schneider Cr equivalent value of lower than 13.5, a minimum Ni_{eq} of 5.5, and FF lower than 8 were necessary to achieve a fully martensitic microstructure of modified 9Cr–1Mo steel welds. Onoro [83] also used the Newhouse and Kaltenhauser equations (3.8 to 3.11), which are a modification of the Schneider empirical formulae. These authors [43] also referred to Schneider equivalent limits to avoid delta ferrite.

Newhouse formulae:

$$Cr_{eq} = Cr + 6Si + 4Mo + 11V + 5Nb + 1.5W \quad (3.8)$$

$$Ni_{eq} = 2Mn + 4Ni + 40C + 30N + 2Co + Cu \quad (3.9)$$

Kaltenhauser formulae:

$$Cr_{eq} = Cr + 6Si + 4Mo + 8Ti + 2Al + 4Nb \quad (3.10)$$

$$Ni_{eq} = 2Mn + 4Ni + 40(N + C) \quad (3.11)$$

Newhouse and Kaltenhauser [89] increased the weighted effects of Mo and Si as ferrite-forming elements and included alloying elements like Ti, Al, W, Cu, and Co.

Sireesha et al. [62] in 2001 used two empirical equations (3.12 and 3.13) to estimate the tendency of ferrite retention. The first was the Cr equivalent, which was a modified Newhouse formula with increased weighting for elements like Al and Ti [90]:

$$Cr_{eq} = Cr + 6Si + 4Mo + 1.5W + 11V + 5Nb + 12Al + 8Ti - 40C - 2Mn - 4Ni - 2Co - 30N - Cu \quad (3.12)$$

The second equation was the Kaltenhauser ferrite factor (KFF):

$$KFF = Cr + 6Si + 4Mo + 4Nb + 2Al + 8Ti - 2Mn - 2Ni - 40(C + N) \quad (3.13)$$

Sireesha et al. [59] recommended that the Newhouse Cr_{eq} and KFF have values of maximum 10 and 8, respectively, to avoid ferrite retention in welds. Sireesha et al. [59] reported that delta ferrite was observed in the microstructure of P91 welds although Cr_{eq} and FF were 6.7 and 4.3, respectively. The observed ferrite was attributed to inhomogeneity in the composition of the weld and rapid cooling rates [45]. Pandey in 2016 [91] reported Cr_{eq} and KFF of 8.05 and 6.45, respectively (calculated based on equations 3.13 and 3.14), yet delta ferrite was observed in several areas of the P91 microstructures. Barnes et al. [88] recommended that to achieved fully martensitic P91 welds, the Cr_{eq} and KFF values should be less than 8 and 6, respectively.

Pandey et al. [21] in 2016 analysed a P91 base metal that was austenitised at 1040°C, air cooled, and tempered at 760°C, where the Kaltenhauser formula was used to calculate Cr_{eq} and FF, which were found to be 7.13 and 5.7, respectively. Pandey et al. [21] stated that to obtain a fully martensitic structure with the absence of delta ferrite, Cr_{eq} should be less than 10 and FF should be less than 8. Although these Cr_{eq} and FF values were well below than recommended required values, delta ferrite patches were observed in the microstructure [24].

Paul et al. [86] in 2007 calculated Cr_{eq} using Equation 3.10 for GMAW (multiple beads). Cr_{eq} was 7.03 and no delta ferrite was observed. Cr_{eq} of the base metal was calculated to be 10.38 and significant amount of delta ferrite was observed in the HAZ [92].

In 2013, Arivazhagan and Kamaraj [57] performed metal-cored welds of modified 9Cr–1Mo steel and the compositions met the AWS A5.28 specification. Three of the welds with FF < 8 were fully martensitic and one weld with FF value of 10.36 contained delta ferrite at less than 2% [60]. Arivazhagan et al. in 2015 [87] reported calculated values of the Schneider Cr_{eq} and Ni_{eq} (Equations 3.6 and 3.7) of P91 weld metal, and obtained

values of 11.44 and 4.29, respectively. The as-welded microstructure contained about 0.5% delta ferrite, predominantly at grain boundaries, even with the Schneider Cr_{eq} and Ni_{eq} well within the recommended values [93].

Using the Cr–Ni balance (CNB) formulation (Equation 3.14) from a modified Newhouse's equation, Swindeman et al. [5] stated that delta ferrite is not usually present if the CNB is less than 10; for CNB above 12, significant quantities of delta ferrite are observed:

$$CNB = Cr + 6Si + 4Mo + 1.5W + 5Nb + 9Ti + 11V + 12Al - 40C - 30N - 2Mn - 4Ni - Cu. \quad (3.14)$$

Table 3.3 summarises the maximum recommended values of the Schaeffler, Schneider, Kaltenhauser, and Newhouse empirical relationships from different authors. Weld metal containing empirical relationships values above the maximum recommended limits increases the possibility of delta ferrite in the as-welded condition.

Table 3.3 *Empirical relationships recommended values to avoid delta ferrite.*

	Cr_{eq} (max)	***Ni_{eq} (min)***	***FF (max)***	***CNB (max)***
Schaeffler	12.5 (Faulkner [86])	–	6 (Faulkner [86])	–
Schneider	13.0 (Faulkner [86]) 13.5 (Onoro [89])	5.5 (Onoro [89])	8 (Faulkner [86]) 8 (Onoro [89])	–
Kaltenhauser	10 (Pandey [24])	–	8 (Sireesha [45]) 6 (Barnes [88]) 8 (Pandey [24])	–
Newhouse	–	–	10 (Sireesha [45]) 8 (Barnes [88])	10 (Swindeman [5])

Weld microstructure prediction methods and related research have been extensively studied to improve their accuracy in different alloys [79]. Significant progress has been reported, but delta ferrite in P91 as-welded microstructures has been observed in alloys with Cr_{eq} and FF values well below the recommended values [24, 45].

3.6 Effect of cooling rate on delta ferrite

The cooling rate during welding is mainly influenced by the heat input and preheat temperature. Abd El-Rahman et al. [94] reported the effect of heat input on the retained volume fraction of delta ferrite in P91 multi-pass SMAW. The reported results were produced using three heat inputs: 1.2, 2.3, and 3.2 kJ/mm. Abd El-Rahman et al. [88] observed that the volume fraction of delta ferrite decreased with increase in heat input. Onoro [83] in 2006 conducted experiments where P91 weld pads were built up by SMAW. The pads were built up with a minimum of eight layers, with the interpass temperature controlled between 200−250°C. The microstructure of the last beads consistently contained 1%−2% more delta ferrite than beads in the centre. Onoro [89] concluded that the higher cooling rate in the last bead increased the delta ferrite content.

Pandey et al. [89] in 2017 stated that autogenous gas–tungsten arc (GTA) welds contained higher volume fraction of delta ferrite because of their fast cooling rate and

wide solidification range, compared with GTAW with filler material, which contained lower delta ferrite because of their slower cooling rate, and narrower solidification range [95].

Zhou et al. in 2017 [36] reported a similar observation on the effect of cooling rate on delta ferrite retention from P92 alloy dilatometric experiments. The samples were rapidly heated to a peak temperature of 1350°C and then cooled at 1°C/s, 30°C/s, 50°C/s, and 200°C/s. It was observed that between 30 and 50°C/s, the delta ferrite remained the same, but a significant increase of delta ferrite volume fraction was observed at 200°C/s cooling rate, as shown in Fig. 3.13 [36]. At the cooling rate of 1°C/s, the austenite-to-delta ferrite transformation persisted above Ae_4 temperature because of the large proportion of austenite relative to the equilibrium fraction. Consequently, the starting amount of delta ferrite increased, which accounts for the high-volume fraction of delta ferrite reported in Fig. 3.13 for 1°C/s cooling rate. This observation of Zhou et al. is applicable in multi-pass welding where previous beads are reheated above the Ae_4 temperature [36].

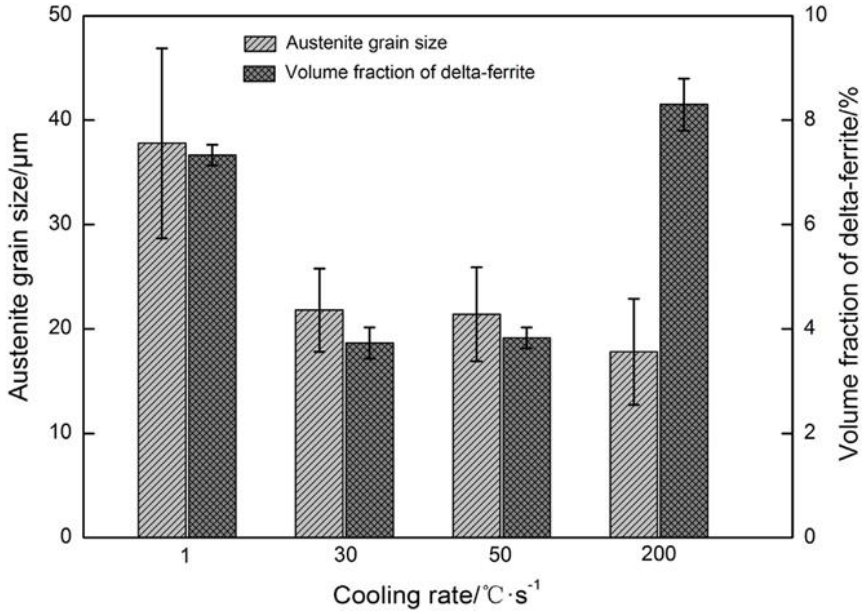

Fig. 3.13 Influence of cooling rate on amount of delta ferrite in P92 [36].

Zhou et al. [33] did not explain the observed high amount of delta ferrite at 200°C/s. A likely explanation could be that the Ae_4 temperature is depressed at fast cooling rates and the diffusion-controlled delta ferrite-to-austenite transformation is suppressed. These two factors limit the delta ferrite-to-austenite transformation during cooling.

A similar observation was reported by Sam et al. in 2014 [84], who studied the effect of cooling rate on reduced-activation ferritic martensitic (RAFM) steel by varying the heat input between 1 to 2.25 kJ/mm and applying different preheats, including no preheat, and preheating at 100°C and 200°C at constant heat input. RAFM steel was developed based on P91 alloy by replacing Mo and Nb with W and Ta, respectively. The results showed that a slower cooling rate by using a higher preheat temperature and heat input reduced the delta ferrite observed in the final microstructure [90]. The retained delta ferrite was formed from liquid during solidification and did not completely transform

to austenite in subsequent cooling. The duration within the respective phase regions (delta ferrite + austenite) and (austenite only) determines the completion of the transformation from delta ferrite to austenite. Increased time spent in these two-phase fields restricts the amount of delta ferrite retained in the final weld microstructure.

Figure 3.14 shows results of experiments conducted on RAFM steel by Arivazhagan et al. [7] in 2011. The reported results were inconsistent with those discussed above. Arivazhagan et al. [6] stated that a higher cooling rate from lower heat inputs resulted in reduction, up to a complete absence, of delta ferrite in the GTAW.

Sam et al. [84] stated that at very high cooling rates, the amount of delta ferrite formed from liquid decreased and more austenite formed directly from the supercooled liquid. This results in a change of solidification mode of the primary phase from ferrite only to ferrite + austenite, and explains the observations of Arivazhagan et al. [6].

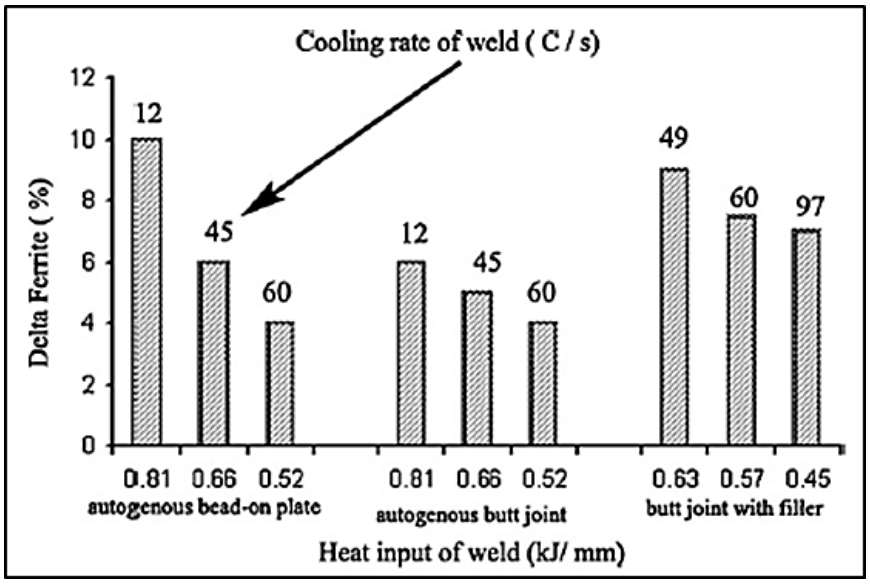

Fig. 3.14 Effect of heat input on the amount of delta ferrite and theoretical cooling rate of reduced-activation ferritic martensitic steel weld [7].

Abd El-Rahman et al. [94] in 2014 commented on the observations of Arivazhagan et al. [6] of delta ferrite increasing with increase of heat input. Abd El-Rahman et al. [88] stated that the amount of delta ferrite increases with the increase in heat input until a critical value of heat input is reached and then decreases with further increase of heat input.

Shanmugarajan et al. [96] investigated the influence of heat input and cooling rate on the final microstructure of autogenous laser welds on P91 steel. Six laser welds were performed with the heat input varied from 0.17 to 1.5 kJ/mm. Delta ferrite was not present in the three welds with the lowest heat inputs (0.17 to 0.21 kJ/mm). Delta ferrite was observed in welds with higher heat inputs and its volume fraction increased with rise in heat input from 0.7 to 1.5 kJ/mm. Shanmugarajan et al. [90] explained that delta ferrite nucleation is suppressed at the very fast cooling rates observed in the laser welds with low heat input and, therefore, solidification occurs from molten metal to austenite, resulting in the absence of ferrite in the weld metal. Conversely, in the larger heat input

welds, the cooling rate might be moderately enough for delta ferrite to form from the molten metal but not slow enough for full transformation of this ferrite into austenite at lower temperatures [96].

Gao et al. [97] conducted thermal treatment on Cr ferritic heat-resistant steel (9.81Cr, 1.73W, and 1.21Co). The samples were heated to 1320°C peak temperature, where only delta ferrite is stable, and the specimens were quenched at varying cooling rates in the range of 0.02−60°C/s. A theoretical model considering site-saturation formation at grain boundaries was used to compute the austenite amount in relation to cooling rate. It was assumed that austenite nucleates at the grain boundaries of delta ferrite and grows in a planar mode. Figure 3.15 presents the equilibrium diagram displaying reliance of the several phases on Cr_{eq} [57, 97]; the experimental steel is shown by the vertical line.

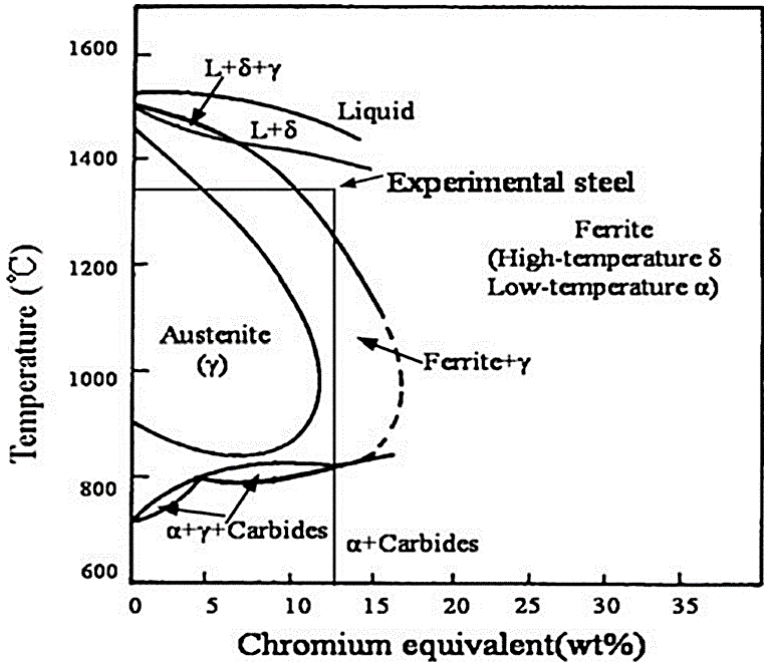

Fig. 3.15 Equilibrium diagram displaying reliance of the several phases Cr equivalent [57].

The results indicated that the amount of austenite decreased with increasing cooling rate, as in Fig. 3.16. This means the second phase in the microstructure, which was delta ferrite, increased with high cooling rates.

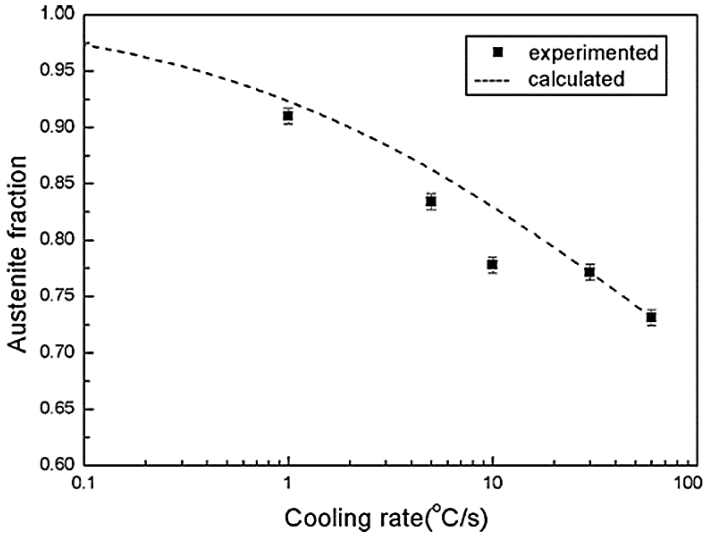

Fig. 3.16 Austenite fraction of high-Cr ferritic in relation to the cooling rate [97].

Chakraborty et al. [63] conducted experiments in which they simulated the fusion zone of P91 steel undergoing a peak temperature of 1450°C. A peak temperature of 1450°C is above T_m and the P91 steel samples experienced partial melting. Their study examined the effect of cooling rates of 1, 20, and 40°C/s on the amount and morphology of the delta ferrite. The observed volume fraction of delta ferrite did not differ much, estimated to be 3.6%, 3.7%, and 4% for cooling rates of 1, 20, and 40°C/s, respectively. A notable difference in the morphology of delta ferrite was observed between the cooling rates, as shown in Fig. 3.17. Sample (a), which was cooled most slowly at 1°C/s, consisted of a fine continuous network of delta ferrite in the martensitic matrix. In Sample (b), which was subjected to intermediate cooling at 20°C/s, the delta ferrite was present in isolated places as large polygonal grains and fine stringers. Sample (c), which experienced the fastest cooling rate at 40°C/s, consisted of small polygonal grains evenly distributed in the martensitic matrix.

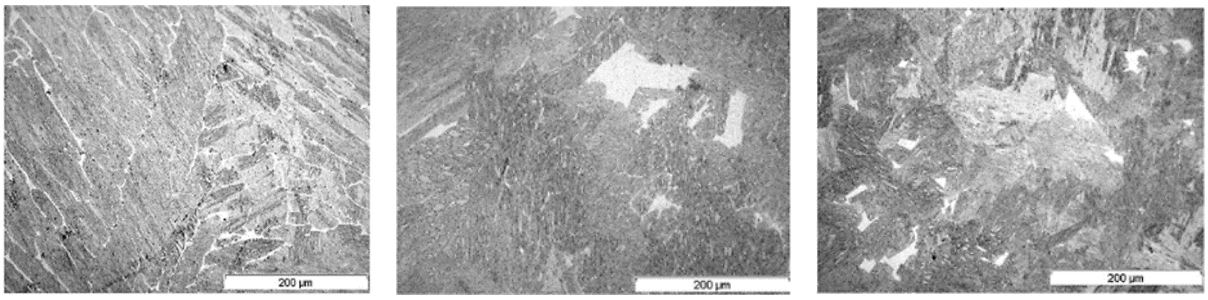

(a) (b) (c)

Fig. 3.17 Optical micrographs of P91 steel cooled at (a) 1, (b) 20, and (c) 40°C/s from a peak temperature of 1450°C [63].

Chakraborty et al. [60] stated various reasons for the observed amount and morphology of delta ferrite. Diffusion-controlled transformation was not effective because of the insufficient time for solid-state transformation of delta ferrite to austenite, even at the

lowest cooling rate, and the delta ferrite morphology was dependent on the type of ferrite nuclei that formed from the liquid [63].

3.6.1 Summary of observations from the literature

The influence of cooling rate on the volume fraction of delta ferrite observed in as-welded final microstructures is dependent on the specific cooling rate in different transformation regions.

i. The general rule observed is that increased cooling rate results in increased delta ferrite but there are instances where this rule does not apply.
ii. Increased cooling rate at peak temperature above solidus/liquidus during solidification limits the presence of delta ferrite in the final microstructure. Moreover, a narrow solidification range limits the volume fraction of delta ferrite.
iii. The amount of delta ferrite increased with time above Ae_4 in multi-pass welds in regions where melting did not occur but peak temperature exceeded the Ae_4 temperature.

3.7 Effect of ($Ae_4 - Ae_3$) temperature range on delta ferrite

Arivazhagan and Kamaraj [60] performed metal-cored arc welds of modified 9Cr−1Mo steel. The welds were completed with two types of metal-cored wires and two kinds of shielding gases; namely, (80% Ar + 20% CO_2) and pure Ar. The four welds varied in composition due to dilution and the oxidising nature of the (80% Ar + 20% CO_2) shielding gas. Thermo-Calc software was applied to calculate the transformation temperatures. It was observed that if ($Ae_4 - Ae_3$) was smaller, the probability of delta ferrite retention in the weld increased. The ($Ae_4 - Ae_3$) temperature range is determined by the balance between ferrite- and austenite-forming elements. A larger ($Ae_4 - Ae_3$) value means that austenite is stable over a wider range of temperature and that delta ferrite has more time to transform to austenite during cooling.

3.8 Current limits of understanding

Weld microstructure prediction methods and related research have been extensively studied to improve their accuracy in ferritic–martensitic steels [79]. Significant progress has been reported, but delta ferrite in P91 as-welded microstructures are observed in alloys with Cr_{eq} and FF values well below the recommended values, as presented in Section 3.4.2. The role of individual elements in the properties and performance of P91 welds alloys is well understood but the allowable range according to the chemical composition requirements of the AWS A5.28/A5.28M:2020 (ER90S-B9) and ISO 21952:2007 (CrMo91) standards seems to be insufficient to prevent the presence of delta ferrite in weld metal. The chemical composition determines the transformation temperatures and Arivazhagan et al. [6] stated that the probability of delta ferrite retention in the weld increases with a lower value of ($Ae_4 - Ae_3$). This relationship between the ($Ae_4 - Ae_3$) temperature range and amount of delta ferrite in the final

microstructure of the welds is not widely reported in literature yet does seem to play an important role.

The influence of cooling rate on P91 steel weld microstructure has been reported by several authors. Onoro [89], Faulkner et al. [86], and Abd El-Rahman et al. [94] support the generally accepted observation that P91 welds show an increase in delta ferrite volume fraction with faster cooling rates. Contradictory results have nevertheless been observed. The influences of both the chemical composition and cooling rate are not clearly demonstrated in literature.

P91 steels have good weldability if appropriate welding procedures, like preheating and PWHT to temper the martensitic weld, are applied. There is, however, limited knowledge of how PWHT affects delta ferrite, if observed in the weld metal.

Section II

Experimental Procedures

Chapter 4

Experimental Procedures

4.1 Introduction

The presence of delta ferrite in P91 weld metal has been demonstrated in Section 3.7 to be detrimental to the performance of P91 components. The goal of the current study was to analyse the thermodynamics and kinetics of phase transformation, with the objective of making recommendations on avoiding delta ferrite in P91 weld metal in the as-welded condition. The current study was done by altering the composition of the weld metal and cooling rate during welding. The experiments and characterisation techniques (Fig. 4. 1) performed were designed to achieve this objective.

This chapter describes the materials, experiments, equipment, and characterisation techniques that were used in the study.

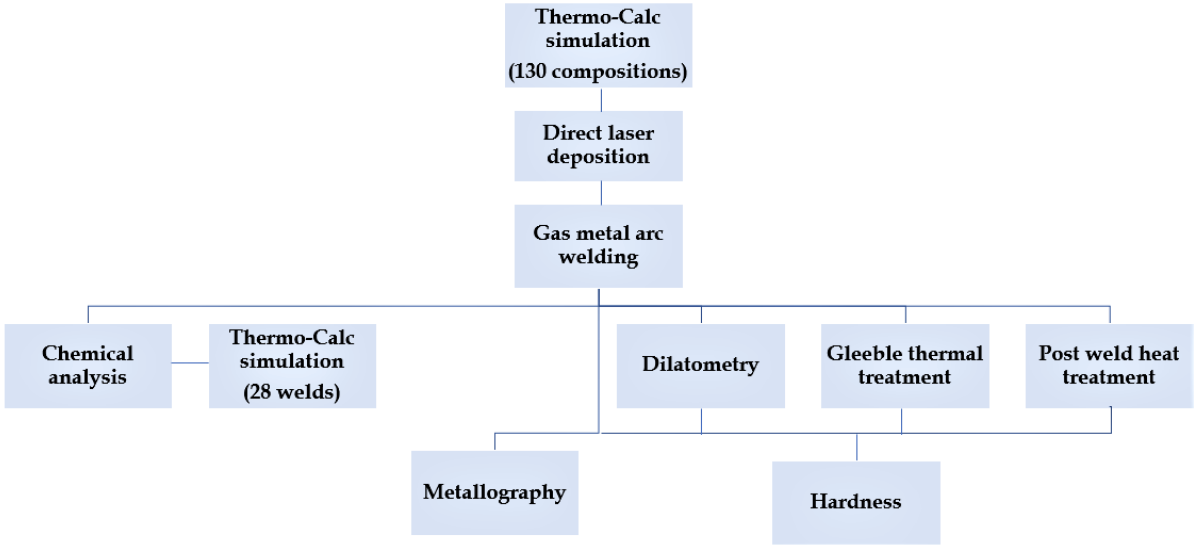

Fig. 4. 1 Experimental and characterisation flow diagram.

4.2 Thermo-Calc simulation

4.2.1 Introduction to Thermo-Calc

Thermo-Calc is a software and database package used for calculation of phase diagrams, phase transformations, and thermodynamic properties assessment. In the current experiments, Thermo-Calc software was used with the TCFE7 database to construct property diagrams (temperature vs. mole fraction of phases).

Since welding is non-equilibrium process, the Thermo-Calc predicted phase transformation temperatures were only used as a guide in selecting some experimental parameters and the interpretation of results. Attempts to determine the non-equilibrium transformation temperatures especially the Ae_4 and Ae_5 temperature were done. Preliminary work such as Scheil simulation, differential scanning calorimetry

(DSC) and high-temperature anneal heat-treatments was conducted in preparation for the current study. Scheil calculations in the Thermo-Calc software are used to estimate the solidification range under non-equilibrium conditions. Scheil simulation results of various P91 alloys revealed the same solidification sequence, with the delta ferrite as the primary phase, followed by austenite before solidification was completed. The observed delta ferrite in the final as-welded microstructure was mainly influenced by what occurs during the solid-state phase transformation and factors like the (Ae_4 - Ae_3) temperature range and cooling rate [98]. Differential scanning calorimetry (DSC) tests were performed on P91 steel base metal, HAZ and weld metal specimens. The Ac_1 and Ac_3 temperatures were determined during heating cycle (10°C/min) and were very similar to Thermo-Calc results. High transformation temperature (Ac_4 and Ac_5) could not be determined. The DSC test was very unstable during cooling and no valid results were obtained. High-temperature anneal heat-treatments on P91 SMAW bead was carried out at 1320°C and 1420°C with soaking times of 1 h followed by a subsequent water quench to determine the high-temperature structures. The specimen annealed at 1320°C for 1 h comprised of a martensitic matrix with 23% delta ferrite and at 1420°C the microstructure contained 72% delta ferrite. This experiment confirmed that at 1350°C, the structure was a mixture of delta ferrite and austenite which confirmed the Thermo-Calc prediction. In this dissertation, the results of experiments conducted as preliminary work are not presented.4.2.2 Selection of composition

Over 130 variations of P91 alloy compositions within the EN ISO 21952:2020 (CrMo91) chemical specification were evaluated by Thermo-Calc calculations. The objective for all Thermo-Calc simulations was to utilise the information to select the alloying elements that have the most effect on: (a) observed delta ferrite, (b) empirical values (Cr_{eq}, Ni_{eq}, FF, CNB), and (c) transformation temperature. Based on analysis of the above information, 28 alloy compositions were selected to achieve welds that would allow the main objectives of the study of weld beads in the as-welded condition to be realised, which were to:

- Study the influence of various weld metal compositions on delta ferrite phase fraction;
- Determine the optimum chemical composition to avoid retention of delta ferrite during welding;
- Evaluate the accuracy of empirical formulae in predicting the P91 final microstructure;
- Evaluate the significance of the ($Ae_4 - Ae_3$) temperature range in limiting the presence of delta ferrite.

4.2.3 Results

Property diagrams were constructed based on the 130 compositions and their equilibrium phase-transformation sequence and transformation temperatures were determined. Equilibrium phase diagrams were also constructed for the P91 reference composition. The reference composition used for constructing the pseudo-phase

diagrams was based on the AWS A5.28/A5.28M:2020 (ER90S-B9) mid-points of the element range and is as follows: 0.1% C, 0.9% Mn, 9.0% Cr, 0.25% Si, 1.0% Mo, 0.2% V, 0.07% Nb, 0.04% N, and 0.7% Ni.

The main alloying elements in P91 steel are classified under the below two categories:

Austenite formers: Ni, Mn, C, and N
Ferrite formers: Cr, Si, and Mo

In some instances, the elements were varied collectively as austenite formers and ferrite formers but always limited within the AWS A5.28/A5.28M:2020 (ER90S-B9) recommended ranges. The Thermo-Calc calculations were done to investigate the influence of individual elements on the transformation temperatures of P91 alloy.

4.2.4 Applying the empirical formulae

The Schaeffler and Schneider empirical formulae were used with the designed compositions to predict the final weld microstructures to identify weld compositions that would have a high probability of delta ferrite in the final weld metal. Thermo-Calc software was used to calculate the ($Ae_4 - Ae_3$) temperature range, which is an important indicator in predicting the presence of delta ferrite in the as-welded structure [60].

All Thermo-Calc information was utilised in selecting the five alloying elements (Cr, Ni, Mn, Si, and Mo), which were varied in the alloy designs of the 28 GMA welds performed in the current study.

4.3 Outline of experimental work and characterisation

To meet the objectives of the study, 28 GMA welds of varying compositions were deposited on a P91 steel pipe. Systematic variations in chemical composition of the GMAW beads were achieved by preliminary deposition of a single or multiple laser beads consisting of different alloying metal powders prior to overlaying them with a single-pass GMAW bead, as illustrated in Fig. 4.2.

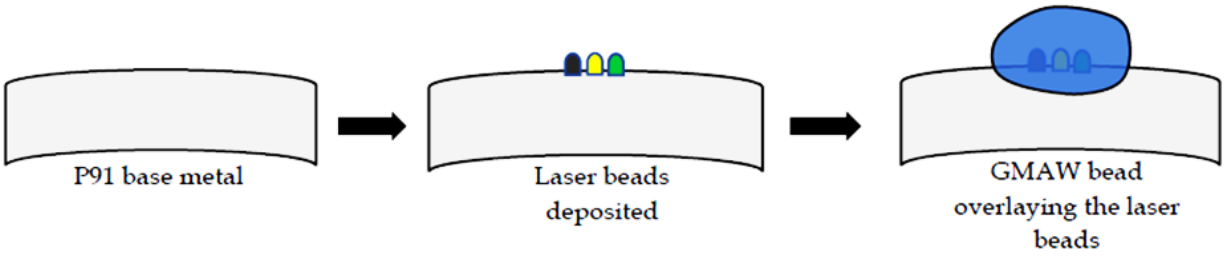

Fig. 4.2 Schematic illustration of alloying technique to systematically vary the chemical composition of the gas–metal arc weld beads.

The laser beads were deposited according to a specific target composition, with the aim of achieving a GMAW bead that met the requirements of the AWS A5.28/A5.28M:2020 (ER90S-B9) specification. Six of the 28 welds were deposited after preheating at 250°C, to investigate the effect of slower cooling rate on the delta ferrite content in the as-welded condition. The other welds were carried out without preheating.

The following characterisation was performed:

- Metallography (scanning electron microscopy (SEM) and optical microscopy);
- Chemical analysis (optical emission spectroscopy (OES) and energy-dispersive X-ray spectroscopy (SEM-EDS);
- Thermo-Calc simulation;
- Hardness testing.

Additional experimental techniques were performed on selected welds:

- Dilatometry;
- Gleeble thermal treatment;
- PWHT.

Table 4.1 summarises the experimental work and characterisation techniques conducted on the weld beads. Preliminary work done on Thermo-Calc calculations and the screening to determine the 28 compositions is not included in Table 4.1.

Some experimental work and characterisation were performed on selected beads based on the presence or absence of delta ferrite in the as-welded microstructure and the alloying elements applied.

Table 4.1 *Overview of experimental work and characterisation techniques.*

GMAW beads	Chemical analysis (OES)		SEM-EDS		Metallography	Dilatometry	Gleeble	PWHT	Vickers Hardness
	All GMAW beads	*Along the bead length*	*Laser beads*	*GMAW beads*	*Stereoscope and Light microscope*	*Determine Ac_1 and Ac_3 temp.*			
250°C Pre-heat									
PH 1	✓			✓	✓				✓
PH 2	✓		✓	✓	✓				✓
PH 3	✓		✓	✓	✓				✓
PH 4	✓		✓	✓	✓			✓	✓
PH 5	✓		✓	✓	✓		✓	✓	✓
PH 6	✓	✓	✓	✓	✓				✓
No Pre-heat									
AW 1	✓	✓		✓	✓				✓
AW 2	✓		✓	✓	✓				✓
AW 3	✓		✓	✓	✓				✓
AW 4	✓		✓	✓	✓	✓			✓
AW 5	✓		✓	✓	✓				✓
AW 6	✓		✓	✓	✓	✓			✓
AW 7	✓		✓	✓	✓				✓
AW 8	✓		✓	✓	✓				✓
AW 9	✓		✓	✓	✓		✓		✓
AW 10	✓		✓	✓	✓			✓	✓
AW 11	✓		✓	✓	✓				✓
AW 12	✓		✓	✓	✓				✓
AW 13	✓		✓	✓	✓				✓
AW 14	✓		✓	✓	✓				✓
AW 15	✓		✓	✓	✓				✓
AW 16	✓		✓	✓	✓		✓		✓
AW 17	✓	✓	✓	✓	✓			✓	✓
AW 18	✓		✓	✓	✓		✓		✓
AW 19	✓		✓	✓	✓				✓
AW 20	✓		✓	✓	✓				✓
AW 21	✓		✓	✓	✓		✓	✓	✓
AW 22	✓	✓	✓	✓	✓	✓			✓

4.4 Base and filler material

4.4.1 Background

During welding of P91 steels, filler metals must match the creep strength of the parent material. Preferably, these would also have similar toughness at room temperature because weldments are exposed to stresses at ambient temperature during maintenance [99]. However, as early development results revealed, the weld metal could not meet both criteria at the same time. Consequently, available filler materials tend to have a matching composition to the parent metal, with similar creep strength but inferior toughness. The filler metal often contains increased amounts of Mn (0.6−0.7 mass%) and Ni (0.4−0.6 mass%) for improved toughness in the weld metal [99].

The correct chemical composition for P91 filler metal must be selected with care to ensure a good balance between the austenite formers and ferrite formers to prevent residual ferrite and to guarantee a complete martensitic microstructure in the weld

metal [61]. In general, P91 steels are also difficult to temper, with high PWHT temperatures required to lower hardness and develop the necessary toughness in the weld metal [100].

4.4.2 Base and filler material

In the current study, a seamless pipe of X10CrMoVNb9−1(P91) steel grade with heat number 223399 was used as the base material. The pipe was sectioned into shorter lengths and a small thickness of material was skimmed from the outside of the pipe to remove any rust or contamination and to ensure an even surface on which the weld beads were deposited. The uniform surface finish also ensured improved bead size consistency and limited variation in chemical composition along the bead length. The final dimensions of the sectioned pipes were 245 mm outside diameter, a thickness of 27 mm, and a length of 330 mm. The chemical composition of the base material is shown in Table 4.2, and complies with the ASTM A335/A335M−21 specification standard.

A 1 mm diameter Böhler C 9 MV−UP wire was used as the GMAW filler material. The chemical composition of the filler wire, as provided by the supplier, is shown in Table 4.3. The supplier inspection certificate stipulated that the chemical composition was for hot-rolled wire with heat number 101798. The AWS A5.28/A5.28M (ER90S-B9) and ISO 21952:2020 (CrMo91) specifications are included in Table 4.3 for the purpose of comparing the two standards.

Table 4.2 *Chemical composition (%) of P91 base material steel pipe (ASTM A335/A335M−21)*

	C	*Mn*	*Cr*	*Si*	*Mo*	*V*	*Nb*	*N*	*Ni*	*Al*
ASTM A335/A335M-21	0.08–0.12	0.30–0.60	8.0–9.5	0.20–0.50	0.85–1.05	0.18–0.25	0.06–0.10	0.03–0.07	0.4 max	0.02 max
Base material	0.11	0.53	8.21	0.33	0.93	0.24	0.10	0.06	0.25	0.005

Table 4.3 *Böhler C 9 MV-UP filler wire chemical composition (%), as provided by the supplier (AWS A5.28/A5.28M:2020 (ER90S-B9) and ISO 21952:2020 (CrMo91) specification)*

AWS A5.28/A5.28M (ER90S-B9)	*C*	*Mn*	*Cr*	*Si*	*Mo*	*V*	*Nb*	*N*	*Ni*	*Al*	*Cu*
	0.07–0.13	1.20 max	8.0–10.5	0.15-0.50	0.85–1.20	0.15–0.30	0.02–0.10	0.03–0.07	0.8 max	0.04 max	0.2 max
ISO 21952 (CrMo91)	0.07–0.15	0.4–1.5	8.0–10.5	0.6 max	0.80–1.20	0.15–0.30	0.03–0.10	0.02–0.07	0.4–1.0	–	0.25 max
Filler wire	0.10	0.60	8.80	0.24	0.94	0.20	0.06	0.04	0.50	–	0.03

4.5 Welding

The majority of welding processes can be applied to weld P91 steel successfully. The welding process is selected based on the welding position, filler metal, thickness of the plate, shielding gas mixtures, flux, and duration and PWHT temperature [101].

In this study, direct laser deposition (DLD) was used to deposit the alloying metal powders as preliminary laser beads to systematically vary the final GMAW bead composition. Single-pass GMA beads were deposited to overlay the laser beads, resulting in slight differences in the compositions of the GMA beads.

4.5.1 Powder-fed direct laser deposition

4.5.1.1 Introduction to direct laser deposition process and variables

Laser is a coherent, parallel, convergent ,and monochromatic beam of electromagnetic radiation with a wavelength in the ultraviolet to infrared range [102]. A laser beam possesses the capability to produce a power density surpassing 10^6 W/cm^2; when such energy is absorbed by a material, it causes melting and evaporation. The laser used in this study was an IPG YLR 3000 − ST fibre laser with a maximum power output of 3 kW.

Powder-fed direct laser deposition (DLD) combines simultaneous powder metal/energy delivery for deposition of the laser beads, as shown in Fig. 4.3.

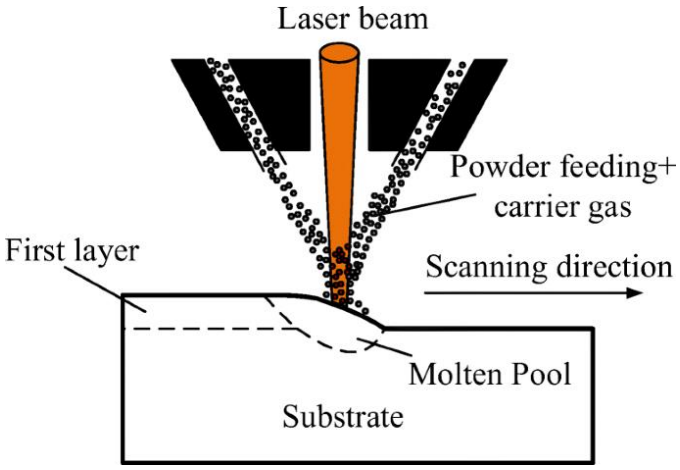

Fig. 4.3 Powder-fed direct laser deposition mechanism.

Laser beams provide enough thermal energy to melt metal particles as they are deposited.

Metal powder is transported to the DLD molten pool through an integrated powder-delivery system. Modern DLD equipment may have up to four nozzles to deliver the metal powder. These employ inert gas, such as Ar, to minimise elevated oxidization rates [102]. Metal powder was supplied from a gas-pressurized vessel that was linked to the gas/powder feed lines and was mixed with a carrier gas.

The powder suppliers claimed a particle size that ranged from 10 µm to 100 µm. As the laser bead was an intermediate step, no attempt was made verify these values. The particle feed rate is the average amount of particles exiting the DLD nozzle against time, and with a range between 1−10 g/min [102]. Typical applications for a powder-fed DLD process are cladding, coating components, or in additive manufacturing (AM).

The DLD process has various settings that are controlled to guarantee deposition of the desired bead size. For powder-fed DLD machines, continuous wave-mode lasers are

used and focused/de-focused to ensure the desired spot diameter for the material processing. When the powder feed rate is increased while maintaining a constant laser power, there will be a slight reduction in the average temperature of the powder stream and an increased level of laser attenuation.

The controllable operating parameters, as stipulated in ISO 15609−4 (2009) for laser beam welding, include:

1. Beam parameters
    a. Laser beam power
    b. Laser beam orientation
    c. Continuous wave
2. Mechanical parameters
    a. Travel speed
    b. Powder feed rate
3. Shielding and backing gas parameters
    a. Gas flow rate
    b. Gas purity
    c. Purge procedure
4. Working distance
5. Shape and dimensions of the beam on the workpiece

ASME IX (2010 ASME Boiler and Pressure Vessel Code) specifies the variables listed for qualification of the laser-beam welding procedure specification as shown in Table 4.4.

Table 4.4 *Laser-beam welding variables as per ASME IX (2010).*

ASME IX paragraph		***Process variable***
QW−402 Joints	.1	Groove design
QW−403 Base metals	.3	Penetration
QW−408 Gas	.2 .12	Single, mixture, or % Flow rate
QW−409 Electrical characteristics	.20 .21	Mode, energy Power, speed
QW−410 Technique	.17 .37 .77 .80	Type/model of equipment Single to multiple pass Wavelength Spot size

4.5.1.2 Direct laser deposition experimental work

Five alloying elements were chosen to be systematically varied in the P91 weld metal to study the influence of composition on delta ferrite retention in the final weld microstructure. The alloying elements were chosen after taking into consideration their effect on transformation temperature based on Thermo-Calc results and their reported contribution to delta ferrite retention in the final welded P91 structure. The five chosen

elements were Cr, Ni, Mn, Si, and Mo. Table 4.5 shows the metal alloy powders used in the DLD and their respective compositions and particle sizes.

Table 4.5 *Metal alloying powders and properties.*

Commercial name	***Composition (mass%)***	***Particle size (μm)***
TLS (Cr99.2)	99.2 Cr	45−90
METCO 56C-NS (Ni powder)	99.3 Ni	45−90
Weartech (Mo99.5)	99.5 Mo	20−45
Manganese Metal Co powder	99.8 Mn	60−200
FeSi (6F)	16.6 Si and 82.5 Fe	~ 45

Twenty-eight primary welds with varying compositions were evaluated. Images of the preliminary laser beads are shown in Fig. 4.4. The laser beads were deposited according to a specific target composition, with the aim of achieving a GMAW bead that met the requirements of the AWS A5.28/A5.28M:2020 (E90S-B9) composition specification.

Fig. 4.4 Images of preliminary laser beads of different elements deposited on the seamless P91 steel pipe.

The metal alloying powder of each element was deposited on the P91 base material using an IPG YLR 3000-ST fibre laser, shown in Fig. 4.5. The welding head that houses the nozzle through which the metal powder is directly fed into the weld pool was mounted on an articulated arm robot. Ar was used as the shielding gas.

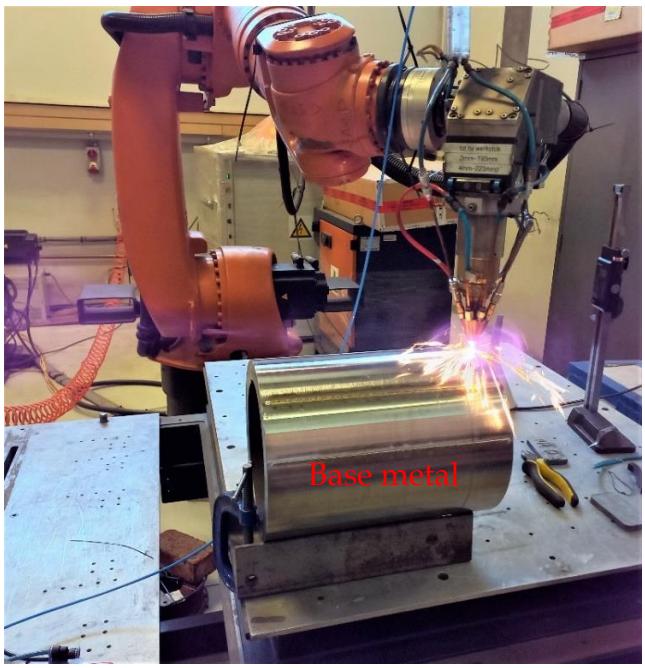

Fig. 4.5 Image of laser metal deposition set-up showing the IPG YLR 3000-ST fibre laser and P91 base metal.

Table 4.6 shows the DLD parameters for the specific powder deposits. Additional welding variables used to produce the laser welds are presented in Table A in Appendix A. The DLD parameters detailed in Table 4.6 were established so that DLD beads with the desired geometry could be produced. This enabled the target weld metal compositions to be achieved.

Table 4.6 *Direct laser deposition parameters*

Metal alloy powder	*Spot size (mm)*	*Laser power (kW)*	*Laser speed (m/min)*	*Powder feed rate*
TLS (Cr99.2)	4	2.0	0.5	1.4 rpm: 4.00 g/min
METCO 56C-NS (Ni powder)	2	1.2	1.2	1.5 rpm: 4.05 g/min
Weartech (Mo99.5)	2	1.2	1.2	1.2 rpm: 3.90 g/min
Manganese Metal Co powder	2	1.0	1.2	2.5 rpm: 2.13 g/min
FeSi (6F)	4	2.2	0.5	1.4 rpm: 2.10 g/min

As a first step towards determining the DLD parameters, GMAW trials were carried out to determine the ideal weld bead size and typical weld dilution and penetration. The GMAW trials were bead-on-plate depositions of the P91 filler wire with different welding parameters. An ideal GMA weld bead was one that was large enough to fully cover the preliminary laser beads and with sufficient dilution to achieve the target composition after alloy addition.

To determine the required amount of alloying metal powder to be added to achieve the target weld bead composition, the following factors were considered:

a) Composition of the base material, the filler wire, and the alloying metal powder;

b) Target GMA bead size;
c) Dilution.

Table 4.7 shows the laser bead size required to increase the mass percentage of the chosen elements to the target values in the final GMA beads.

Table 4.7 *Laser bead size required to achieve desired target mass% of each element in GMAW beads*

Alloying element	*Starting composition (mass%)*	*Target in GMAW bead (mass%)*	*Laser bead size (mm)*		*No. of beads*
			Width	*Height*	
Cr	8.80	10.5 9.50	4.0	0.38	2 1
Mo	0.94	1.20	2.0	0.2	1
Mn	0.60	0.80	2.0	0.2	1
Ni	0.50	0.70	2.0	0.2	1
Si	0.24	0.60	4.0	0.4	2

To evaluate the effectiveness of laser metal deposition as an alloying technique, ten GMA welds were initially performed. These were analysed to determine the weld geometry, chemical composition, and metallography. After satisfactory results were achieved, the remaining 18 welds were performed. Some compositions from the initial batch of ten welds were repeated at lower cooling rate, achieved by applying a preheat at 250°C.

4.5.2 Gas–metal arc welding

4.5.2.1 Process and variables

GMAW is an arc-welding process where metals are fused together through heating generated by an arc formed between a consumable continuous filler-metal electrode and the workpiece [103]. The wire is provided from a reel and is conveyed to the welding gun by drive rollers that drive it through a flexible hose package to reach the gun. Electricity for the arc is transferred to the electrode via a contact tube located within the welding gun. The size of electrode is determined based on the welding current [104]. The arc and the weld pool are protected by the shielding gas supplied through the gas nozzle that surrounds the contact tube. Shielding is obtained entirely from an externally supplied gas or gas mixture. A gas (usually based on Ar, He, or a mixture) entering through a cup on the welding gun shields both the weld pool and the electrode.

Important parameters in the GMAW process are the voltage and wire feed speed. Increased voltage increases the arc length and gives a wider weld bead. Undercut is a sign of too high a voltage. The wire feed speed and diameter of the wire indirectly control the current. Current is the main parameter for welding and is chosen based on the plate thickness and welding speed.

For qualification of the GMAW welding procedure, ASME IX (2010 ASME Boiler and Pressure Vessel Code) specifies the variables listed in Table 4.8.

Table 4.8 *Gas–metal arc essential welding variables as per ASME IX.*

ASME IX paragraph		***Process variable***
QW–403 Base Metals	.9 .10	Base metal thickness Temperature limits
QW–404 Filler Metals	.30 .32	Change in thickness of weld deposit Thickness limit
QW–405 Positions	.2	Position
QW–406 Preheat	.1	Decrease > (55°C)
QW–407 PWHT	.1 .2	PWHT Temperature limits
QW–408 Gas	.2 .3 .9 .10	Single, mixture, or % Flow rate Backing gas Shielding gas
QW–409 Electrical Characteristics	.1 .2 .4 .8	Heat input Transfer mode Polarity Current and voltage
QW–410 Technique	.7 .9 .25	Oscillation Multi to single pass/side Manual or automatic

4.5.2.2 Preheating and post-weld heat treatment

Figure 4.6 illustrates the preheating temperature control during welding and PWHT [105]. It is important to adhere to the prescribed parameters of preheating, interpass, and PWHT temperatures to avoid weld defects and ensure adequate mechanical properties. The recommended minimum preheating temperature is 200°C to prevent hydrogen cracking and cold cracking [39]. When using GTAW, the root pass can be done at temperatures as low as 150°C because of low hydrogen content [101]. During multi-pass welding, the recommended interpass temperature is between a minimum of 200°C and maximum of 300°C to ensure that each bead at least partially transforms to martensite [39]. Arivazhagan et al. [60] applied a preheat of 200°C and maintained an interpass temperature of 250°C during multi-pass welding of P91 steel.

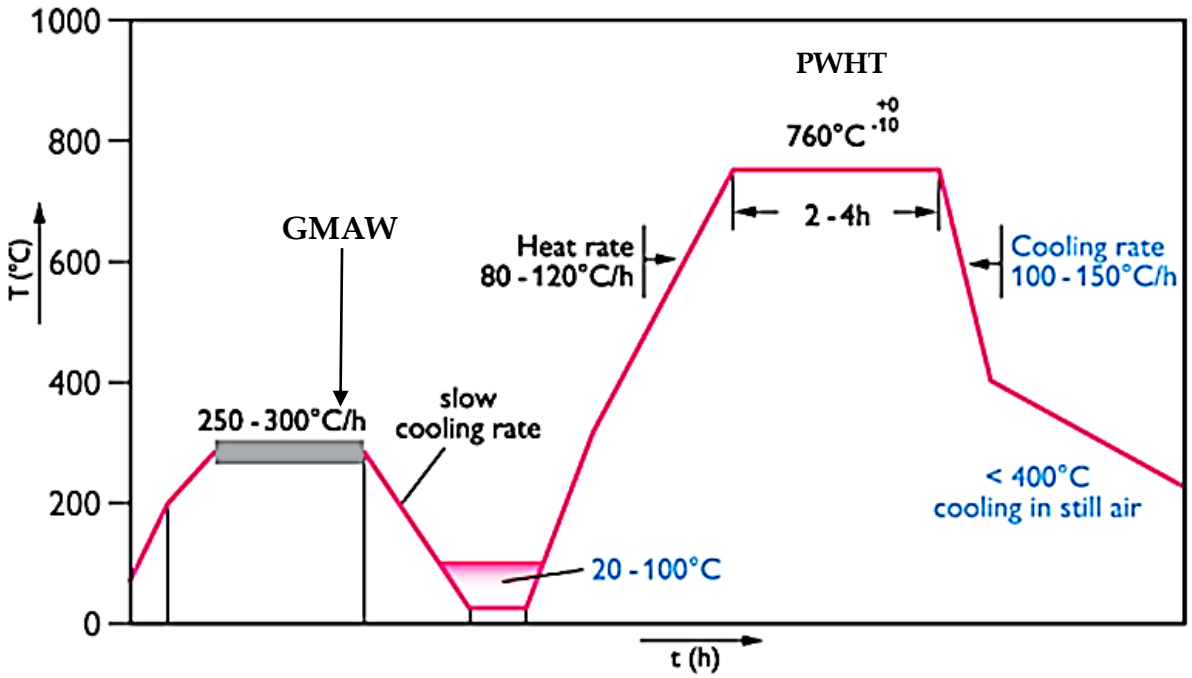

Fig. 4.6 Preheating and post-weld heat treatment (PWHT) temperature cycles and heating/cooling control during welding of P91 steel [105].

Post-heating can be applied to P91 welds with thick sections if PWHT is not immediately applied. The post-heating is performed by maintaining the preheat temperature for an extended time after completion of welding. This ensures that hydrogen diffuses out of the weld and thus reduces the risk of cracking [101]. The required heat treatment also depends on the thickness of the components being welded and has to be determined by the fabricator as part of the welding procedure development [105]. It is also important to control the heating and cooling rates to prevent development of excessive stresses in the weld joint. Care must be taken during heat treatment because P91 weld metal can suffer temper embrittlement, which is detrimental to ductility and toughness, when exposed to temperatures of 400–500°C for prolonged time [106].

PWHT is applied to temper the martensitic matrix and enable precipitation of the carbo-nitrides that are critical for high-temperature properties. PWHT is performed below the Ae_1 critical transformation temperature to optimise the mechanical properties and relieve some residual stresses [106]. After welding is completed, the P91 weldment must be allowed to cool below 100°C before PWHT to ensure complete transformation of the austenite phase to martensite [4].

The selected PWHT parameters may vary, depending on the welding process applied and the weld joint size, but it is critical to select the correct PWHT temperature. The time at temperature for PWHT depends on the thickness of the part [61]. Where the PWHT is excessively low, the required impact toughness will not be achieved; if the PWHT is excessively high, the creep-rupture strength is degraded [107]. The AWS standard recommends a PWHT temperature range of 730−760°C for a minimum 1 h hold time [108]. The ASME Boiler and Pressure Vessel Code, ASME section VIII [16],

recommends a PWHT for P91 steel between 740°C and 760°C, with 2 to 8 h holding time, depending on the thickness and geometry [109]. Bush [39] suggested that an optimum PWHT temperature is 760°C with a minimum hold time not shorter than 2 h.

The PWHT temperature and hold time can be dependent on a welding process that introduces different dynamics; for example, submerged-arc welding (SAW) results in large grain size and segregation, therefore a holding time of 4 h may be required for optimum tempering but 2 h holding time may be satisfactory for SMAW or GTAW [101]. Table 4.9 and Table 4.10 show the recommended thermal treatment procedures as per the various codes.

Table 4.9 *Specifications for P91 thermal treatments for various welding codes [108]*

Consumable type	***Specification/Code***	***Preheat and interpass temperature (°C)***	***PWHT procedure***
Covered electrode	BS EN 1599:1997; ECrMo91B	200–300	750–770°C 2–3 h
Solid wire	EN 12070: 1996; CrMo91	250–350	750–760 °C 3 h
Covered electrode	AWS A5.5−96; E90XX−B9	232–288	730–760°C 1 h
Solid wire	AWS a5.28−96; ER90S−B9	150–260	730–760°C 1 h

Table 4.10 *P91 ASME code for PWHT parameter requirements [39]*

Code	***PWHT temperature (°C)***	***Minimum PWHT time***
ASME B&PV Code Section VIII Div 1	704	15 min
ASME b31.1 Power Piping Code	704 to 760	15 min
ASME B31.1 Process Piping Code	704 to 760	2 h

In practice, overheating may occur if the PWHT temperature exceeds the lower critical temperature (Ae_1). Above the Ae_1 temperature, both austenite and ferrite become stable, which means the martensitic weld will begin to transform to austenite and then, during cooling, the austenite will convert to untempered martensite. Alexandrov et al. [100] reported the formation of ferrite during the PWHT process after exceeding the Ae_1 temperature. This could be a result of a very slow cooling rate after PWHT, which can allow the cooling curve to touch the ferrite nose and the austenite would thus transform to ferrite instead of martensite.

4.5.2.3 Weaving

A weaving technique with parameters in Table 4.11 was applied during deposition of the GMA beads to ensure that the laser-alloyed beads were fully melted. Weaving is a

welding technique in which the torch is transversely oscillated as it progresses along the weld path. Applying the weaving technique has been widely used to obtain better weld quality by avoiding the lack of side-wall fusion and to improve efficiency by obtaining a wide weld bead [110].

Table 4.11 *Weaving parameters.*

Process variable	***Value***
Welding path	Weaving (trapezoid)
Oscillation width (mm)	7
Oscillation position delay (s)	0.3
Oscillation travel speed (cm/min)	20

Lu et al. [104] stated that it is difficult to automate the weaving process due to challenges associated with parameter selection and in evaluating the influence of weaving parameters on the welding heat input. The weaving parameters are illustrated in Fig. 4.7.

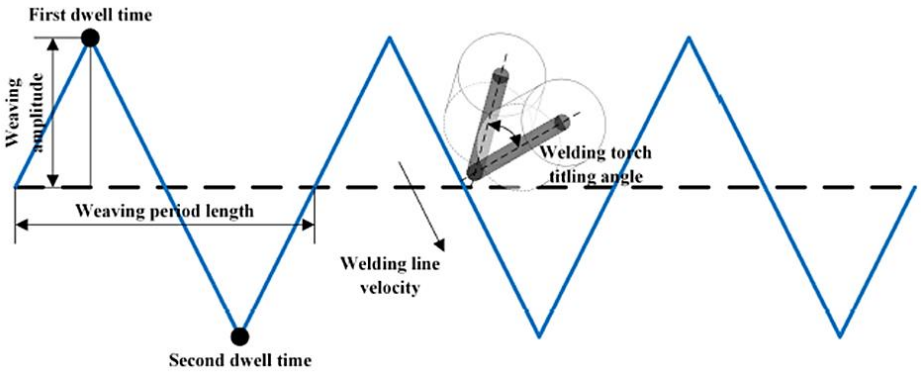

Fig. 4.7 Illustration of weaving parameters.

The weaving parameters are defined as follows [111]:

1. Welding velocity: the moving velocity of the end point of the welding wire, which is controlled by the inclination of the welding torch;
2. Weaving amplitude: the maximum distance from the weaving position to the centre line of the weaving path;
3. Weaving period length: the distance of a weaving period along the welding direction per unit time;
4. Dwell time: the time of movement suspension when the end point of the welding wire is at the weaving amplitude point;
5. Welding torch inclination: the angle between the axis of welding torch and the vertical direction.

4.5.2.4 Dilution

Dilution is an important consideration in ensuring that the target composition was achieved in the GMAW beads. Dilution is defined as the change in the chemical composition of the welding filler material caused by admixture with the base material in the deposited weld bead [112]. Mathematically, dilution is the ratio of the amount of the melted base metal (including the laser bead) to the total amount of fused metal. This is shown schematically in Fig. 4.8, where A is material from the filler wire; B is the laser bead, and C is the contribution from the base metal:

$$\text{Dilution } (\%) = \frac{B+C}{A+B+C} \times 100. \tag{4.1}$$

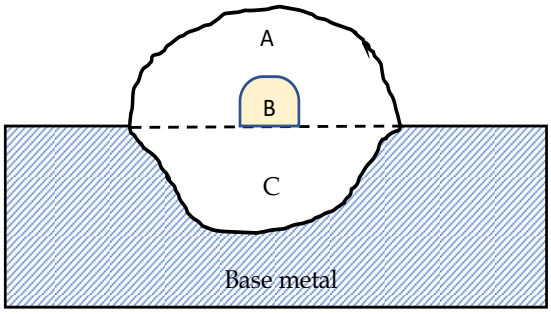

Fig. 4.8 Schematic illustration of determination of dilution in a weld.

4.5.2.5 Experimental work

The GMAW process was used to deposit primary beads that overlaid the preliminary laser beads. The welding process was semi-automated, with the torch clamped to an arm that was controlled by the rail-runner welding carriage, as shown in Fig. 4.9. The carriage permitted a weaving welding path.

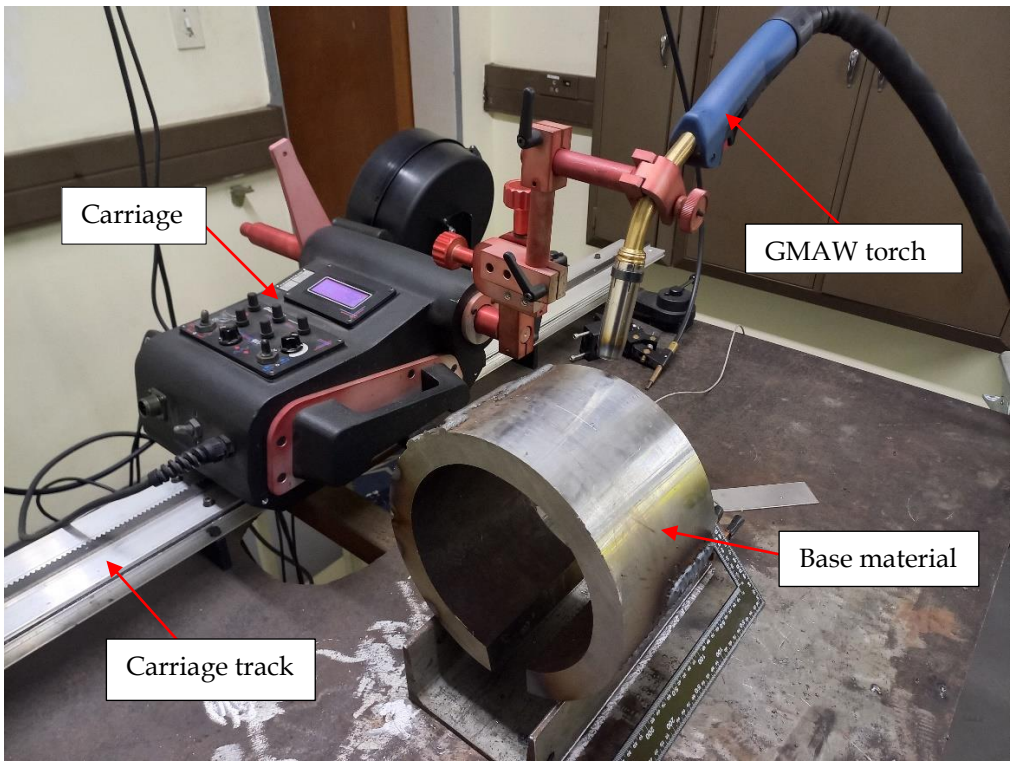

Fig. 4.9 Semi-automated gas–metal arc welding set-up.

All GMA welds were bead-on-plate welds undertaken using the parameters shown in Table 4.12. To ensure consistency in heat input, all welds were performed with the same parameters.

Six welds were performed at a preheat temperature of 250°C, designated PH 1 to PH 6. Preheating at 250°C was applied for the purpose of investigating the effect of cooling rate on delta ferrite presence in the as-welded microstructure. Twenty-two welds, designated AW 1 to AW 22, did not receive any preheating. Thermocouples were placed on the base metal to monitor the temperature, especially during the application of the 250°C preheating. A portable contact temperature monitor was also used to measure the temperature before the deposition of each bead. The base material P91 pipe was allowed to cool down before the subsequent bead was deposited. The shielding gas was Ar with 2% O_2 at a flow rate of 15 L/min.

Table 4.12 *Gas–metal arc welding parameters applied on all welds.*

Process variable	***Value (no preheat)***	***Value (preheat @ 250°C)***
Welding speed (cm/min)	20	20
Wire feed speed (m/min)	13.2	13.2
Welding current (A)	218 average	218 average
Welding voltage (V)	28.5 average	31.5 average
Contact tip to work distance (mm)	20	20
Welding path	Weaving (trapezoid)	Weaving (trapezoid)
Oscillation width (mm)	7	7
Oscillation position delay (s)	0.3	0.3
Oscillation travel speed (cm/min)	20	20
Heat input (kJ/mm) (0.85 arc efficiency)	1.4–2.0	1.7
Average cooling time (1200°C to 800°C) $\Delta t_{12\text{-}8}$ (s)	4.2	6.5
Average weld cooling rate (°C/s) (estimated from $\Delta t_{12\text{-}8}$)	96	62

Figure 4.10(i) shows the GMA welds deposited along the length of the P91 steel pipe. Multiple laser beam welds of different alloys are shown in Fig. 4.10(ii) overlaid with a single-pass GMA weld. Weaving was applied to ensure that the GMAW beads were wide enough to sufficiently overlay and dissolve the laser beads.

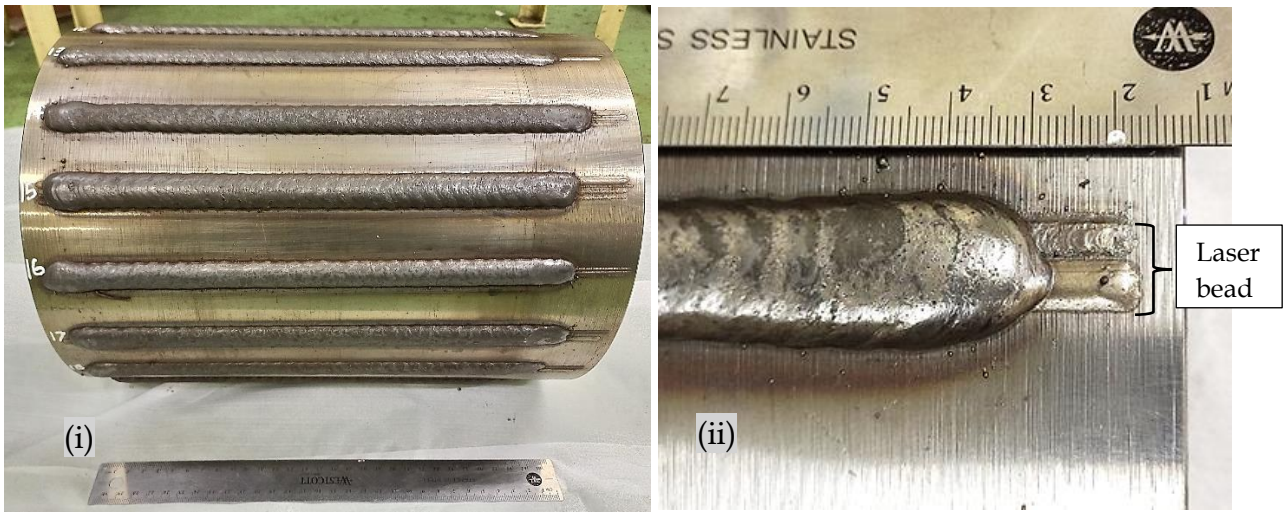

Fig. 4.10 Image (i) shows the P91 pipe with gas–metal arc welded beads. Image (ii) shows the laser beads overlaid by a gas–metal arc welded bead.

The Lincoln Electric power supply used in these experiments indicated the total energy utilised for depositing each bead, which is referred to as "total true energy". The total

true energy was used to calculate the heat input (HI) for each weld by dividing this value by the bead length. A GMAW 0.85 arc efficiency (η) was applied [113]:

$$HI\ (kJ/mm) = \eta \times \text{Total true energy (kJ)} / \text{bead length (mm)}. \quad (5.1)$$

HI is the measure of energy transferred per unit length of a weld to the weld pool during welding. HI is important mainly because of its influence on the heating and cooling rates of the weld; consequently, this thermal cycle affects the weld size and influences the final metallurgical structure and mechanical behaviour [103].

Table 4.13 shows the calculated HI, incorporating the typical 0.85 GMAW arc efficiency (η). The cooling rate through the transformation temperature range (1200–800°C) is critical because it determines the resulting metallurgical transformation products and their properties. The resulting microstructure in the weld, as reported in Chapter 3, is influenced by the cooling rate, which is a function of HI.

Table 4.13 *Effective heat inputs of all gas–metal arc welds and cooling time. Calculations are based on the Rosenthal equation.*

Weld ID	***Bead length (mm)***	***Total true energy (kJ)***	***Heat input with 0.85 arc efficiency (kJ/mm)***	***T_o (°C)***	***Calculated $\Delta t_{12\text{-}8}$ (s)***	***Cooling rate (°C/s)***
PH 1	282	573.6	1.73	241	6.9	58.4
PH 2	270	547.0	1.72	225	6.5	61.4
PH 3	273	555.5	1.73	245	6.6	60.2
PH 4	246	510.4	1.76	230	6.8	59.3
PH 5	282	455.4	1.70	245	5.5	72.9
PH 6	268	541.2	1.72	239	6.8	59.1
AW 1	289	474.2	1.37	75	3.6	110.5
AW 2	284	582.6	1.74	38	4.2	95.9
AW 3	284	582.6	1.74	42	4.2	95.0
AW 4	272	543.9	1.70	36	4.1	98.5
AW 5	268	515.1	1.63	60	4.1	97.6
AW 6	285	603.0	1.80	19	4.1	96.6
AW 7	284	512.7	1.53	65	3.9	102.8
AW 8	199	332.4	1.42	97	3.9	102.3
AW 9	280	600.8	1.82	37	4.4	92.0
AW 10	274	516.9	1.60	90	4.3	92.8
AW 11	290	563.9	1.65	45	4.0	99.5
AW 12	275	562.8	1.74	18	4.0	100.3
AW 13	276	563.2	1.73	34	4.1	97.3
AW 14	275	583.1	1.80	23	4.2	95.7
AW 15	270	620.2	1.95	34	4.6	86.4
AW 16	271	641.0	2.01	41	4.9	82.5
AW 17	292	549.7	1.60	97	4.4	91.3
AW 18	277	553.9	1.70	35	4.1	98.8
AW 19	289	562.6	1.65	75	4.3	93.2
AW 20	280	588.0	1.79	45	4.4	91.7
AW 21	276	637.6	1.96	22	4.5	88.1
AW 22	275	564.3	1.14	34	4.1	96.9
Min.	199	332.4	1.37	18	3.6	58.4
Max.	292	641.0	2.01	245	6.9	110.5
Ave.	275	551.3	1.72	88.8	4.7	88.5

T_o is the temperature of the base metal at the beginning of welding.

In applying the Rosenthal equation, the influence of the welded plate thickness needs to be considered because of its influence in characterising the heat flow as either two- or three-dimensional [114]. Table 4.14 lists the P91 alloy material properties that were applied in the Rosenthal equation calculations, as published by Haarmann et al. [4].

Table 4.14 *Material properties of P91 alloy at 650°C [4]*

Melting temperature (K)	1773
Plate thickness (m)	27×10^{-3}
Thermal diffusivity (m^2/s)	4.49×10^{-6}
Thermal conductivity at 300–500 K (W/(m K) or J/(m s K))	30
Volume thermal capacity ($J/(m^3 K)$)	6.68×10^6
Density (kg/m^3)	7770

The volume thermal capacity and thermal diffusivity were calculated using Equations 4.2 and 4.3, respectively.

$$\text{Volume thermal capacity } (\rho_c) = \rho C_\rho \tag{4.2}$$

$$\text{Thermal diffusivity } (a) = \frac{\lambda}{\rho C \rho} \tag{4.3}$$

where ρ is density, C_ρ is specific heat capacity, λ is thermal conductivity, a is thermal diffusivity, and ρ_c is volume thermal capacity.

Below is a sample calculation using the Rosenthal equation for weld PH 1:

Volume thermal capacity (ρ_c) = ρC_ρ (J/m^3K)

6.68×10^6 (J/m^3K) = 7770 (kg/m^3) × (specific heat capacity)

Specific heat capacity (C_ρ) = 861 J/kg K

Bead length = 282 mm

Total true energy = 573.6 kJ

Heat input (HI) = η × Total true energy (kJ) / bead length (mm)

HI = (0.85 × 573.6)/282

HI (q/v) = 1.73 kJ/mm

The thermal cycle is a function of the plate thickness, so it is necessary to determine the critical thickness (d'), which is the transition thickness between the thick and thin plates. This critical thickness was calculated according to Equation 4.4:

$$d' = \{\frac{\left(\frac{q}{v}\right)}{2\rho}\left(\frac{1}{1073-T_0} + \frac{1}{1473-T_0}\right)\}^{1/2}. \tag{4.4}$$

The critical diameter was determined to be

d' = 17.5 mm

The base metal thickness was 27 mm, which was above the critical diameter (d'); therefore, the 'thick-plate' equation was used when calculating the cooling time (Δt_{12-8})

in Table 4.13. The cooling time (Δt_{12-8}) of all welds presented in Table 4.13 was calculated by substituting the required values in Equations (4.5) and (4.6), which are thick-plate equations:

$$\text{Cooling time between 1200 to 800°C } (\Delta t_{12-8}) = \frac{q/v}{2\pi\lambda\theta_1} \quad (4.5)$$

$$\frac{1}{\theta_1} = \left(\frac{1}{1073-T_0} - \frac{1}{1473-T_0}\right) \quad (4.6)$$

$\frac{1}{\theta_1} = \left(\frac{1}{1073-T_0} - \frac{1}{1473-T_0}\right)$, where T_0 is 241°C

$\theta_1 = 1340°C$

$\Delta t_{12-8} = 1.73 / (2 \times 3.142 \times 30 \times 1340)$

$\Delta t_{12-8} = 6.85$ s

Cooling rate = (1200 – 800) / 6.85

Cooling rate = 58.4°C/s

4.6 Characterisation

4.6.1 Sectioning

The 28 GMAW beads were sectioned in the positions shown in Fig. 4.11. The sectioning was performed using a horizontal swing-arm band saw and an abrasive cut-off machine. During both sectioning operations, a water-based coolant was used to avoid thermal damage. The weld specimens removed from the section indicated by the red arrow were used for chemical analysis and metallography. For consistency of the reported chemical compositions and microstructures of all 28 welds, it was important that the analysed specimens were removed in the same position along the length of all weld beads.

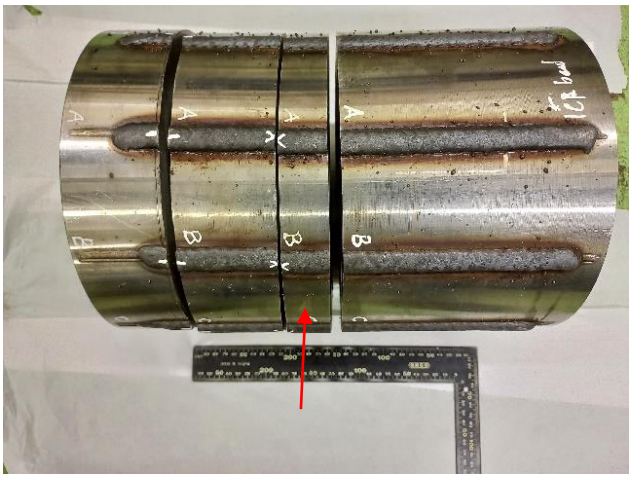

Fig. 4.11 Image shows the sectioned P91 pipe with GMAW beads. The section indicated by the red arrow was removed for chemical analysis and metallography.

4.6.2 Metallography

4.6.2.1 Optical microscopy

The GMAW beads were sectioned in the transverse and longitudinal planes for optical microscopy. These weld specimens were mounted in a Bakelite resin, ground, and fine-polished to 1 µm to obtain a mirror finish. To reveal the microstructural constituents, all specimens were etched using Vilella's reagent (100 mL ethanol, 1 g picric acid, and 5 mL HCl) [20]. The etched specimens were examined using an Olympus SZX7 stereoscope for macrostructures and Olympus BX51M for microstructures.

Delta ferrite phase fraction was quantified by the point-counting method. Over 20 micrograph images per weld were analysed (100× magnification), covering the transverse cross-section of the GMAW bead. A total of 210 points were placed on the microstructure image and the number of points within the delta ferrite phase were counted to estimate the fraction against the total number of points.

4.6.2.2 Scanning electron microscopy image analysis

The same weld specimens used for optical microscopy were examined with a JEOL JSM IT300LV SEM utilising secondary electron imaging (SEI) at 20 kV and an average working distance (WD) of 11 mm. The Bakelite mounting is a poor conductor, so aluminium tape was used to avoid sample charging. SEM was used to study in more detail the changes that occurred after PWHT.

4.6.3 Chemical analysis

4.6.3.1 Optical emission spectroscopy

Chemical compositions of all GMAW beads were analysed by an external accredited laboratory using optical emission spectroscopy (OES). In addition, four of the 28 GMA welds were selected and their compositions was analysed in five positions about 40 mm apart along the length of the weld bead, as illustrated in Fig. 4.12. This was performed to determine the uniformity of the chemical composition along the length of the beads. The average bead length was about 275 mm.

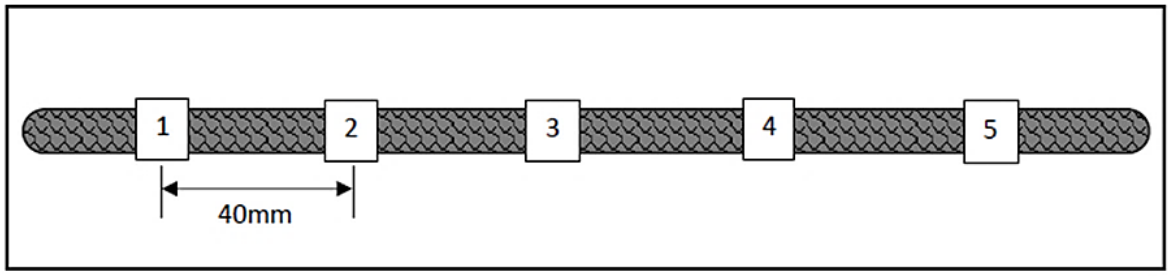

Fig. 4.12 Sketch illustrating the positions where specimens were sectioned along the GMAW beads for chemical analysis.

4.6.3.2 Energy-dispersive spectroscopy

Energy-dispersive spectroscopy (EDS) is a technique that enables the elemental analysis of a material to be performed in an SEM. This chemical composition analysis technique

is based on the characteristic X-ray peaks that are generated when a high-energy electron beam interacts with the specimen. Each element emits X-rays with a characteristic spectrum based on its atom of origin, which can be used to identify the presence of that element. This allows for compositional analysis of a given sample volume that has been excited by the energy source [115]. The positions of the peaks in the spectrum identify the element, whereas the intensity of the signal corresponds to the concentration of the element.

The accelerating voltage determines the velocity at which the electrons travel down the column in an SEM, which increases the interaction volume. The interaction volume (excitation volume) is the volume of the sample in which the primary beam electrons have sufficient energy to affect or interact with. The main factors that determine the interaction volume are the atomic number of the material being examined, the accelerating voltage, and the angle of incidence for the electron beam [116]. The optimum choice of accelerating voltage is determined by the elements present in the specimen. The accelerating voltage (in kV) should be more than twice the highest excitation energy (in keV) of any element present to obtain adequate intensity. Line intensities increase with accelerating voltage, but so does electron penetration, making spatial resolution worse and increasing the absorption suffered by the emerging X-rays. An acceleration voltage of 20 kV was selected for this EDS analysis to improve accuracy of the results, particularly for the alloys (Mn, Mo, Cr, Ni, Si added). Minor elements with small atomic mass and at low concentrations are harder to accurately detect using EDS, especially at high acceleration voltage. To avoid reporting erroneous results, minor elements and those with low concentrations are not reported with the EDS results.

The SEM-EDS analyses were primarily performed to determine whether the elements added through laser metal deposition were homogeneously distributed in the GMAW beads. The transverse cross-section EDS analyses were performed in seven locations, as demonstrated in Fig. 4.13. The orientation of the analysed surface to the electron beam ensured that the excitation volume was contained within the weld metal. SEM-EDS was also performed on the laser beads to determine their composition before overlaying them with the GMAW bead.

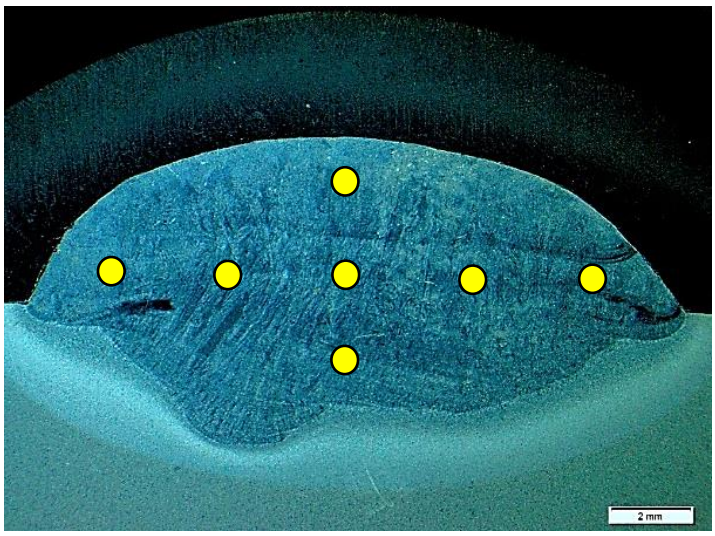

Fig. 4.13 Transverse cross-section image showing the seven locations where SEM−EDS analysis was performed on the bead.

4.7 Post-weld heat treatment

The focus of the PWHT experiments was to investigate the response of the general microstructure and the often-observed delta ferrite in P91 as-welded structures to PWHT. Table 4.15 describes the five GMA welds selected for the experiment. It was important that the selected beads contained certain amounts of delta ferrite in the weld structure. Included in Table 4.15 are the delta ferrite volume fraction measured in the as-welded condition and the Ae_1 transformation temperature calculated using Thermo-Calc software.

Table 4.15 *Selected welds for post-weld heat treatment experiments*

Selected weld	*% Delta ferrite (± 95% CI)*	*Ae_1 temperature (°C)*
PH 4	0.3 ± 0.1	773
PH 5	3.5 ± 0.9	803
AW 10	2.2 ± 0.7	814
AW 17	6.2 ± 1.2	817
AW 21	2.6 ± 0.6	793

The applied PWHT thermal cycle was:

Peak temperature: 760, 795, and 815°C
Heating rate: 200°C/h
Hold time: 2 h
Cooling rate: < 200°C/h

A 760°C PWHT temperature and two additional temperatures (795°C and 815°C), which are above the recommended limit, were applied. In some of the selected welds, the applied PWHT peak temperatures were above their lower critical temperature (Ae_1).

A hole was drilled in the specimens and external thermocouples were inserted to record the actual thermal cycle experienced by the specimens.

4.8 Simulation of multi-pass weld thermal cycle using Gleeble thermal treatment

Multiple-pass welding is often performed in practice during the fabrication of P91 steel. Gleeble thermal treatment was performed to simulate the thermal cycle experienced by a weld bead when a subsequent bead is deposited in a multiple-pass weld. In a multiple-pass weld, the bead that has been previously laid will experience different peak temperatures from the weld thermal cycle of the subsequent bead. The resultant microstructure evolution in the bead overlaid by subsequent passes is determined by the extent of austenitisation and grain growth. This may result in the formation of different zones, similar to that observed in the traditional base metal HAZ, and significant changes of the delta ferrite in the previously deposited weld beads.

The main interest from the Gleeble thermal treatment simulation experiment was to evaluate the effect of the subsequent bead thermal cycle on the morphology and volume fraction of delta ferrite in the previously deposited weld bead. The Gleeble was preferred over dilatometry in simulating the weld thermal cycle because of the larger specimen size. The Gleeble also heats the sample through resistivity which limits the thermal gradient in the specimen where the thermocouple is attached.

Five welds that contained significant amounts of delta ferrite in the as-welded condition were selected for the Gleeble experiment. Onoro [89] stated that thermal cycling to high temperatures in multiple-pass P91 welds reduced the amount of delta ferrite. Weld metal that did not contain any delta ferrite in the as-welded condition were therefore not included in this experiment. Specimens were all machined from the centre of the length of the bead. Table 4.16 lists the selected welds, the delta ferrite volume fraction in the as-welded condition, and the transformation temperature calculated using Thermo-Calc software.

Table 4.16 *Welds selected for Gleeble experiment and their transformation temperatures.*

Weld ID	***% Delta ferrite (± 95% CI)***	***Equilibrium transformation temperatures* (°C)***			
		Ae_1	Ae_3	Ae_4	Ae_5
PH 5	3.5 ± 0.9	803	887	1157	1375
AW 9	3.8 ± 0.6	810	866	1213	1383
AW 16	6.0 ± 1.1	817	883	1184	1374
AW 18	1.8 ± 0.4	784	847	1232	1400
AW 21	2.6 ± 0.6	793	857	1209	1381

** Calculated using Thermo-Calc software.*

The thermal cycle experienced in the HAZ was physically simulated using a Gleeble 1500 thermo-mechanical simulator. The specimens were machined from the weld metal to a rectangular prism (15 mm × 7 mm × 10 mm (L × H × W)) with rounded edges. A Type S thermocouple was attached to the specimen surface in the centre to measure the

actual temperature of the specimen during treatment. The specimens were mounted between W electrodes fixed to water-cooled copper grips and resistively heated. To improve contact between the W electrodes and the specimens, a 1 kN clamp pressure was applied prior to initiating the simulation thermal treatment. During the thermal treatment, the chamber was purged with an inert gas (He) to prevent oxidation of the specimen.

4.8.1 Applied thermal cycles

The following peak temperatures were selected for the thermal treatment of the five welds:

- 1350°C: between the (Ae_4−Ae_5) temperature range
- 1100°C: middle of (Ae_3−Ae_4) temperature range
- 900°C: immediately above the Ae_3 temperature

Figure 4.14 shows a P91 compositional phase diagram indicating the positions of the selected peak temperatures. The applied heating rate was 300°C/s and the cooling rate was 25°C/s. The Gleeble cooling rate was much lower than the 60 to 110°C/s range achieved during GMAW. It was desired to select heating and cooling rates that simulated the GMAW thermal cycle but the parameters applied were due to the limited capabilities of the Gleeble instrument used.

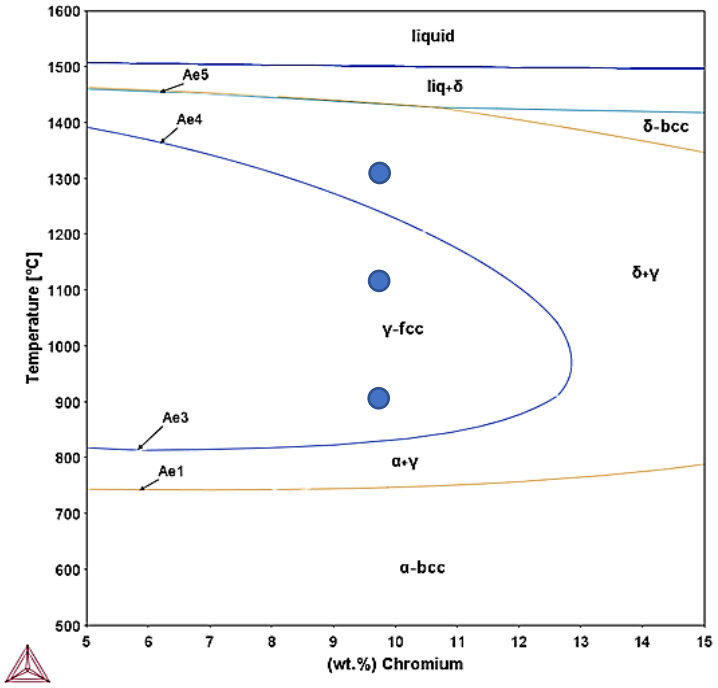

Fig. 4.14 P91 compositional phase diagram in the 5 to 15 mass% Cr range constructed using Thermo-Calc software. The blue dots indicate the position of the Gleeble peak temperatures applied.

4.9 Dilatometry

The dilatometry technique allows real-time monitoring of phase transformation, which made possible the investigation of austenite/delta ferrite phase transformation thermodynamics in P91 welds. Dilatometry measures linear dimensional changes that occur as a function of temperature and time. In these experiments, dilatometry was performed to achieve the following two objectives:

- Studying the influence of cooling rate on delta ferrite/austenite phase transformation. These results provided some insight into the role the cooling rate plays in the observed delta ferrite in the final weld microstructure. On multi-bead welds, the effect of various thermal cycles on the initial weld bead by the latter bead could be better understood.
- To determine the transformation temperatures (Ae_1 and Ae_3) of the selected GMA welds and compare these results with the values calculated using Thermo-Calc software.

A Bahr dilatometer was utilized. An S-type thermocouple was spot-welded on the specimens to control the programmed temperature cycle and to ensure recording of the actual temperature of the specimen during thermal treatment. The process involved placing the specimen between two quartz tubes and using inductive heating. Prior to starting the thermal cycle, the specimen chamber was evacuated and flushed with He gas for better cooling control.

To achieve the above objectives, two experiments were conducted.

1. *Austenite/delta ferrite phase-transformation thermodynamics in P91 alloy*

This experiment was performed using solid cylindrical specimens (10 mm length × 5 mm diameter), as recommended by the ASTM A−1033 standard, sectioned from the P91 base metal. A peak temperature of 1350°C was chosen to achieve a starting microstructure that consisted of approximately equal volume fractions of austenite and delta ferrite phases. For P91 steel, the critical cooling rate for martensitic transformation is about 0.06°C/s [38]. It was necessary for the chosen cooling rates to be higher than the minimum required for martensite formation to avoid the austenite transforming to alpha ferrite below the Ae_1 temperature.

Uninterrupted cooling thermal cycles: The specimens were heated at 200°C/s to a peak temperature of 1350°C with no holding time. The specimens were then cooled at rates of 1, 10, 30, 50, 100, 200°C/s to ambient temperature, as illustrated in Fig. 4.15. The thermodynamics of the transformation of delta ferrite to austenite was studied under continuous cooling, as occurs during welding.

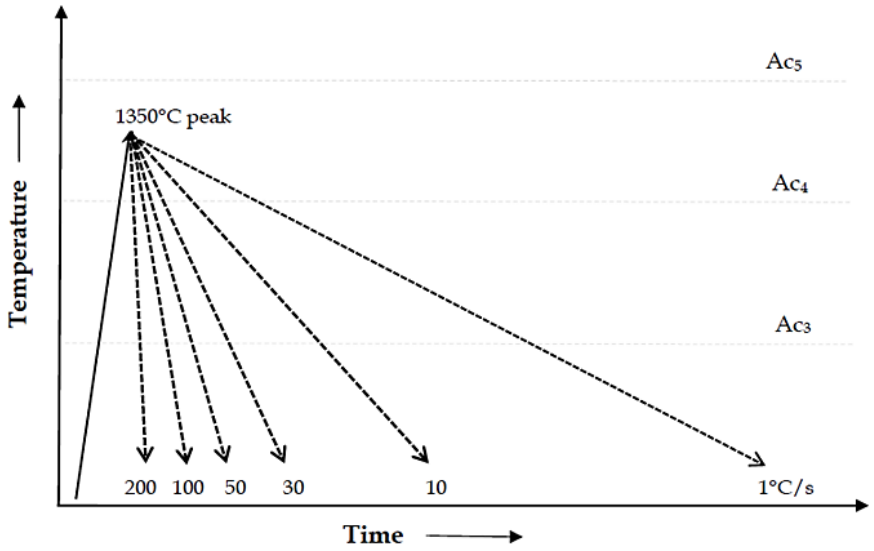

Fig. 4.15 Uninterrupted cooling thermal cycle applied on P91 base metal. The specimens were heated to 1350°C peak temperature, then cooled to ambient at different rates.

Interrupted cooling thermal cycles: The specimens were heated at 200°C/s to a peak temperature of 1350°C with no holding time, then cooled at rates of 0.1, 1, 10, and 50°C/s to 1270°C before quenching to ambient temperature, as illustrated in Fig. 4.16. The 1270°C temperature was determined using Thermo-Calc software to be just above the Ae_4 equilibrium transformation temperature. This study was designed to determine the microstructures at high temperatures incorporating cooling rates just above the Ae_4 transformation temperature, below which only austenite is stable.

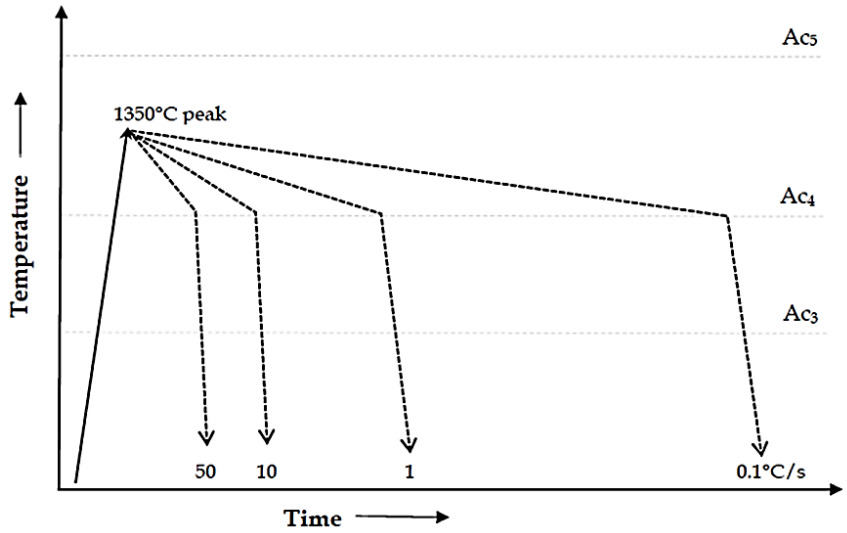

Fig. 4.16 Interrupted thermal cycle applied on P91 base metal. The specimens were heated to 1350°C peak temperature, then cooled to 1270°C at different rates before quenching.

2. *Determining the Ae_1 and Ae_3 transformation temperatures of selected welds*

The purpose of this investigation was to experimentally determine the Ae_1 and Ae_3 transformation temperatures of selected welds and compare these with the transformation temperatures calculated using Thermo-Calc. Three samples were selected for these experiments; namely, AW 4, AW 6, and AW 22. Specimens were all machined from the centre of the length of the bead.

The applied thermal cycle, as prescribed by the ASTM A1033-04 standard, is described below:

Specimen stabilization: The specimens were heated at 10°C/s to 650°C and then held for 10 min. The specimens were then cooled to 100°C at 20°C/s.

Actual thermal cycle to determine the critical temperature: The specimens were heated without removing them from the apparatus after stabilization to 600°C at 10°C/s, then heated at 28°C/h to 1000°C peak temperature before ending the cycle.

4.10 Hardness measurements

All hardness testing was performed using a Duramin-40 fully automatic micro/macro-Vickers, which has a load range of 1 gf−62.5 kgf. The Vickers hardness technique was preferred because of the latitude in applied loads, which allows for bulk average and local phase hardness measurements.

Hardness testing was carried out on all specimens, including the as-welded beads, Gleeble, PWHT, and dilatometry specimens. After metallography analysis on the welds was completed, the same specimens were used for hardness measurements.

Macro-Vickers hardness: The P91 welds varied in composition and thus their microstructure consisted of a martensitic matrix with delta ferrite in some instances. The macro-Vickers hardness measures the contributions of both martensite and delta ferrite. Testing was performed with a 10 kgf (Hv_{10}) load with a dwell time of 10 s. At least five measurements were taken on each specimen with 2 mm indent spacing.

Micro-Vickers hardness: The micro-hardness testing method is used to measure local variations in hardness of a material. Micro-Vickers hardness testing was performed on the as-welded beads, targeting the delta ferrite phase, applying a 25 gf ($Hv_{0.025}$) load with a dwell time of 10 s. The dilatometry specimens were tested with a 300 gf ($Hv_{0.3}$) load. To be able to analyse the different phases present in the microstructure, the specimens were tested in the polished and etched condition.

Section III

Results & Discussion

Chapter 5
Thermo-Calc simulation

5.1 Determination of 130 compositions for Thermo-Calc evaluation

Different composition scenarios were imagined and used in designing the 130 compositions. In some instances, the elements were collectively varied as austenite formers and ferrite formers but always limited within the AWS A5.28/A5.28M:2020 (ER90S-B9) specified ranges. A starting position was the reference composition based on the AWS A5.28/A5.28M:2020 (ER90S-B9) mid-points of the element range. The starting composition was 0.1% C, 0.9% Mn, 9.0% Cr, 0.25% Si, 1.0% Mo, 0.2% V, 0.07% Nb, 0.04% N, and 0.7% Ni.

Below are some of the scenarios considered:

- All elements were varied from upper limit of the range to lower limit of the range based on the AWS A5.28/A5.28M:2020 (ER90S-B9) standard.
- Individual elements were varied from the minimum–maximum range with other elements fixed on the reference composition.
- Varied ferrite formers ranged from minimum–maximum with other elements fixed on the reference composition.
- Varied austenite formers ranged from minimum–maximum with other elements fixed on the reference composition.
- Varied ferrite formers ranged from minimum–maximum with all austenite formers on minimum limits.
- Varied austenite formers ranged from minimum–maximum with all ferrite formers on minimum.

To illustrate the variation of compositions, Table 5.1 shows an example of a few compositions that were systematically varied.

Table 5.1 *Systematically varied P91 compositions for Thermo-Calc simulations.*

Designed compositions	**C**	**Mn**	**Cr**	**Si**	**Mo**	**V**	**Nb**	**N**	**Ni**
	0.08-0.13	1.20 max	8.0-10.5	0.5 max	0.85-1.20	0.15-0.30	0.02-0.10	0.03-0.07	0.80 max
Reference composition	0.10	0.9	9.00	0.25	1.00	0.20	0.07	0.04	0.7
All elements (upper to lower limits)	0.13	1.2	10.5	0.50	1.20	0.30	0.10	0.07	0.8
	0.11	1.0	9.5	0.40	1.10	0.26	0.08	0.06	0.7
	0.10	0.8	9.0	0.30	1.00	0.23	0.06	0.05	0.6
	0.09	0.6	8.5	0.20	0.90	0.19	0.04	0.04	0.5
	0.08	0.4	8.0	0.10	0.85	0.15	0.02	0.03	0.4
*Vary **Mn** with reference composition*	0.10	1.2	9.0	0.25	1.00	0.20	0.07	0.04	0.7
	0.10	1.0	9.0	0.25	1.00	0.20	0.07	0.04	0.7
	0.10	0.8	9.0	0.25	1.00	0.20	0.07	0.04	0.7
	0.10	0.6	9.0	0.25	1.00	0.20	0.07	0.04	0.7
	0.10	0.4	9.0	0.25	1.00	0.20	0.07	0.04	0.7
*Vary **ferrite formers** with reference composition*	0.10	0.9	10.5	0.50	1.20	0.20	0.07	0.04	0.7
	0.10	0.9	9.5	0.40	1.10	0.20	0.07	0.04	0.7
	0.10	0.9	9.0	0.30	1.00	0.20	0.07	0.04	0.7
	0.10	0.9	8.5	0.20	0.90	0.20	0.07	0.04	0.7
	0.10	0.9	8.0	0.10	0.85	0.20	0.07	0.04	0.7

5.1.1 Empirical formulae application on designed compositions

The Schaeffler and Schneider empirical values were calculated based on the designed compositions to predict the final weld microstructures and to identify weld compositions that have a high probability of delta ferrite in the final weld metal. Table 5.2 presents calculated Schneider (Cr_{eq}, Ni_{eq}, FF) [86] and CNB values [5] with recommended limits, based on the compositions in Table 5.1. The values in red font exceeded the recommended limits for the Schneider and Newhouse values and the final weld metal had a high probability of containing delta ferrite in the final weld metal. This was despite the designed alloy compositions complying with the AWS A5.28/A5.28M:2020 (ER90S-B9) specification. The empirical formulae calculations also highlighted the effect of individual or collective elements (ferrite or austenite formers) on limiting or increasing the presence of delta ferrite.

Table 5.2 *Schneider* (Cr_{eq}, Ni_{eq}, FF) *and CNB values calculated from the designed P91 compositions. Weld metal (✗) improbable or (✓) probable to contain delta ferrite*

Designed compositions	**Schneider**			**Newhouse**	**Delta ferrite presence**
	Cr_{eq} (≤ 13.5)	Ni_{eq}	FF (≤ 8)	CNB (≤ 10)	
Reference	12.1	5.2	6.9	7.2	✗
All elements (upper to lower limits)	**15.2**	7.1	**8.1**	8.8	✓
	13.9	6.1	7.9	8.7	✓
	12.7	5.0	7.7	8.5	✗
	11.4	4.0	7.5	8.4	✗
	10.2	2.9	7.3	8.2	✗
*Vary **Mn** with reference composition*	12.1	5.5	6.7	6.1	✗
	12.1	5.3	6.8	6.6	✗
	12.1	5.2	7.0	7.3	✗
	12.1	5.0	7.1	7.7	✗
	12.1	4.9	7.2	8.3	✗
*Vary **ferrite formers** with reference composition*	**14.6**	5.2	**9.5**	**11.7**	✓
	13.6	5.2	**8.4**	9.9	✓
	12.6	5.2	7.4	8.1	✗
	11.5	5.2	6.4	6.3	✗
	10.5	5.2	5.4	4.6	✗

5.1.2 Property diagrams and phase transformation temperature of designed compositions

Property diagrams were constructed based on the 130 compositions and their equilibrium transformation temperatures were determined. Figure 5.1 shows two of the many equilibrium property diagrams constructed. Peritectic transformation was observed in Fig. 5.1(a), highlighted by the red circle where austenite formed from both liquid and delta ferrite during cooling. A small temperature range exists where liquid, delta ferrite and austenite coexist. The property diagram from a P91 alloy with increased amount of ferrite formers shown in Fig. 5.1(b) displays a different transformation sequence. The liquid solidifies to 100% delta ferrite phase and, subsequently, austenite forms later from delta ferrite due to a solid-state phase transformation. Thermo-Calc software was also used to calculate the ($Ae_4 - Ae_3$) temperature range, which is an important indicator in predicting the presence of delta ferrite in the as-welded structure [60].

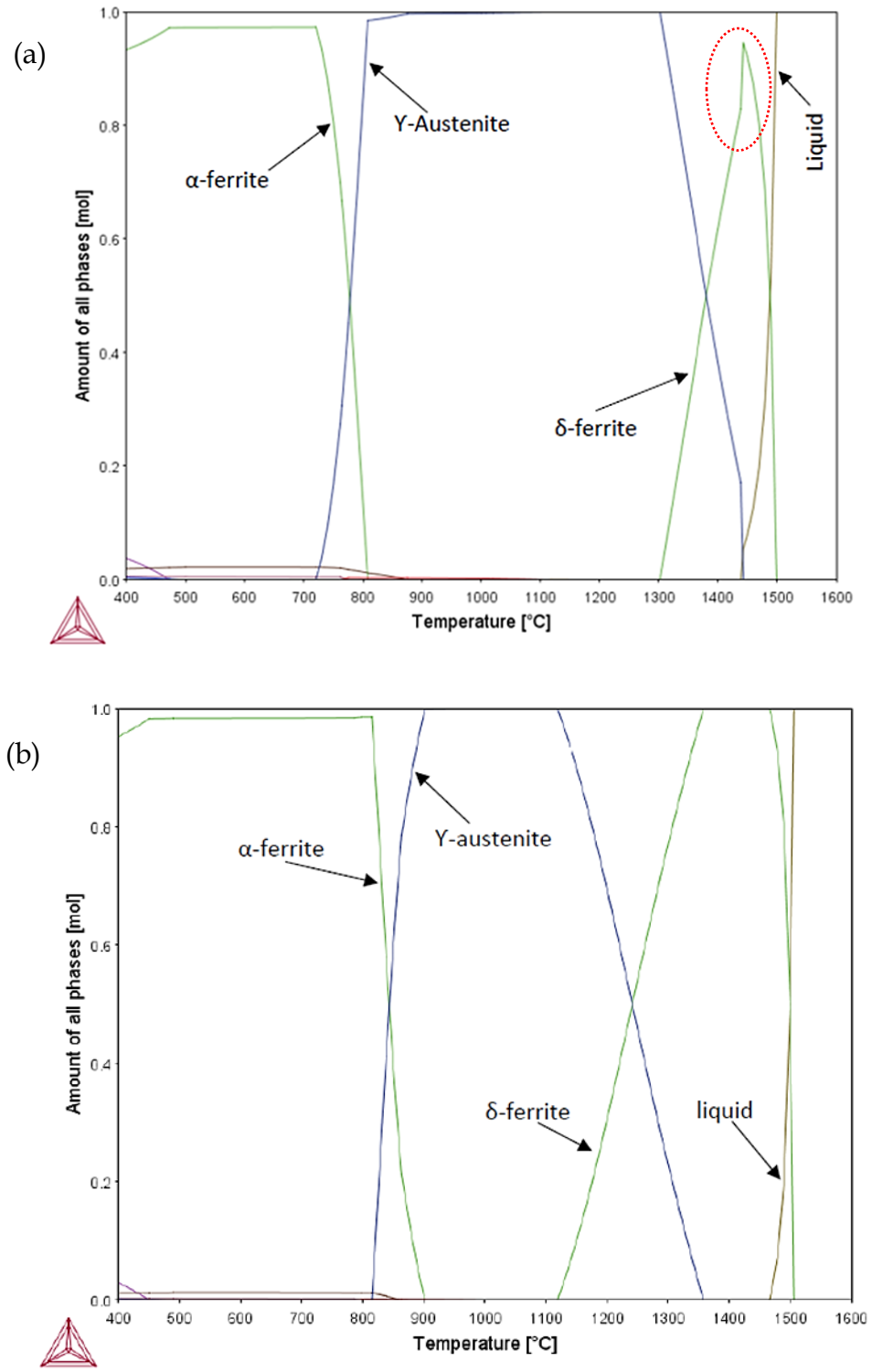

Fig. 5.1 Property diagrams for (a) reference composition and (b) high ferrite formers, with reference composition showing the mole fractions of phases as a function of temperature. The red circle in (a) highlights evidence of a peritectic transformation.

The acquired information from Thermo-Calc simulation results, empirical values, and ($Ae_4 - Ae_3$) temperature ranges was utilised in selecting the five alloying elements (Cr, Ni, Mn, Si, and Mo) that were varied in the alloy design of the 28 GMA welds performed in this research.

5.2 Phase diagrams

The Thermo-Calc results presented in this subsection were performed based on the reference alloy with variation of the five alloying elements. Figure 5.2 and Fig. 5.3 show P91 equilibrium phase diagrams with the amounts of Cr and Ni varied. The red lines on the diagrams indicate the AWS A5.28/A5.28M (ER90S-B9) specified ranges of the elements. Additional phase diagrams with mass% ranges of Si, Mn, and Mo are included in Appendix A.

Figure 5.2 shows the effect of variation in Cr content between 5 and 15 mass%. Cr is the main alloying element in P91 steel because of its influence in both oxidation resistance and creep strength, and is a strong ferrite former. The equilibrium phase diagrams with Cr variation clearly demonstrate the influence of Cr on transformation temperatures and on restricting the austenite phase field, mainly by reducing the Ae_4 temperature.

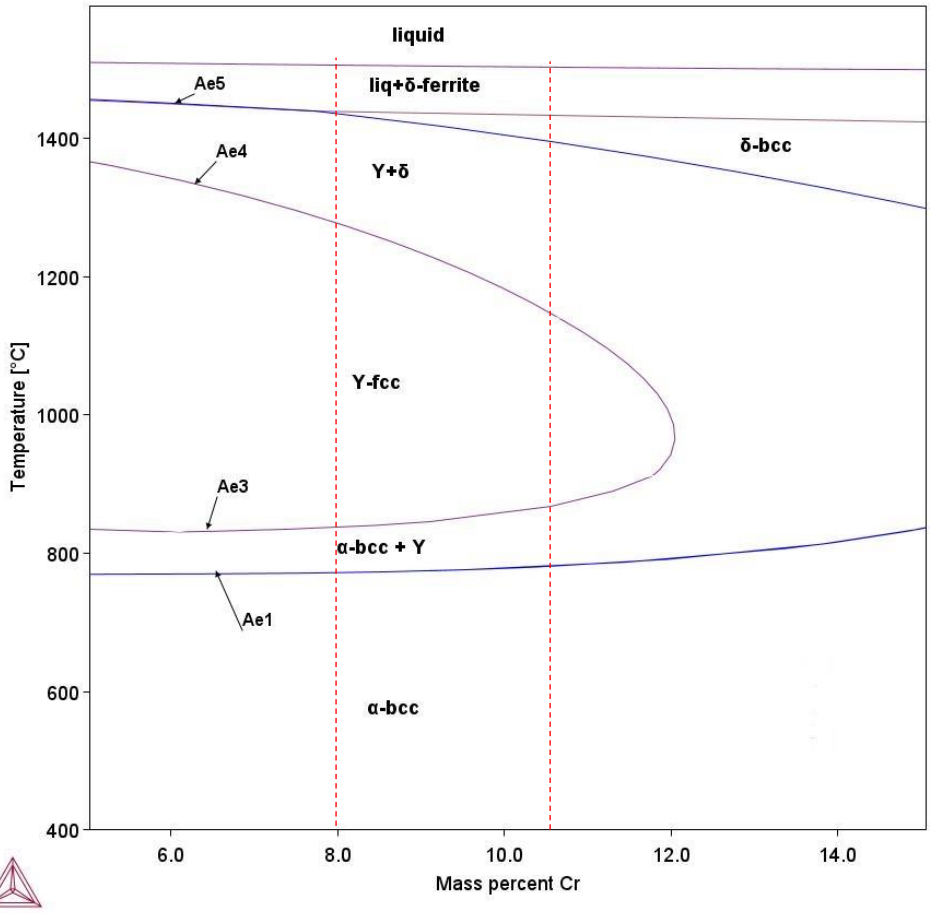

Fig. 5.2 P91 compositional phase diagram showing 5 to 15 mass% Cr. P91 Cr range is between 8.0% to 10.5%, indicated by the red dashed lines.

Figure 5.3 shows the effect of variation in Ni content between 0 and 1.8 mass%. Ni is a strong austenite former and is an important addition for avoiding delta ferrite and improving toughness and solid-solution strengthening. An increase of Ni in P91 steel widens the (Ae_4 − Ae_3) temperature range and depresses the Ae_1 temperature, as observed in Fig. 5.3, bringing it closer to the PWHT temperature. Thus, care must be

taken to ensure that Ae_1 is not so low that PWHT causes some austenite to form, which, upon cooling, will transform to fresh martensite.

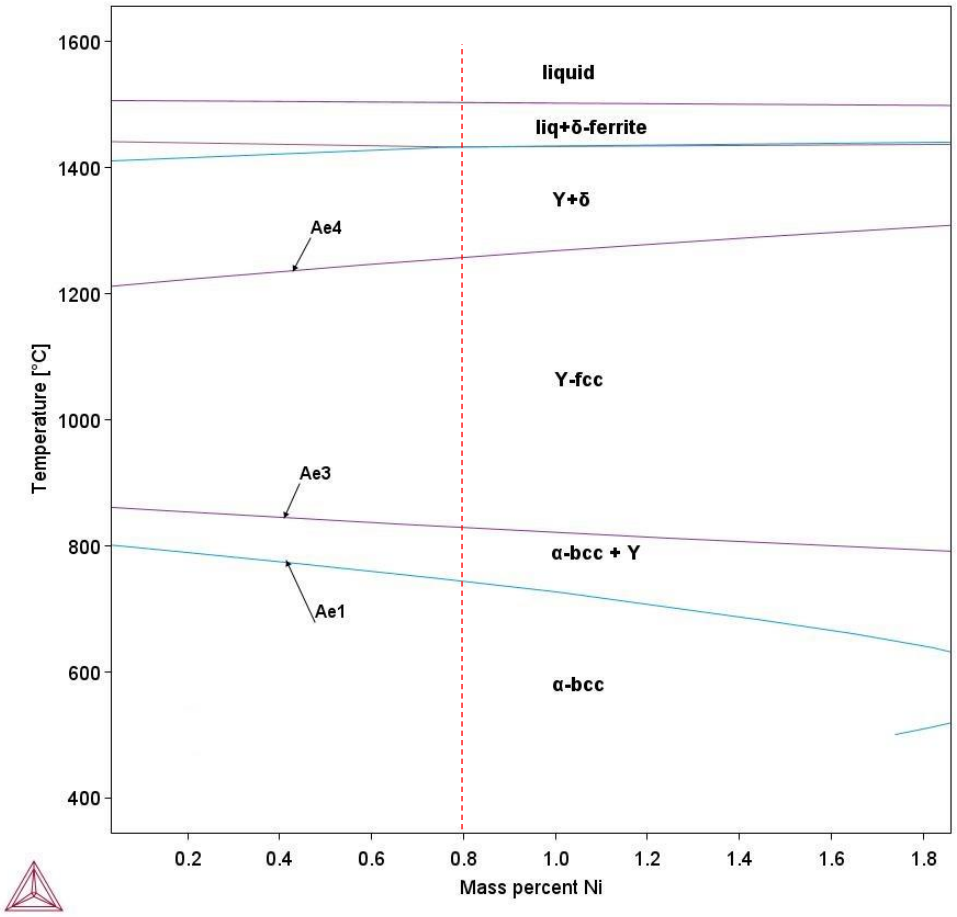

Fig. 5.3 P91 compositional phase diagram showing 0 to 1.8 mass% Ni. P91 Ni range is specified to be 0.8% maximum, indicated by the red dashed lines.

5.2.1 Transformation sequence

All 28 GMA welds followed the below transformation sequences from solidification to ambient temperature:

$$\text{Liquid} \rightarrow \text{liquid} + \delta \rightarrow \delta \rightarrow \delta + \gamma \rightarrow \gamma \rightarrow \text{martensite} \quad (6.1)$$

In the case where the welds contained delta ferrite in as-welded condition:

$$\text{Liquid} \rightarrow \text{liquid} + \delta \rightarrow \delta \rightarrow \delta + \gamma \rightarrow \text{martensite} + \delta \quad (6.2)$$

5.3 Equilibrium critical transformation temperature of GMA welds

Table 5.3 presents the Thermo-Calc equilibrium transformation temperatures of the 28 GMA welds selected from the 130 designed compositions. The transformation temperatures were calculated based on the chemical compositions of the GMAW beads presented later in Table 7.3. The ($Ae_4 - Ae_3$) temperature ranges are included in Table

5.3 because Arivazhagan and Kamaraj [60] observed that the chances of delta ferrite retention in the weld increased if the ($Ae_4 - Ae_3$) is low.

Table 5.3 *Equilibrium critical transformation temperatures (°C) of selected GMAW beads calculated using Thermo-Calc software.*

GMAW beads	Alloying added (laser beads deposited)	Ae_1 (°C)	Ae_3 (°C)	Ae_4 (°C)	Ae_5 (°C)	Liquidus (°C)	($Ae_4 - Ae_3$) (°C)
250°C Preheat							
PH 1	No alloying	802	847	1277	1412	1505	430
PH 2	(0.5)Cr	803	852	1257	1404	1504	405
PH 3	(1)Cr	805	858	1231	1394	1503	373
PH 4	(2)Cr, (2)Mn	773	844	1216	1391	1500	372
PH 5	(2)Cr, (1)Mn, (1)Mo	803	887	1157	1375	1501	270
PH 6	(1)Cr, (1)Mn, (0.5)Ni	775	837	1252	1404	1501	415
No Preheat							
AW 1	No alloying	798	844	1277	1411	1503	433
AW 2	(1)Cr	797	845	1268	1414	1503	423
AW 3	(2)Cr	800	860	1213	1397	1501	353
AW 4	(2)Cr, (0.5)Mo	806	866	1206	1387	1501	340
AW 5	(2)Cr, (1)Mo	813	891	1167	1380	1501	276
AW 6	(2)Cr, (0.5)Ni	791	850	1226	1390	1500	376
AW 7	(2)Cr, (1)Ni	748	822	1259	1418	1498	437
AW 8	(2)Cr, (2)Ni	730	813	1263	1410	1499	450
AW 9	(2)Cr, (1)Si	810	866	1213	1383	1499	347
AW 10	(2)Cr, (2)Si	814	879	1178	1373	1500	299
AW 11	(2)Cr, (2)Mn	752	823	1259	1414	1499	436
AW 12	(2)Mn, (0.5)Mo	767	831	1289	1417	1500	458
AW 13	(2)Mn, (1)Si	767	828	1292	1415	1499	464
AW 14	(0.5)Mo, (1)Si	809	856	1263	1399	1502	407
AW 15	(2)Cr, (0.5)Mo, (1)Si	811	864	1232	1390	1501	368
AW 16	(2)Cr, (1)Mo, (1)Si	817	883	1184	1374	1501	301
AW 17	(2)Cr, (1)Mo, (2)Si	817	884	1192	1391	1499	308
AW 18	(2)Cr, (0.5)Mo, (1)Mn	784	847	1232	1400	1498	385
AW 19	(2)Cr, (1)Mo, (1)Mn	780	852	1243	1421	1497	391
AW 20	(2)Cr, (0.5)Mo, (0.5)Ni	795	852	1238	1396	1502	386
AW 21	(2)Cr, (1)Mn, (1)Si	793	857	1209	1381	1499	352
AW 22	(0.5)Mo, (2)Mn, (1)Si	771	835	1282	1406	1498	447
	Min.	*730*	*813*	*1157*	*1373*	*1497*	*270*
	Max.	*817*	*891*	*1292*	*1421*	*1505*	*464*

Chapter 6

Characterisation of direct laser deposition weld beads

6.1 Laser weld metal geometry

Cr, Ni, Mn, Si, and Mo powder metals were deposited in P91 base metal using the DLD process. Figure 6.1 shows laser beads of the different elements.

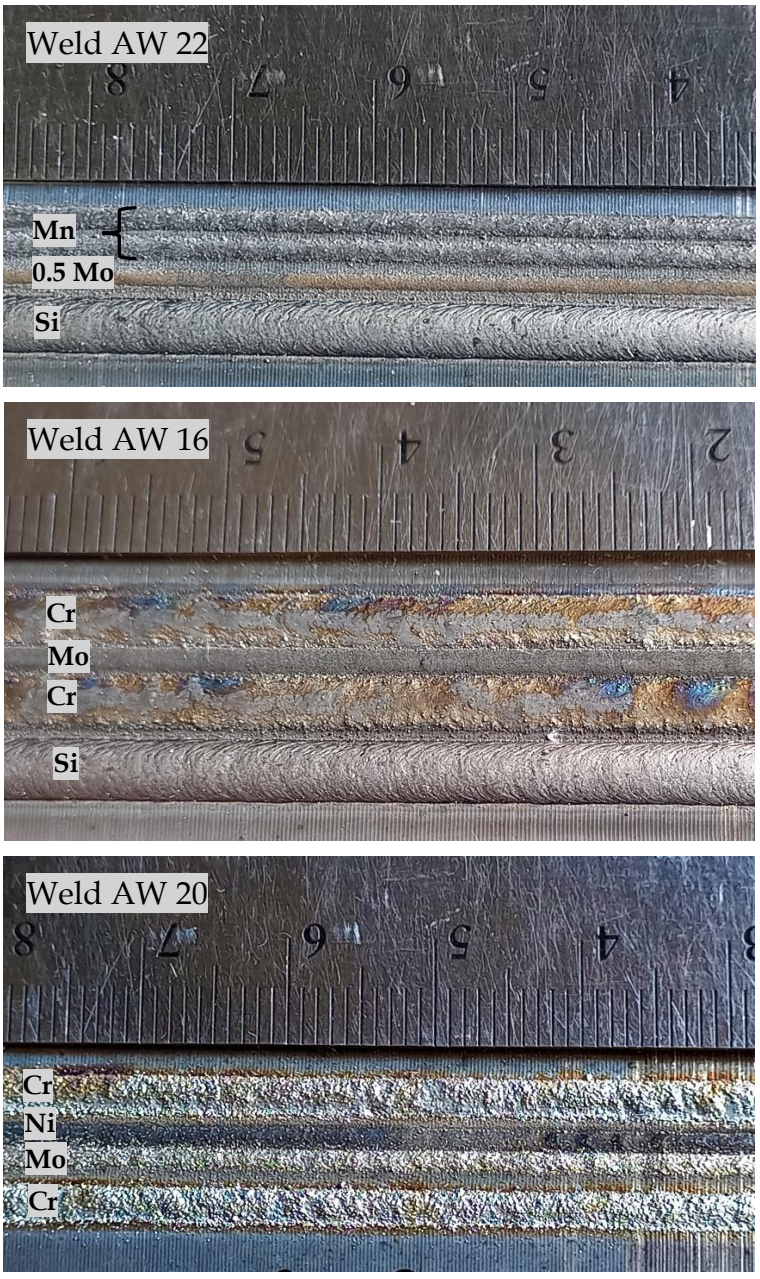

Fig. 6.1 Deposited laser beads of welds AW 22, AW 16, and AW 20.

Various process parameters (spot size, laser power, torch speed, and powder feed rate) were determined to ensure the correct bead size was achieved. Obtaining the desired compositional changes in the GMA beads required the correct laser bead size.

Figure 6.2 shows representative micrograph images of cross-sections of the laser welds captured using a stereoscope (20× magnification).

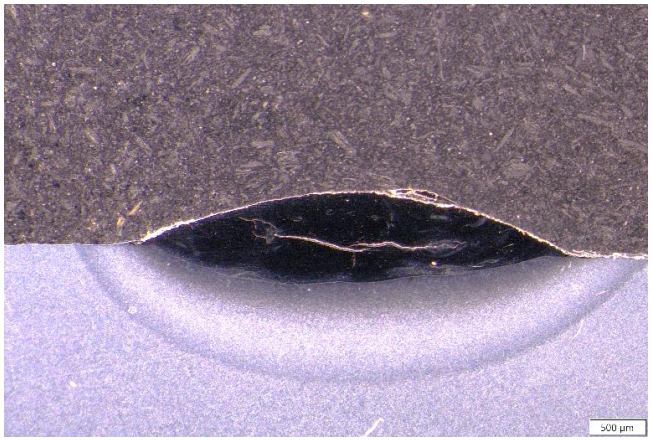

Si (AW 22)

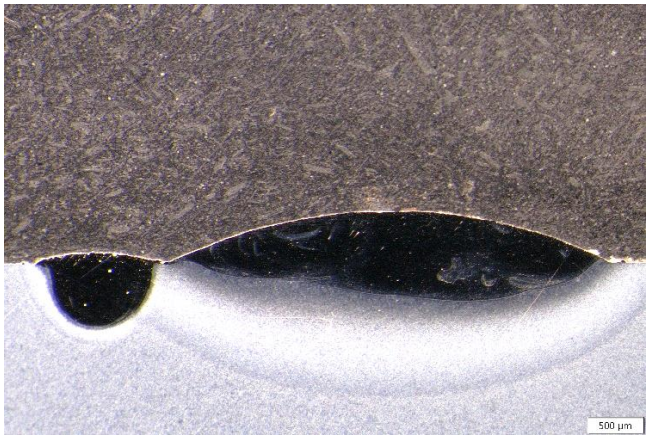

Mo and Si (AW 14)

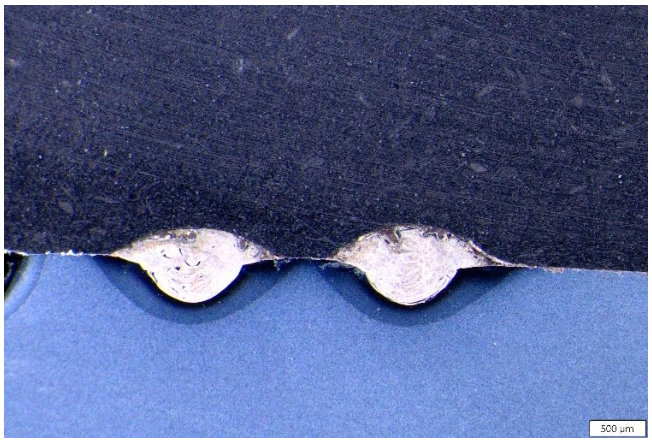

Mn (AW 12)

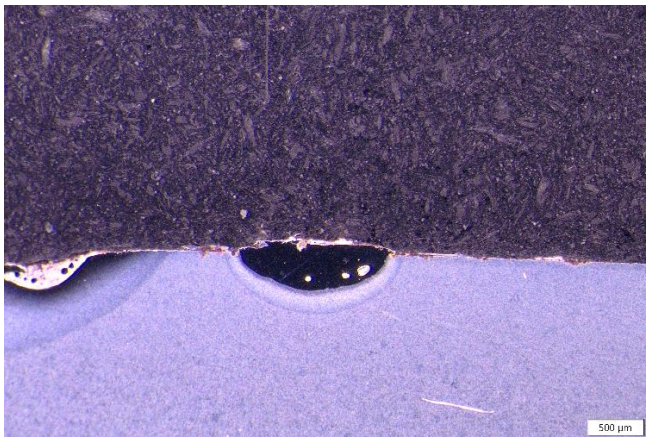

Ni (PH 6)

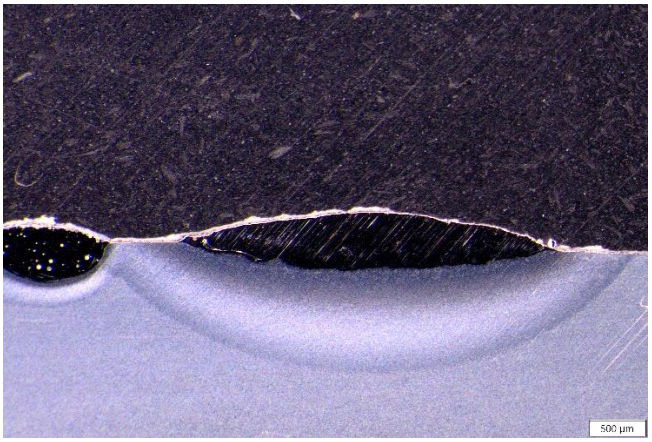

Cr (PH 5)

Fig. 6.2 Stereoscope images of laser bead cross-sections (20× magnification).

Si and Cr were deposited with 4 mm spot size and at 0.5 m/min laser speed, which explains why these beads were wider than those of Ni, Mo, and Mn, which were deposited with 2 mm spot size and at 1.2 m/min. During deposition of the Si beads, the laser beam was very stable and the beads were smooth and uniform. Cr deposition was accompanied by a lot of sparks and the bead surface was rough and non-uniform.

Figure 6.3 shows a schematic drawing to illustrate the bead geometry terms. Table 6.1 describes the laser beads geometries of the five alloying elements.

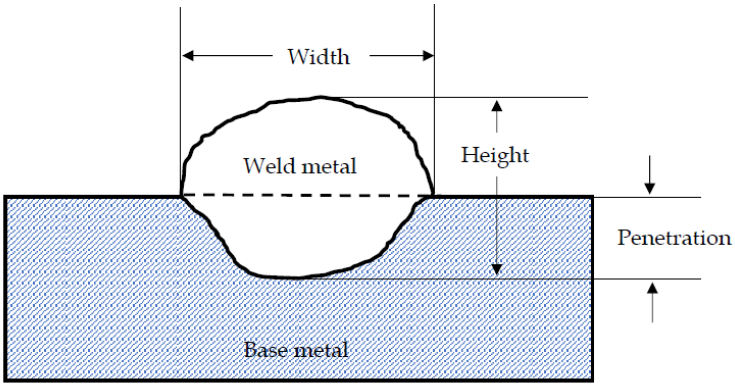

Fig. 6.3 Schematic illustration of weld metal geometry determination.

Table 6.1 *Laser bead geometry from stereoscope micrograph images*

	Laser bead size (average µm)		
Metal alloy powder	**Width**	**Height**	**Penetration**
TLS (Cr99.2)	3200	550	240
METCO 56C-NS (Ni powder)	1500	500	350
Weartech (Mo99.5)	1700	580	490
Manganese Metal Co powder	1500	720	410
FeSi (6F)	3900	840	360

6.2 Laser weld composition analysis

Energy-dispersive spectroscopy (EDS) analysis was performed with a JEOL JSM IT300LV scanning electron microscope (SEM) with the following settings:

i. Working distance (WD): 10–11 mm
ii. Accelerating voltage: 20 kV
iii. Scan time: 100 s

Figure 6.4 presents an example of the positions at which EDS analysis was performed in the laser beads.

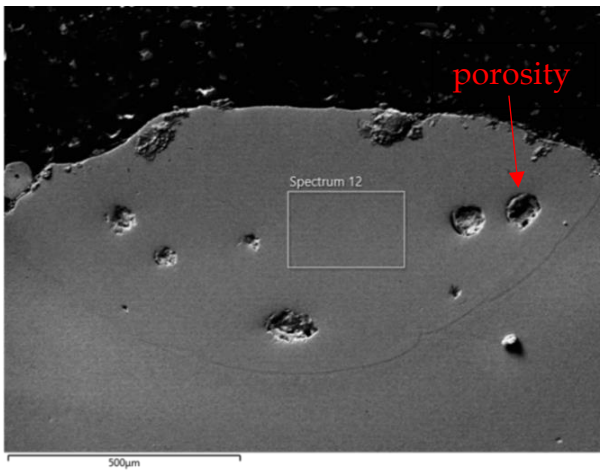

Fig. 6.4 Scanning electron micrograph of a laser bead in P91 base metal indicating the typical area selected for energy-dispersive spectroscopic analysis.

Table 6.2 shows the deposited metal powder and laser bead compositions before they were overlaid by GMAW. The laser bead compositions reflect the dilution between the powder metal deposited and the P91 base metal, which is influenced by the laser welding parameters.

Table 6.2 *Metal powder composition and mass percentage of added elements in laser beads as analysed using energy-dispersive spectroscopy*

Alloy element	*Nominal composition of metal powder*	*Average mass% in the deposited laser beads*	*Dilution (%)*
TLS (Cr99.2)	99.2% Cr	54	44
Weartech (Mo99.5)	99.5% Mo	17	83
METCO 56C-NS (Ni powder)	99.3% Ni	37	63
FeSi (6F)	16.6% Si and 82.5% Fe	9	42
Manganese Metal Co powder	99.8% Mn	43	53

6.3 Alloying technique to alter gas–metal arc weld bead composition

Table 6.3 shows the percentage increase in the alloy contents of the GMAW bead compositions owing to the DLD-added elements. The average mass% increases were calculated from the GMAW bead compositions without alloying addition, which were as follows: 0.48% Mn, 8.51% Cr, 0.3% Si, 0.96% Mo, 0.35% Ni. The elemental mass% increases in the GMAW beads aimed to achieve a composition that met the requirements of the AWS A5.28/A5.28M specification. The maximum allowable increases to remain within the specification range were 0.72% for Mn, 1.9% for Cr, 0.2% for Si, 0.24% for Mo, and 0.45% for Ni.

Ten welds were alloyed with additional Mn and all were within the allowable elemental limits. Cr was added to 22 welds and the final mass% increase was within the allowable

range for all welds. Nine welds received additional Si alloying; the three that were alloyed with two Si laser beads exceeded the maximum limit. Mo exceeded the upper elemental limit in four of 12 welds and Ni in two of five welds with additional alloying.

Table 6.3 *Mass% increase of added alloying elements in weld metals.*

GMAW beads	*Alloying added (laser beads deposited)*	*Mn*	*Cr*	*Si*	*Mo*	*Ni*
PH 1	No alloying					
PH 2	(0.5)Cr		0.37			
PH 3	(1)Cr		0.97			
PH 4	(2)Cr, (2)Mn	0.60	1.51			
PH 5	(2)Cr, (1)Mn, (1)Mo	0.27	1.83		0.37	
PH 6	(1)Cr, (1)Mn, (0.5)Ni	0.33	0.89			0.17
AW 1	No alloying					
AW 2	(1)Cr		0.62			
AW 3	(2)Cr		1.81			
AW 4	(2)Cr, (0.5)Mo		1.72		0.10	
AW 5	(2)Cr, (1)Mo		1.68		0.42	
AW 6	(2)Cr, (0.5)Ni		1.75			0.19
AW 7	(2)Cr, (1)Ni		1.80			0.78
AW 8	(2)Cr, (2)Ni		1.69			1.04
AW 9	(2)Cr, (1)Si		1.45	0.18		
AW 10	(2)Cr, (2)Si		1.59	0.40		
AW 11	(2)Cr, (2)Mn	0.68	1.24			
AW 12	(2)Mn, (0.5)Mo	0.63			0.18	
AW 13	(2)Mn, (1)Si	0.64		0.13		
AW 14	(0.5)Mo, (1)Si			0.19	0.10	
AW 15	(2)Cr, (0.5)Mo, (1)Si		0.68	0.16	0.07	
AW 16	(2)Cr, (1)Mo, (1)Si		1.31	0.16	0.20	
AW 17	(2)Cr, (1)Mo, (2)Si		1.42	0.29	0.25	
AW 18	(2)Cr, (0.5)Mo, (1)Mn	0.31	1.72		0.07	
AW 19	(2)Cr, (1)Mo, (1)Mn	0.43	1.21		0.39	
AW 20	(2)Cr, (0.5)Mo, (0.5)Ni		1.05		0.08	0.19
AW 21	(2)Cr, (1)Mn, (1)Si	0.30	1.44	0.14		
AW 22	(0.5)Mo, (2)Mn, (1)Si	0.65		0.21	0.09	

Table 6.4 shows the amount of alloying powder (g/mm) added and the resulting average mass% increase from the alloying. The added mass was calculated based on the laser speed, powder feed rate, powder composition, and length of the deposited laser bead.

Table 6.4 *Average elemental mass% increase with standard deviation and 95% confidence interval*

Alloying element	***Alloy added (g/mm)***	***Number of laser beads***	***Starting composition (mass%)***	***Mass% increase (ave.)***	***Std. deviation***	***95% CI***
Mn	0.0018	1	0.48	0.32	0.06	0.05
	0.0036	2		0.64	0.03	0.03
Cr	0.004	0.5	8.51	0.37	0.00	0.00
	0.008	1		0.83	0.18	0.21
	0.016	2		1.54	0.24	0.11
Si	0.0007	1	0.30	0.16	0.02	0.02
	0.0014	2		0.26	0.11	0.11
Mo	0.003	0.5	0.96	0.10	0.04	0.03
	0.006	1		0.34	0.10	0.08
Ni	0.0034	0.5	0.35	0.18	0.01	0.01
	0.0068	1		0.78	0.00	0.00
	0.136	2		1.04	0.00	0.00

Considering the difficulty in accurately controlling the small quantities of alloying powder required, the applied alloying technique was satisfactory in achieving the desired compositional changes for this study. By optimising the DLD parameters and ensuring better control of the powder particle size, better reliability in altering the weld metal composition could possibly be achieved using this alloying technique.

Chapter 7

Characterisation of gas–metal arc weld bead analysis in as-welded condition

7.1 Gas–metal arc weld bead geometry

Weld bead cross-sections in the transverse (AW 14) and longitudinal (AW 17) planes are shown in Fig. 7.1. The uneven base-metal penetration and wave-like fusion line observed along the length of the weld bead in Fig. 7.1(ii) are attributed to the weaving technique. Table 7.1 shows the GMAW bead geometry and dilution. Use of the weaving technique in GMAW was effective in increasing the weld width and heat input.

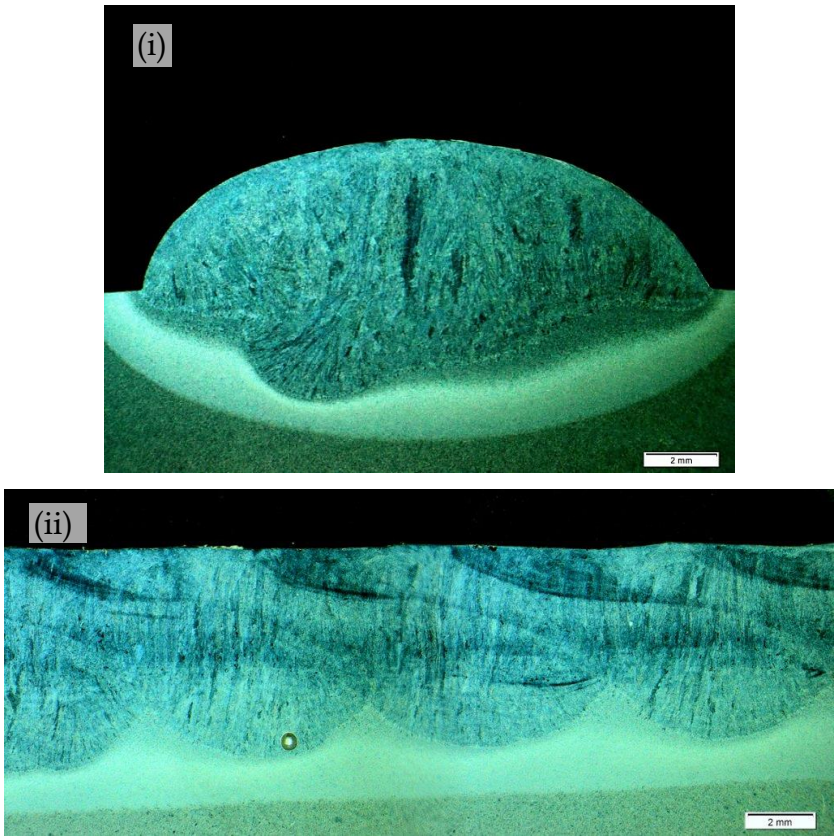

Fig. 7.1 Stereoscope images of weld bead cross-sections in the (i) transverse plane (AW 14) and (ii) longitudinal plane (AW 17) (10× magnification).

Table 7.1 GMAW bead geometry and dilution

GMAW beads	Alloying added (laser beads deposited)	Bead height	Bead width	Depth of penetration	Dilution
		mm	mm	mm	%
250°C Preheat					
PH 1	No alloying	4.3	16.3	3.0	35
PH 2	(0.5)Cr	4.1	16.3	3.3	32
PH 3	(1)Cr	4.2	16.2	3.6	31
PH 4	(2)Cr, (2)Mn	4.2	15.5	3.5	33
PH 5	(2)Cr, (1)Mn, (1)Mo	3.9	14.7	3.2	31
PH 6	(1)Cr, (1)Mn, (0.5)Ni	4.3	15.9	3.3	30
No Preheat					
AW 1	No alloying	4.2	14.0	3.2	40
AW 2	(1)Cr	4.4	14.1	2.6	31
AW 3	(2)Cr	3.8	15.8	2.8	33
AW 4	(2)Cr, (0.5)Mo	4.5	14.8	2.4	28
AW 5	(2)Cr, (1)Mo	4.1	16.2	3.0	33
AW 6	(2)Cr, (0.5)Ni	4.4	15.8	2.7	32
AW 7	(2)Cr, (1)Ni	4.2	15.7	2.6	36
AW 8	(2)Cr, (2)Ni	4.4	14.9	2.6	29
AW 9	(2)Cr, (1)Si	4.1	16.6	2.9	30
AW 10	(2)Cr, (2)Si	4.3	17.5	2.5	27
AW 11	(2)Cr, (2)Mn	4.3	16.6	3.6	33
AW 12	(2)Mn, (0.5)Mo	4.6	14.5	3.1	30
AW 13	(2)Mn, (1)Si	4.5	16.0	2.9	24
AW 14	(0.5)Mo, (1)Si	4.2	16.3	3.2	33
AW 15	(2)Cr, (0.5)Mo, (1)Si	4.5	17.3	2.8	23
AW 16	(2)Cr, (1)Mo, (1)Si	4.5	17.6	2.8	30
AW 17	(2)Cr, (1)Mo, (2)Si	4.0	17.1	3.0	36
AW 18	(2)Cr, (0.5)Mo, (1)Mn	4.6	15.5	2.7	28
AW 19	(2)Cr, (1)Mo, (1)Mn	4.3	16.8	3.6	39
AW 20	(2)Cr, (0.5)Mo, (0.5)Ni	4.4	15.3	2.7	32
AW 21	(2)Cr, (1)Mn, (1)Si	4.5	17.8	2.4	31
AW 22	(0.5)Mo, (2)Mn, (1)Si	4.4	15.9	3.1	26

To ensure that the observed delta ferrite changes in the weld microstructures were due to the varied bead compositions, it was critical to maintain consistent heat input during GMAW. Heat input influences the heating and cooling rate of a weld, which consequently affects the weld size and influences the final metallurgical structure and mechanical behaviour [103]. To maintain consistent heat input, weaving and GMAW parameters were held constant. Even with similar welding parameters, there were differences in the weld metal geometries. The depth of penetration varied from 2.5 to

3.6 mm and the bead width varied from 14.1 to 17.5 mm. The weld dilution (ratio of molten base metal to the total fusion zone) varied from 24% to 40%. Differences in weld bead geometry and dilution between the weld beads were attributed, but not limited, to the elements and number of laser beads added.

The weaving technique in GMAW was effective in increasing the weld width and heat input, but resulted in an uneven fusion line, which made accurate weld geometry calculation difficult. No significant effect of preheating was observed on the geometry of the weld bead.

7.2 Chemical composition results and analysis of gas–metal arc welds

7.2.1 Optical emission spectroscopy

Chemical compositions of all GMAW beads were analysed using optical emission spectroscopy (OES). Chemical analysis was performed on each weld specimen sectioned halfway through the bead length on the transverse cross-section, as shown in Fig. 4.12 (specimen 3). Table 7.2 presents the alloying elements added on each GMAW bead and the chemical compositions of the welds. Welds PH 1 and AW1 comprised only the GMAW filler wire deposit (i.e., without additional laser beads). Eight welds, highlighted in Table 7.2, exceeded the upper limit of the elemental specification range and thus did not fully comply with the AWS A5.28/A5.28M:2020 (ER90S-B9) specification. This standard does not specify the minimum requirements for Mn and Ni, but does specify that their sum (Mn + Ni) shall be 1.5% maximum. Welds AW 7, AW 8, and AW 11 exceeded this limit. The chemical composition of all preheated welds conformed to this specification, with the exception of weld PH 5, which contained 1.32 mass% Mo.

Table 7.2 *Metal alloys deposited and compositions (mass%) of GMAW beads (AWS A5.28/A5.28M:2020 (ER90S-B9) specification). Elements above the specified limits are highlighted.*

GMAW beads	***Alloying added (laser beads deposited)***	***C***	***Mn***	***Cr***	***Si***	***Mo***	***V***	***Nb***	***N***	***Ni***	***Al***	***(Mn+Ni)***
		0.08–0.13	*1.20 max*	*8.0–10.5*	*0.15-0.50*	*0.85–1.2*	*0.15–0.30*	*0.02–0.10*	*0.03–0.07*	*0.8 max*	*0.04 max*	*1.5 max*
250°C Preheat												
PH 1	No alloying	0.090	0.48	8.40	0.28	0.97	0.22	0.081	0.052	0.35	0.005	0.83
PH 2	(0.5)Cr	0.089	0.47	8.88	0.28	0.97	0.22	0.077	0.051	0.36	0.004	0.83
PH 3	(1)Cr	0.087	0.47	9.47	0.28	0.97	0.22	0.078	0.054	0.36	0.005	0.83
PH 4	(2)Cr, (2)Mn	0.085	1.08	10.01	0.28	0.96	0.22	0.079	0.053	0.34	0.005	1.42
PH 5	(2)Cr, (1)Mn, (1)Mo	0.085	0.75	10.33	0.28	1.32	0.22	0.078	0.055	0.34	0.006	1.09
PH 6	(1)Cr, (1)Mn, (0.5)Ni	0.087	0.81	9.39	0.27	0.96	0.22	0.079	0.053	0.52	0.003	1.33
No Preheat												
AW 1	No alloying	0.090	0.48	8.61	0.31	0.94	0.22	0.088	0.056	0.35	0.003	0.83
AW 2	(1)Cr	0.100	0.48	9.12	0.30	0.93	0.21	0.082	0.055	0.35	0.004	0.83
AW 3	(2)Cr	0.100	0.49	10.3	0.29	0.94	0.22	0.086	0.059	0.36	0.010	0.85
AW 4	(2)Cr, (0.5)Mo	0.094	0.47	10.2	0.25	1.05	0.22	0.082	0.065	0.36	0.003	0.83
AW 5	(2)Cr, (1)Mo	0.090	0.48	10.2	0.30	1.37	0.22	0.088	0.057	0.35	0.006	0.83
AW 6	(2)Cr, (0.5)Ni	0.089	0.47	10.3	0.24	0.94	0.23	0.082	0.070	0.54	0.003	1.01
AW 7	(2)Cr, (1)Ni	0.100	0.48	10.3	0.30	0.91	0.22	0.083	0.057	1.13	0.005	1.61
AW 8	(2)Cr, (2)Ni	0.080	0.48	10.2	0.28	0.90	0.21	0.085	0.057	1.39	0.006	1.87
AW 9	(2)Cr, (1)Si	0.088	0.46	9.95	0.47	0.92	0.23	0.086	0.069	0.34	0.005	0.80
AW 10	(2)Cr, (2)Si	0.080	0.47	10.1	0.69	0.89	0.22	0.089	0.056	0.34	0.006	0.81
AW 11	(2)Cr, (2)Mn	0.100	1.16	9.74	0.29	0.92	0.22	0.083	0.059	0.35	0.004	1.51
AW 12	(2)Mn, (0.5)Mo	0.091	1.11	8.39	0.24	1.13	0.23	0.080	0.062	0.36	0.002	1.47
AW 13	(2)Mn, (1)Si	0.088	1.12	8.38	0.42	0.95	0.23	0.084	0.063	0.36	0.002	1.48
AW 14	(0.5)Mo, (1)Si	0.085	0.47	8.42	0.48	1.05	0.23	0.083	0.061	0.35	0.003	0.82
AW 15	(2)Cr, (0.5)Mo, (1)Si	0.085	0.46	9.18	0.45	1.02	0.23	0.089	0.060	0.35	0.004	0.81
AW 16	(2)Cr, (1)Mo, (1)Si	0.082	0.46	9.81	0.45	1.15	0.23	0.086	0.060	0.35	0.003	0.81
AW 17	(2)Cr, (1)Mo, (2)Si	0.100	0.46	9.92	0.58	1.20	0.22	0.085	0.056	0.34	0.005	0.80
AW 18	(2)Cr,(0.5)Mo, (1)Mn	0.102	0.79	10.3	0.23	1.02	0.22	0.078	0.070	0.36	0.003	1.15
AW 19	(2)Cr, (1)Mo, (1)Mn	0.120	0.91	9.71	0.29	1.34	0.22	0.086	0.059	0.34	0.008	1.25
AW 20	(2)Cr, (0.5)Mo, (0.5)Ni	0.088	0.47	9.55	0.25	1.03	0.23	0.083	0.059	0.54	0.003	1.01
AW 21	(2)Cr, (1)Mn, (1)Si	0.081	0.78	9.94	0.43	0.93	0.23	0.085	0.061	0.35	0.004	1.13
AW 22	(0.5)Mo, (2)Mn, (1)Si	0.081	1.13	8.27	0.50	1.04	0.23	0.088	0.065	0.35	0.003	1.48

7.2.2 Chemical composition of gas–metal arc welds along the bead length

Four of the 28 GMA welds (PH 6, AW 1, AW 17, and AW 22) were selected and their composition analysed in five positions, about 40 mm apart along the length of the weld bead, to determine the uniformity of the chemical composition along the length of the GMAW beads. The analysed welds were selected on the basis of whether preheating was applied, the presence or absence of delta ferrite, and the specific added alloying elements. PH 6 received preheating; AW 1 contained no additional alloying and was used as a reference bead. All alloying elements were accounted for. PH 6, AW 17, and AW 22 had three additional alloying elements. Of the four welds, only AW 17 contained delta ferrite. The results are presented in Table 7.3.

Table 7.3 *Chemical compositions (mass%) in different positions along the length of selected gas–metal arc weld beads*

GMAW beads	***Position***	***Alloying added (laser beads deposited)***	***C***	***Mn***	***Cr***	***Si***	***Mo***	***V***	***Nb***	***Ni***	***(Mn+Ni)***
			0.08–0.13	*1.20 max*	*8.0–10.5*	*0.15-0.50*	*0.85–1.20*	*0.15–0.30*	*0.02–0.10*	*0.80 max*	*1.50 max*
PH 6	1	(1)Cr, (1)Mn, (0.5)Ni	0.091	0.76	9.33	0.27	0.96	0.22	0.078	0.49	1.25
	2		0.088	0.81	9.39	0.27	0.96	0.22	0.079	0.50	1.31
	3		0.087	0.81	9.39	0.27	0.96	0.22	0.079	0.52	1.33
	4		0.093	0.81	9.40	0.27	0.96	0.22	0.079	0.52	1.33
	5		0.083	0.82	9.50	0.27	0.95	0.22	0.080	0.51	1.33
AW 1	1	No alloying	0.089	0.49	8.62	0.32	0.93	0.23	0.089	0.35	0.84
	2		0.087	0.48	8.61	0.31	0.94	0.22	0.088	0.35	0.83
	3		0.090	0.48	8.61	0.31	0.94	0.22	0.088	0.35	0.83
	4		0.089	0.48	8.63	0.31	0.93	0.22	0.088	0.36	0.84
	5		0.085	0.48	8.64	0.31	0.91	0.22	0.088	0.35	0.83
AW 17	1	(2)Cr, (1)Mo, (2)Si	0.089	0.46	10.05	0.64	1.16	0.22	0.085	0.34	0.80
	2		0.090	0.47	9.91	0.59	1.21	0.22	0.083	0.34	0.81
	3		0.100	0.46	9.92	0.58	1.20	0.22	0.085	0.34	0.80
	4		0.098	0.46	9.90	0.65	1.54	0.22	0.085	0.34	0.80
	5		0.089	0.46	10.37	0.60	1.13	0.22	0.082	0.34	0.80
AW 22	1	(0.5)Mo, (2)Mn, (1)Si	0.083	0.98	8.42	0.51	1.03	0.22	0.087	0.35	1.33
	2		0.085	1.11	8.28	0.50	1.05	0.22	0.088	0.35	1.46
	3		0.081	1.13	8.27	0.50	1.04	0.22	0.088	0.35	1.48
	4		0.083	1.24	8.24	0.50	1.12	0.22	0.089	0.35	1.59
	5		0.099	1.24	8.29	0.46	1.09	0.23	0.088	0.35	1.59

Figure 7.2 to 7.6 illustrate the distribution of the added elements along the bead length of welds PH 6, AW 1, AW 17, and AW 22. Figure 7.2 shows the Cr distribution, where the AW 17 weld contained two Cr laser beads: its distribution was fairly uniform except for the far end of the bead where a significant increase was observed. PH 6 weld contained one Cr laser bead. The AW 1 and AW 22 beads did not contain additional Cr laser beads. Between positions 2 to 4 along the GMAW bead length, all welds showed uniform distribution of Cr.

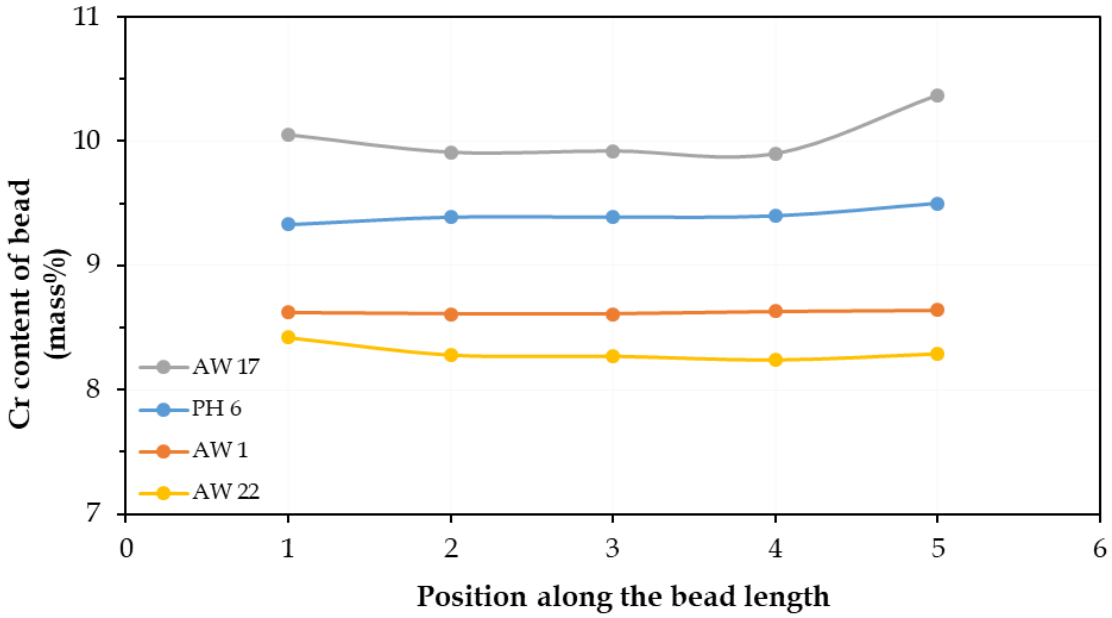

Fig. 7.2 Variation in Cr concentration along the bead length of four gas–metal arc welds at five positions (40 mm apart). Total length of a weld bead was typically about 250 mm.

Figure 7.3 shows the analogous Mn distributions. AW 1 and AW 17 welds had no additional Mn alloying, one Mn laser bead was added to PH 6 weld, and two beads were added to AW 22. Three welds showed uniform distribution of Mn along the GMAW bead length, but the AW 22 weld showed significant differences in mass% of Mn.

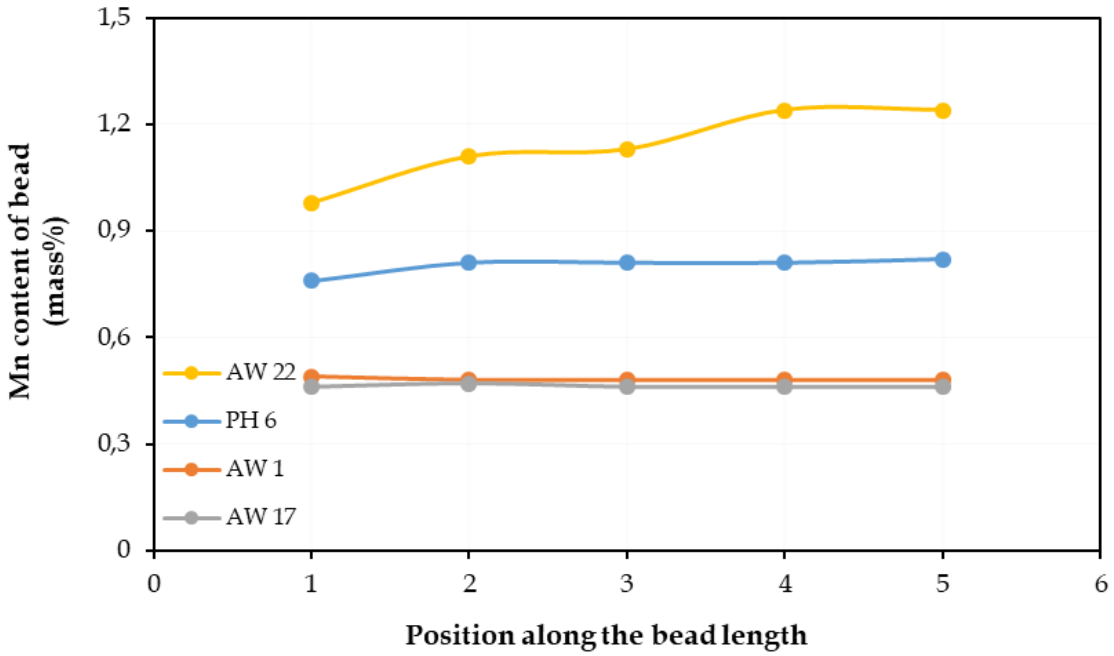

Fig. 7.3 Variation in Mn concentration along the bead length of four gas–metal arc welds at five positions (40 mm apart).

Figure 7.4 shows the corresponding Si distributions. Two Si beads were added in AW 17, one was added in AW 22, while PH 6 and AW 1 contained no additional Si. The AW 22 bead showed uniform Si distribution except for lower content in position 5. AW 17 showed significant differences along the bead length, ranging from 0.58−0.64 mass% Si.

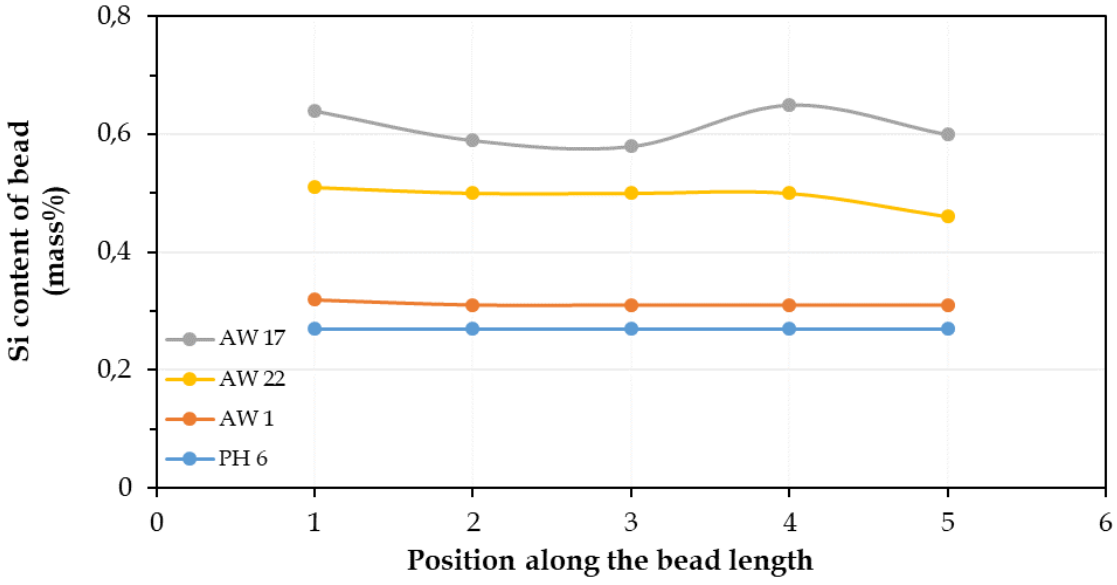

Fig. 7.4 Variation in Si concentration along the bead length of four gas–metal arc welds at five positions (40 mm apart).

Figure 7.5 shows the Ni distributions. Only PH 6 weld contained additional Ni alloying. The Ni distribution was fairly uniform for all four welds.

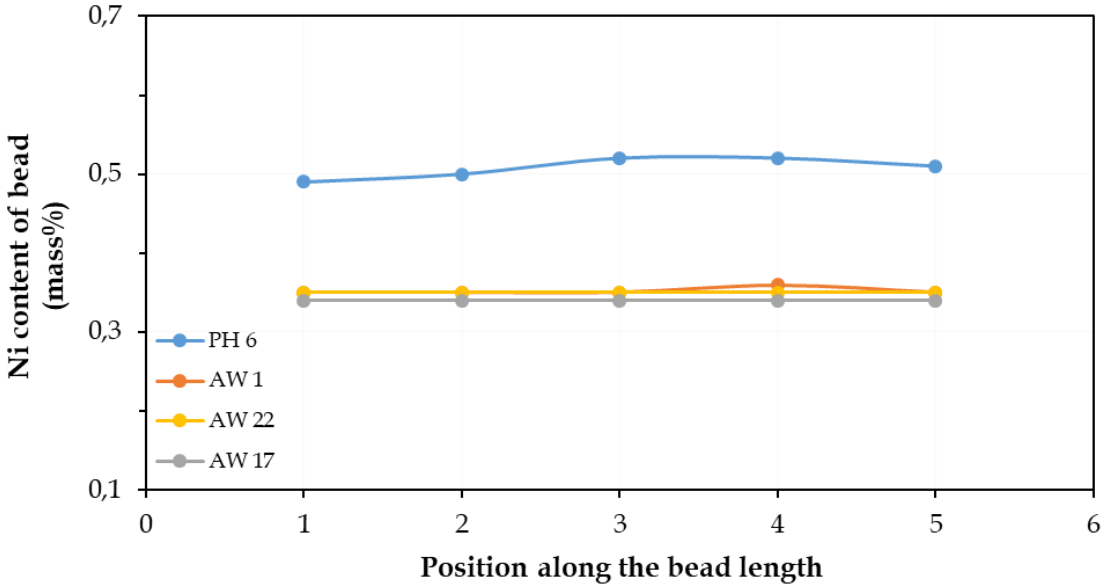

Fig. 7.5 Variation in Ni concentration along the bead length of four gas–metal arc welds at five positions (40 mm apart).

Figure 7.6 shows the corresponding Mo distributions. AW 17 and AW 22 contained additional Mo alloying. It was expected that PH 6 and AW 1 welds would show uniform Mo distribution along the length because there was no additional Mo alloying. AW 22 showed a small increase at positions 4 and 5. Weld AW 17 showed fairly consistent Mo composition except for a sharp increase observed at position 4.

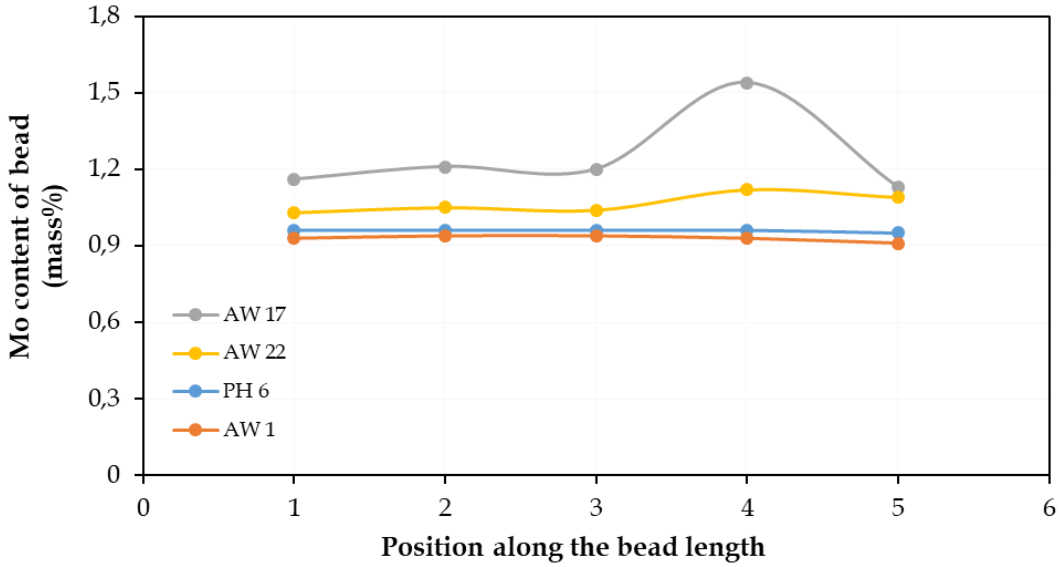

Fig. 7.6 Variation in Mo concentration along the bead length of four gas–metal arc welds at five positions (40 mm apart).

7.2.2.1 Composition homogeneity along the gas–metal arc weld bead length

The elemental mass percentage was fairly uniform between the five positions, as shown in Fig. 7.2 to Fig. 7.6. Weld AW 17 showed the most inconsistency for all the three added alloying elements; namely, 2(Cr), 2(Si), and 1(Mo). AW 17 consisted of five laser beads, of which four were deposited with a 4 mm spot size. PH 6 and AW 22 welds were mainly consistent with respect to Ni, Mn, and Mo laser beads, which were deposited with 2 mm spot size. The number and large size of laser beads deposited in the AW 17 bead likely contributed to the non-uniform composition along the bead length. There is some recognition that Mo powder can be difficult to fully melt in powder-fed direct laser deposition. But it is unlikely that undissolved Mo in the GMAW beads was the cause for non-uniform composition along the bead length in AW17 based on the following observations:

i. The Mo powder composition was 99.5 mass% Mo. The EDS analysis for the Mo laser bead indicated a composition of 17 mass% Mo, which shows a dilution of 83% with the P91 base metal. The GMAW bead overlaid a Mo laser which was already significantly diluted.
ii. Over 20 microstructure images were taken in each weld bead and there was no evidence of undissolved Mo particles or any of the alloying elements.
iii. EDS analysis was performed in seven positions on the GMAW bead cross section and the average standard deviation for all 28 welds was 0.09

Mn was non-uniform along the bead length in weld AW 22. The inhomogeneities observed along the welds bead length are attributed to the DLD process. Some issues encountered during the DLD process are as follows:

i. The alloying powder was fed to the laser through three inlets. At times, one inlet would block and the powder would only be fed through two pipes.
ii. Changing DLD parameters (spot size, powder feed rate, and working distance) between the beads could have introduced inconsistencies to the process, especially the first bead after change-over.

Uniform alloying of a GMAW bead along its length can be achieved when the issues stated above (i–ii) are better controlled or avoided. Limiting the number of alloying elements and laser beads added in each GMAW bead at a given time can also likely improve composition consistency.

7.2.3 Scanning electron microscopy energy-dispersive spectroscopy analysis of gas–metal arc welds

EDS analyses of the GMAW beads were performed at seven positions, as demonstrated in Section 4.6.3.2, Fig. 4.13. The average elemental results (mass%) calculated from the EDS analysis on the seven locations in the transverse cross-section of each GMA weld are listed in Table 7.4, which only includes the elements of interest (Cr, Mo, Mn, Ni, Si). The first objective of reporting the weld compositions from EDS analysis was to compare these results with the OES analyses. Many factors can influence EDS results, so it was necessary to establish a correlation and calibrate these with the OES results to improve confidence in the reported EDS values.

Table 7.4 *Average elemental concentration (mass%) of gas–metal arc weld beads, as measured using energy-dispersive spectroscopy*

GMAW beads	***Alloying added (laser beads deposited)***	***Mn***	***Cr***	***Si***	***Mo***	***Ni***
		1.20 max	*8.0–10.5*	*0.5 max*	*0.85–1.2*	*0.8 max*
250°C preheat						
PH 1	No alloying	0.56	9.2	0.31	0.91	0.36
PH 2	(0.5)Cr	0.57	9.6	0.33	1.10	0.37
PH 3	(1)Cr	0.61	10.4	0.31	0.87	0.33
PH 4	(2)Cr, (2)Mn	1.23	11.0	0.30	0.84	0.30
PH 5	(2)Cr, (1)Mn, (1)Mo	0.91	11.1	0.30	1.41	0.41
PH 6	(1)Cr, (1)Mn, (0.5)Ni	1.00	10.1	0.30	0.86	0.47
No preheat						
AW 1	No alloying	0.60	9.2	0.35	1.06	0.36
AW 2	(1)Cr	0.57	9.8	0.37	1.01	0.37
AW 3	(2)Cr	0.53	10.8	0.30	1.01	0.39
AW 4	(2)Cr, (0.5)Mo	0.59	11.0	0.34	1.37	0.36
AW 5	(2)Cr, (1)Mo	0.60	10.9	0.33	1.20	0.39
AW 6	(2)Cr, (0.5)Ni	0.58	10.8	0.34	1.13	0.53
AW 7	(2)Cr, (1)Ni	0.57	10.7	0.36	1.05	0.80
AW 8	(2)Cr, (2)Ni	0.53	10.8	0.31	1.02	1.29
AW 9	(2)Cr, (1)Si	0.53	10.7	0.50	1.05	0.33
AW 10	(2)Cr, (2)Si	0.53	10.4	0.83	1.03	0.35
AW 11	(2)Cr, (2)Mn	1.31	10.6	0.31	1.00	0.36
AW 12	(2)Mn, (0.5)Mo	1.30	9.1	0.31	1.39	0.31
AW 13	(2)Mn, (1)Si	1.24	9.0	0.56	1.15	0.34
AW 14	(0.5)Mo, (1)Si	0.59	9.0	0.53	1.29	0.37
AW 15	(2)Cr, (0.5)Mo, (1)Si	0.53	10.0	0.50	1.34	0.39
AW 16	(2)Cr, (1)Mo, (1)Si	0.54	10.9	0.50	1.43	0.31
AW 17	(2)Cr, (1)Mo, (2)Si	0.59	10.6	0.62	1.27	0.35
AW 18	(2)Cr, (0.5)Mo, (1)Mn	1.01	10.9	0.36	1.31	0.34
AW 19	(2)Cr, (1)Mo, (1)Mn	0.93	10.5	0.33	1.42	0.34
AW 20	(2)Cr, (0.5)Mo, (0.5)Ni	0.60	10.1	0.30	1.00	0.59
AW 21	(2)Cr, (1)Mn, (1)Si	0.90	10.7	0.46	0.91	0.33
AW 22	(0.5)Mo, (2)Mn, (1)Si	1.19	9.1	0.53	1.37	0.31

Figure 7.7 to 7.11 show the OES mass percentages plotted against the corresponding EDS values for Cr, Mo, Mn, Ni, and Si, respectively.

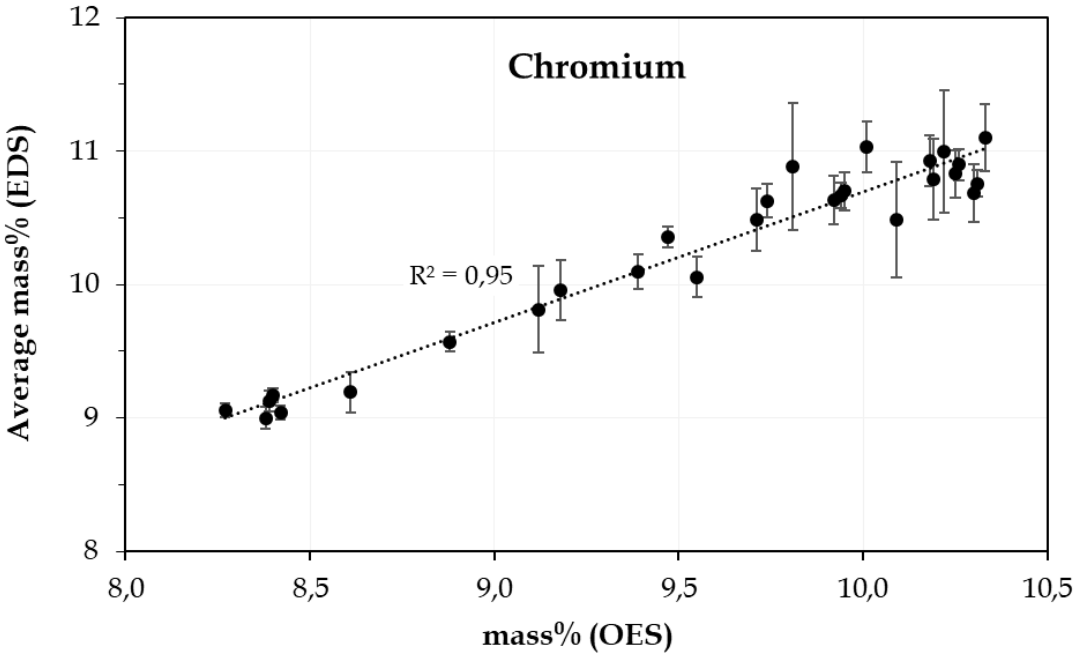

Fig. 7.7 Comparison of Cr analyses by optical emission spectroscopy and energy-dispersive spectroscopy for the 28 gas–metal arc weld beads.

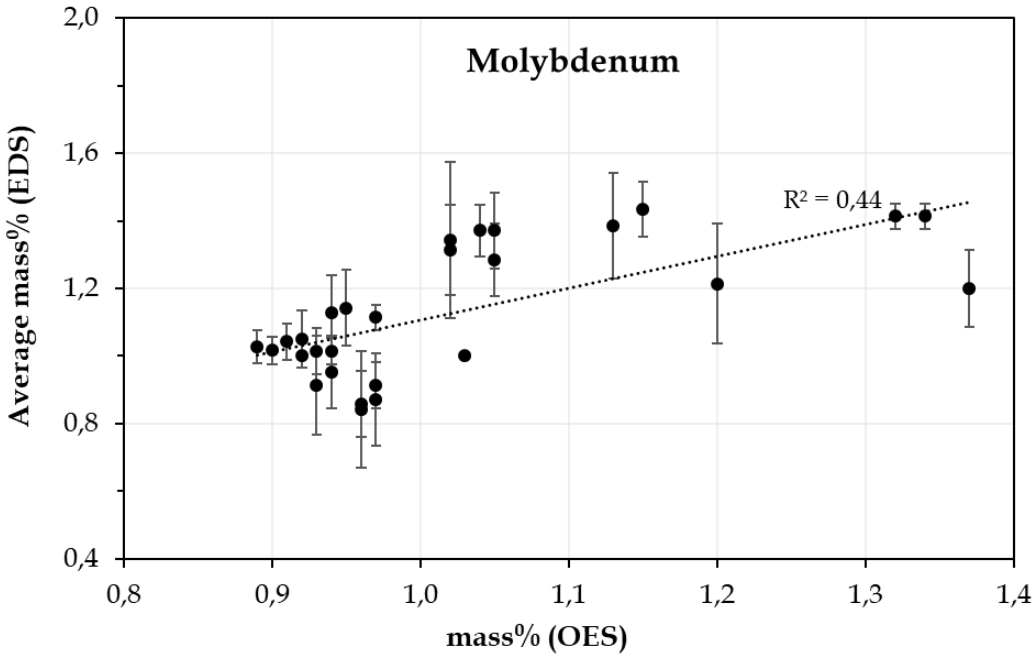

Fig. 7.8 Comparison of Mo analyses by optical emission spectroscopy and energy-dispersive spectroscopy for the 28 gas–metal arc weld beads.

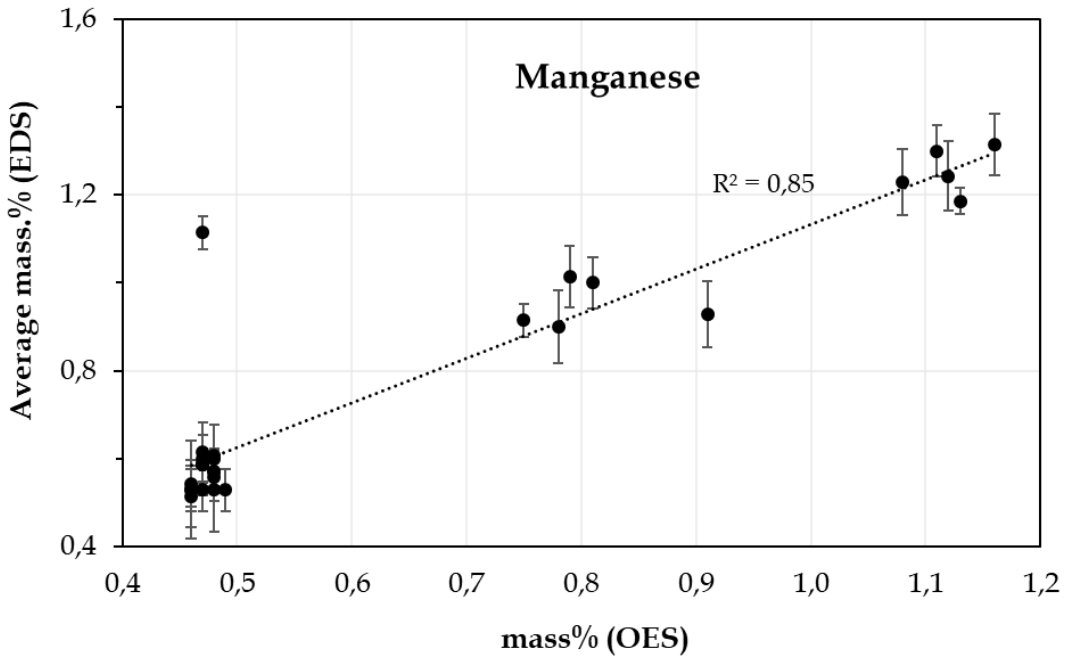

Fig. 7.9 Comparison of Mn analyses by optical emission spectroscopy and energy-dispersive spectroscopy for the 28 gas–metal arc weld beads.

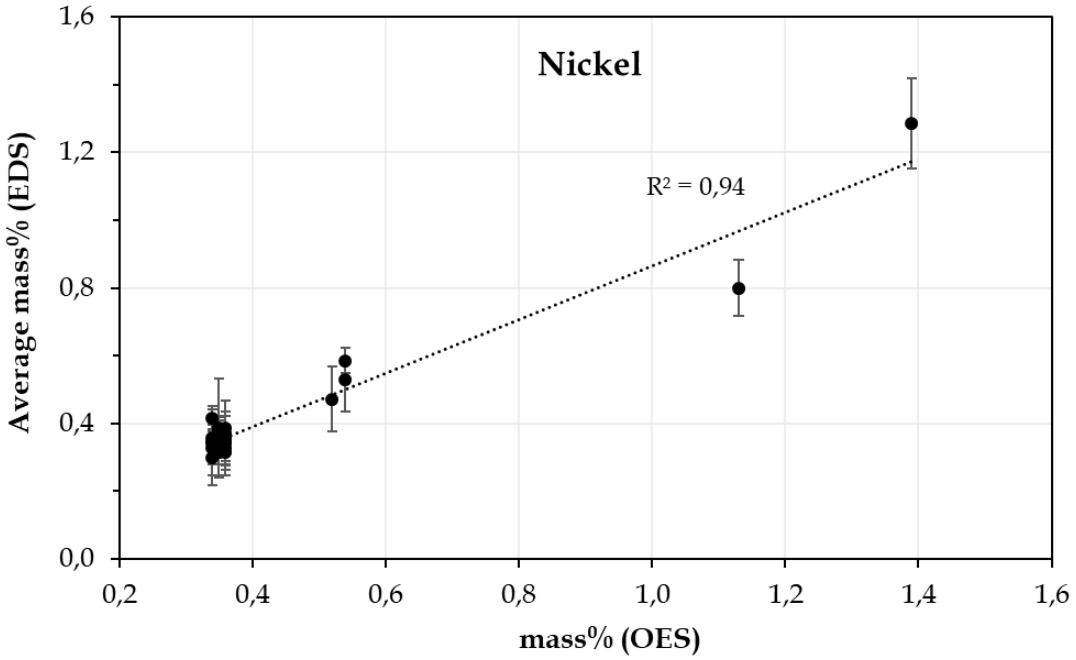

Fig. 7.10 Comparison of Ni analyses by optical emission spectroscopy and energy-dispersive spectroscopy for the 28 gas–metal arc weld beads.

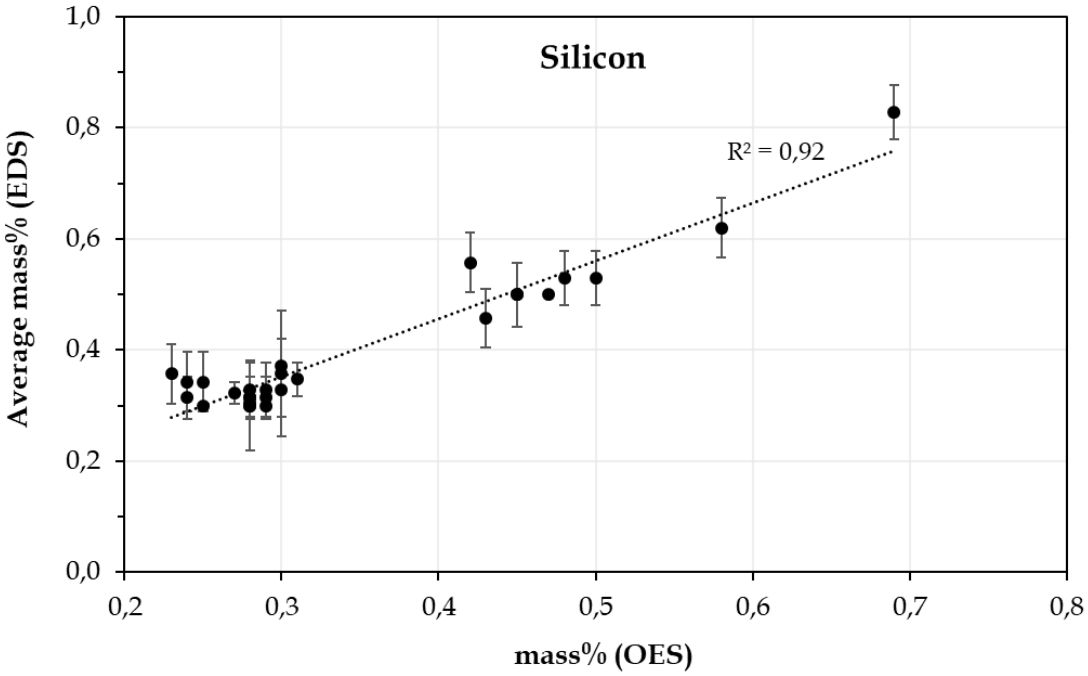

Fig. 7.11 Comparison of Si analyses by optical emission spectroscopy and energy-dispersive spectroscopy for the 28 gas–metal arc weld beads.

A sample calculation of the confidence intervals (CI) shown in these graphs is presented below.

Example: 95% CI Cr EDS mass% in weld AW 1

Seven EDS analyses of Cr mass%:	9.10, 9.00, 9.05, 9.40, 9.15, 9.08, 9.31
Average Cr mass% ($\bar{X}$):	9.16
Standard deviation (σ):	0.15
Sample size:	7
Z value:	1.960
95% CI:	$\bar{X} \pm Z \times (\sigma / \sqrt{n})$
95% CI:	0.11

The EDS results were, in some instances, inconsistent, but there was a good correlation between the results of the two chemical analysis methods, as demonstrated in Fig. 7.7 to Fig. 7.11.

The second objective for EDS analysis at the seven positions in the weld cross-sections was to establish homogeneity of the welds and distributions of the added alloying elements in the cross-sections. Figure 7.12 to Fig. 7.16 show the average mass percentages of each element from the seven positions plotted against the standard deviation and relative deviation percentage. Poor homogeneity is indicated by a large relative deviation percentage.

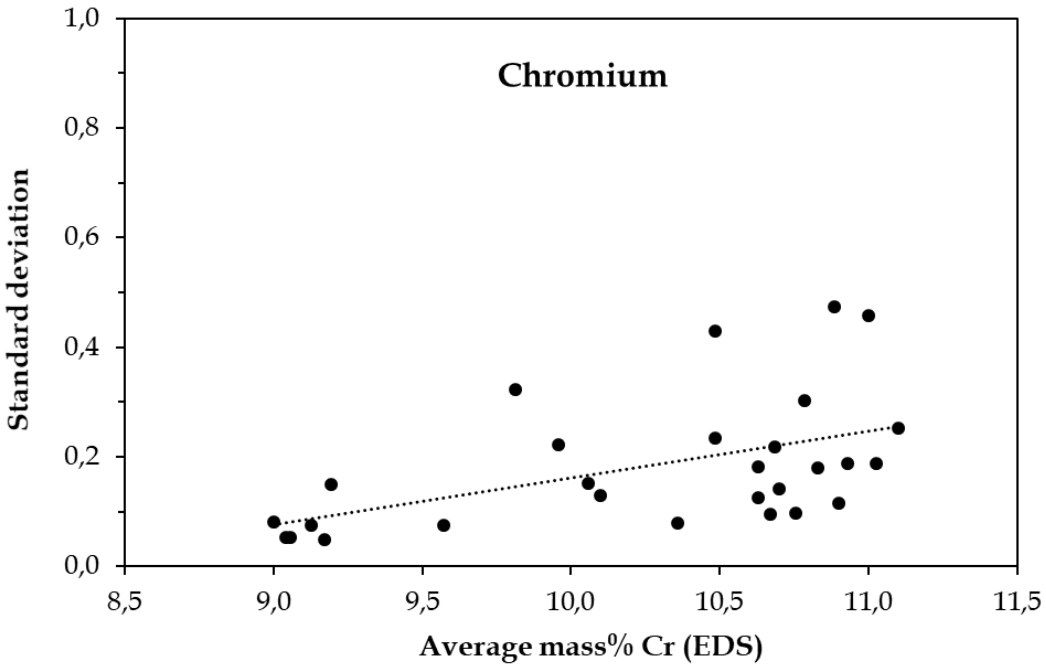

(a)

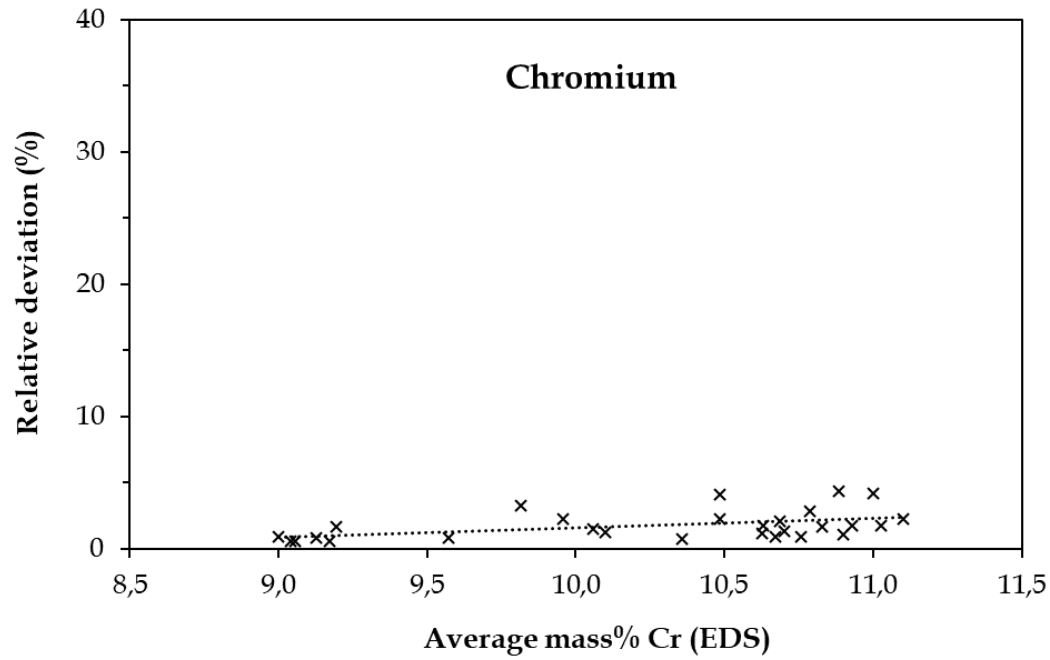

(b)

Fig. 7.12 Variation of average mass% Cr against (a) standard deviation and (b) relative deviation % for the 28 GMAW beads.

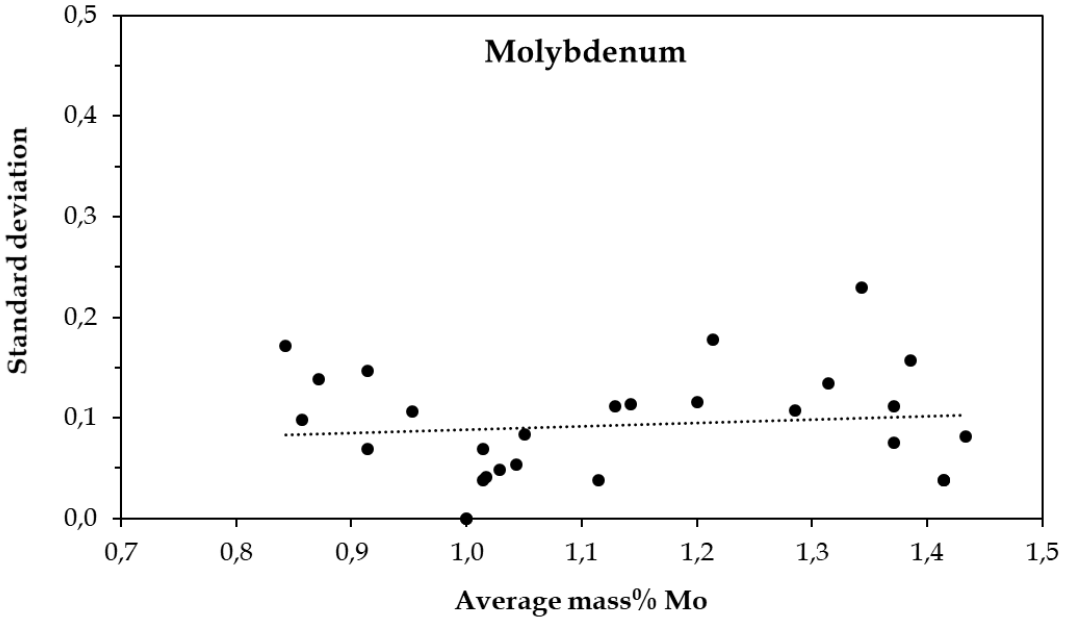

(a)

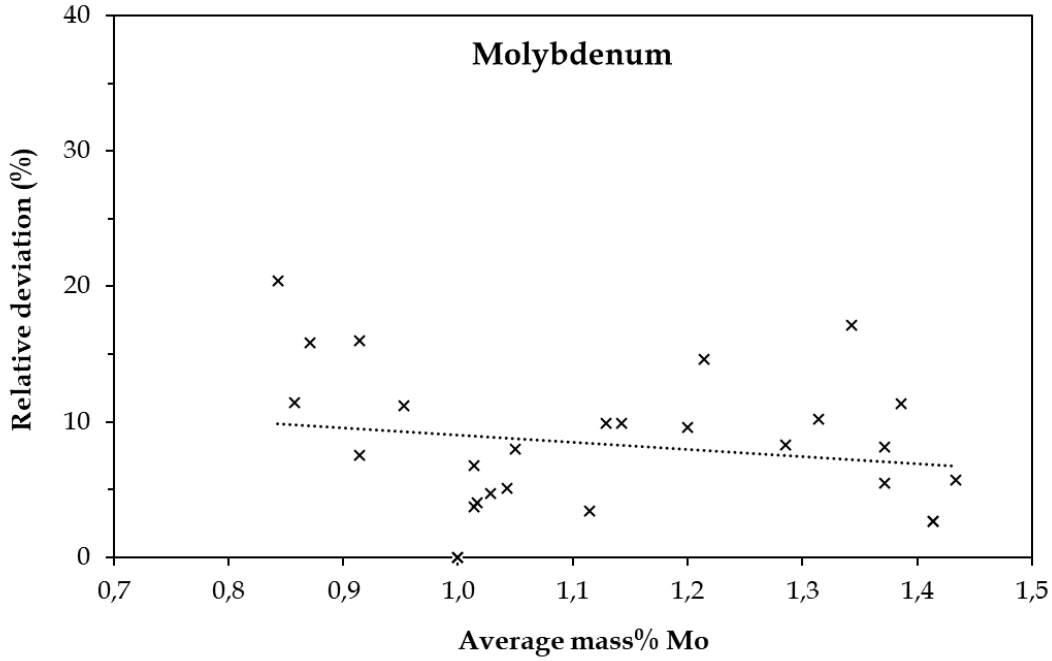

(b)

Fig. 7.13 Variation of average mass% Mo against (a) standard deviation and (b) relative deviation % for the 28 GMAW beads.

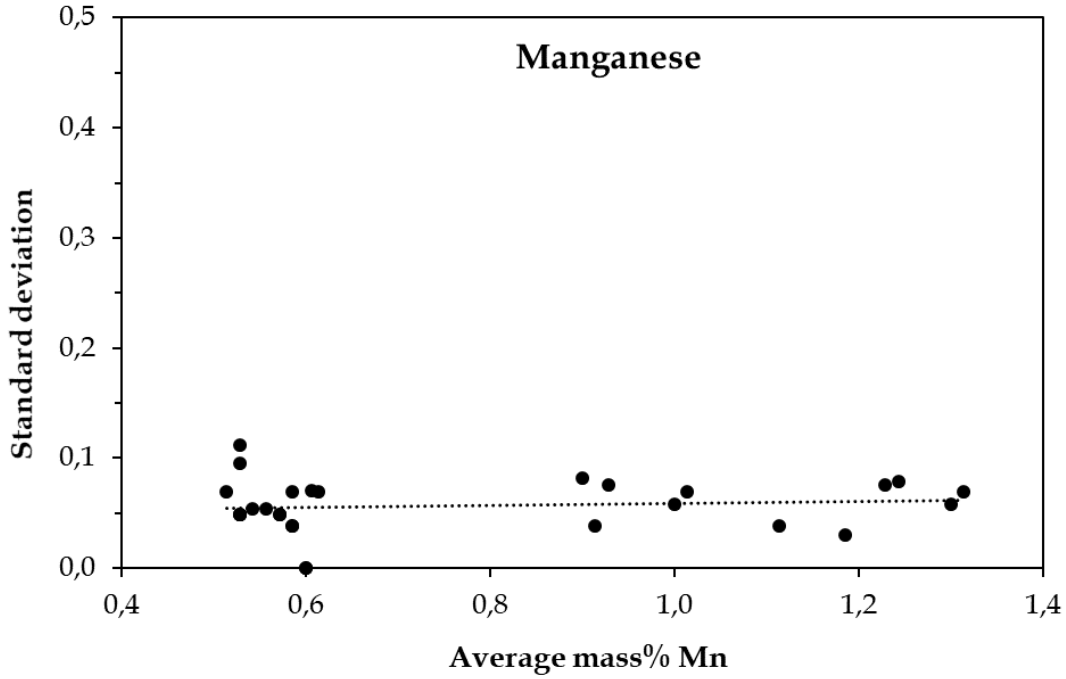

(a)

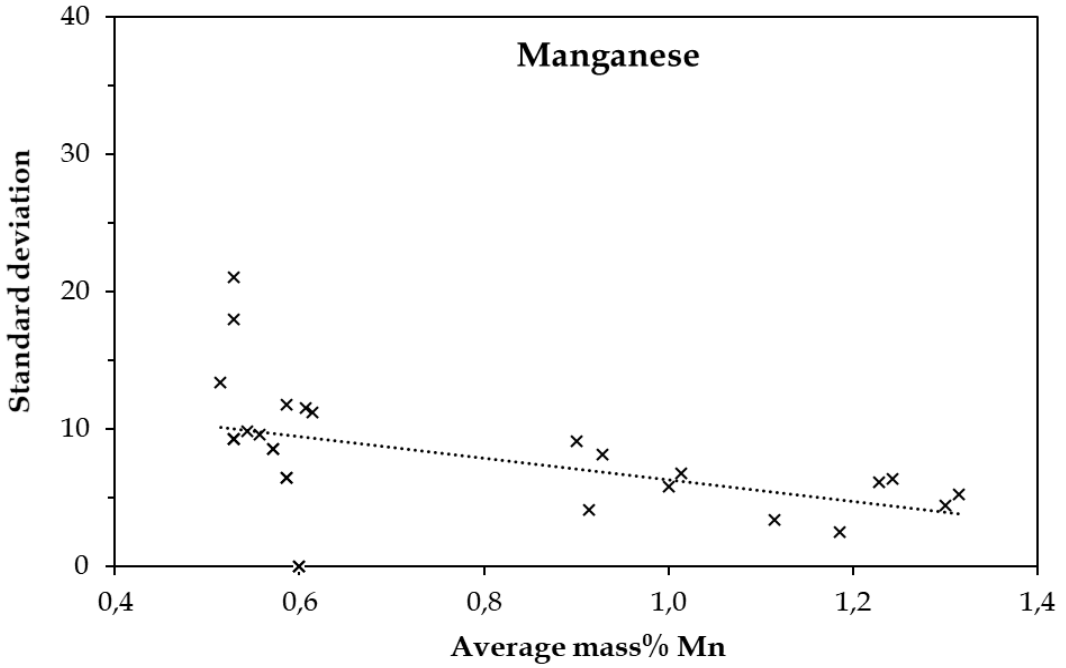

(b)

Fig. 7.14 Variation of average mass% Mn against (a) standard deviation and (b) relative deviation % for the 28 GMAW beads.

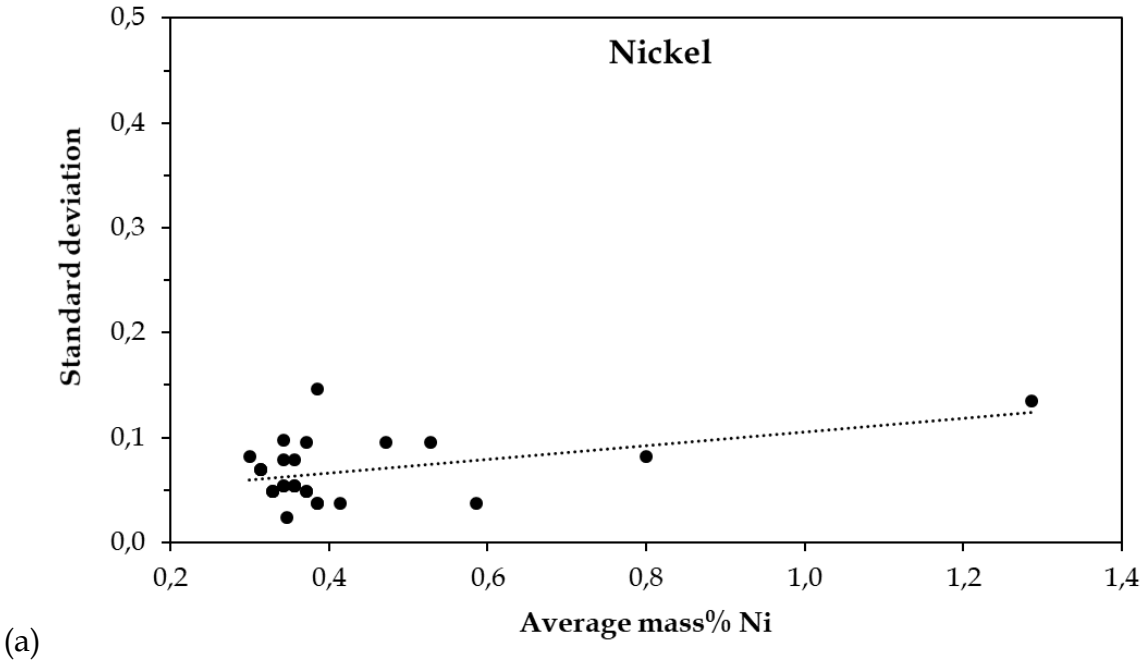

(a)

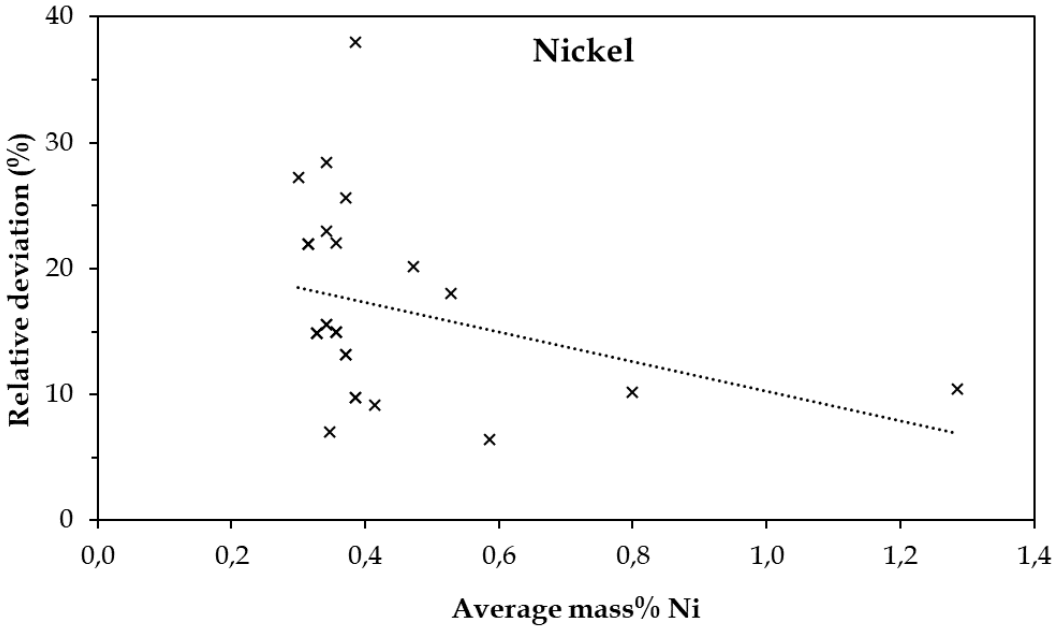

(b)

Fig. 7.15 Variation of average mass% Ni against (a) standard deviation and (b) relative deviation % for the 28 GMAW beads.

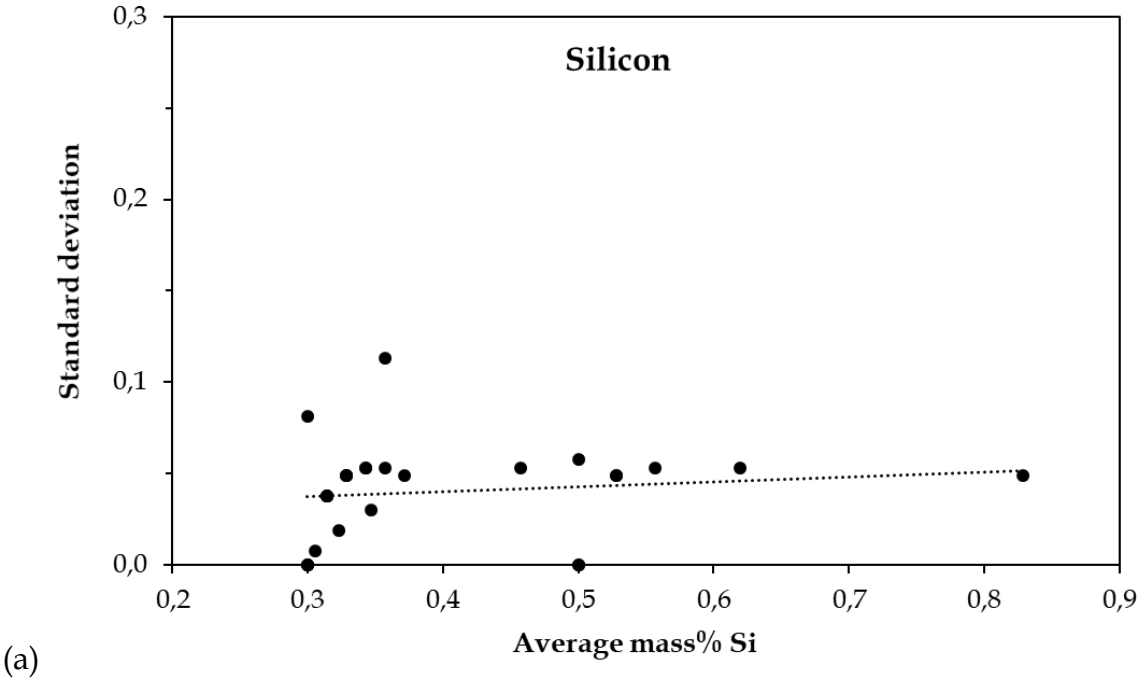

(a)

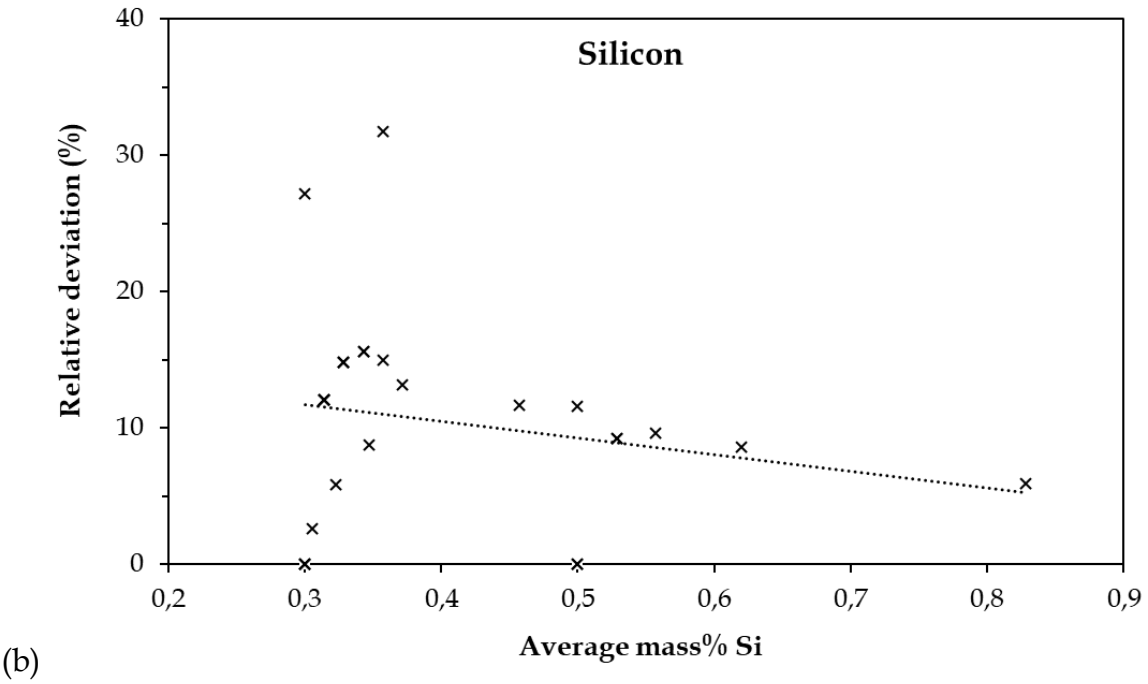

(b)

Fig. 7.16 Variation of average mass% Si against (a) standard deviation and (b) relative deviation % for the 28 GMAW beads.

A presence of element concentration differences between the seven positions was indicated by a large relative deviation percentage. Significant scatter of relative deviation percentage, even in beads that contained no additional alloying, was observed. For example, Ni was added in only five GMA welds, but significant relative deviation percentage was observed in many beads that did not contain additional Ni alloying. The scatter in relative deviation percentage was attributed to the nature of the EDS analysis technique and not actual element mass% differences in the bead cross section.

7.3 Metallography of gas–metal arc weld beads in as-welded condition

In this section, results pertaining to the influence of chemical composition on the presence of delta ferrite in the as-welded microstructure are presented. Microstructures of the GMAW beads and the application of empirical formulae to predict the as-welded microstructures are presented.

7.3.1 General microstructural observations

The delta ferrite phase was not uniformly distributed throughout the bead cross-sections in many of the GMA welds. Figure 7.17 shows weld AW 19, in which one area of the weld contained approximately 4.3% delta ferrite, whereas the microstructure was fully martensitic in other areas.

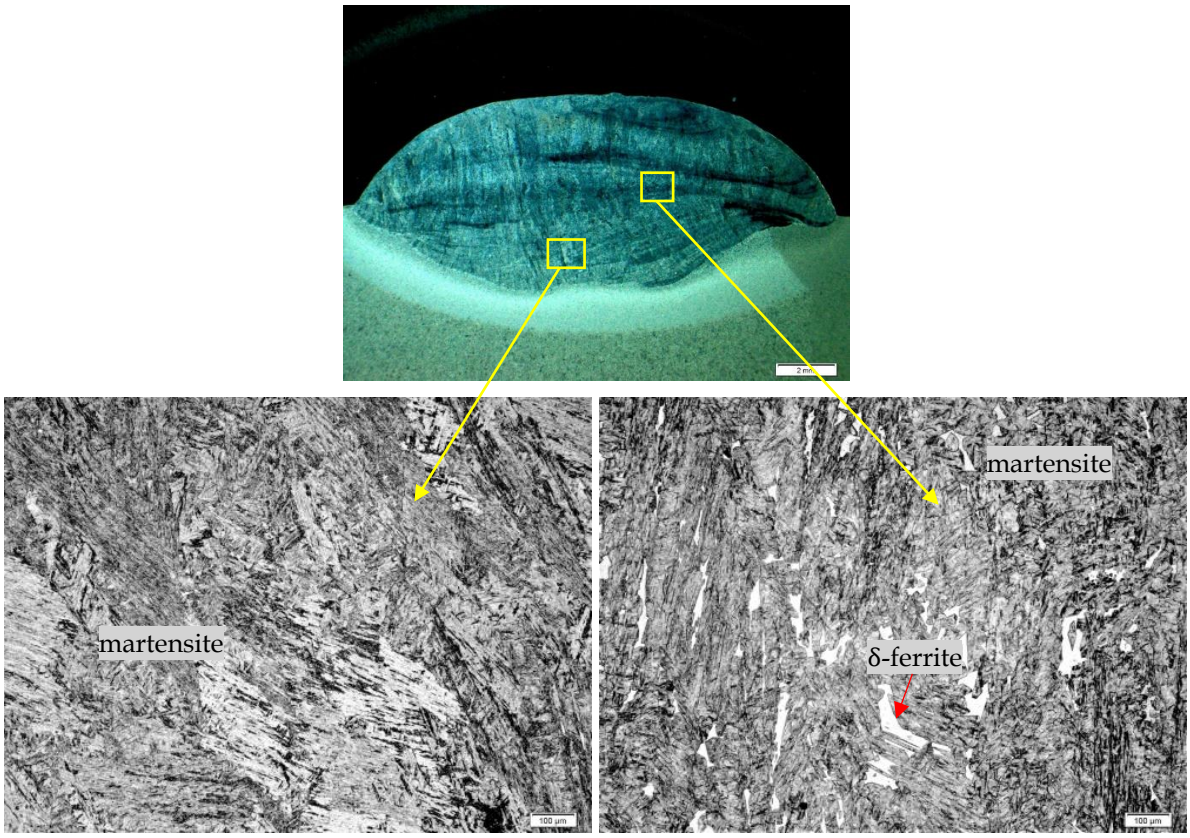

Fig. 7.17 Microstructure images of AW 17 from different locations in the bead cross-section.

The variability of delta ferrite content in the welds is demonstrated in Fig. 7.18, which shows the amount of delta ferrite in each of the 22 microstructure images taken from the cross-section of weld AW 19. The amount of delta ferrite observed ranged from 0% to 4.3%, with an average volume fraction of 2.4%. The reported delta ferrite volume fraction in each of the 20 GMA welds is the average of the analysed microstructure images.

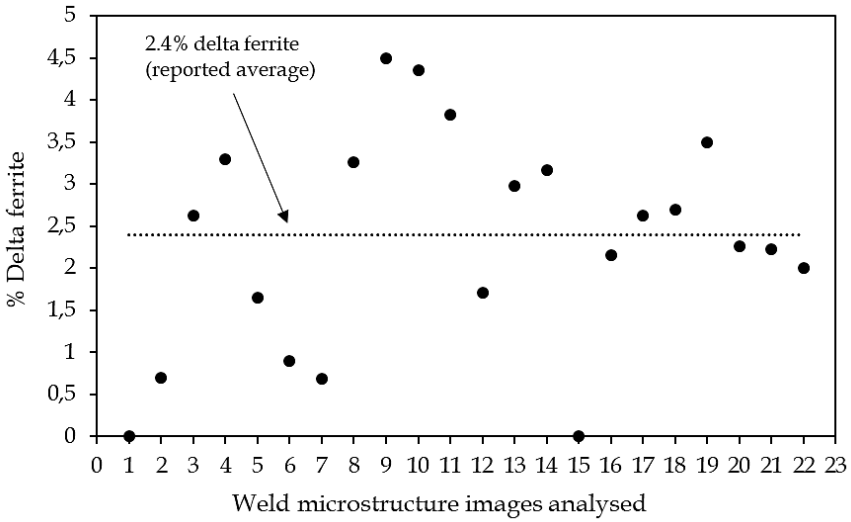

Fig. 7.18 Variability of delta ferrite content in 20 microstructure images analysed from Weld AW 19. The percentage volume fraction of delta ferrite with a 95% confidence interval of AW 19 was 2.4 ± 0.5.

7.3.2 Microstructure of preheated gas–metal arc weld beads in as-welded condition

The microstructure images presented in this section are selected to best represent the average delta ferrite contents of the weld beads. Four of the six welds that received preheat treatment were fully martensitic, represented by the weld PH 2 microstructure image shown in Fig. 7.19. Welds PH 4 and PH 5 consisted of a martensitic matrix with 0.3% and 3.5% delta ferrite, respectively, shown in Fig. 7.20 and Fig. 7.21. Weld PH 5 contained additional Mo and Cr, which are both strong ferrite formers, and a single laser bead of Mn, which is an austenite stabiliser.

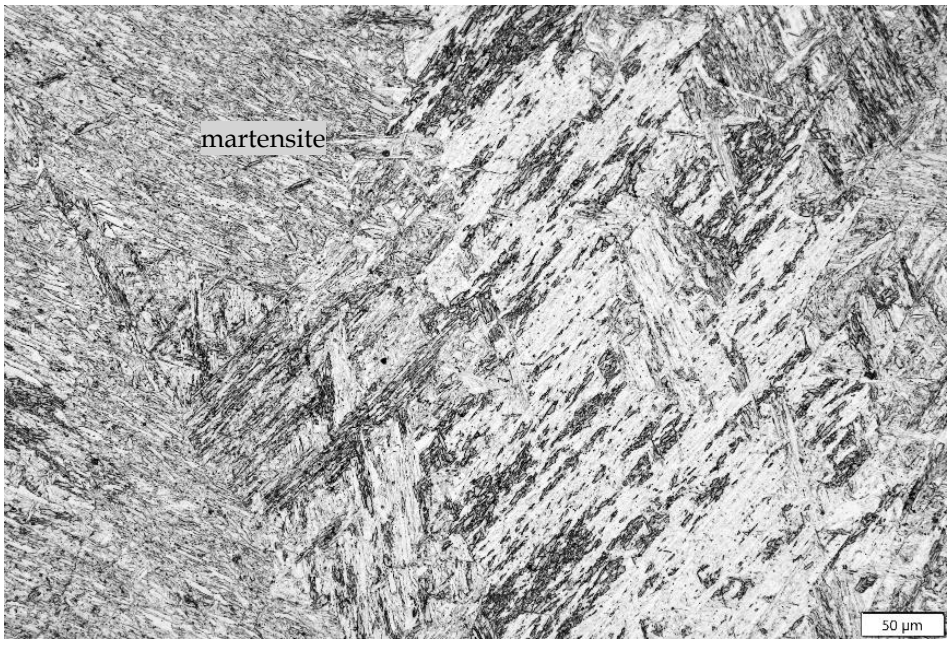

Fig. 7.19 Optical microstructure image of preheated PH 2 bead in as-welded condition, comprising a fully martensitic matrix (200× magnification).

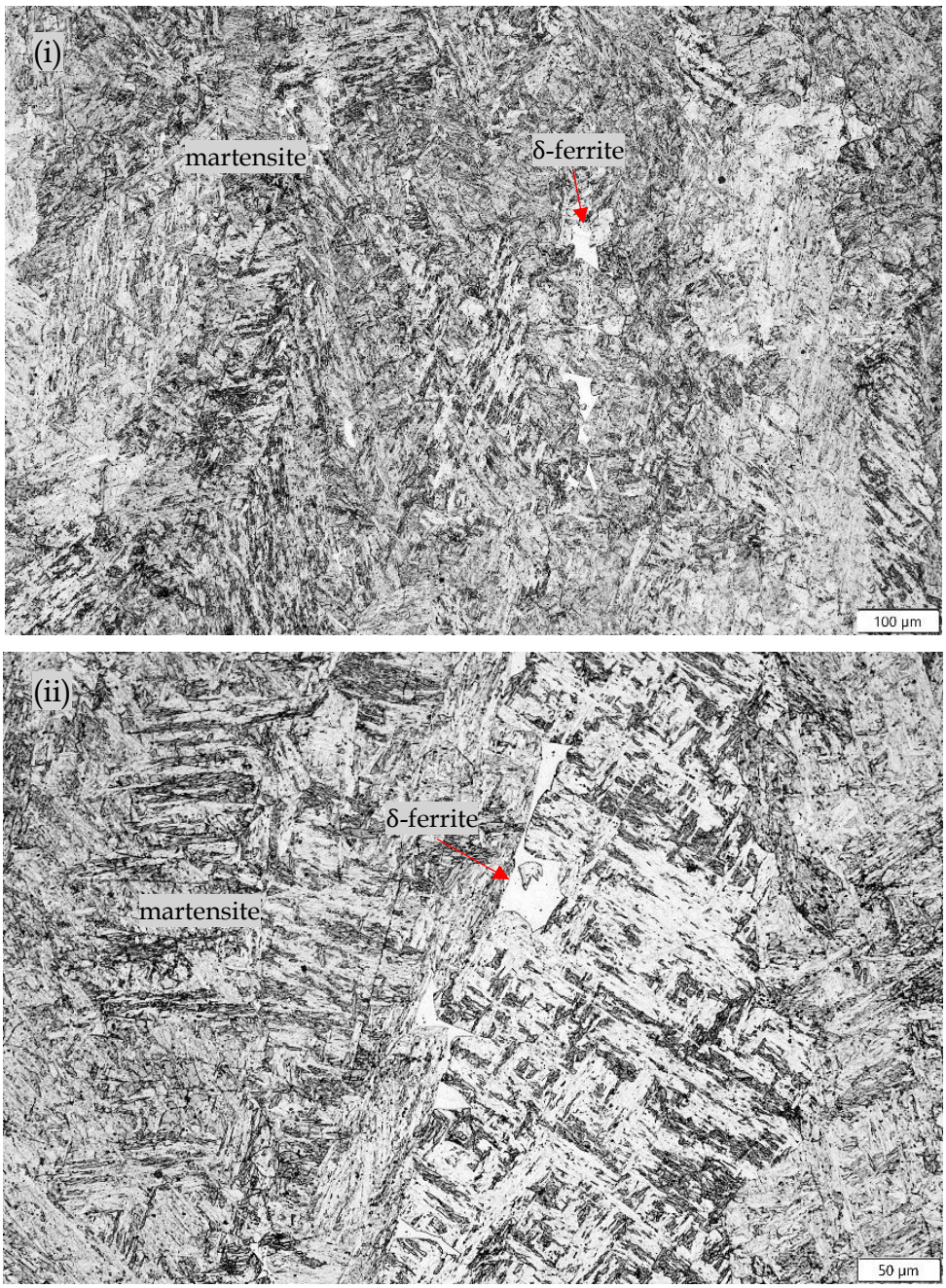

Fig. 7.20 Optical microstructure images of preheated PH 4 bead in as-welded condition, comprising 0.3% delta ferrite in a martensitic matrix ((i) 100× and (ii) 200× magnification).

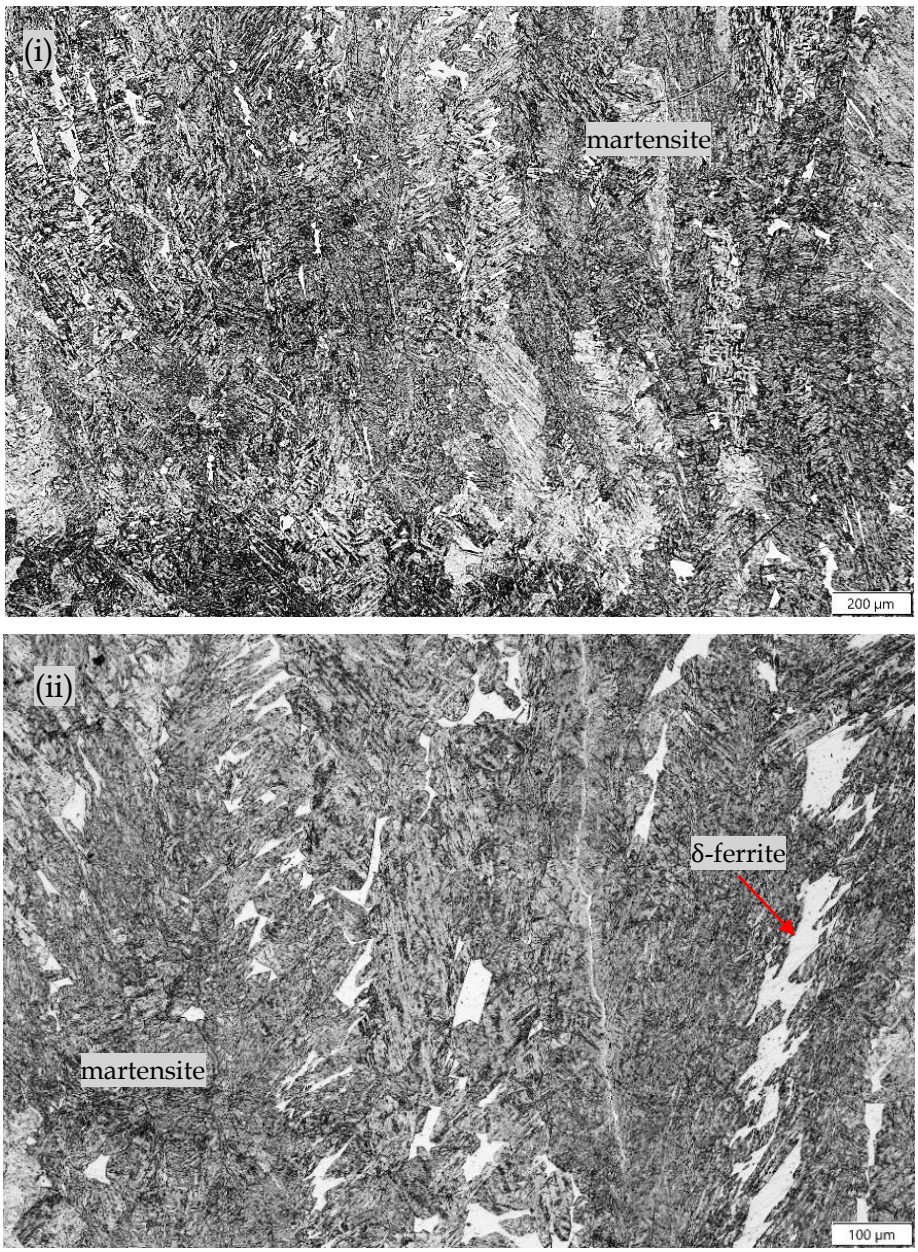

Fig. 7.21 Optical microstructure images of preheated PH 5 bead in as-welded condition, comprising a martensitic matrix with 3.5% delta ferrite ((i) 50× and (ii) 100× magnification).

7.3.3 Microstructure of gas–metal arc weld beads with no preheat applied

Only six of the 22 welds (AW 1, 7, 8, 12, 13, and 22) comprised a fully martensitic microstructure, typified by Fig. 7.22. AW 1 bead was deposited without any laser bead alloying. Ni contents in welds AW 7 and AW 8 were above the AWS specification limit because of the added Ni laser beads. Welds AW 12, 13, and 22 contained additional Mn, which is an austenite stabiliser, but had no additional Cr laser beads, so it was expected that delta ferrite would not be observed in the final microstructures.

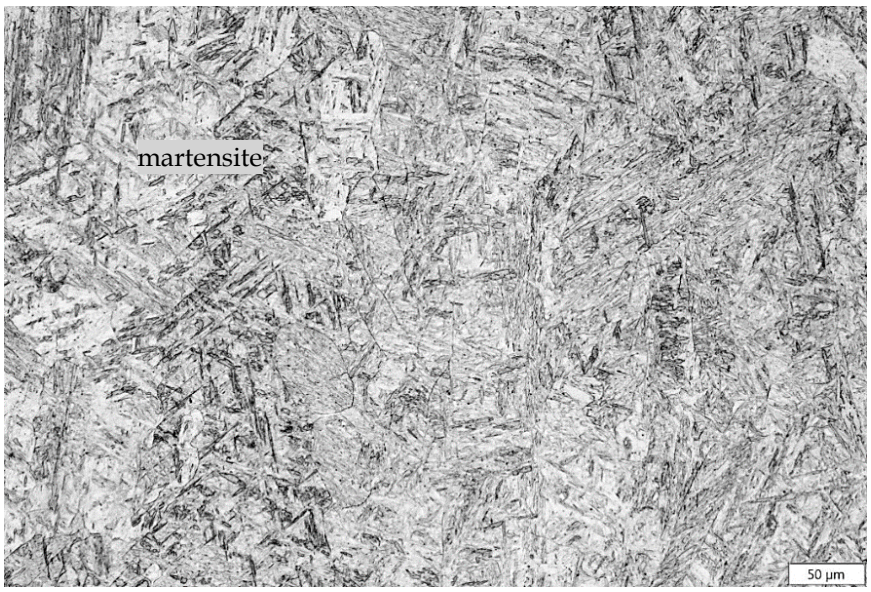

Fig. 7.22 Optical microstructure image of AW 12 weld bead consisting of a fully martensitic matrix in as-welded condition (200× magnification).

Welds AW 2, 11, 14, and 20 contained less than 0.5% volume fraction of small polygonal delta ferrite grains, typified by Fig. 7.23. The chemical compositions of these four welds complied with the AWS A5.28/A5.28M specification, yet their microstructures contained delta ferrite.

Eight welds; namely, AW 3, 4, 6, 10, 15, 18, 19, and 21, contained delta ferrite volume fractions between 1% and 2.6%. Figure 7.23 shows a microstructure of weld AW 19, which contained 2.4% delta ferrite in a martensitic matrix. All eight welds contained laser beads of both ferrite- and austenite-forming elements. Six of the eight welds complied with the AWS A5.28/A5.28M composition specification.

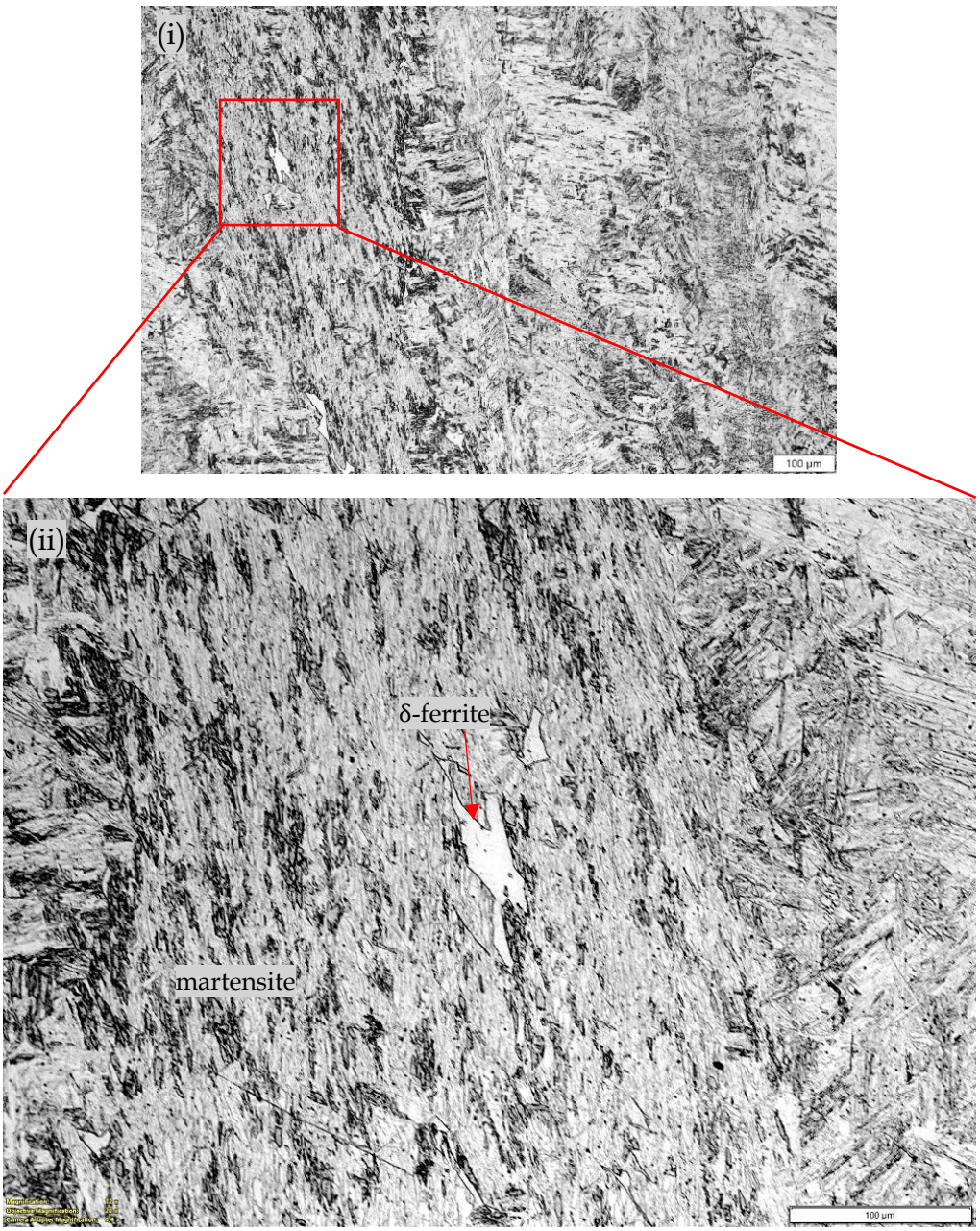

Fig. 7.23 Optical microstructure images of AW 14 weld bead containing 0.5% delta ferrite in a martensitic matrix in as-welded condition ((i) 100× and (ii) 200× magnification).

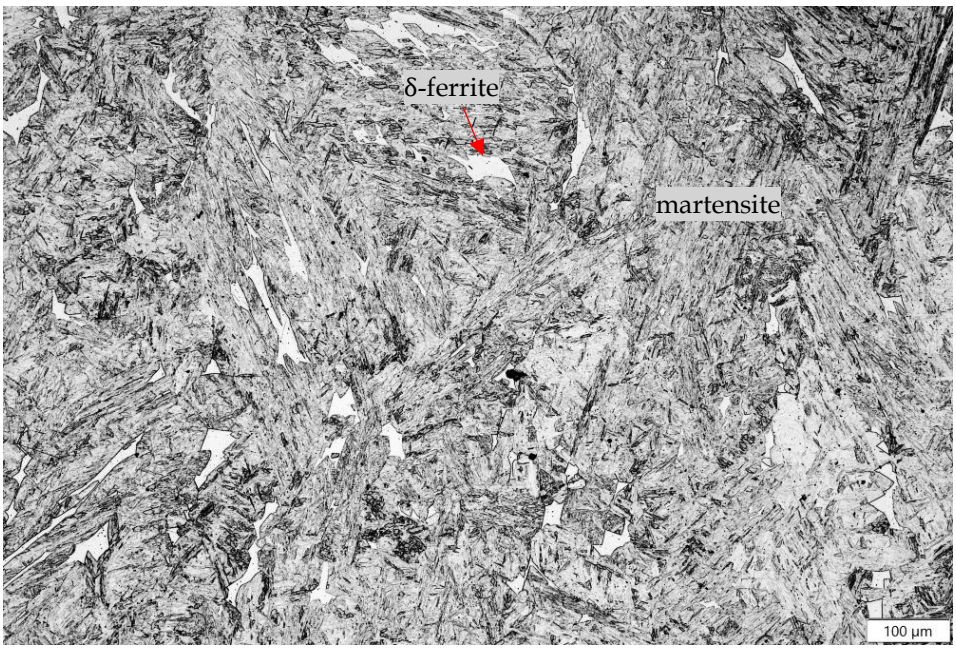

Fig. 7.24 Optical microstructure image of AW 19 weld bead containing 2.4% delta ferrite in a martensitic matrix in as-welded condition (100× magnification).

The four other welds (AW 5, 9, 16, and 17) contained between 3.8% and 6.2% delta ferrite. Figure 7.25(i) and (ii) show the microstructures of welds AW 5 and AW 17, which contained 4.3% and 6.2% delta ferrite, respectively. The delta ferrite morphology was a mixture of small to large polygonal grains and fine elongated grains. Laser beads deposited on these four welds were of Cr, Mo, or Si, which are all ferrite formers. Welds AW 9 and AW 16 complied with the composition specification, yet contained significant amounts of delta ferrite.

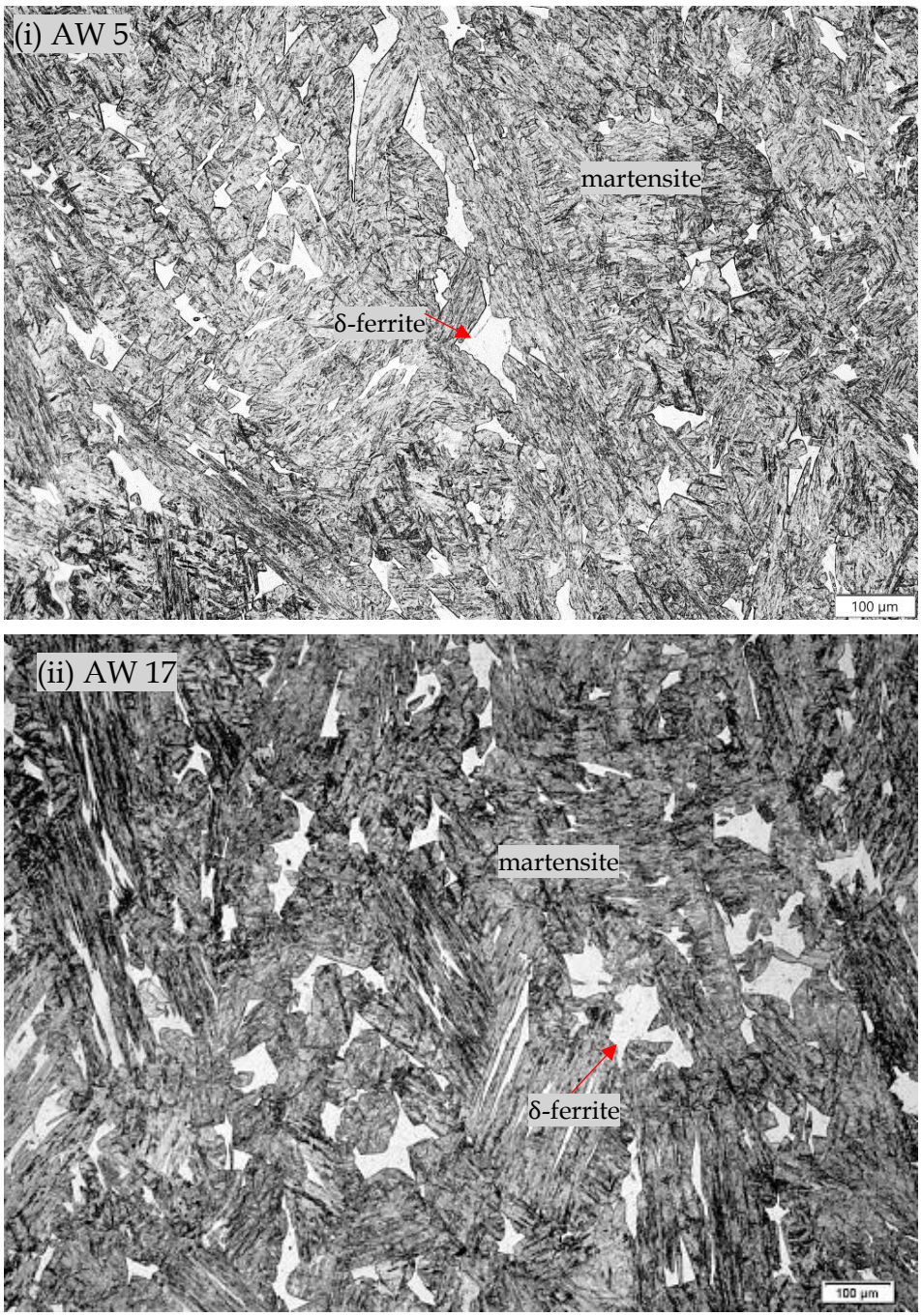

Fig. 7.25 Optical microstructure images of (i) AW 5 and (ii) AW 17 weld beads containing 4.3% and 6.2% delta ferrite, respectively, in a martensitic matrix in as-welded condition (100× magnification).

7.3.4 General analysis of gas–metal arc weld bead microstructures

7.3.4.1 Presence of delta ferrite in welds that complied with composition specification

Twenty of the 28 GMA welds fully complied with both specifications, including the limit of the sum of (Mn + Ni). Thirteen of these 20 welds contained delta ferrite in their microstructures. This represents 64% of welds that complied with the composition specifications and contained delta ferrite. More than 60% of these thirteen welds contained more than 1% delta ferrite. These results clearly demonstrate that compliance

of weld metal chemical composition to the AWS A5.28/A5.28 M:2020 (ER90S-B9) and EN ISO 21952-A CrMo91 specification ranges does not ensure a fully martensitic as-welded microstructure.

7.3.4.2 Effect of alloying elements on delta ferrite

Table 7.5 details selected welds that show the degree by which the elemental mass percentage increased with additional alloying and how that affected the observed delta ferrite.

Table 7.5 *Mass percentage increase from added alloying elements with corresponding delta ferrite% in as-welded GMAW beads*

GMAW beads	***Alloying added (laser beads deposited)***	***Mn***	***Cr***	***Si***	***Mo***	***Ni***	***Delta ferrite (%)***
		1.20 max	*8.0–10.5*	*0.5 max*	*0.85–1.2*	*0.8 max*	
AW 1	No alloying		8.61				0.0
AW 2	(1)Cr		9.12				0.5±0.1
AW 3	(2)Cr		10.31				1.4±0.4
AW 4	(2)Cr, (0.5)Mo		10.22		1.05		1.9±0.5
AW 5	(2)Cr, (1)Mo		10.18		1.37		4.3±0.6
AW 6	(2)Cr, (0.5)Ni		10.25			0.54	1.0±0.2
AW 7	(2)Cr, (1)Ni		10.30			1.13	0.0
AW 9	(2)Cr, (1)Si		9.95	0.47			3.8±0.6
AW 11	(2)Cr, (2)Mn	1.16	9.74				0.4±0.15
AW 16	(2)Cr, (1)Mo, (1)Si		9.81	0.45	1.15		6.0±1.1

Welds AW 1, AW 2, and AW 3 demonstrated how addition of Cr increased the amount of delta ferrite observed in the as-welded GMA beads. Cr and Mo are both ferrite formers, and the addition of Mo in weld AW 4 and AW 5 further increased delta ferrite. The addition of half a laser bead of Ni (an austenite former) in AW 6 decreased the amount of delta ferrite, even with two Cr laser beads. The addition of a full Ni bead in AW 7 raised the mass% Ni above the maximum recommended limit, which completely suppressed the delta ferrite phase in the final as-welded microstructure. Mn is an austenite stabiliser and had the same effect as Ni in reducing the observed delta ferrite when added in weld AW 11. Cr, Mo, and Si are ferrite formers and were added to AW 16. The element mass% of the added elements were within the required specification limits, yet their combined effect resulted in significant increases in delta ferrite.

7.3.4.3 Effect of preheating on gas–metal arc weld microstructure

A 250°C preheat was applied to six welds to achieve a lower cooling rate to study the effect of cooling rate on delta ferrite content. The welds with no preheating were deposited with an average heat input of 1.6 kJ/mm and the calculated $\Delta t_{12\text{-}8}$ was 3.7 s. With a preheat of 250°C, the $\Delta t_{12\text{-}8}$ increased to 6.5 s, based on the Rosenthal equation (4.5) calculation.

Four of the six preheated welds (PH 1, PH 3, PH 4, and PH 5) were comparable in composition with some welds that did not receive preheating (AW 1, AW 2, AW 11, and AW 19). Table 7.6 compares the microstructures of preheated and non-preheated welds with similar compositions.

Table 7.6 *Microstructure comparison between preheated and non-preheated welds*

Comparable welds		***Comments***	
Preheat	*Non-preheated*	*Composition*	*Microstructure*
PH 1	AW 1	No additional alloying on both welds	Both welds were fully martensitic
PH 3	AW 2	Both welds alloyed with an additional 1Cr laser bead	PH 3 was fully martensitic, whereas AW 2 contained 0.5% delta ferrite
PH 4	AW 11	Both welds received additional 2Cr and 2Mn	PH 4 and AW 11 contained 0.3% and 0.4% delta ferrite, respectively
PH 5	AW 19	Both alloyed with additional 2Cr, 1Mn, and 1Mo laser beads	PH 5 contained 3.5% delta ferrite, whereas AW 19 contained 2.4% delta ferrite. This is the only instance where the preheated weld contained more delta ferrite than welds without preheating

The influence of cooling rate when comparing welds of similar compositions was inconsistent. Welds PH 3 and PH 4 showed a marginal decrease in delta ferrite with slower cooling rate, but PH 5 showed an increase in the amount of delta ferrite.

As discussed in Chapter 3, Sam et al. [90] studied the effect of cooling rate in GTAW metal and their results showed that a slower cooling, achieved by higher preheat temperature and heat input, reduced the delta ferrite observed in the final microstructure. Onoro [89] and Faulkner et al. [86] also observed reduced amounts of delta ferrite in P91 SMAW at slower cooling rates. The time spent in the (delta ferrite + austenite) and (austenite only) phase fields determines completion of the transformation from delta ferrite to austenite. Increased time spent in the austenite-only region limits the delta ferrite volume fraction retained in the final weld microstructure.

The non-preheated welds of comparable composition to those that received preheating were limited in number but, generally, slower cooling rate was observed to limit delta ferrite in weld metal.

7.4 Hardness of as-welded gas–metal arc weld beads

Macro-Vickers hardness tests were performed on all 28 GMAW beads in as-welded condition. Five hardness measurements were performed with 10 kgf (HV_{10}) load with a dwell time of 10 s. Table 7.7 presents the average hardness results with 95% CI of the GMAW beads. An example of a 95% CI calculation for hardness values is shown in Appendix A

Table 7.7 *Vickers hardness (Hv_{10}) results showing average of five measurements.*

Weld ID	***Alloys added***	***Delta ferrite (%)***	***Average hardness (Hv_{10}) with 95% CI***
250°C preheat			
PH 1	No alloying	0.0	408 ± 5
PH 2	(0.5)Cr	0.0	403 ± 6
PH 3	(1)Cr	0.0	407 ± 4
PH 4	(2)Cr, (2)Mn	0.3 ± 0.1	398 ± 6
PH 5	(2)Cr, (1)Mn, (1)Mo	3.5 ± 0.9	380 ± 9
PH 6	(1)Cr, (1)Mn, (0.5)Ni	0.0	410 ± 5
No preheat			
AW 1	No alloying	0.0	398 ± 6
AW 2	(1)Cr	0.5 ± 0.1	411 ± 8
AW 3	(2)Cr	1.4 ± 0.4	410 ± 8
AW 4	(2)Cr, (0.5)Mo	1.9 ± 0.5	405 ± 12
AW 5	(2)Cr, (1)Mo	4.3 ± 0.6	396 ± 15
AW 6	(2)Cr, (0.5)Ni	1.0 ± 0.2	416 ± 5
AW 7	(2)Cr, (1)Ni	0.0	421 ± 7
AW 8	(2)Cr, (2)Ni	0.0	438 ± 14
AW 9	(2)Cr, (1)Si	3.8 ± 0.6	401 ± 13
AW 10	(2)Cr, (2)Si	2.2 ± 0.7	412 ± 10
AW 11	(2)Cr, (2)Mn	0.4 ± 0.15	435 ± 12
AW 12	(2)Mn, (0.5)Mo	0.0	413 ± 6
AW 13	(2)Mn, (1)Si	0.0	424 ± 6
AW 14	(0.5)Mo, (1)Si	0.13 ± 0.06	405 ± 7
AW 15	(2)Cr, (0.5)Mo, (1)Si	1.1 ± 0.3	426 ± 5
AW 16	(2)Cr, (1)Mo, (1)Si	6.0 ± 1.1	395 ± 9
AW 17	(2)Cr, (1)Mo, (2)Si	6.2 ± 1.2	393 ± 7
AW 18	(2)Cr, (0.5)Mo, (1)Mn	1.8 ± 0.4	421 ± 6
AW 19	(2)Cr, (1)Mo, (1)Mn	2.4 ± 0.5	409 ± 12
AW 20	(2)Cr, (0.5)Mo, (0.5)Ni	0.3 ± 0.14	414 ± 5
AW 21	(2)Cr, (1)Mn, (1)Si	2.6 ± 0.6	414 ± 9
AW 22	(0.5)Mo, (2)Mn, (1)Si	0.0	424 ± 6

Figure 7.26 shows the weld bead average hardness values plotted against delta ferrite volume fraction. Preheated welds are highlighted with red symbols. GMAW beads containing less than 1% delta ferrite showed significant scatter, with an hardness ranging from 398 to 438 Hv_{10}. A clear trend of decreasing hardness with increase in delta ferrite was observed in welds containing more than 1% delta ferrite, as shown in

Fig. 7.26. Welds with about 1% delta ferrite had an average hardness of 421 Hv_{10}; with an increase to 6% delta ferrite, the hardness decreased to approximately 394 Hv_{10}.

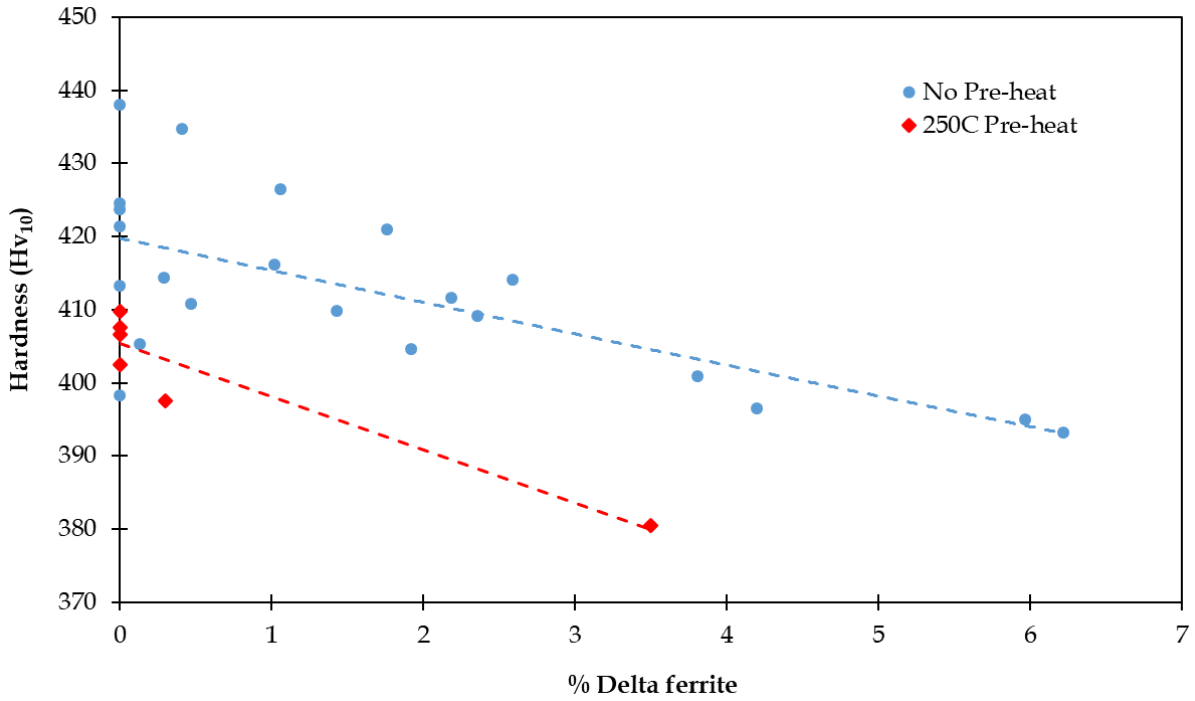

Fig. 7.26 Average hardness (Hv_{10}) as a function of amount of delta ferrite content. Red symbols represent preheated welds.

The hardness results of as-welded P91 welds were within the same range of those reported in literature. Arivazhagen et al. [42] reported hardness of P91 martensitic steel in the as-welded condition to be between 421 and 507 Hv_{10}. Merchant [43] reported a slightly lower hardness value of 350 Hv_{10} in the as-welded condition.

7.4.1 Micro-Vickers hardness of delta ferrite phase

Micro-Vickers hardness testing was performed on selected as-welded beads to measure the local hardness of delta ferrite phase. Testing was performed with 25 gf ($HV_{0.025}$) load with a dwell time of 10 s. Table 7.8 shows the hardness results, with ten measurements taken for each weld specimen.

Table 7.8 *Delta ferrite average micro-Vickers hardness in as-welded beads from ten measurements*

Weld ID	*Delta ferrite (%)*	*Average delta ferrite hardness ($Hv_{0.025}$)*	*Minimum hardness ($Hv_{0.025}$)*	*Maximum hardness ($Hv_{0.025}$)*	*95% CI*
AW 2	0.5 ± 0.1	186	164	204	9
AW 3	1.4 ± 0.4	213	168	250	16
AW 5	4.3 ± 0.6	206	176	272	21
AW 11	0.4 ± 0.15	179	148	220	17
AW 17	6.2 ± 1.2	202	153	244	17

The results in Table 7.8 are graphically presented in Fig. 7.27, which shows the change in hardness with increasing amount of delta ferrite. There is significant scatter in the hardness values, as evident from the large CI values.

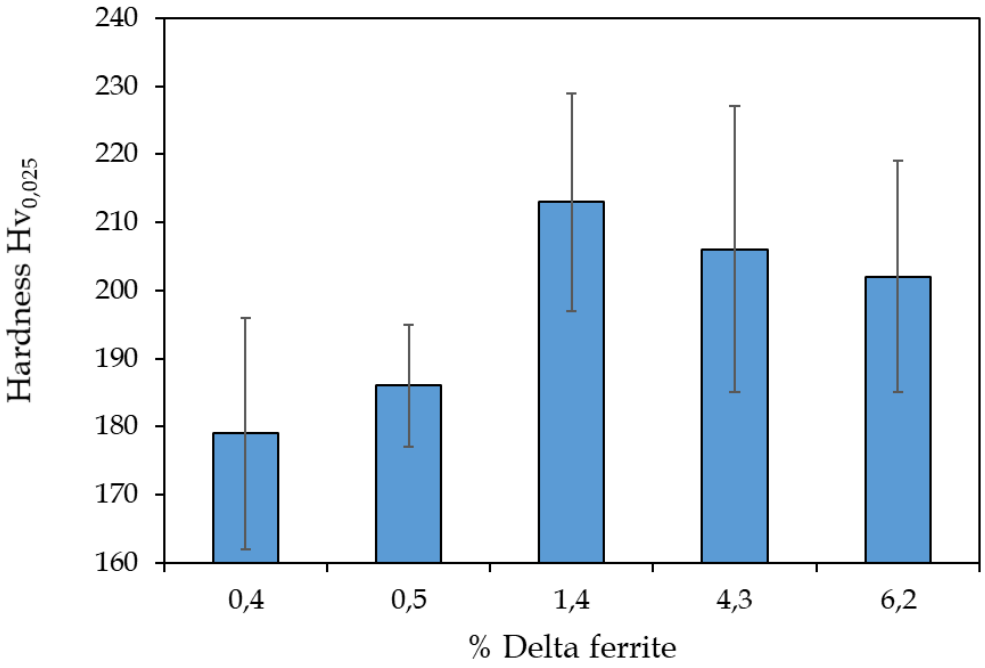

Fig. 7.27 Variation in hardness with delta ferrite content, showing the 95% confidence interval

The delta ferrite average hardness ranged from 179 to 213 $Hv_{0.025}$. The hardness was observed to marginally increase with Cr content, as illustrated in Fig. 7.28.

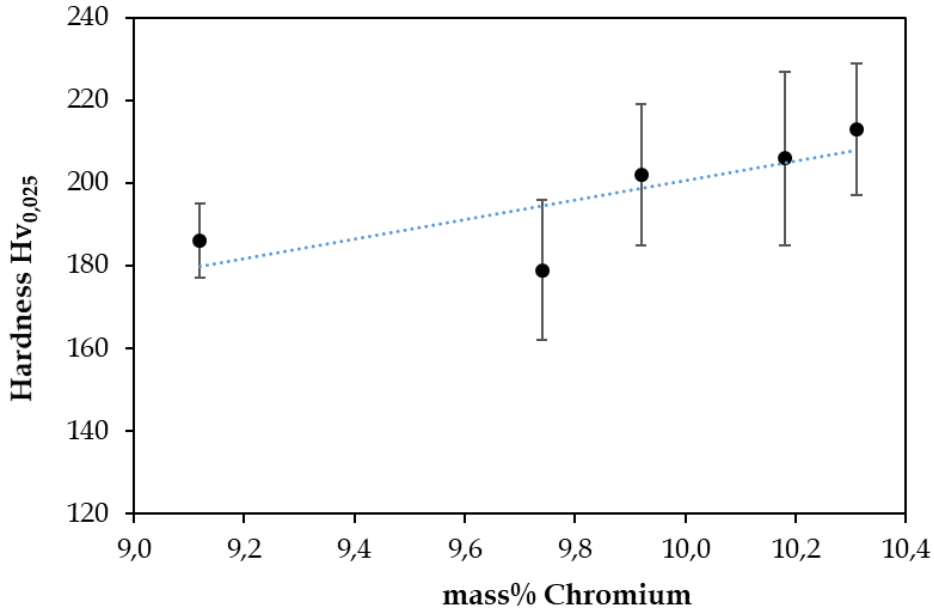

Fig. 7.28 Micro-hardness ($Hv_{0.025}$) of delta ferrite with increasing Cr content.

Chapter 8

Delta ferrite content as a function of transformation temperature

The alloying elements in P91 steel either decrease or increase the transformation temperature, which can influence the delta ferrite presence. In this chapter, the correlation between the transformation temperatures of the 28 welds, calculated using Thermo-Calc, is examined. The amount of observed delta ferrite is systematically presented as a function of calculated equilibrium transformation temperature.

8.1 Correlation between transformation temperatures (Thermo-Calc)

Figure 8.1 to 8.3 show the correlations between Ae_1, Ae_3, and Ae_4 phase transformation temperatures. Ae_1 is defined as the temperature at which austenite formation begins on heating. Figure 8.1 shows the relationship between Ae_1 and Ae_3: the coefficient of determination (R^2) of 0.81 indicates a good correlation. Figure 8.2 shows the relationship between Ae_1 and Ae_4, which has R^2 = 0.41, indicating a poor correlation. The relationship between Ae_3 and Ae_4 (Figure 8.3) has R^2 = 0.78, indicating a good correlation.

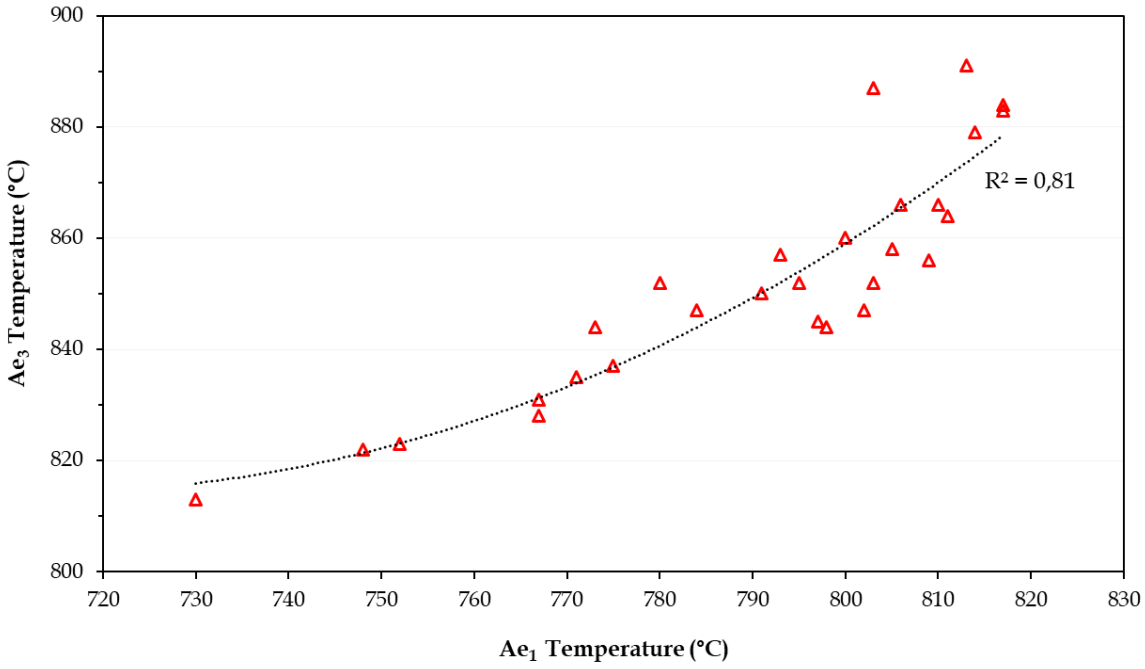

Fig. 8.1 Relationship between Ae_1 and Ae_3 transformation temperatures.

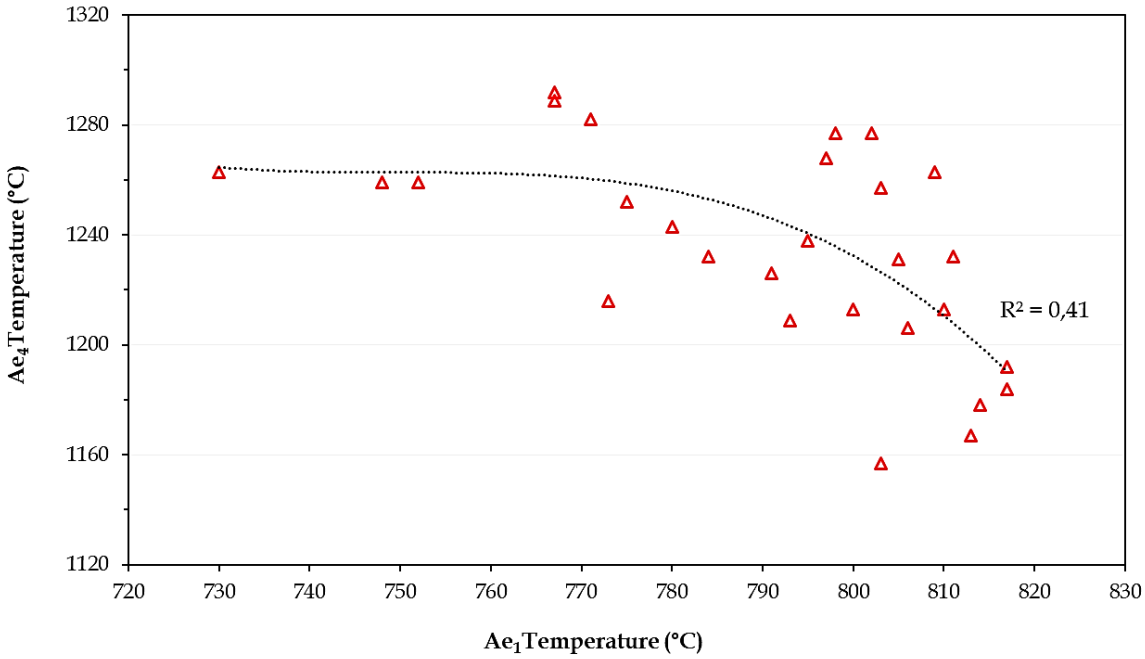

Fig. 8.2 Relationship between Ae_1 and Ae_4 transformation temperatures.

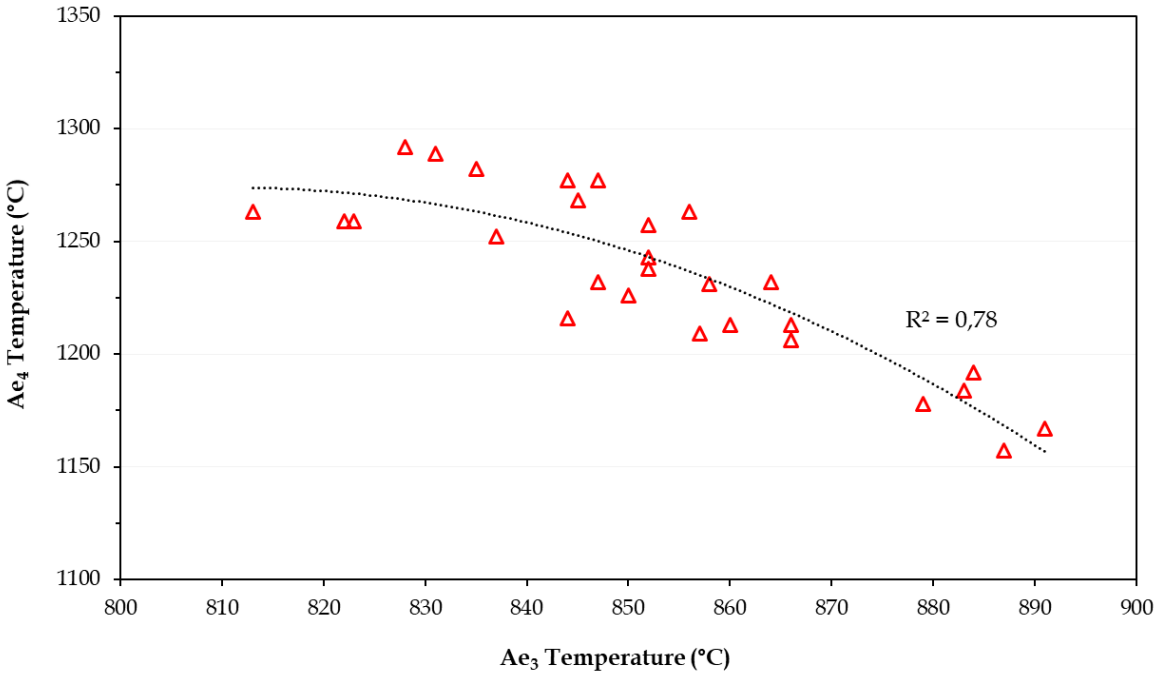

Fig. 8.3 Relationship between Ae_3 and Ae_4 transformation temperatures.

Figure 8.4 to 8.6 show the relationships between the ($Ae_4 - Ae_3$) temperature ranges and the Ae_1, Ae_3, and Ae_4 transformation temperatures. The ($Ae_4 - Ae_3$) temperature range is the region where only austenite is stable in the P91 equilibrium phase diagram. Figure 8.4 shows the relationship between ($Ae_4 - Ae_3$) and Ae_1, which has an R^2 value of 0.55, indicating a moderate correlation. The relationship between ($Ae_4 - Ae_3$) and Ae_3, shown in Figure 8.5, has a coefficient of determination of 0.88, which indicates a good

correlation. Figure 8.6 similarly shows the relationship between ($Ae_4 - Ae_3$) and Ae_4, which has $R^2 = 0.96$, which is a very good correlation.

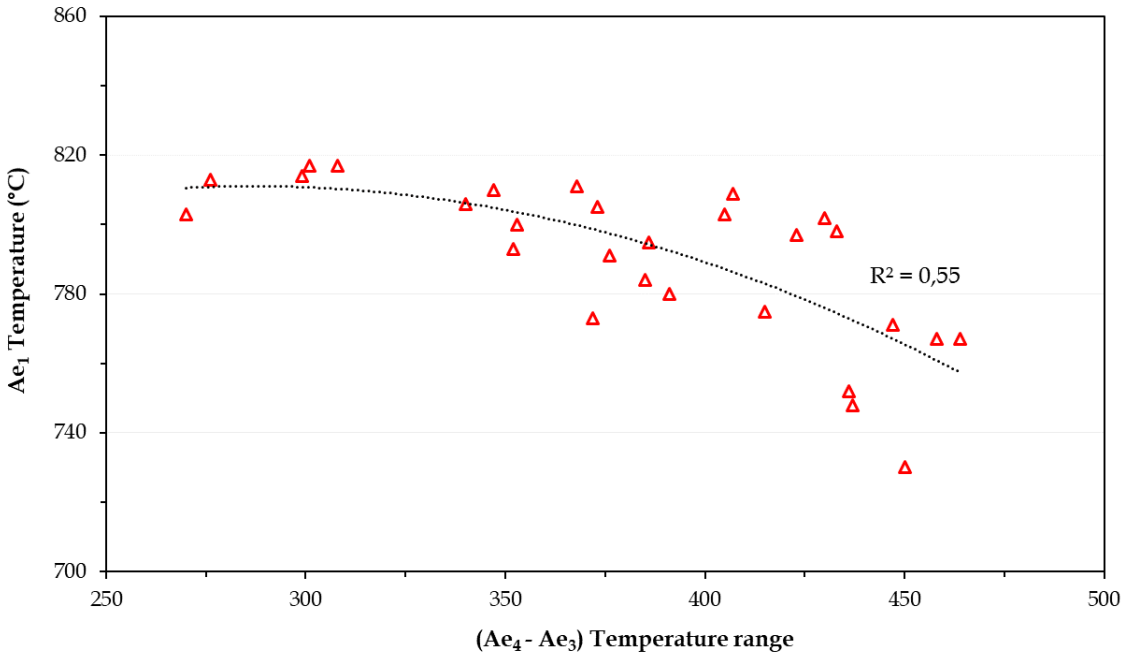

Fig. 8.4 Relationship between ($Ae_4 - Ae_3$) temperature range and Ae_1 transformation temperature.

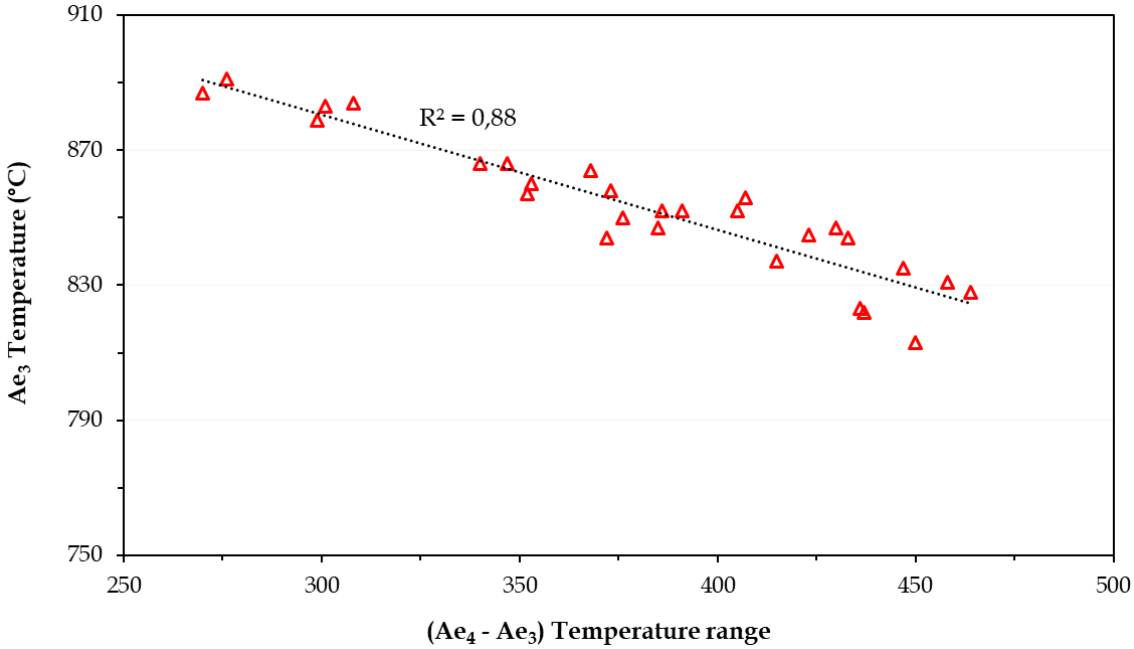

Fig. 8.5 Relationship between ($Ae_4 - Ae_3$) temperature range and Ae_3 transformation temperature.

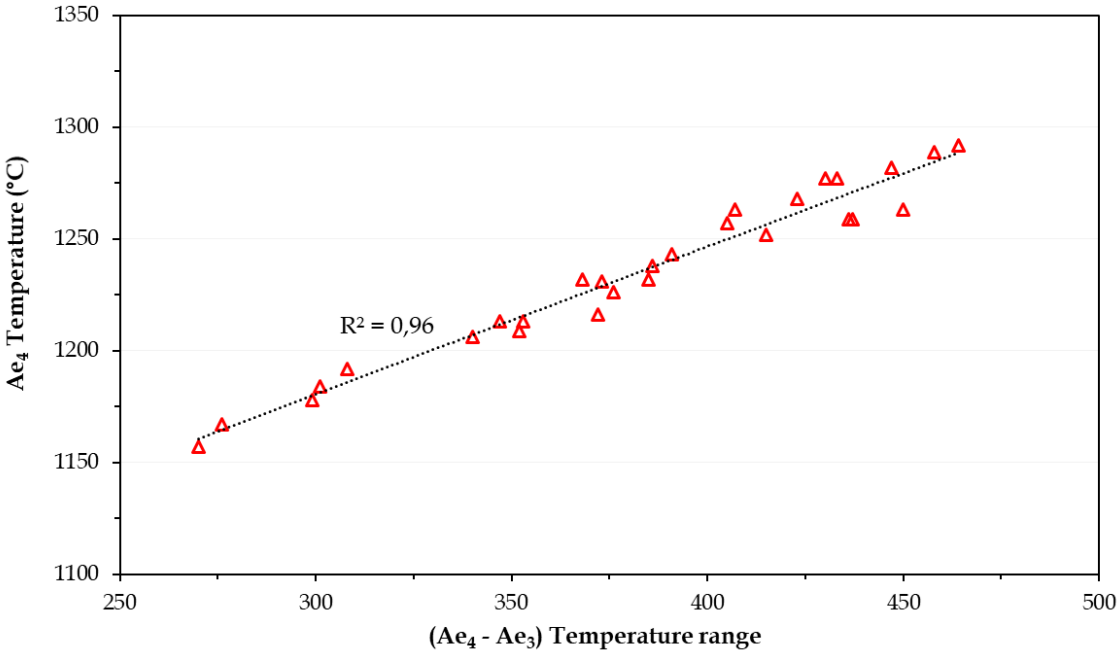

Fig. 8.6 Relationship between ($Ae_4 - Ae_3$) temperature range and Ae_4 transformation temperature.

8.2 Correlation between phase-transformation temperatures (Thermo-Calc) and delta ferrite content

Figure 8.7 to 8.10 show the relationship between the Ae_1, Ae_3, Ae_4, and Ae_5 transformation temperatures (as determined by Thermo-Calc) and the amount of delta ferrite in the final microstructure of the welds with and without preheating at 250°C.

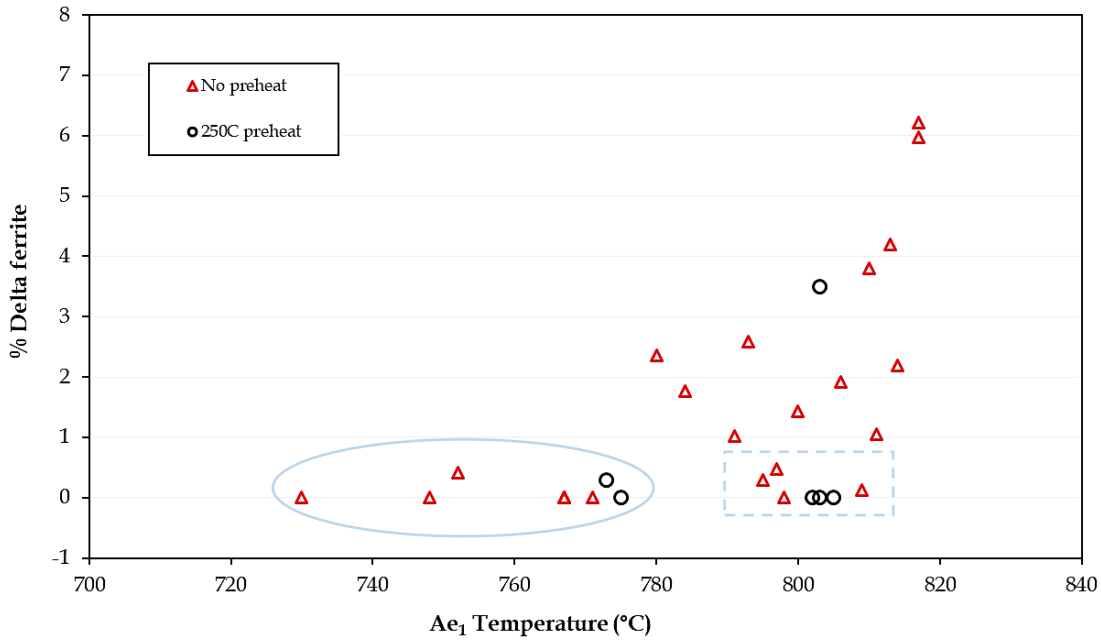

Fig. 8.7 Relationship between Ae_1 transformation temperature and amount of delta ferrite in final microstructure in as-welded condition. The circled welds contained no or very little delta ferrite with an Ae_1 below 780°C. The squared welds contained no or very little delta ferrite and their Ae_1 temperature was on the conservative side with respect to post-weld heat treatment.

The eight welds circled in Fig. 8.7 (PH 4, PH 6, AW 7, AW 8, AW 11, AW 12, AW 13, and AW 22) had Ae_1 < 780°C and contained no delta ferrite, with the exceptions of PH 4 and AW 11 welds that contained 0.3% and 0.4% delta ferrite, respectively. It is not desirable to have such low Ae_1 temperatures because these are close to or below the recommended PWHT (760°C) temperature. The squared welds (PH 1, PH 2, PH 3, AW 1, AW 2, AW 14, and AW 20) contained no delta ferrite, with the exceptions of AW14 and AW 20 welds that contained 0.13% and 0.30% delta ferrite, respectively, but their Ae_1 was conservative with respect to the PWHT, which ranged between 795 and 809°C.

The GMA welds with Ae_1 < 780°C contained either additional alloying of Mn and Ni, or two laser beads of each of these elements. The results confirm that Mn and Ni are effective in suppressing the presence of delta ferrite in the as-welded microstructure. Generally, increased amounts of delta ferrite were observed in welds with higher Ae_1 due to the addition of two Cr beads in most welds. There were four welds with Ae_1 > 800°C that comprised a fully martensitic structure and did not contain additional Cr alloying. Two welds that were alloyed with a single or half Cr bead had a high Ae_1 temperature and a fully martensitic microstructure. These two welds were deposited with a preheating temperature of 250°C.

Figure 8.8 shows the relationship between the Ae_3 transformation temperature and amount of delta ferrite in the final weld microstructure. Ae_3 is defined as the temperature at which a fully austenitic phase is achieved on heating.

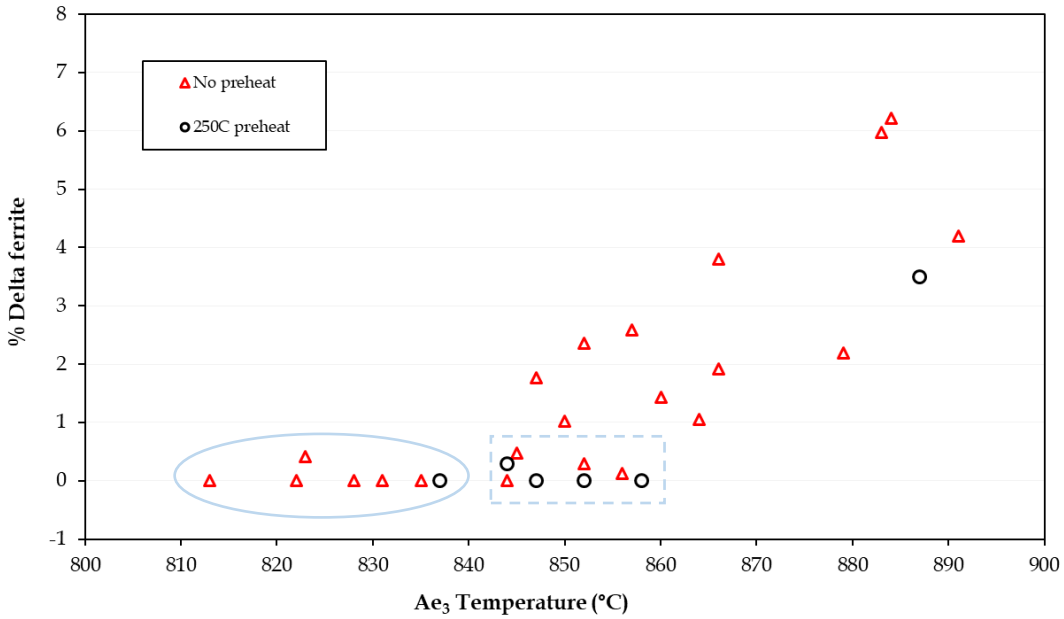

Fig. 8.8 Relationship between Ae_3 transformation temperature and amount of delta ferrite in final microstructure in as-welded condition. In the circled welds, there was little or no delta ferrite, but an Ae_3 below 840°C. The squared welds contained little or no delta ferrite and their Ae_3 temperatures ranged between 844 and 858°C.

PH 6, AW 7, AW 8, AW 11, AW 12, AW 13, and AW 22, circled in Fig. 8.8, were welds with $Ae_3 < 840$°C and contained no delta ferrite, with the exception of the AW 11 that had 0.4% delta ferrite. PH 1, PH 2, PH 3, PH 4, AW 1, AW 2, AW 14, and AW 20 contained no delta ferrite, with the exceptions of PH 4, AW 14, and AW 20 welds that had delta ferrite contents between 0.13% and 0.30%, but their Ae_3 temperatures were on the slightly higher side, ranging between 844 and 858°C. Welds with $Ae_3 > 858$°C contained delta ferrite of 1% and above. No alloying element was observed to have a dominant effect in suppressing both the Ae_3 temperature and delta ferrite. At $Ae_3 > 840$°C, the amount of delta ferrite was observed to increase with Ae_3 temperature. There were four welds with $Ae_3 > 840$°C that consisted of a fully martensitic microstructure and that were alloyed with a single or half Cr bead. These welds contained < 9.47 mass% Cr. Preheating was observed to suppress delta ferrite in welds with $Ae_3 > 840$°C.

Figure 8.9 shows the relationship between the Ae_4 transformation temperatures and the amount of delta ferrite in the final microstructure of the welds. Ae_4 is defined as the temperature at which delta ferrite formation begins ($\gamma \rightarrow \delta + \gamma$) on heating.

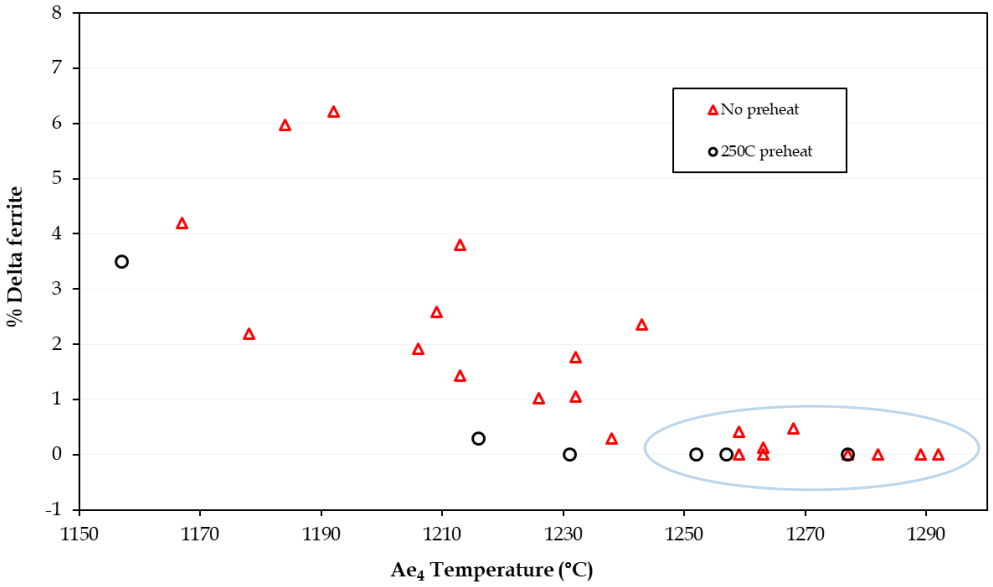

Fig. 8.9 Relationship between Ae_4 transformation temperature and amount of delta ferrite in final microstructure in as-welded condition. The circled welds contained little or no delta ferrite and had an Ae_4 above 1260°C.

Twelve of the 28 welds, circled in Fig. 8.9, contained no delta ferrite, with the exceptions of AW 2, AW 11, and AW 14 that contained 0.5%, 0.4%, and 0.13% delta ferrite, respectively. These 12 welds had $Ae_4 \geq 1260$°C. Only at $Ae_4 \leq 1216$°C did the preheated welds contain delta ferrite in their microstructures. The preheated welds showed a consistent decrease in delta ferrite content with increasing Ae_4 temperature. No individual elements were observed to have a dominant influence on the Ae_4 temperature. Application of 250°C preheating decreased the minimum Ae_4 temperature required to suppress delta ferrite from 1260°C to 1230°C. Generally, the delta ferrite was observed to decrease with increasing Ae_4 temperature.

Figure 8.10 shows the relationship between the Ae_5 transformation temperatures and the amount of delta ferrite in the final microstructure of the welds. Ae_5 is defined as the temperature at which the austenite-to-delta ferrite transformation is completed ($\delta + \gamma \rightarrow \delta$) on heating. The eleven welds circled in Fig. 8.10 contained no delta ferrite, except for welds AW 2 and AW 11, which consisted of 0.5% and 0.4% delta ferrite, respectively. The welds with no delta ferrite had $Ae_5 \geq 1404$°C. AW 19 is an outlier containing 2.4% delta ferrite with an Ae_5 of 1421°C. The delta ferrite content decreased with increasing Ae_5 temperature.

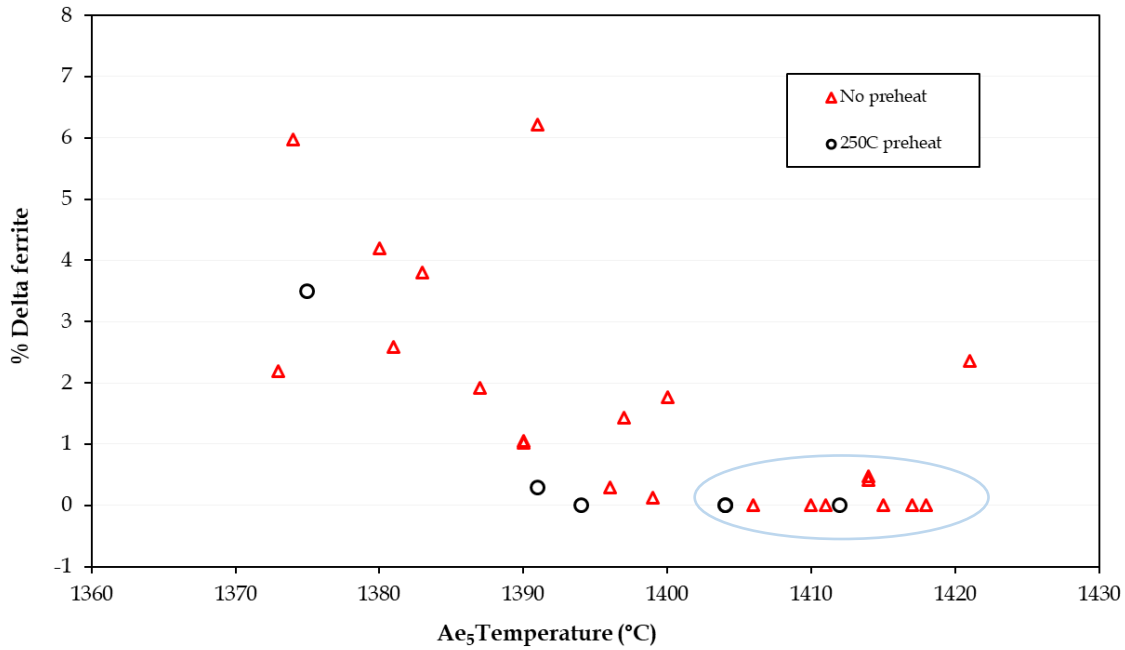

Fig. 8.10 Relationship between Ae_5 transformation temperature and amount of delta ferrite in final microstructure in as-welded condition. The circled welds contained little or no delta ferrite and had an Ae_5 above 1404°C.

8.2.1 General observations

- The transformation temperatures (Ae_1, Ae_3, Ae_4, and Ae_5), when considered as single parameters, do not have significant predictive capability.
- Chemical composition and cooling rate are the main parameters that influence delta ferrite transformation.

8.3 Influence of ($Ae_4 - Ae_3$) temperature range on amount of delta ferrite

Figure 8.11 shows the relationship between the ($Ae_4 - Ae_3$) temperature range and amount of delta ferrite in the final microstructure of the welds. Arivazhagan and Kamaraj [6] stated that the probability of delta ferrite retention in the weld increases with a lower value of ($Ae_4 - Ae_3$). Results of previous work conducted on SMAW beads [18] are incorporated in Fig. 8.11 and show good agreement with the present GMAW results on beads deposited without any preheating. An ($Ae_4 - Ae_3$) temperature range above 415°C for welds that are not preheated seems to be necessary to suppress delta ferrite in the as-welded microstructure. The required ($Ae_4 - Ae_3$) range decreased to 385°C when 250°C preheating was applied. These results indicate that both the chemical composition, which determines the ($Ae_4 - Ae_3$) temperature range, and the cooling rate through this temperature range are important in suppressing delta ferrite in the final as-welded microstructure.

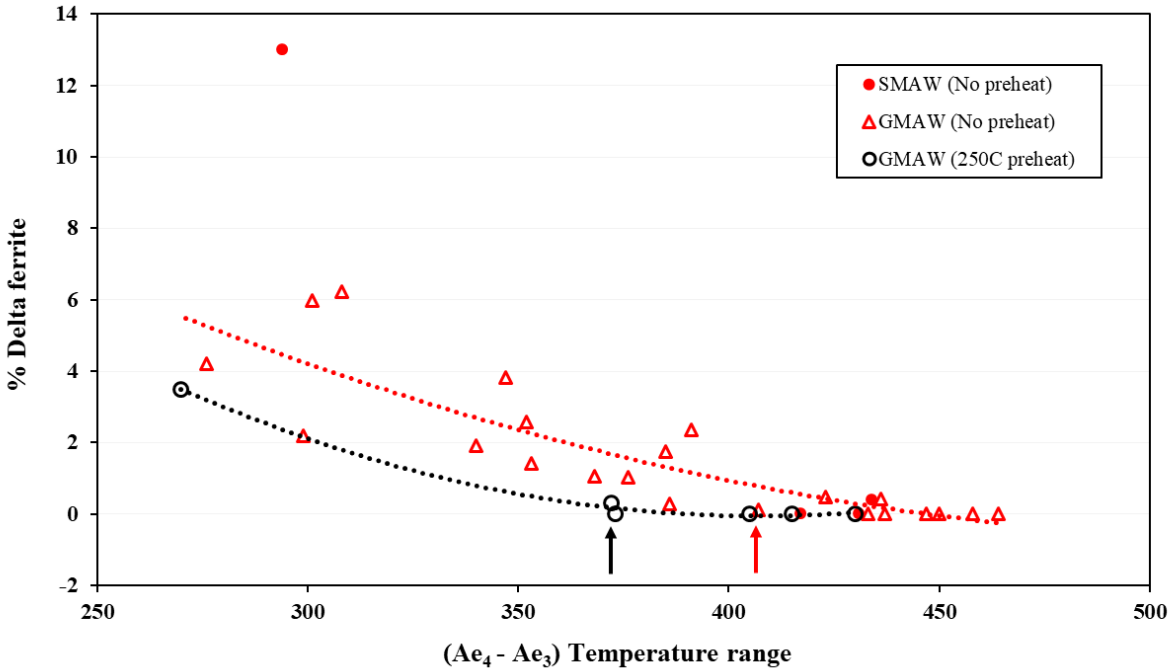

Fig. 8.11 Relationship between ($Ae_4 - Ae_3$) temperature range and amount of delta ferrite in final microstructure of weld. The red and black arrows indicate the estimated ($Ae_4 - Ae_3$) values necessary to suppress delta ferrite without and with preheating, respectively.

Chapter 9

Prediction of as-welded microstructure from empirical formulae

9.1 Empirical formulae recommended limits

The potential for delta ferrite presence in the as-welded final microstructure of modified 9Cr–1Mo steel can be estimated using empirical formulae. Faulkner [86] concluded based on experimental results that for a weld metal to be fully martensitic, that the Cr_{eq} and FF should not exceed 13.5 and 8, respectively, based on the Schneider relationships, and 12.5 or 6.0, respectively, using the modified Schaeffler relationship. Sireesha [62] recommended that the Kaltenhauser FF should have a maximum value of 8 to avoid ferrite retention in P91 welds. Using the CNB formulation (Equation 9.6) from a modified Newhouse's equation, Swindeman et al. [5] stated that delta ferrite is not usually present if CNB < 10; for CNB > 12, significant quantities of delta ferrite are observed. The most commonly used predictive empirical formulae for P91 steel welds are summarised from Chapter 3 for ease of reference.

a) Schaeffler modified equations:

$$Cr_{eq} = Cr + 1.5Si + Mo + 0.5Nb + 0.75W \quad (9.1)$$

$$Ni_{eq} = Ni + 0.5Mn + 30C + 30N + 0.3Cu + Co \quad (9.2)$$

b) Schneider formulae:

$$Cr_{eq} = Cr + 2Si + 1.5Mo + 5V + 1.75Nb + 0.75W \quad (9.3)$$

$$Ni_{eq} = Ni + 0.5Mn + 30C + 25N + 0.3Cu \quad (9.4)$$

c) Kaltenhauser formula

$$(KFF) = Cr + 6Si + 4Mo + 4Nb + 2Al + 8Ti - 2Mn - 2Ni - 40(C + N) \quad (9.5)$$

d) Newhouse formulae:

$$CNB = Cr + 6Si + 4Mo + 1.5W + 5Nb + 9Ti + 11V + 12Al - 40C - 30N - 2Mn - 4Ni - 1Cu \quad (9.6)$$

9.2 Prediction of delta ferrite in as-welded beads

Table 9.1 presents the values calculated using the empirical formulae from Schaeffler, Schneider, Kaltenhauser, and Newhouse based on the GMAW chemical composition. The highlighted values are above the recommended limits that predict the presence of delta ferrite in the P91 as-welded microstructure.

Table 9.1 *Empirical formulation values based on gas–metal arc weld composition. Values above the recommended limits (indicative of the risk of delta ferrite) are highlighted*

Weld ID	***Schaeffler***			***Schneider***			***Kaltenhauser***	***Newhouse***
	Cr_{eq} (< 12.5)	Ni_{eq}	FF (< 6)	Cr_{eq} (< 13.5)	Ni_{eq}	FF (< 8)	KFF (< 8)	CNB (< 10)
250°C preheat								
PH 1	9.8	4.9	5.0	11.7	4.6	7.0	7.0	9.3
PH 2	10.3	4.8	5.5	12.1	4.6	7.6	7.5	9.8
PH 3	10.9	4.8	6.1	12.7	4.6	8.1	8.1	10.4
PH 4	11.4	5.0	6.4	13.2	4.8	8.5	7.5	9.8
PH 5	12.1	4.9	7.2	14.1	4.7	9.4	9.8	12.2
PH 6	10.8	5.1	5.7	12.6	4.9	7.7	6.9	8.9
No preheat								
AW 1	10.1	5.0	5.1	11.9	4.7	7.2	7.1	9.4
AW 2	10.5	5.3	5.3	12.3	5.0	7.3	7.1	9.3
AW 3	11.7	5.4	6.3	13.6	5.1	8.4	8.1	10.4
AW 4	11.7	5.4	6.3	13.5	5.1	8.5	8.2	10.6
AW 5	12.0	5.0	7.0	14.1	4.7	9.3	10.3	12.6
AW 6	11.6	5.6	6.0	13.4	5.3	8.2	7.3	9.5
AW 7	11.7	6.1	5.6	13.5	5.8	7.7	6.6	7.4
AW 8	11.6	5.8	5.8	13.3	5.5	7.8	6.6	6.7
AW 9	11.6	5.3	6.3	13.6	5.0	8.6	8.9	11.5
AW 10	12.1	4.7	7.4	14.1	4.4	9.7	11.1	13.5
AW 11	11.1	5.7	5.4	12.9	5.4	7.5	6.0	8.4
AW 12	9.9	5.5	4.4	11.9	5.2	6.6	5.6	8.1
AW 13	10.0	5.5	4.5	11.9	5.2	6.8	6.0	8.5
AW 14	10.2	5.0	5.2	12.3	4.7	7.6	8.4	10.9
AW 15	10.9	4.9	6.0	12.9	4.6	8.3	8.9	11.4
AW 16	11.7	4.9	6.8	13.7	4.6	9.2	10.2	12.6
AW 17	12.0	5.3	6.8	14.1	5.0	9.1	10.7	13.1
AW 18	11.7	6.0	5.6	13.5	5.7	7.8	6.7	9.2
AW 19	11.5	6.2	5.3	13.6	5.9	7.7	7.5	9.9
AW 20	11.0	5.2	5.8	12.9	4.9	8.0	7.6	9.7
AW 21	11.6	5.0	6.5	13.5	4.7	8.8	8.6	11.2
AW 22	10.1	5.5	4.6	12.1	5.0	7.1	7.0	9.5

The correct or incorrect prediction of GMA welds microstructure by the various empirical formulae is indicated in Table 9.2, as well as the percentage volume fractions of delta ferrite with 95% CI. Over 20 micrograph images per weld were analysed, covering the transverse cross-section of each GMAW bead to quantify the amount of delta ferrite. A point-counting method was applied, with a total of 210 points placed on the microstructure images.

Table 9.2 *Correct (✓) and incorrect (×) predictions of delta ferrite presence*

Weld ID	*Schaeffler*	*Schneider*	*Kaltenhauser*	*Newhouse*	*Delta ferrite (%)*
PH 1	✓	✓	✓	✓	0.0
PH 2	✓	✓	✓	✓	0.0
PH 3	×	×	×	×	0.0
PH 4	✓	✓	×	×	0.3±0.1
PH 5	✓	✓	✓	✓	3.5±0.9
PH 6	✓	✓	✓	✓	0.0
AW 1	✓	✓	✓	✓	0.0
AW 2	×	×	×	×	0.5±0.1
AW 3	✓	✓	✓	✓	1.4±0.4
AW 4	✓	✓	✓	✓	1.9±0.5
AW 5	✓	✓	✓	✓	4.3±0.6
AW 6	✓	✓	×	×	1.0±0.2
AW 7	✓	×	✓	✓	0.0
AW 8	✓	✓	✓	✓	0.0
AW 9	✓	✓	✓	✓	3.8±0.6
AW 10	✓	✓	✓	✓	2.2±0.7
AW 11	×	×	×	×	0.4±0.15
AW 12	✓	✓	✓	✓	0.0
AW 13	✓	✓	✓	✓	0.0
AW 14	×	×	✓	✓	0.13±0.06
AW 15	✓	✓	✓	✓	1.1±0.3
AW 16	✓	✓	✓	✓	6.0±1.1
AW 17	✓	✓	✓	✓	6.2±1.2
AW 18	×	✓	×	×	1.8±0.4
AW 19	×	✓	×	×	2.4±0.5
AW 20	×	✓	×	×	0.3±0.14
AW 21	✓	✓	✓	✓	2.6±0.6
AW 22	✓	✓	✓	✓	0.0

(✓) Presence or absence of delta ferrite was correctly predicted.
(×) Presence or absence of delta ferrite was incorrectly predicted.

A demonstration on how the CI for the delta ferrite percentage was calculated is shown in Appendix A.

When considering the recommended limits, the following observations were made in the prediction of the presence or absence of delta ferrite in the final GMA weld microstructures.

Schaeffler formula: All GMA welds were within the recommended Cr_{eq} of 12.5. Thirteen welds were predicted to contain delta ferrite based on the FF. Welds AW 2, AW 11, AW 14, AW 18, AW 19, and AW 20 were predicted to be fully martensitic, but delta ferrite was observed in their microstructures. Delta ferrite was predicted to be present in weld PH 3 because of the FF value of 6.1, which was slightly above the recommended limit, but the microstructure was fully martensitic. Seven of the 28 welds were incorrectly predicted. The Schaeffler values in Table 9.1 are superimposed on the 1949 Schaeffler prediction diagram in Fig. 9.1.

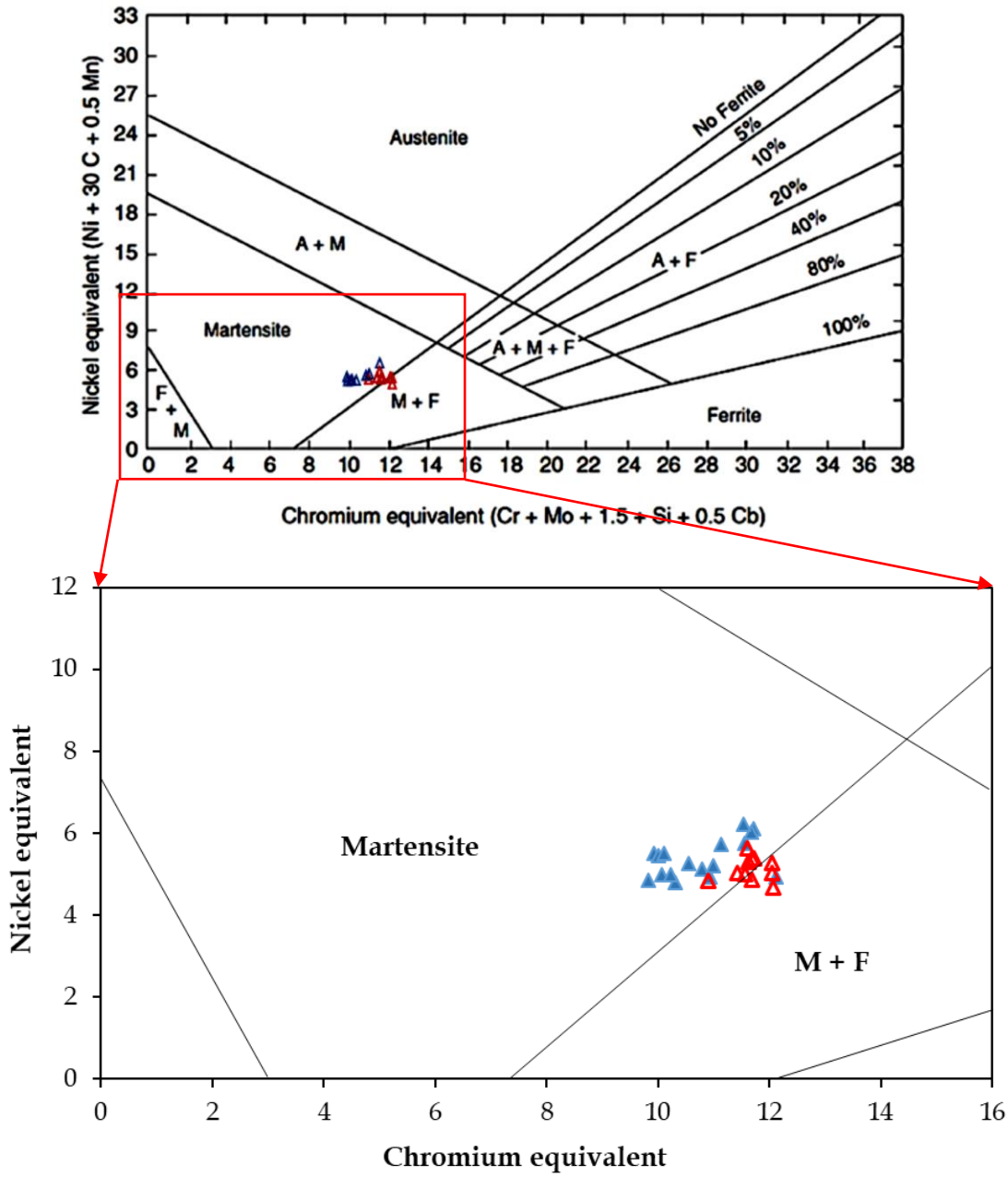

Fig. 9.1 1949 Schaeffler prediction diagram with superimposed Cr_{eq} and Ni_{eq} values calculated from the gas–metal arc weld bead compositions. The red symbols represent weld metal with Cr_{eq} and Ni_{eq} values above the recommended maximum limits, and were predicted to contain delta ferrite. The blue symbols were predicted to be fully martensitic.

Schneider formula: Twelve welds were equal or above the recommended Cr_{eq} of 13.5. Fourteen welds were equal or above the FF limit of 8. Weld PH 3 had FF = 8.1 and AW 7 showed Cr_{eq} = 13.5: both welds comprised a fully martensitic microstructure. Welds AW 2, AW 11, and AW 14 were predicted to be fully martensitic, but delta ferrite was observed in their microstructures. Five welds were incorrectly predicted. The Schneider values in Table 9.1 are superimposed on the Schneider predictive diagram shown on Fig. 9.2.

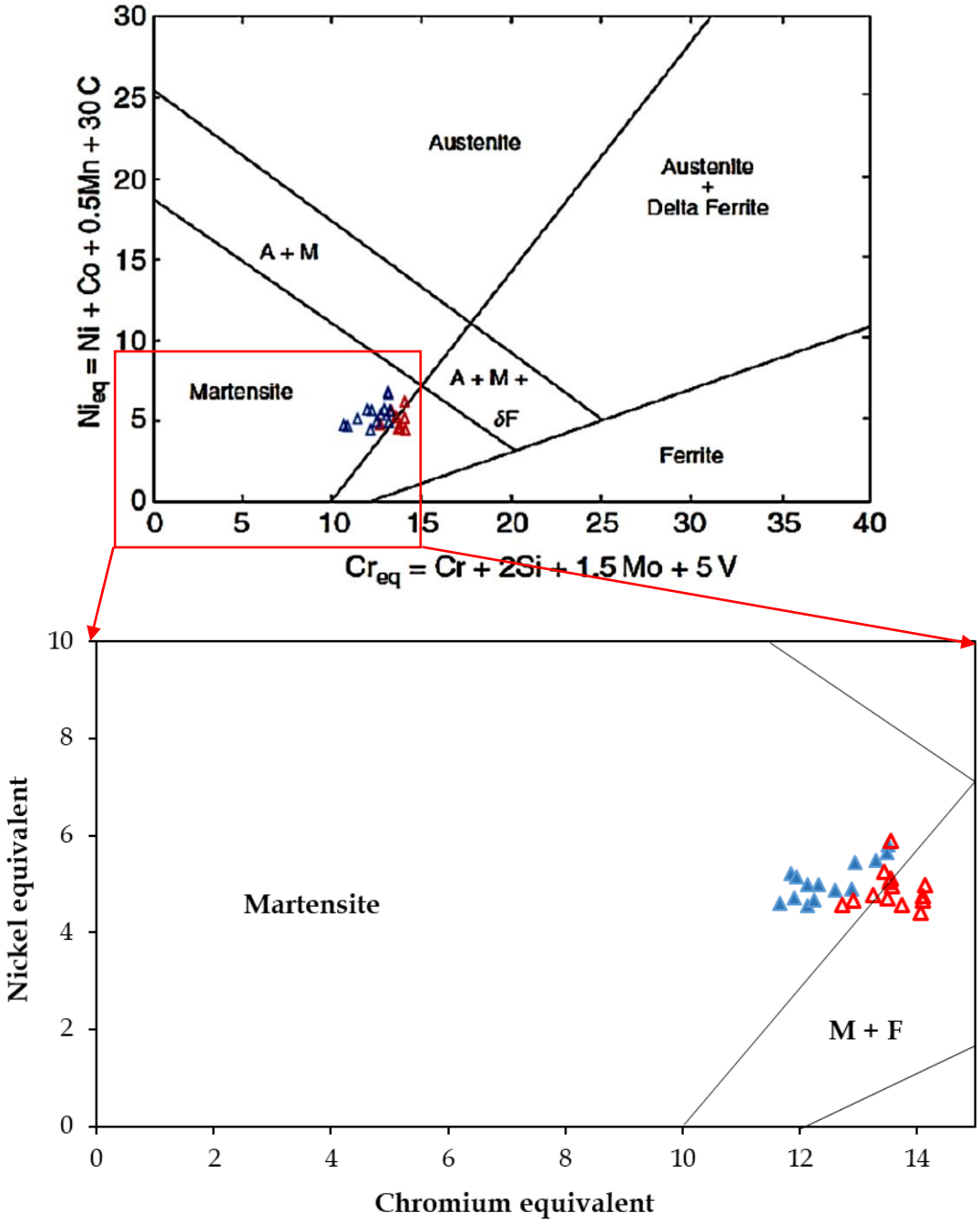

Fig. 9.2 Schneider predictive diagram with superimposed Cr_{eq} and Ni_{eq} values calculated from the gas–metal arc weld compositions. The red symbols represent weld metal with Cr_{eq} and Ni_{eq} values above the recommended maximum limits, and were predicted to contain delta ferrite. The blue symbols were predicted to be fully martensitic.

Kaltenhauser formula and Newhouse CNB: KFF and CNB showed similar predictions. Twelve welds were predicted to contain delta ferrite in their microstructures: eight welds were incorrectly predicted. PH 3 was predicted to contain delta ferrite, yet its microstructure was fully martensitic. Welds PH 4, AW 2, AW 6, AW 11, AW 18, AW 19, and AW 20 were predicted to be fully martensitic, but delta ferrite was observed in their microstructures.

9.3 Summary

(i) Three welds; namely, PH 3, AW 2, and AW 11, were predicted incorrectly by all empirical formulae. PH 3, which received 250°C preheating, consisted of a fully martensitic structure, contrary to prediction. AW 2 and AW 11 were predicted to be fully martensitic, yet delta ferrite was observed in their microstructures.

(ii) Eighteen of 28 welds (64%) were correctly predicted by all empirical formulae.

(iii) In both the Schaeffler and Schneider prediction diagrams, several welds that were predicted to contain delta ferrite (shown by the red symbols) fell within the martensite-only region. This highlights why the Cr_{eq} and Ni_{eq} formulae required modification to improve their predictive accuracy.

Cr_{eq} are plotted against the amount of delta ferrite in Fig. 9.3. For the Schaeffler Cr_{eq}, a steep increase was observed from 11.5, which is below the 12.5 limit recommended by Faulkner [86]. Based on these results, the recommended Schaeffler Cr_{eq} value to limit the presence of delta ferrite in P91 GMA welds should be lowered to 11.5. A steep increase in delta ferrite was observed above the recommended Schneider Cr_{eq} of 13.5, indicated by the broken red line in Fig. 9.3.

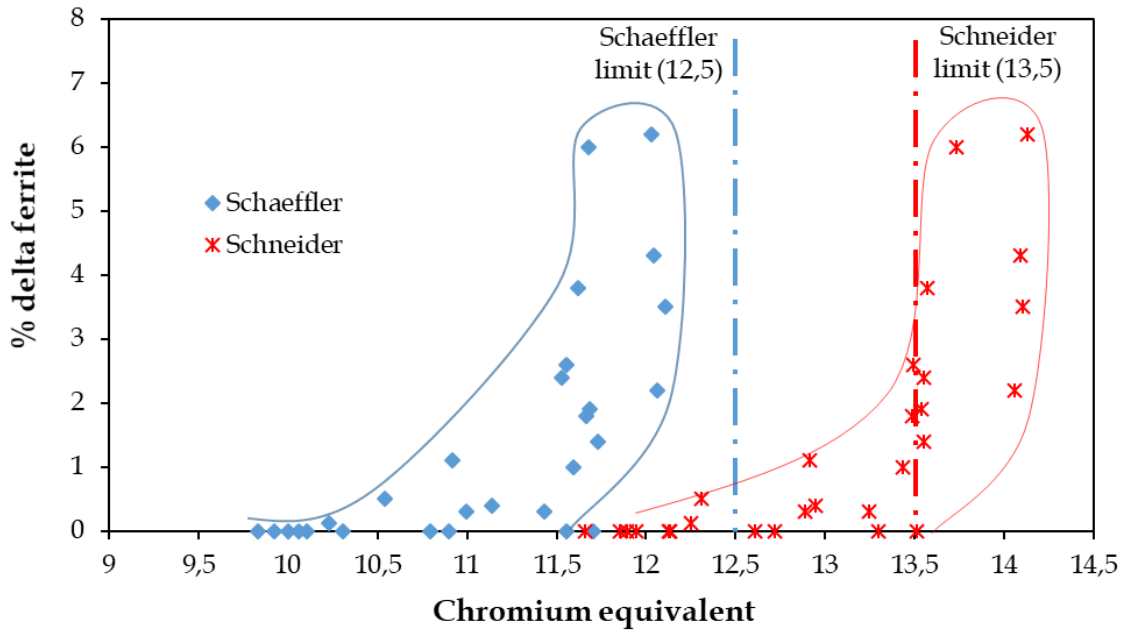

Fig. 9.3 Effect of Cr_{eq} on delta ferrite in deposited gas–metal arc as-welded metal.

Figure 9.4 shows a lot of scatter in the data, but a trend of increasing amount of delta ferrite with KFF and CNB is observed. Several welds with delta ferrite were observed with KFF below the limit of 8, recommended by Sireesha et al. [45]. The results in Fig. 9.4 agree with Barnes et al. [88], who recommended that a KFF limit of 6 is necessary to achieved fully martensitic P91 welds.

Delta ferrite was observed in seven welds with CNB < 10, which is the limit recommended by Swindeman et al. [5].

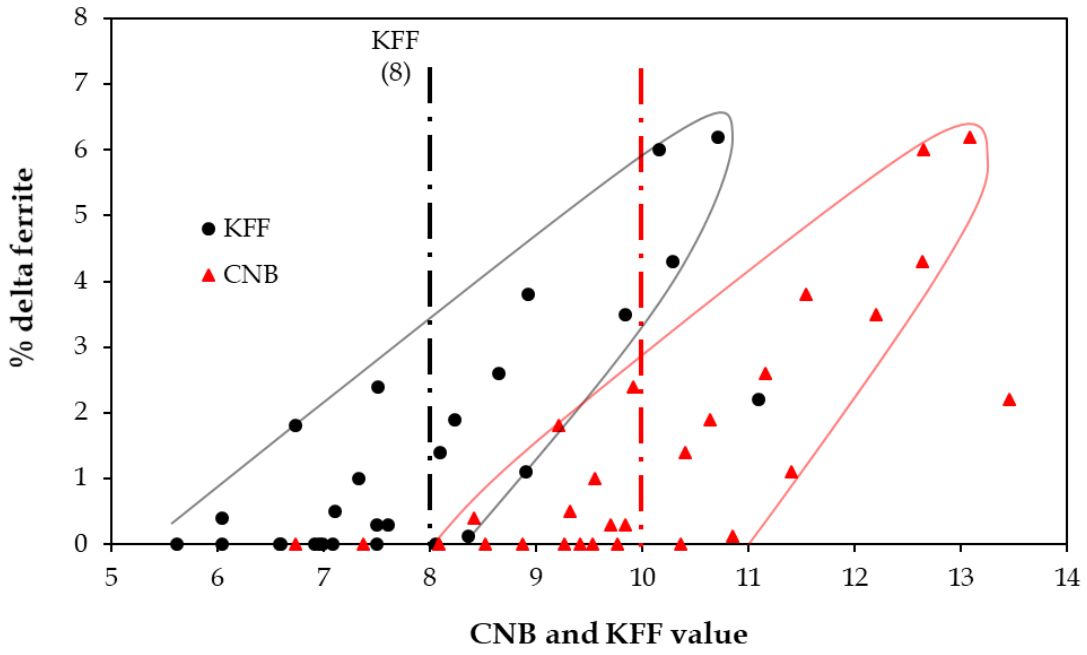

Fig. 9.4 Effect of Kaltenhauser ferrite factor (KFF) and chromium nickel balance (CNB) on delta ferrite in deposited gas–metal arc as-welded metal.

These results show that these empirical formulae cannot exclusively be relied upon to accurately predict weld microstructures with the current recommended limits, especially where small amounts of delta ferrite are probable.

Chapter 10

Effect of post-weld heat treatment on delta ferrite content

10.1 Background

PWHT was performed on five welds for which the microstructure consisted of a martensitic matrix with different amounts of delta ferrite in the as-welded condition. The effect of PWHT temperature on the delta ferrite content and the weld microstructure was investigated. AWS A5.28−96 ER90S−B9 PWHT recommends a maximum temperature of 760°C and minimum hold time of 1 h, depending on the thickness of the P91 weldment. A 760°C PWHT temperature and two additional temperatures of 795°C and 815°C that were above the recommended limit were applied. The specimens were held at specific PWHT temperatures for 2 h.

The selected welds (PH 4, PH 5, AW 10, AW 17, and AW 21) had Ae_1 temperatures ranging from 773°C to 814°C, based on Thermo-Calc results. Figure 10.1 shows where the Ae_1 of the welds were positioned in relation to the three applied PWHT temperatures. The Ae_1 equilibrium temperatures were deemed relevant because PWHT is an isothermal treatment with an extended soak time. When the PWHT temperature exceeds Ae_1, martensite will begin to transform to austenite and then during cooling will convert to untempered martensite, which is hard and brittle. The 795°C PWHT temperature was above the Ae_1 temperatures of AW 21 and PH 4. The 815°C PWHT temperature was above the Ae_1 temperatures of all the welds, except for AW 17. These temperatures were intentionally selected to investigate the response of the weld microstructure in a scenario where the thermal cycle overshoots the PWHT temperature.

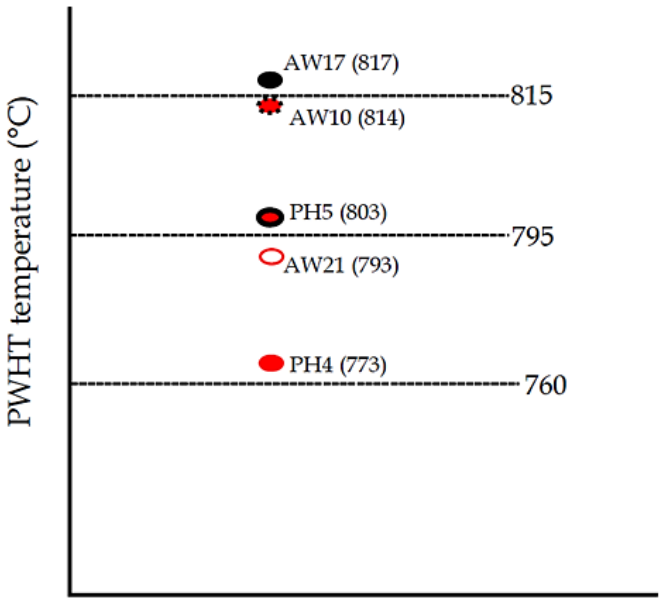

Fig. 10.1 Sketch showing Ae_1 temperatures of the welds in relation to PWHT temperatures.

10.2 Weld metal microstructures after post-weld heat treatment

Table 10.1 lists the selected welds, their delta ferrite volume fraction, and Ae_1 transformation temperature, as calculated using Thermo-Calc software. Figure 10.2 to 10.6 show optical microscopy weld microstructure images in the as-welded condition and after PWHT at 760, 795, and 815°C peak temperatures (500× magnification). All five welds showed a similar response to PWHT.

Table 10.1 *Observed amounts of delta ferrite in as-welded condition and after post-weld heat treatment*

Weld ID **Ae_1 (°C)**	**PWHT condition**	**Delta ferrite (%) (± 95% CI)**
PH 4 (773)	As-welded	0.3 ± 0.1
	760°C	0.3 ± 0.1
	795°C	0.4 ± 0.0
	815°C	0.4 ± 0.1
PH 5 (803)	As-welded	3.5 ± 0.9
	760°C	3.3 ± 0.8
	795°C	3.2 ± 0.7
	815°C	3.2 ± 0.8
AW 10 (814)	As-welded	2.1 ± 0.7
	760°C	2.7 ± 1.0
	795°C	2.8 ± 0.7
	815°C	2.3 ± 0.6
AW 17 (817)	As-welded	6.2 ± 1.2
	760°C	7.8 ± 1.4
	795°C	8.2 ± 1.5
	815°C	6.8 ± 1.9
AW 21 (793)	As-welded	1.7 ± 0.6
	760°C	1.8 ± 0.7
	795°C	1.5 ± 0.5
	815°C	0.9 ± 0.2

Figure 10.2 shows PH 4 weld microstructure images. The microstructure in the as-welded condition comprised untempered martensite with 0.3% delta ferrite. No precipitates were observed. The PWHT microstructure consisted of tempered martensite with delta ferrite; precipitates are seen in the martensitic and along prior austenite grain boundaries (PAGB).

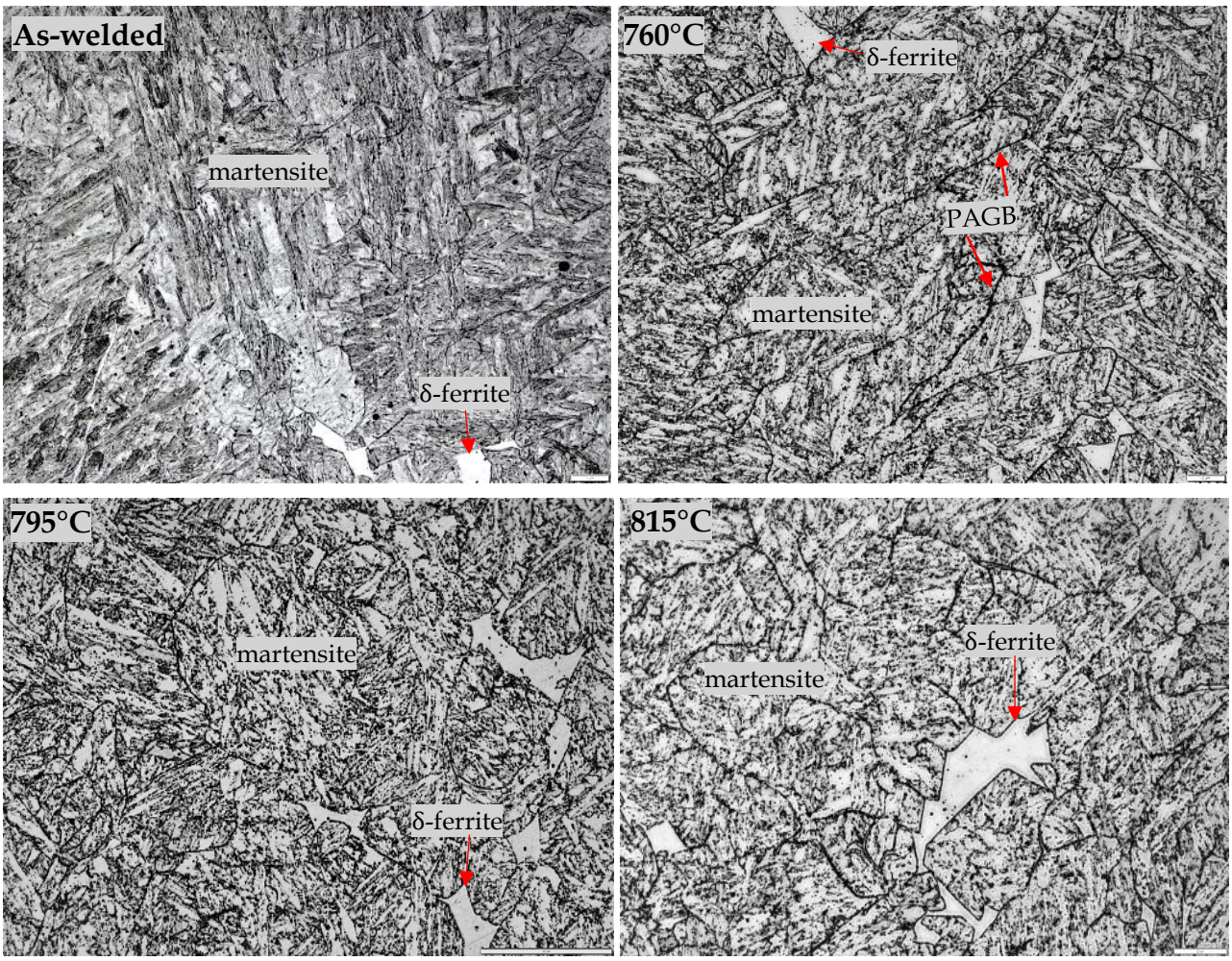

Fig. 10.2 Optical microstructure image of PH 4 in as-welded condition and after post-weld heat treatment (PWHT) at 760, 795, and 815°C peak temperatures. The microstructure in as-welded condition is untempered martensite with 0.3% delta ferrite. The PWHT microstructure consists of tempered martensite with delta ferrite. Precipitates are seen in the martensite structure (500× magnification).

Figure 10.3 shows PH 5 weld microstructure images. The as-welded microstructure comprised untempered martensite with 3.5% delta ferrite. No precipitates were observed. The PWHT microstructure consisted of tempered martensite with delta ferrite. Precipitates were seen in the martensitic and along PAGB. No precipitates observed in the delta ferrite phase, even after PWHT.

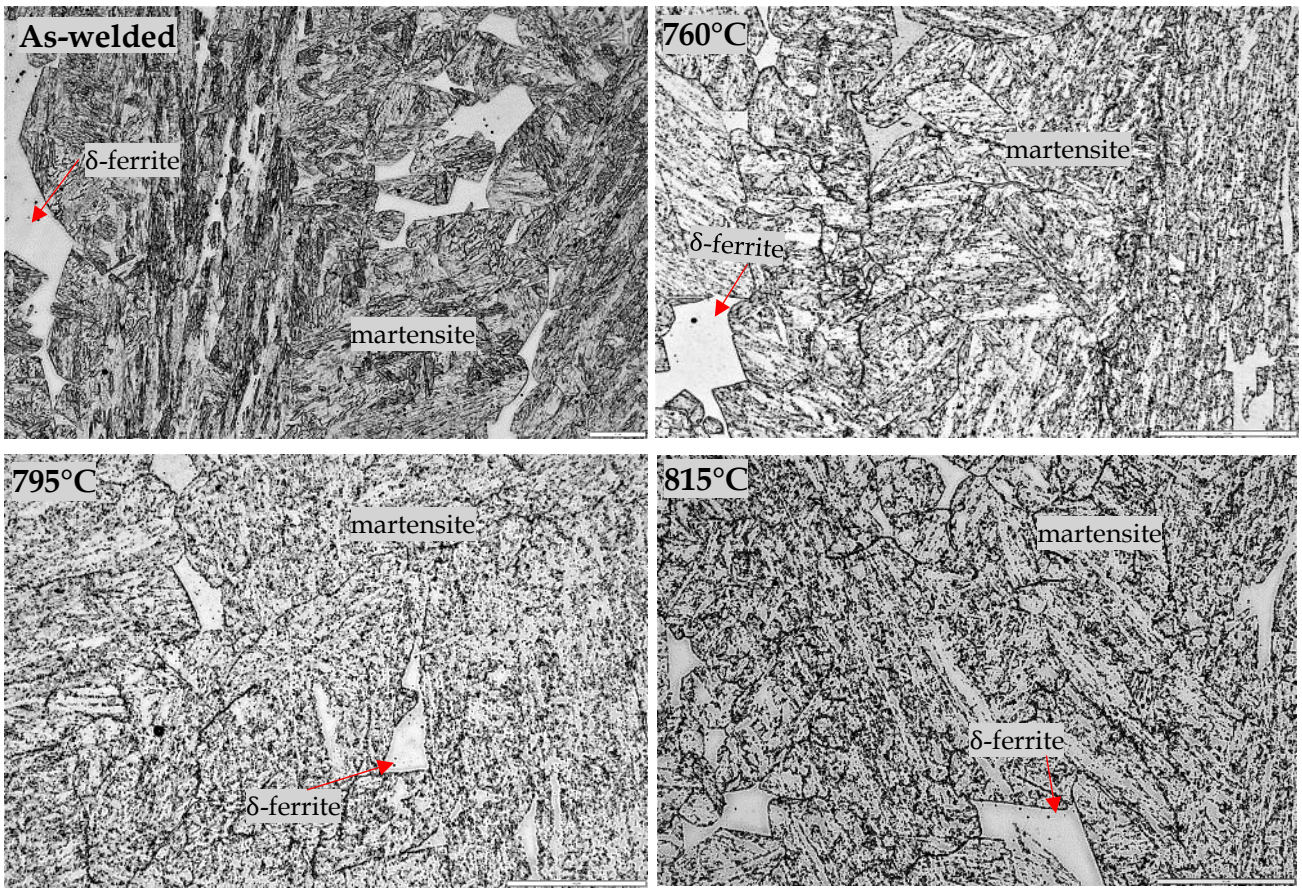

Fig. 10.3 Optical microstructure image of PH 5 in as-welded condition and after post-weld heat treatment (PWHT) at 760, 795, and 815°C peak temperatures. The microstructure in as-welded condition is untempered martensite with 3.5% delta ferrite. The PWHT microstructure consists of tempered martensite with delta ferrite. Precipitates are seen in the martensite (500× magnification).

Figure 10.4 shows AW 10 weld microstructure images. The microstructure in the as-welded condition was untempered martensite with 2.1% delta ferrite. No precipitates were observed. The PWHT microstructure consisted of tempered martensite with delta ferrite. Precipitates were seen in the martensitic and along PAGB. No precipitates were observed in the delta ferrite phase, even after PWHT.

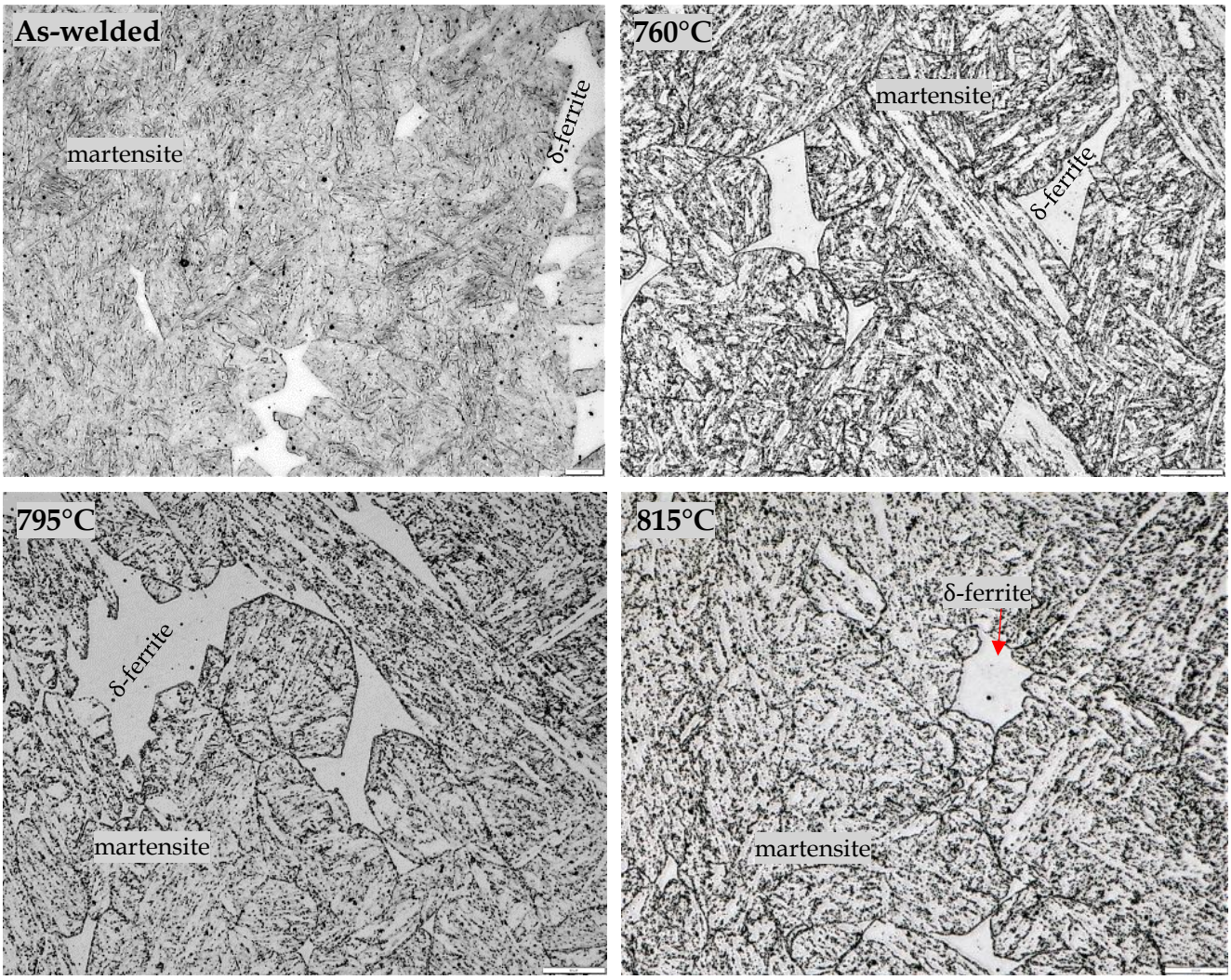

Fig. 10.4 Optical microstructure image of AW 10 in as-welded condition and after post-weld heat treatment (PWHT) at 760, 795, and 815°C peak temperatures. The microstructure in as-welded condition is untempered martensite with 2.1% delta ferrite. The PWHT microstructure consists of tempered martensite with delta ferrite. The precipitation population appears to increase with temperature (500× magnification).

Figure 10.5 shows AW 17 weld microstructure images. The as-welded microstructure consisted of untempered martensite with 6.2% delta ferrite. No precipitates were observed. The PWHT microstructure comprised tempered martensite with delta ferrite. Precipitates are seen in the martensitic and along PAGB. No precipitates were observed in the delta ferrite phase, even after PWHT.

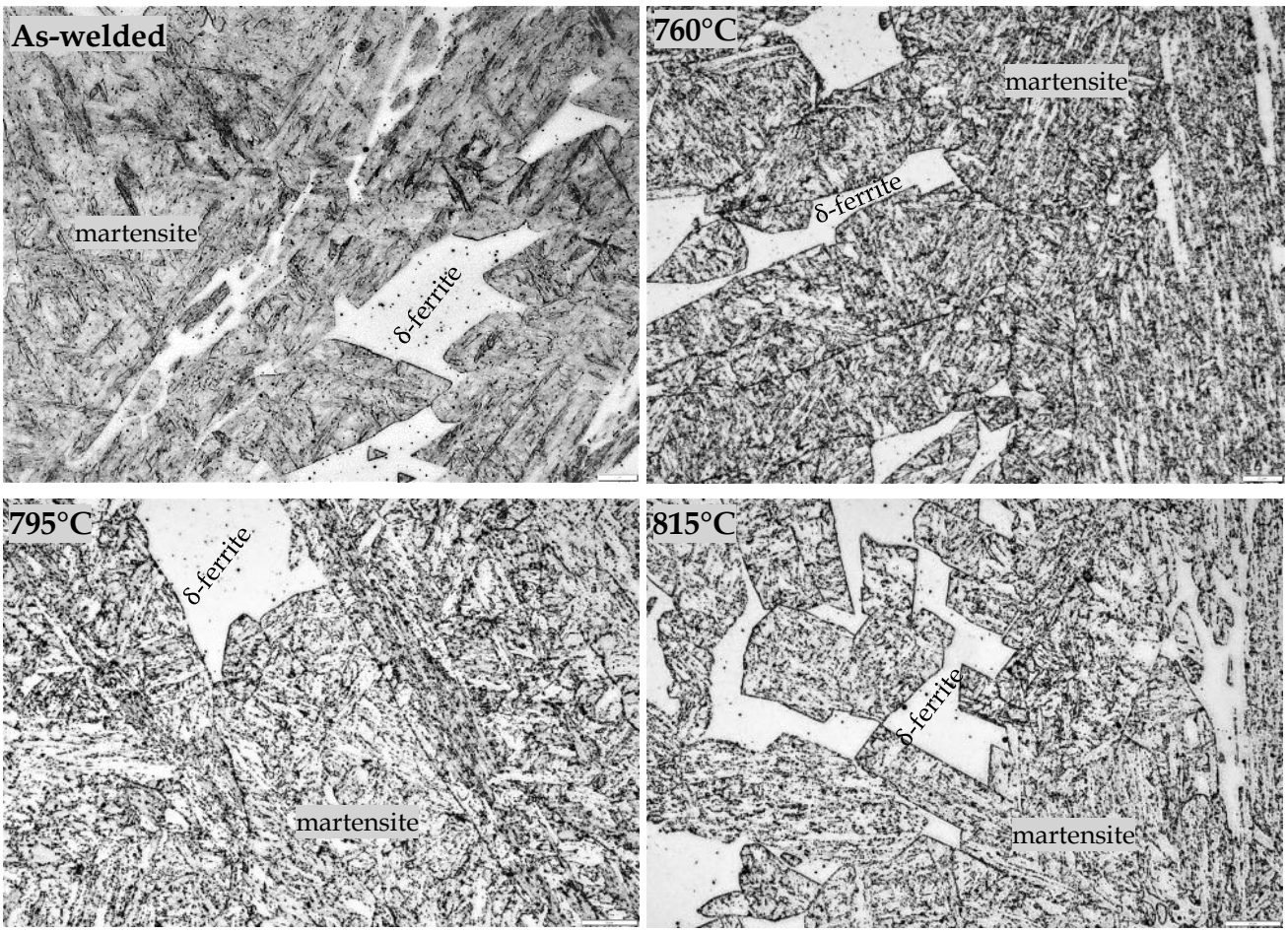

Fig. 10.5 Optical microstructure image of AW 17 in as-welded condition and after post-weld heat treatment (PWHT) at 760, 795, and 815°C peak temperatures. The microstructure in as-welded condition is untempered martensite with 6.2% delta ferrite. The PWHT microstructure consists of tempered martensite with delta ferrite (500× magnification).

Figure 10.6 shows AW 21 weld microstructure images. The microstructure in the as-welded condition consisted of untempered martensite with 1.7% delta ferrite. No precipitates were observed. The PWHT microstructure comprised tempered martensite with delta ferrite. Precipitates are seen in the martensitic and along PAGB. No precipitates were observed in the delta ferrite phase, even after PWHT.

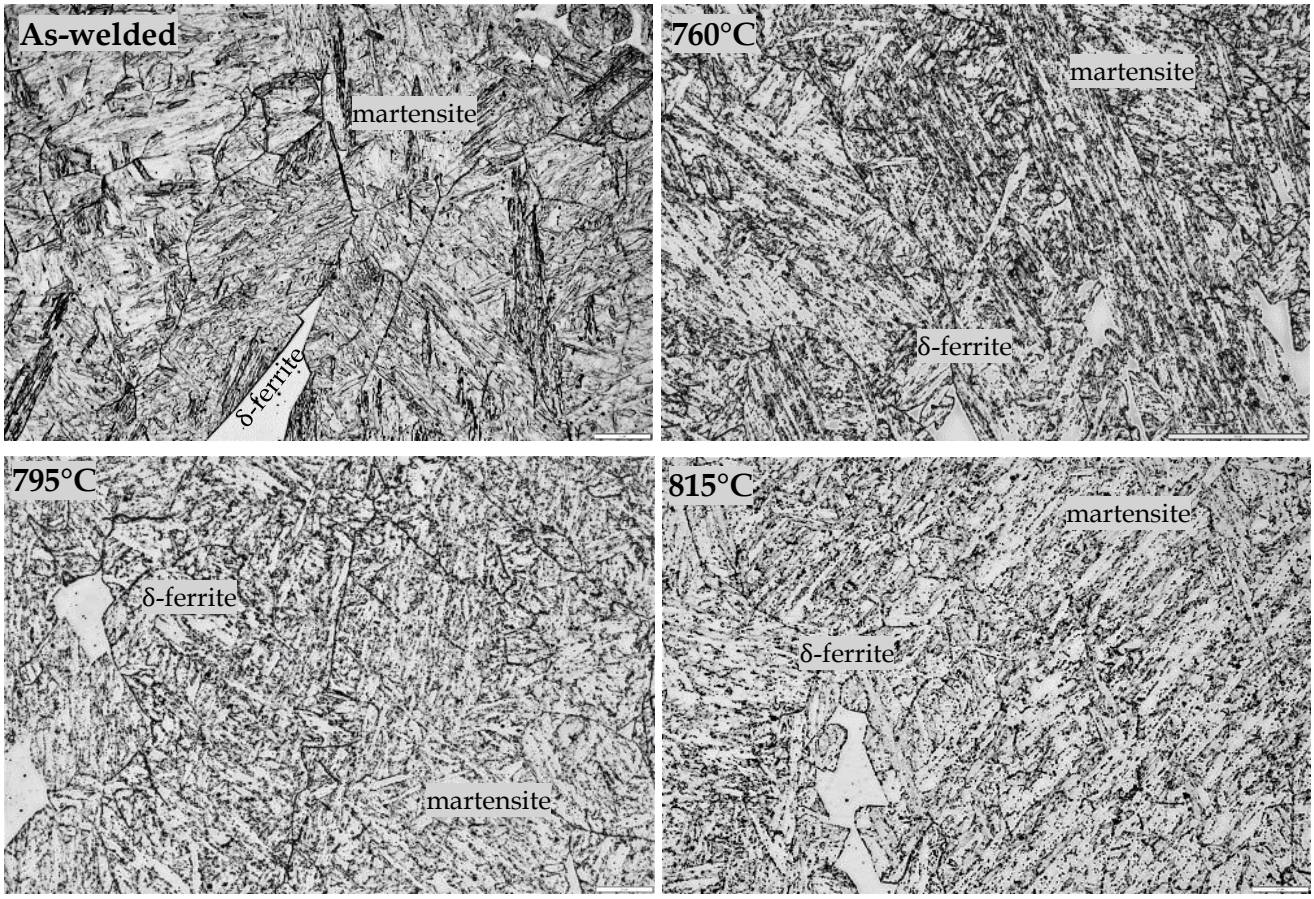

Fig. 10.6 Optical microstructure image of AW 21 microstructure in as-welded condition and after post-weld heat treatment (PWHT) at 760, 795, and 815°C peak temperatures. The microstructure in as-welded condition is untempered martensite with 1.7% delta ferrite. The PWHT microstructure consists of tempered martensite with delta ferrite (500× magnification).

SEM microstructure images of weld (AW 10) in as-welded condition and after PWHT are shown in Fig. 10.7. There were significant precipitates in the martensite and along PAGB after PWHT. No precipitates were visible in the delta ferrite phase. PWHT did not change the amount of delta ferrite as can be seen in Fig. 10.11.

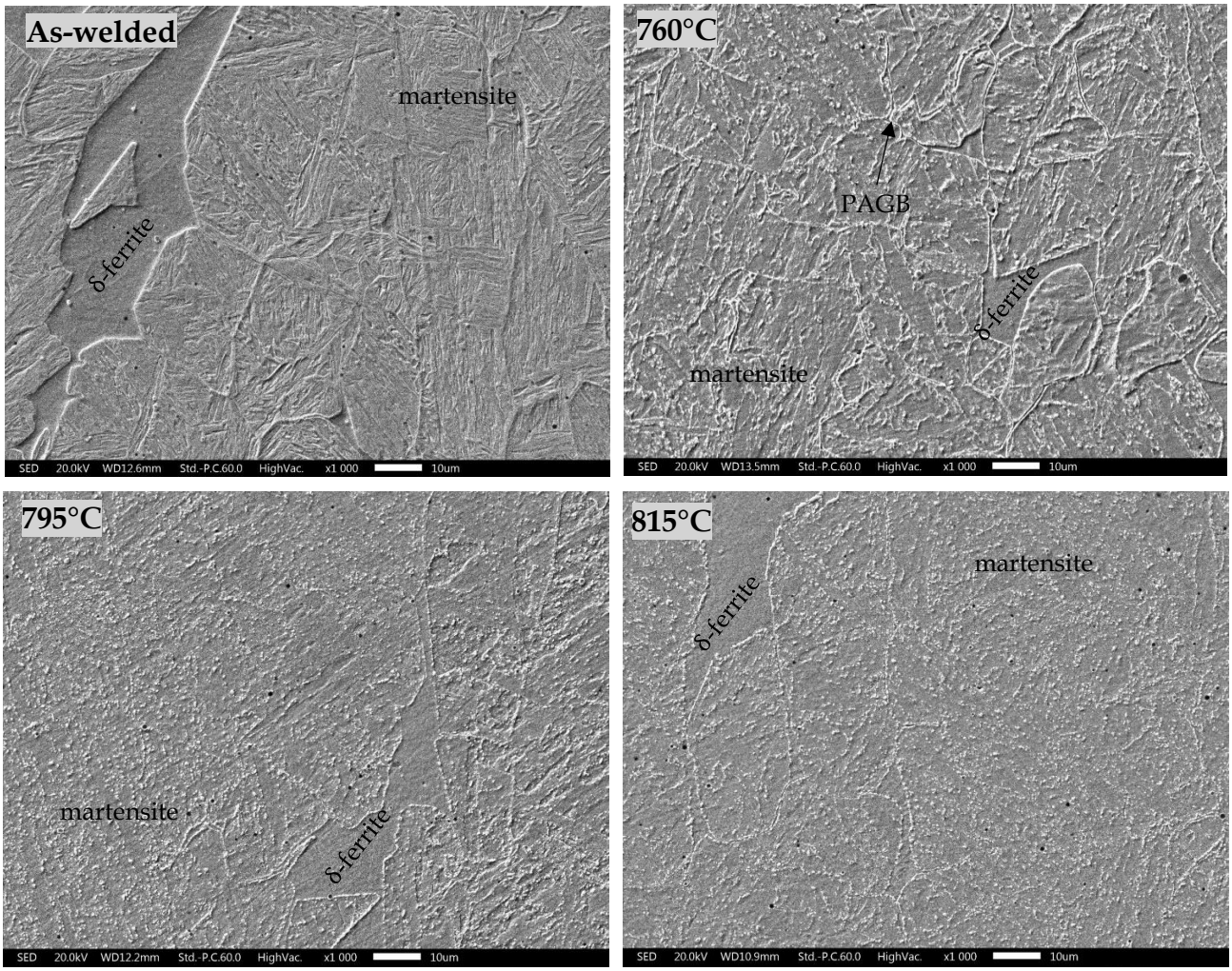

Fig. 10.7 Scanning electron microscopy images of AW 10 microstructure in as-welded condition and after post-weld heat treatment (PWHT) at 760, 795, and 815°C peak temperatures. The microstructure in as-welded condition is untempered martensite with 2.2% delta ferrite and has no visible precipitates. The PWHT microstructure consists of tempered martensite with delta ferrite. The number of precipitates appears to increase with temperature between 760 and 795°C. The Ae_1 temperature was 814°C (1000× magnification).

Figure 10.8 shows higher magnification (2000×) images of the AW 10 microstructure at 760°C and 815°C PWHT, highlighting the difference in precipitate populations and morphologies of the tempered martensite. The martensite laths at 760°C are still distinguishable.

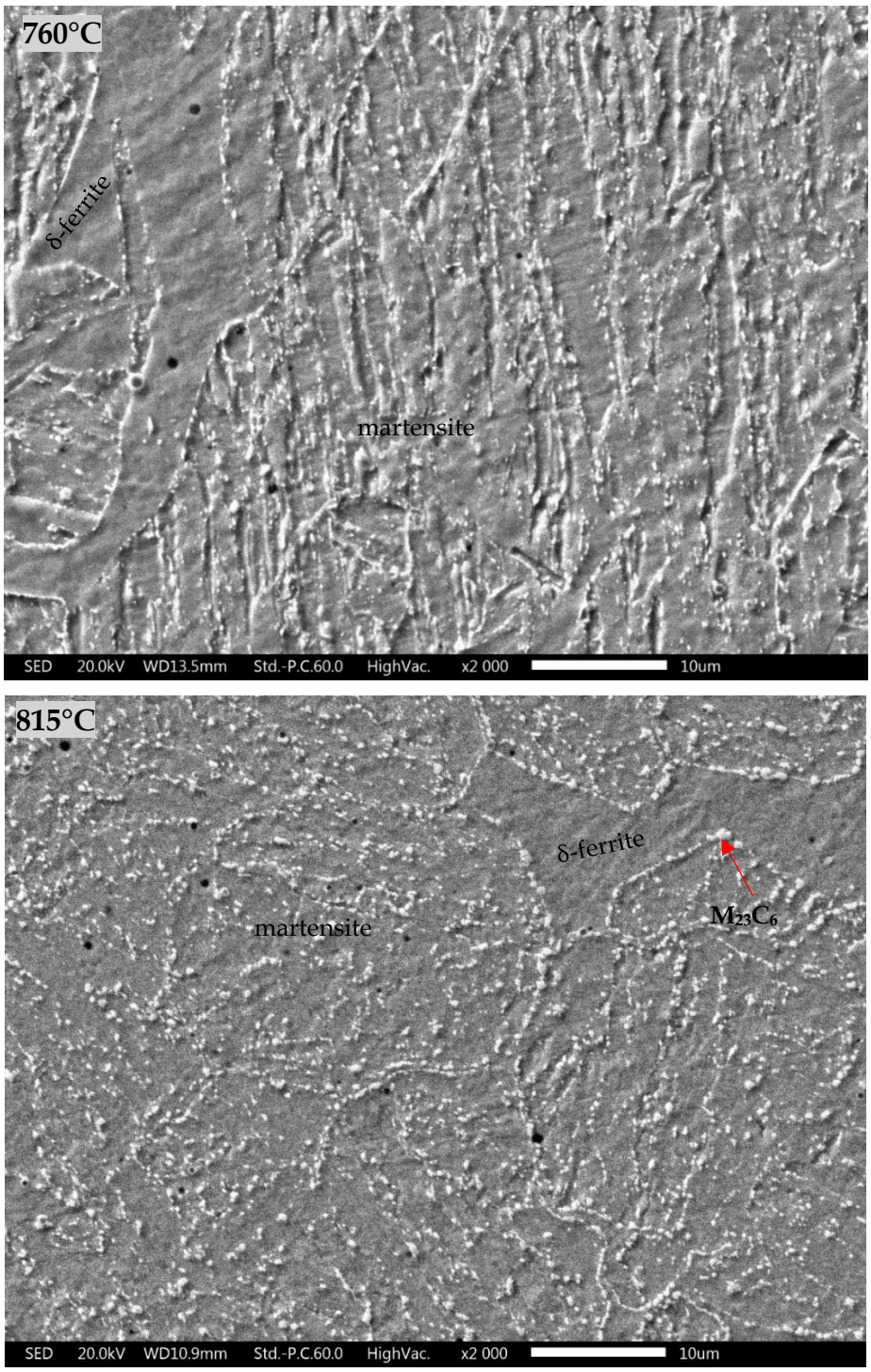

Fig. 10.8 Scanning electron microscopy images of AW 10 microstructures at 760°C and 815°C post-weld heat treatment (2000× magnification)

Examining the influence of the PWHT temperature on P91 weld temper response based on the Ae_1 temperature, Fig. 10.9 compares the microstructures of PH 4 (Ae_1: 773°C) and AW 17 (Ae_1: 817°C) following PWHT at 760°C and 815°C.

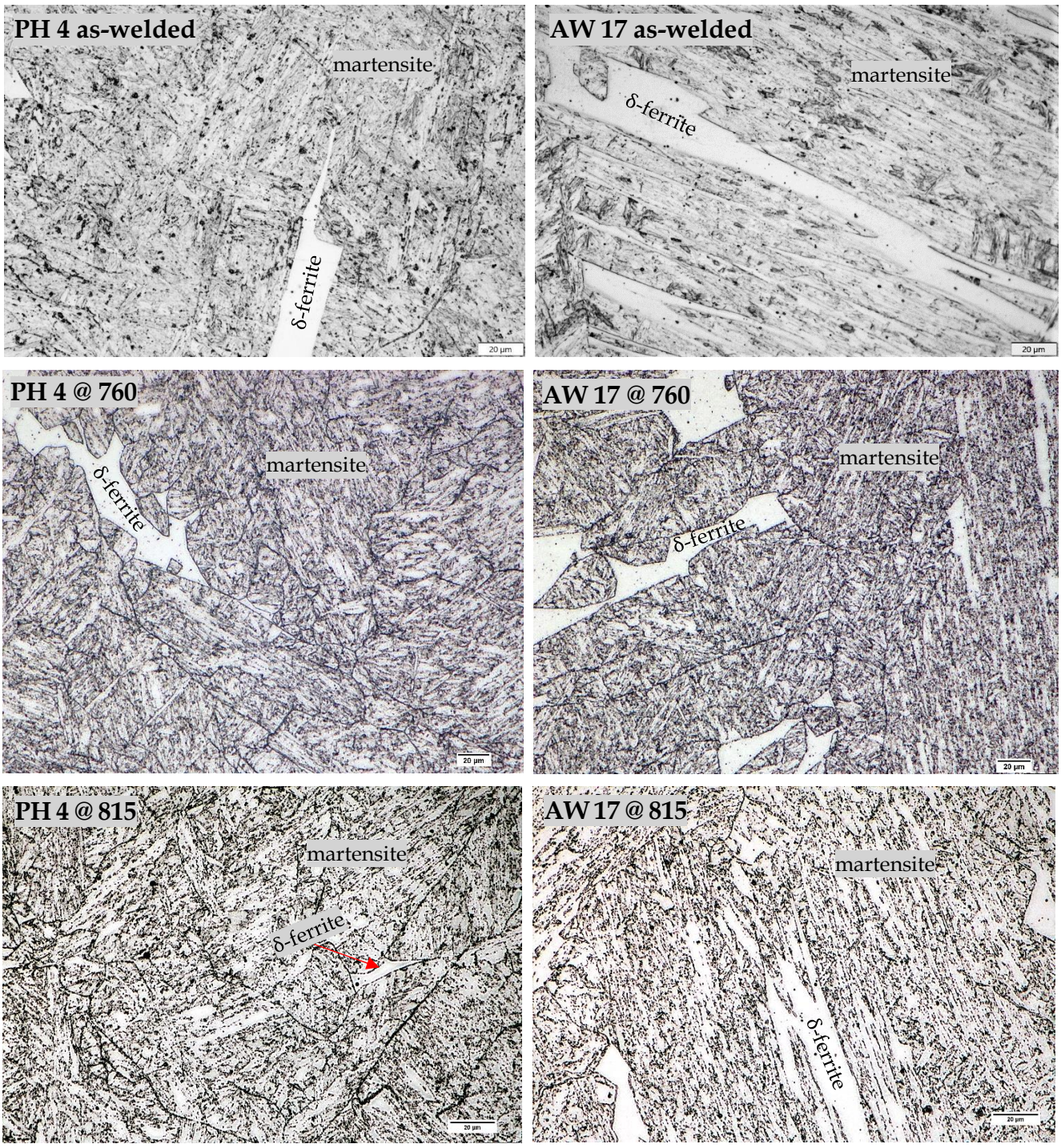

Fig. 10.9 Optical microstructure images of PH 4 and AW 17 weld beads in as-welded condition and following post-weld heat treatment (PWHT) at 760 and 815°C. The microstructures of both welds consist of a martensitic matrix with delta ferrite. Both welds showed significant precipitates in the martensite structure after PWHT (500× magnification).

10.2.1 Analysis of weld microstructural response to post-weld heat treatment

No precipitates were observed in the as-welded condition, in accordance with reports of Pandey et al. [24], who observed no precipitates in P91 steel in normalised condition before temper treatment. All PWHT welds consisted of a tempered martensitic matrix with carbo-nitride precipitates, as shown in Fig. 10.10. Precipitates were only observed in the martensite phase, mainly along PAGB, sub-grain boundaries, and between martensite laths after 760°C PWHT. The precipitates experienced coarsening and increased in population density with increasing PWHT temperature between 760 and 815°C, as seen in the SEM images in Fig. 10.10. The precipitate distribution within the tempered martensite at 815°C was random in nature and not aligned with any boundaries. No precipitates were observed in the delta ferrite phases.

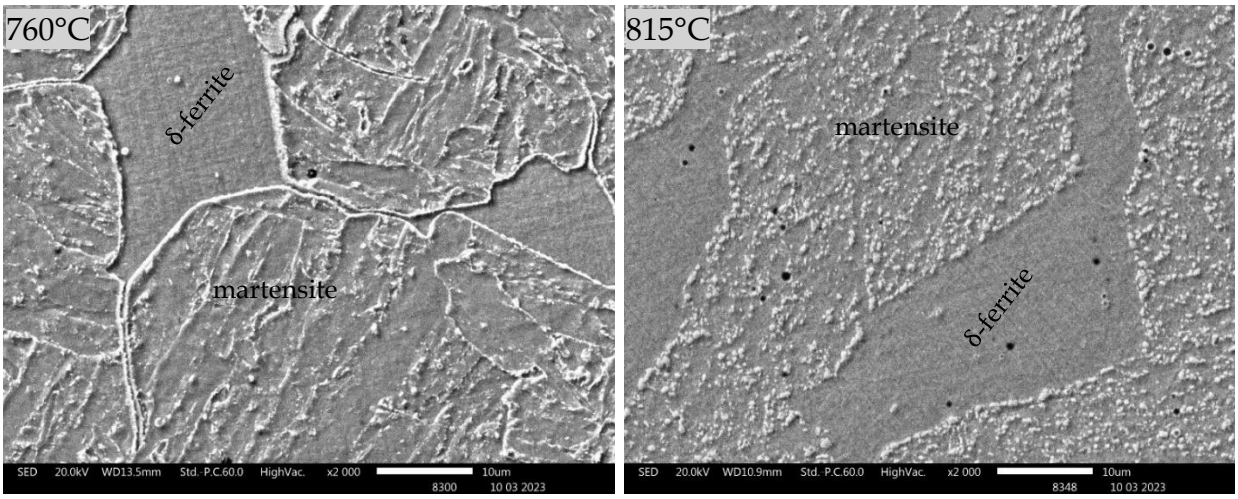

Fig. 10.10 Scanning electron microscopy images of AW 10 microstructure after post-weld heat treatment at 760 and 815°C. The microstructure consists of tempered martensitic matrix decorated with precipitates and delta ferrite (2000× magnification).

Figure 10.11 shows the delta ferrite content in the as-welded condition and after PWHT. Based on the observed amount of delta ferrite, PWHT did not influence the amount of delta ferrite, even at temperatures that exceeded the Ae_1 temperature of the weld. The differences in the amounts of delta ferrite observed between the PWHT conditions is likely due to slight variations in composition along the bead length where the specimens were sectioned as shown in Chapter 7. Weld AW 17 showed most variation in delta ferrite phase fraction with PWHT temperature, which agrees with the results reported in Section 7.2.2, where this weld showed most composition inhomogeneity along the bead length.

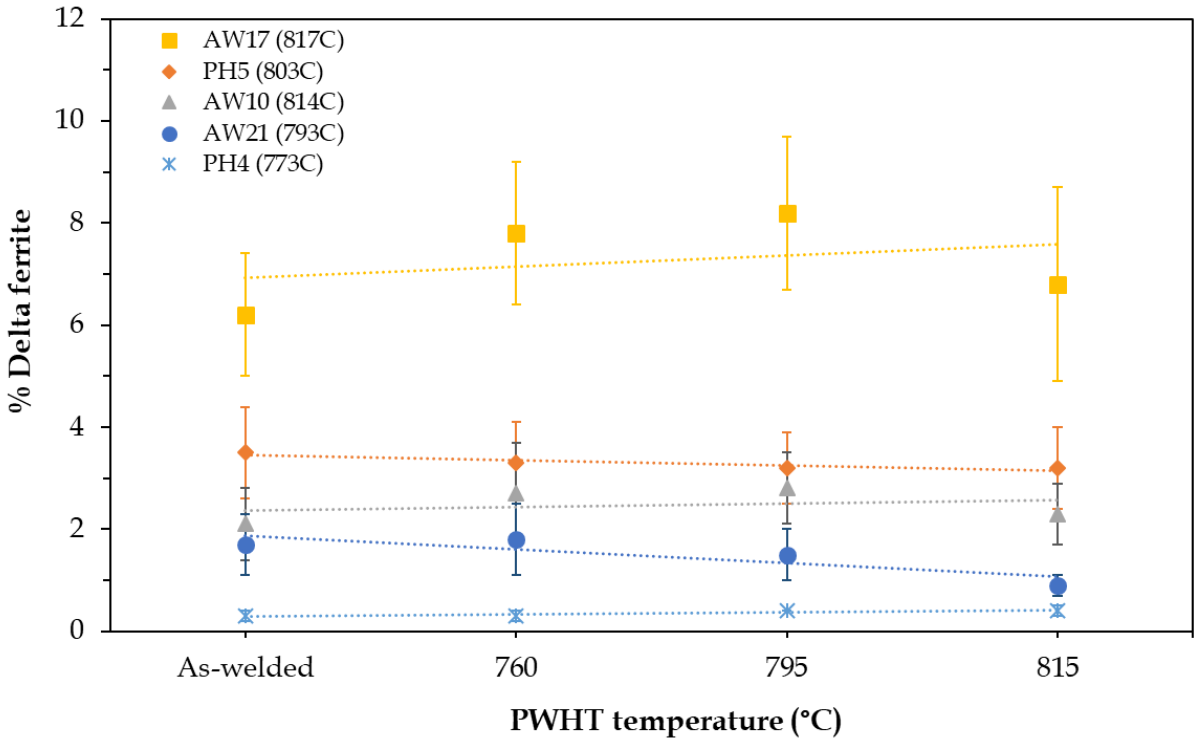

Fig. 10.11 Amount of delta ferrite observed at different post-weld heat treatment temperatures. Ae_1 temperatures are shown in the legend. Remove connecting line

The 815°C PWHT exceeded the weld PH 4 Ae_1 temperature (773°C) by 42°C, yet the observed amount of delta ferrite remained the same as in the as-welded condition. Mayr et al. [23] reported a difference of approximately 50°C between calculated Matcalc equilibrium transformation temperatures and those measured by dilatometry. Mayr et al. [20] attributed the transformation temperature difference to the fact that the ferrite/austenite transformation is diffusion-governed and is strongly kinetically controlled under non-equilibrium conditions.

Above the Ae_1 temperature, ferrite becomes stable and formation of alpha ferrite can occur. This is expected to result in increased amount of ferrite, but this was not observed in these experiments. Other expected transformations above the Ae_1 temperature are the precipitation and coarsening of Cr-rich $M_{23}C_6$ on the martensite lath and PAGB, replacing the M_7C_3 and M_2X (X = C,N) precipitates and the martensite/austenite transformation.

10.3 Hardness of post-weld heat-treated specimens

Vickers hardness measurements were performed in the PWHT specimens using 10 kg.f load and 10 s dwell time. The average hardness of specimens in as-welded condition and after PWHT at 760, 795, and 815°C with soaking time of 2 h are shown in Table 10.2. The corresponding changes in average hardness are shown in Fig. 10.12, in which published P91 weld hardness results from two authors are incorporated: Arivazhagen et al. [42] (as-welded and after 760°C PWHT) and Merchant [43] (720, 740, 760°C PWHT). Hardness in the as-welded condition ranged from 380 to 428 Hv_{10}. Significant softening was observed after PWHT to a hardness from 203 to 253 Hv_{10}. A muted

hardness decrease from 250 to 212 Hv_{10} was observed with increasing PWHT temperature from 760 to 815°C. The hardness of P91 welds in as-welded condition and after PWHT are typical of values reported in literature.

Table 10.2 *Delta ferrite average micro-Vickers hardness in as-welded beads*

Weld ID	***PWHT condition***	***Average hardness (95% CI)***
PH 4	As-welded	403 ± 4
	760°C	251 ± 2
	795°C	223 ± 1
	815°C	218 ± 1
PH 5	As-welded	381 ± 5
	760°C	253 ± 3
	795°C	224 ± 2
	815°C	204 ± 2
AW 10	As-welded	409 ± 1
	760°C	249 ± 4
	795°C	225 ± 2
	815°C	221 ± 2
AW 17	As-welded	388 ± 13
	760°C	251 ± 3
	795°C	226 ± 3
	815°C	216 ± 2
AW 21	As-welded	428 ± 9
	760°C	242 ± 2
	795°C	223 ± 2
	815°C	203 ± 2

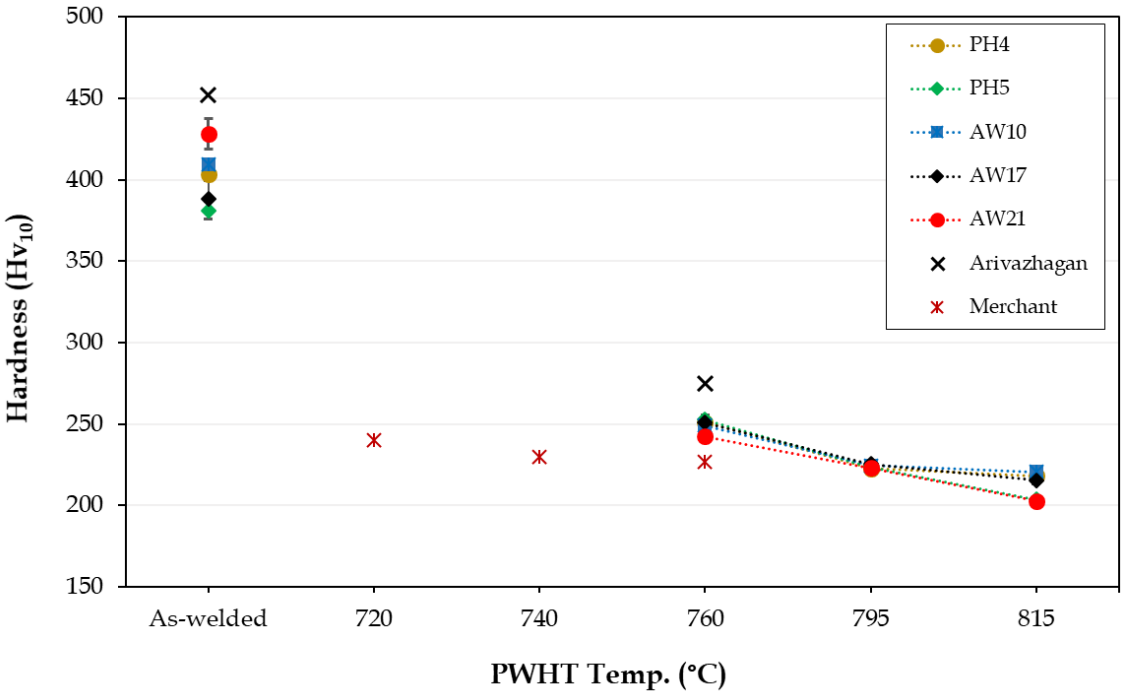

Fig. 10.12 Vickers hardness (Hv_{10}) of specimens at different PWHT temperatures. Five measurements were performed for each specimen. Hardness values published by Arivazhagen et al. [42] and Merchant [43] are shown.

The decrease in hardness with increase in PWHT temperature is due to the precipitation of Cr, Mo, Mn, and V in the matrix to form MX and $M_{23}C_6$ precipitates (X = C,N). The increased density and coarsening of the carbo-nitride precipitates with higher PWHT temperature reduces the solid-solution strengthening effect of C and N. The 795 and 815°C temperature overshoots the AWS A5.28−96 (ER90S−B9) PWHT recommended maximum temperature of 760°C, resulting in muted hardness softening. When PWHT temperature exceeds the lower critical temperature (Ae_1), a martensitic weld will begin to transform to austenite and, upon cooling, the austenite will convert to untempered martensite. No significant effect on hardness was observed.

Chapter 11

Effect of thermal cycle on delta ferrite in a multi-pass weld

11.1 Introduction

The effect of weld thermal cycle on delta ferrite when a subsequent bead is deposited in a multiple-pass weld was examined using Gleeble experiments. Five welds that contained delta ferrite in the as-welded condition were selected. Table 11.1 lists the selected welds, their delta ferrite volume fraction in the as-welded condition, and weld transformation temperatures calculated using Thermo-Calc software.

Table 11.1 *Welds selected for Gleeble experiments and their transformation temperatures*

Weld ID	***Delta ferrite (%) (± 95% CI)***	***Equilibrium transformation temperatures (°C)***			
		Ae_1	**Ae_3**	**Ae_4**	**Ae_5**
PH 5	3.5 ± 0.9	803	887	1157	1375
AW 9	3.8 ± 0.6	810	866	1213	1383
AW 16	6.0 ± 1.1	817	883	1184	1374
AW 18	1.8 ± 0.4	784	847	1232	1400
AW 21	2.6 ± 0.6	793	857	1209	1381

11.2 Thermal cycle

The following peak temperatures were selected for thermal treatment of the selected welds:

- 1350°C: between the (Ae_4 − Ae_5) temperatures
- 1100°C: midway between the (Ae_3 − Ae_4) temperatures
- 900°C: just above the Ae_3 temperature

Heating and cooling rates of 300°C/s and 25°C/s, respectively, were applied. The programmed thermal cycles and actual thermal curves are shown in Fig. 11.1 for the 1100°C peak temperature cycles. There was a deviation of the actual thermal treatments from the programmed cycles experienced by the Gleeble specimens due to the limited instrument capabilities. The actual cooling rates reported in Table 11.2 were calculated from the recorded peak temperature to 700°C. The value of $\Delta t_{12\text{-}8}$ was not used to calculate the cooling rate because some of peak temperatures were as low as 840°C.

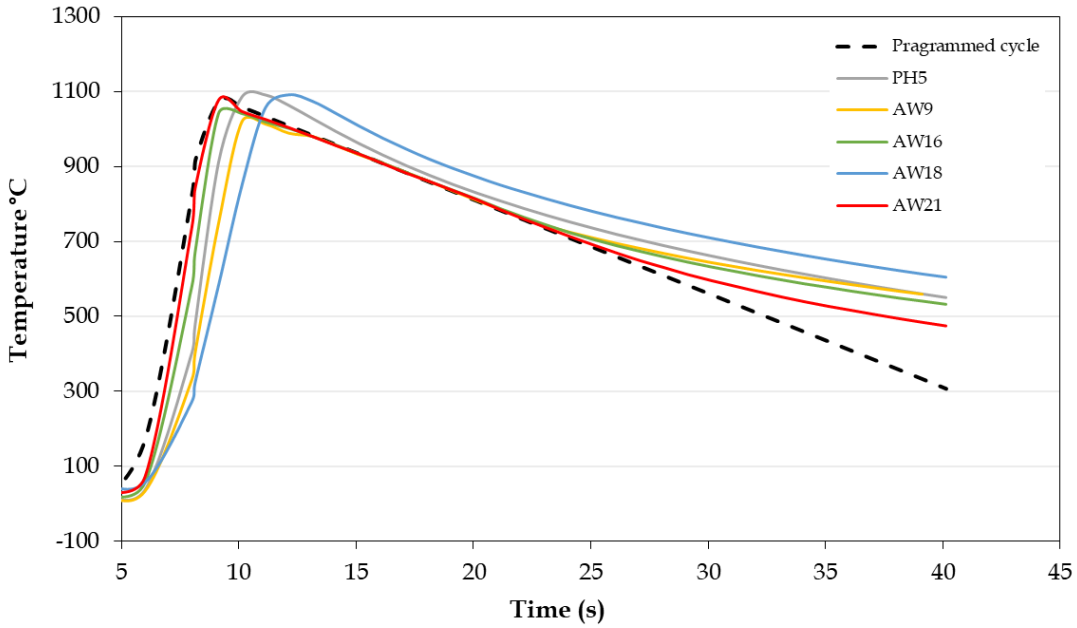

Fig. 11.1 Gleeble thermal curves at 1100°C peak temperature.

Table 11.2 shows the recorded peak temperature, cooling rate, and amount of delta ferrite observed in the thermally treated specimens.

Table 11.2 *Actual peak temperature, cooling rate achieved during the thermal treatment, and delta ferrite content*

Weld ID (as-welded δ-ferrite)	*Peak temperature* (°C)*	*Cooling rate (°C/s)*	*Delta ferrite (%)*
PH 5 (3.5)	880 (900)	24.6	2.2 ± 0.8
	1092 (1100)	26.1	1.0 ± 0.4
	1296 (1350)	24.3	0.0
AW 9 (3.8)	891 (900)	15.9	1.5 ± 0.6
	1021 (1100)	23.2	0.0
	1273 (1350)	23.8	0.0
AW 16 (6.0)	841 (900)	18.9	5.1 ± 1.4
	1042 (1100)	21.3	1.5 ± 0.3
	1263 (1350)	21.2	0.0
AW 18 (1.8)	936 (900)	26.2	0.0
	1091 (1100)	24.6	0.0
	1238 (1350)	20.1	0.0
AW 21 (2.6)	890 (900)	28.7	0.9 ± 0.2
	1078 (1100)	24.2	0.0
	1247 (1350)	24.4	0.0

* *Values in brackets are the actual programmed peak temperatures*

Figure 11.2 shows the peak temperature achieved against the programmed temperature during the Gleeble thermal cycles.

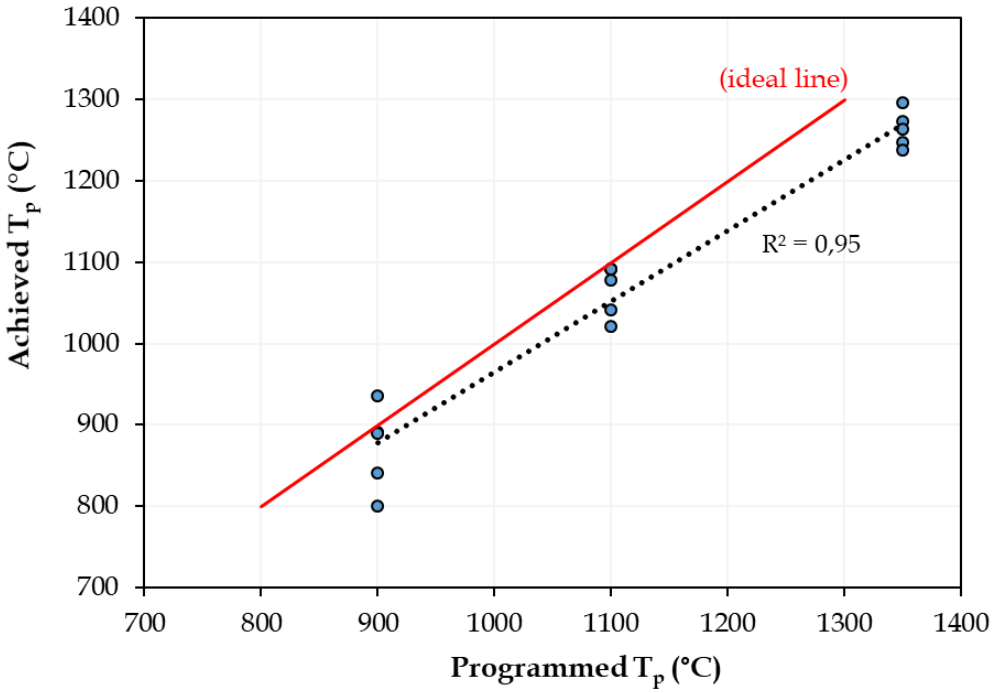

Fig. 11.2 Achieved peak temperature plotted against programmed peak temperature of Gleeble instrument.

11.3 Gleeble microstructures

Figure 11.3 to 11.7 show optical microscopy weld microstructure images in the as-welded condition and after Gleeble treatment at 900, 1100, and 1350°C target peak temperatures (100× magnification).

The PH 5 microstructure (Figure 11.3) in the as-welded condition consisted of martensite with 3.5% delta ferrite. At 880°C Gleeble peak temperature, it was tempered martensite with 2.2% delta ferrite. At 1092°C peak temperature, the microstructure consisted of an untempered martensitic matrix with 1.0% delta ferrite. A fully untempered martensitic structure was observed at 1296°C peak temperature.

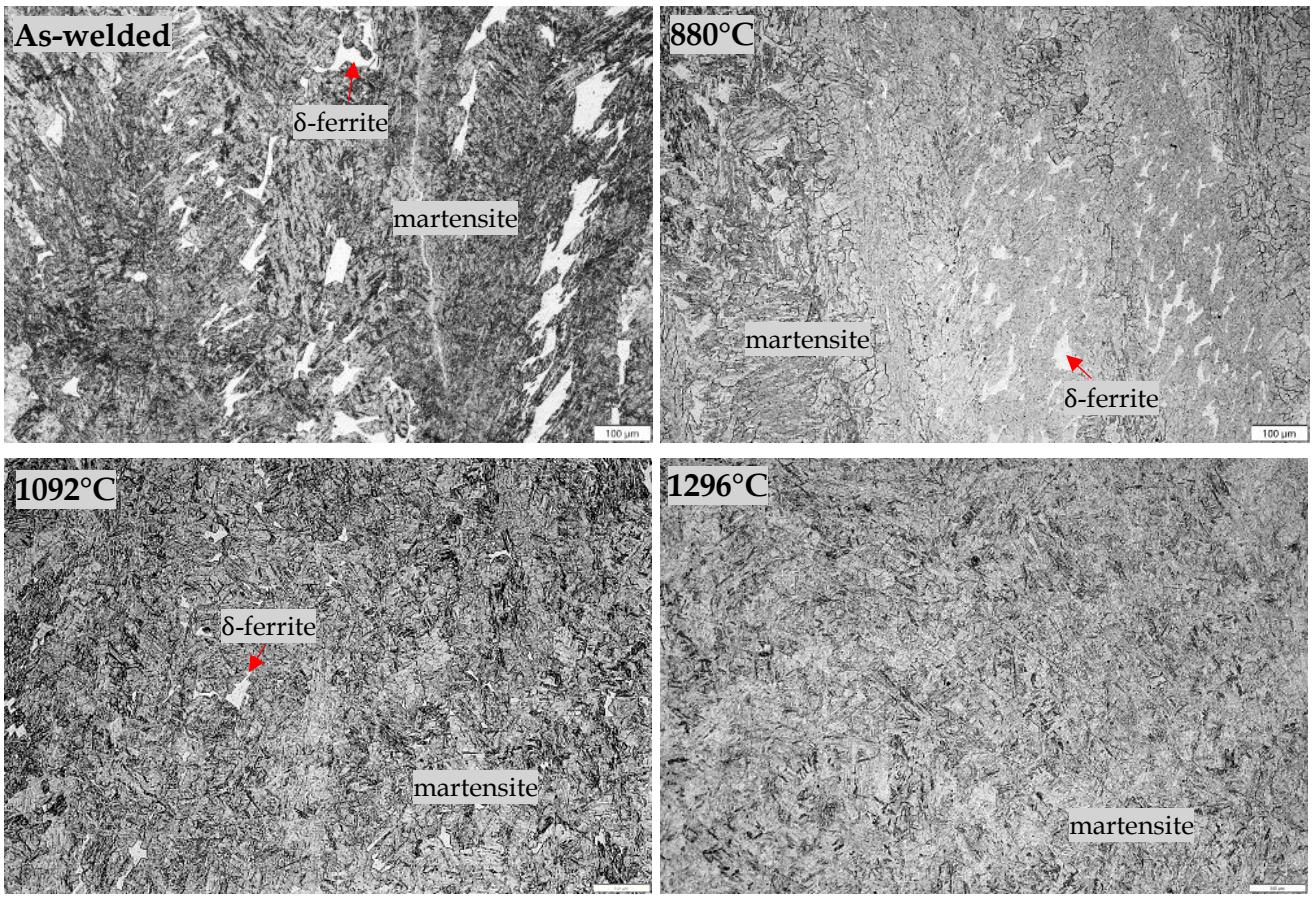

Fig. 11.3 Optical microstructure images of PH 5 microstructure in as-welded condition and after Gleeble thermal treatment. The microstructure in the as-welded condition consisted of martensite with 3.5% delta ferrite. At 880°C, the microstructure consisted of tempered martensite with 2.2% delta ferrite. At 1092°C peak temperature, the microstructure consisted of an untempered martensitic matrix with 1.0% delta ferrite. At 1296°C peak temperature, a fully untempered martensitic structure was observed (100× magnification).

Figure 11.4 shows the analogous AW 9 weld microstructure images. The as-welded microstructure consisted of martensite with 3.8% delta ferrite. At 891°C Gleeble peak temperature, it was tempered martensite with 1.5% delta ferrite. Carbo-nitride precipitates lined the grain boundaries. At 1021°C and 1273°C peak temperatures, a fully untempered martensitic structure was observed.

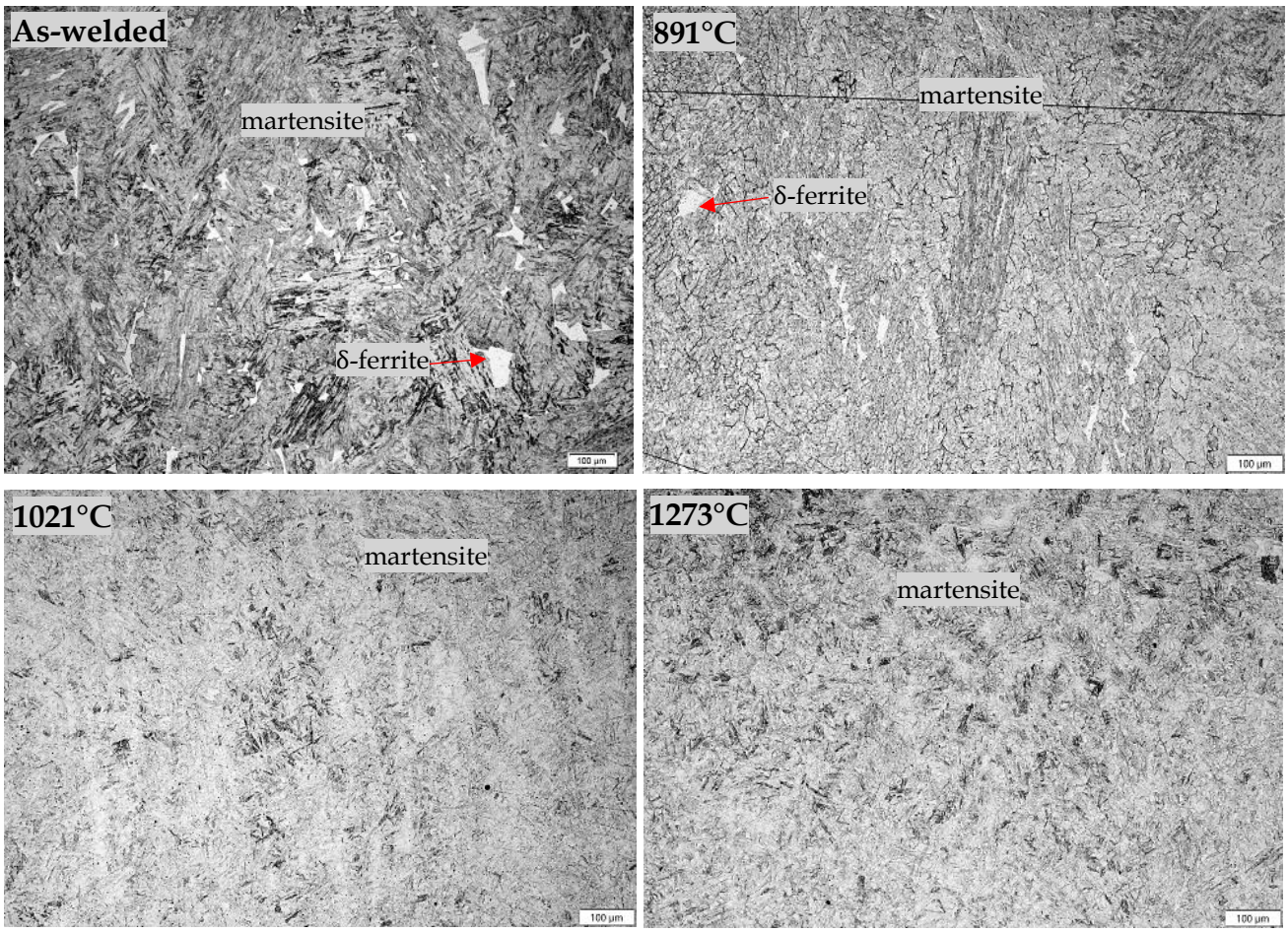

Fig. 11.4 Optical microstructure images of AW 9 microstructure in as-welded condition and after Gleeble thermal treatment. The microstructure in the as-welded condition consisted of martensite with 3.8% delta ferrite. At 891°C, the microstructure consisted of tempered martensite with 1.5% delta ferrite. At 1021°C and 1273°C peak temperatures, a fully untempered martensitic structure was observed (100× magnification).

Figure 11.5 similarly shows the AW 16 weld microstructure. The as-welded condition consisted of martensite with 6.0% delta ferrite. At 841°C Gleeble peak temperature, the microstructure was tempered martensite with 5.1% delta ferrite. Carbo-nitride precipitates lined the grain boundaries. At 1042°C peak temperature, the microstructure consisted of an untempered martensitic matrix with 1.5% delta ferrite. A fully untempered martensitic structure was observed at 1263°C peak temperature.

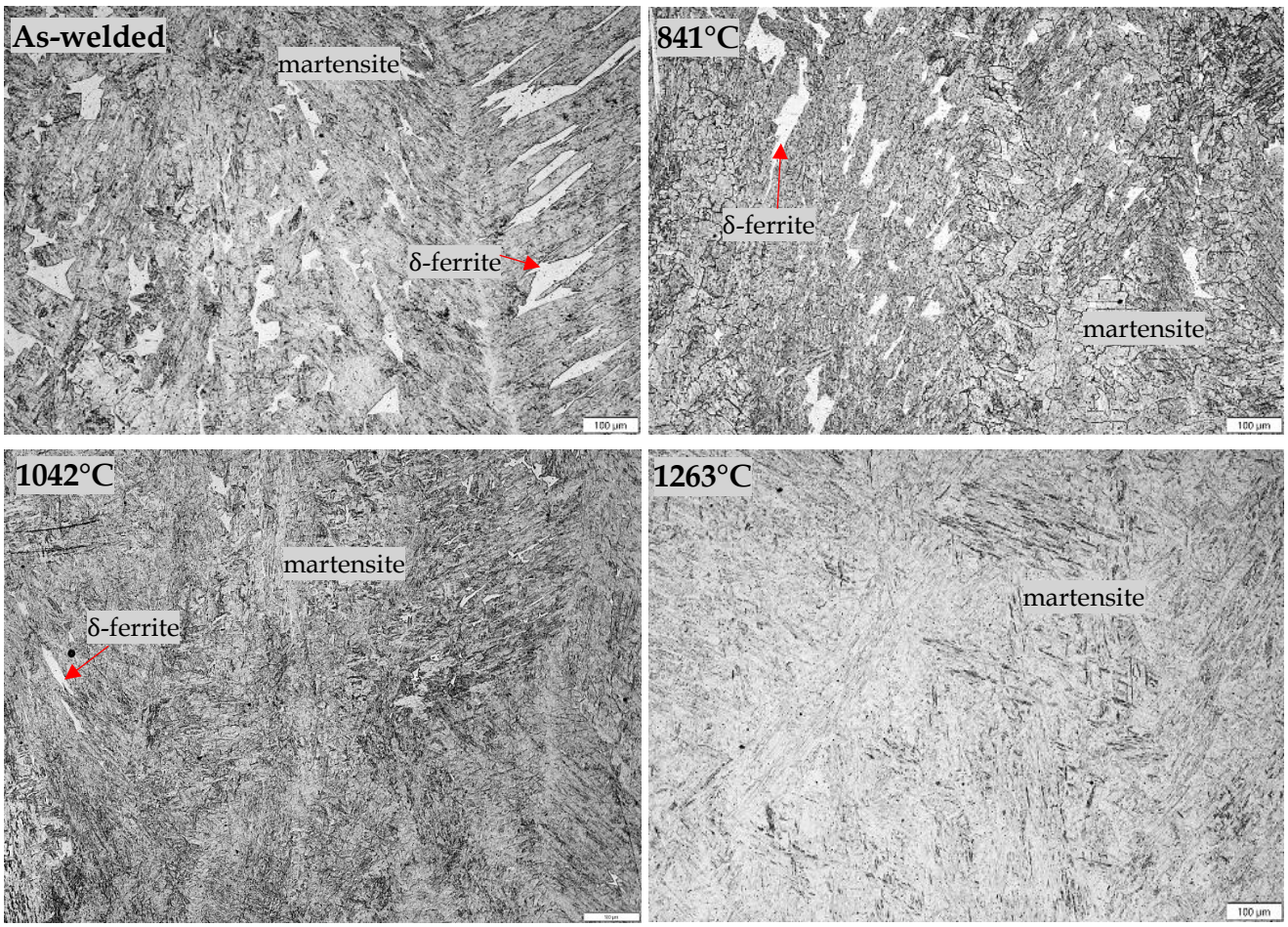

Fig. 11.5 Optical microstructure images of AW 16 microstructure in as-welded condition and after Gleeble thermal treatment. The microstructure in the as-welded condition consisted of martensite with 6.0% delta ferrite. At 841°C, the microstructure consisted of tempered martensite with 5.1% delta ferrite. For 1042°C peak temperature, the microstructure consisted of an untempered martensitic matrix with 1.5% delta ferrite. For 1263°C peak temperature, a fully untempered martensitic structure was observed (100× magnification).

Figure 11.6 shows the analogous AW 18 weld microstructure images. The as-welded microstructure consisted of martensite with 1.8% delta ferrite. At 936, 1091, and 1238°C Gleeble peak temperatures, the microstructure was fully untempered martensite. The Ae_3 transformation temperature was 847°C, which means that the 936°C Gleeble peak temperature was well within the austenite-only region and explains the fully martensitic structure observed.

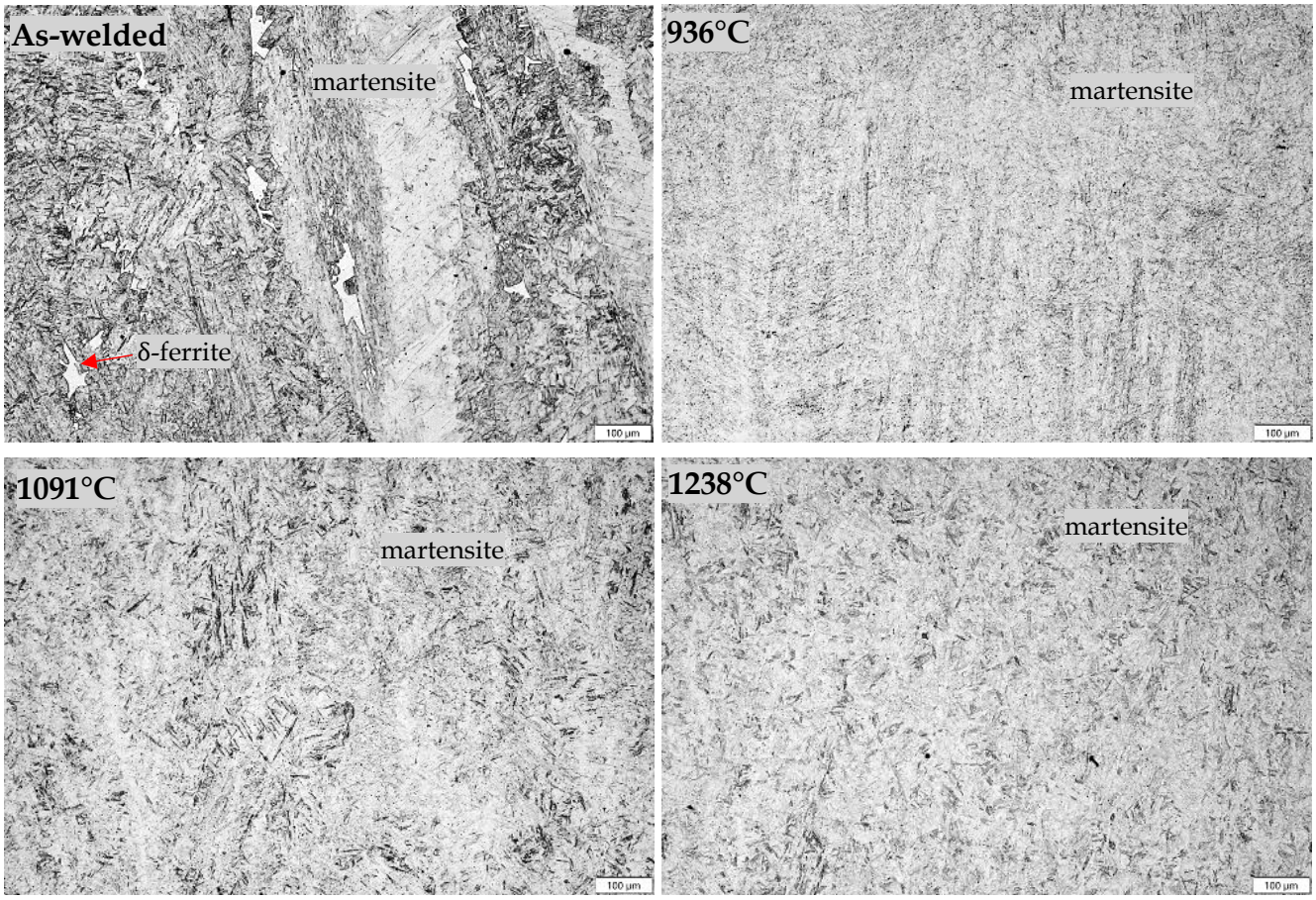

Fig. 11.6 Optical microstructure images of AW 16 microstructure in as-welded condition and after Gleeble thermal treatment. The microstructure in the as-welded condition consisted of martensite with 1.8% delta ferrite. All Gleeble samples consisted of a fully untempered martensitic structure (100× magnification).

Figure 11.7 shows AW 21 weld microstructure images under the same conditions. The as-welded microstructure consisted of martensite with 2.6% delta ferrite. At 890°C Gleeble peak temperature, the microstructure consisted of tempered martensite with 0.9% delta ferrite. Carbo-nitride precipitates lined the grain boundaries. At 1078°C and 1247°C peak temperatures, a fully untempered martensitic structure was observed.

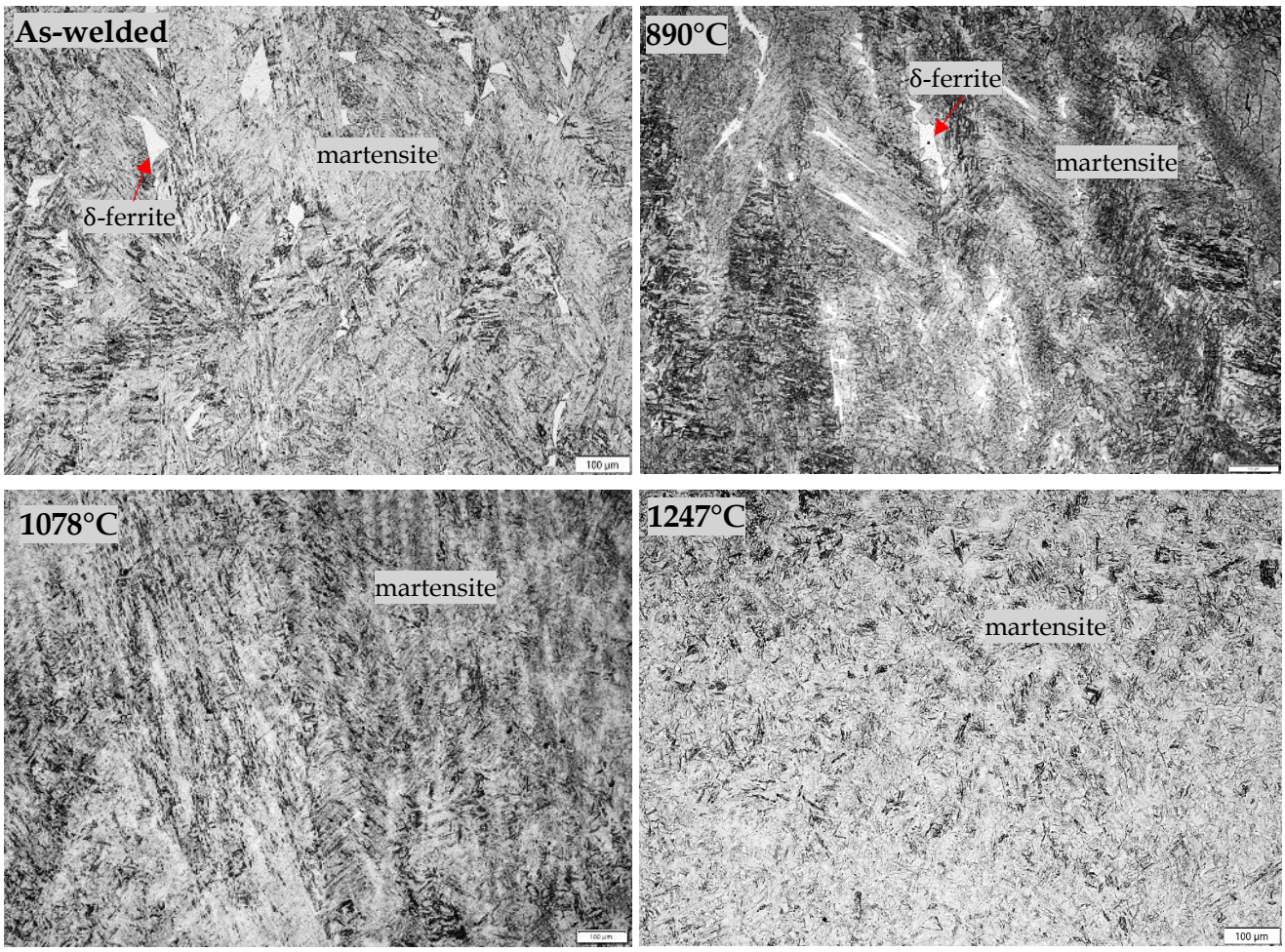

Fig. 11.7 Optical microstructure images of AW 21 microstructure in as-welded condition and after Gleeble thermal treatment. The microstructure in the as-welded condition consisted of martensite with 2.6% delta ferrite. At 890°C, the microstructure consisted of tempered martensite with 0.9% delta ferrite. At 1078°C and 1247°C peak temperatures, a fully untempered martensitic structure was observed (100× magnification).

11.4 Influence of Gleeble thermal treatment on P91 weld microstructure

The delta ferrite in the as-welded condition mainly comprised polygonal morphology and no change in morphology was observed after the Gleeble treatment. Generally, for the applied Gleeble parameters, the amount of delta ferrite decreased with increasing peak temperature, as illustrated in Fig. 11.8.

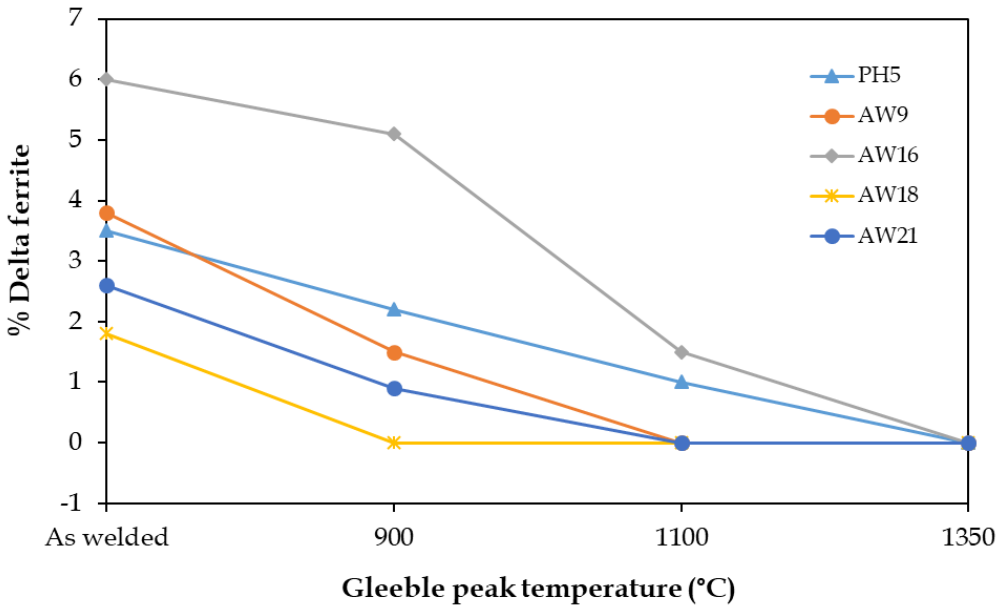

Fig. 11.8 Change in delta ferrite content with Gleeble thermal treatment.

The Gleeble thermal peak temperatures of 900°C and 1100°C are within the (Ae_3 – Ae_4) temperature range where only austenite phase is stable. Owing to phase stability and higher transformation temperatures (superheating) because of the high applied heating rate, reduced amounts of delta ferrite were observed in welds from 900°C peak temperature. Table 11.3 shows the difference between the applied Gleeble temperature and Ae_3 temperature and the percentage reduction in delta ferrite before and after Gleeble treatment.

Table 11.3 *Reduction of delta ferrite content after 900°C Gleeble treatment in relation to the Ae_3 temperature as estimated by Thermo-Calc.*

Welds ID	***Delta ferrite (as-welded) (%)***	***Delta ferrite (after 900°C) (%)***	***Temperature difference (Gleeble – Ae_3)****	***Change in delta ferrite (%)***
PH 5	3.5± 0.9	2.2	-7	37
AW 9	3.8 ± 0.6	1.5	25	61
AW 16	6.0 ± 1.1	5.1	-42	15
AW 18	1.8 ± 0.4	0	89	100
AW 21	2.6 ± 0.6	0.9	33	65

* The negative (−) temperature difference indicates that the applied Gleeble temperature was lower than the Ae_3 temperature.

The change in delta ferrite was calculated as follows:

$$\text{Change in \% delta ferrite} = \frac{\%\ \text{delta ferrite}\ ((\text{as} - \text{welded}) - (\text{after 900°C Tp}))}{\%\ \text{delta ferrite}(\text{as} - \text{welded})} \times 100$$

The results in Table 11.3 indicate that the degree to which the delta ferrite responded after 900°C Gleeble treatment is related to the weld Ae_3 temperature, as illustrated in Fig. 11.9. The percentage reduction of delta ferrite increased with larger difference in (Gleeble – Ae_3) temperature. This applies to Gleeble temperatures close to the Ae_3 temperature.

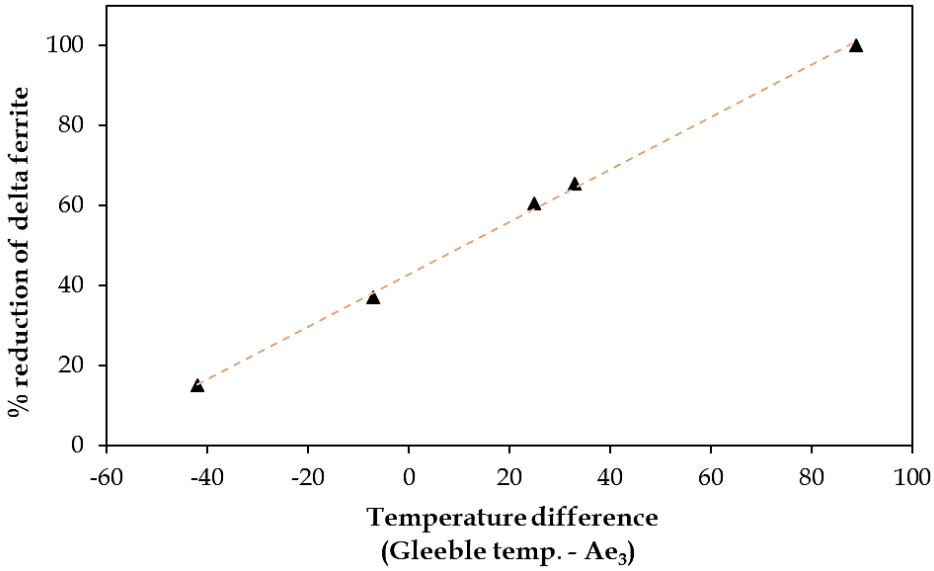

Fig. 11.9 Effectiveness of 900°C Gleeble treatment in reducing delta ferrite content in relation to Ae_3 temperature.

At 1100°C peak temperature, only two of the five welds contained ≤ 1.5% delta ferrite. The observed delta ferrite, even at peak temperatures within the austenite-only region, is attributed to insufficient time allowed for the solid-state diffusion-controlled transformation of delta ferrite to austenite to be completed. The 1350°C peak temperature was in the (Ae_4 − Ae_5) temperature range, where both delta ferrite and austenite phases are stable. At the average cooling rate of 25°C/s during Gleeble thermal treatment, there was sufficient time for any delta ferrite formed at 1350°C to transform back to austenite during cooling. An average of 62°C/s cooling rate for preheated GMA welds and 96°C/s for non-preheated GMA welds was achieved in this study. These results indicate that the amount of delta ferrite can be reduced by applying a subsequent bead. In a multi-pass weld, the last beads to be deposited are likely to contain more delta ferrite than previous beads.

11.5 Hardness of Gleeble specimens

Table 11.4 shows the average Vickers hardness (95% CI) of the Gleeble specimens. Five hardness measurements were taken for each specimen with a 10 kg.f load and 10 s dwell time. The data in Table 11.4 are graphically shown in Fig. 11.10, where the change in hardness is plotted against Gleeble peak temperature.

Table 11.4 *Average Vickers hardness (Hv_{10}) of Gleeble specimens*

Weld ID	***Peak temperature (°C)****	***Average hardness (95% CI)***
PH 5	880 (900)	360 ± 4
	1092 (1100)	418 ± 9
	1296 (1350)	406 ± 6
AW 9	891 (900)	395 ± 33
	1021 (1100)	423 ± 8
	1273 (1350)	410 ± 2
AW 16	841 (900)	338 ± 8
	1042 (1100)	408 ± 14
	1263 (1350)	397 ± 4
AW 18	936 (900)	418 ± 9
	1091 (1100)	422 ± 2
	1238 (1350)	412 ± 4
AW 21	890 (900)	388 ± 24
	1078 (1100)	421 ± 12
	1247 (1350)	413 ± 4

**Values in brackets are programmed peak temperatures*

The hardness at 900°C peak temperature showed scatter (actual peak temperature was 841–936°C), with the values ranging between 338 to 418 Hv_{10}. Gleeble specimens at 1100 and 1350°C peak temperatures showed no hardness change when compared with the as-welded specimens, with the exception of AW 21 at 1350°C.

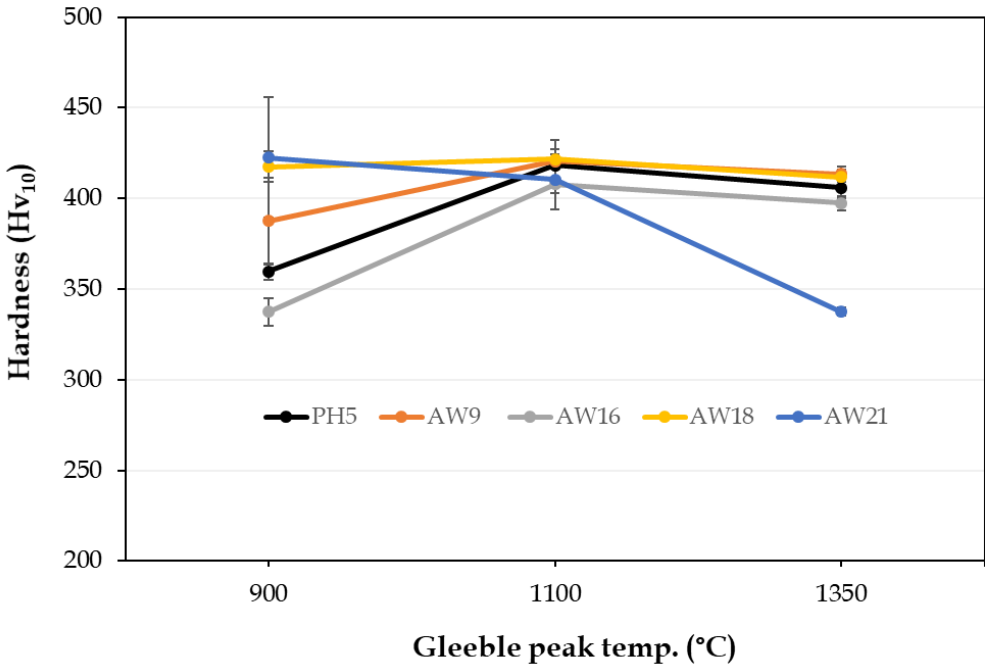

Fig. 11.10 Hardness (Hv_{10}) change with Gleeble thermal treatment

Figure 11.11 shows the Gleeble hardness values plotted against the delta ferrite volume fraction. Gleeble specimens containing < 2% delta ferrite showed significant scatter, with hardness ranging between 388 and 423 Hv_{10}. A significant decrease in hardness with increase in delta ferrite was observed in welds containing > 2% delta ferrite.

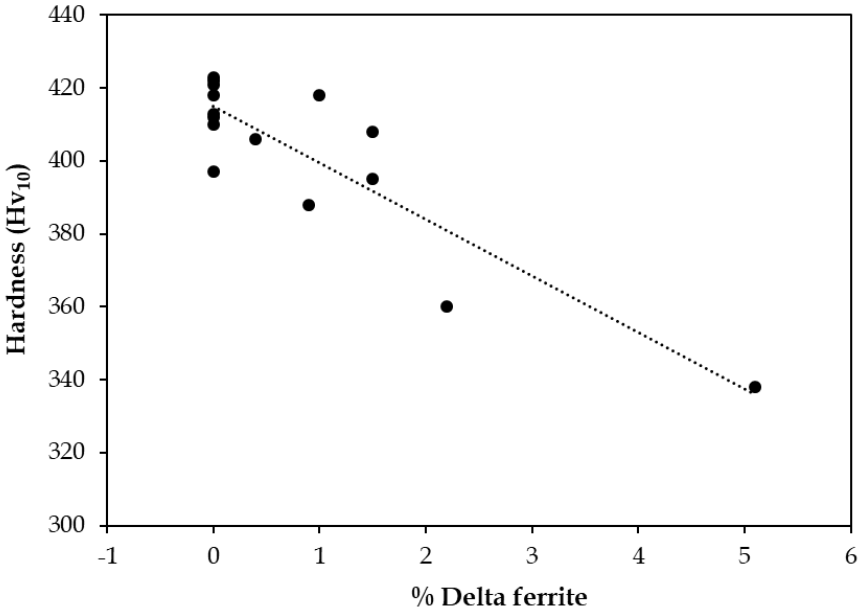

Fig. 11.11 Hardness (Hv_{10}) as a function of delta ferrite content.

11.5.1 Analysis of Gleeble hardness results

Table 11.5 contains Gleeble specimen data relevant to the 900°C peak temperature. The AW 16 specimen showed significant softening of 57 Hv_{10}, which indicated a reasonable degree of tempering of the martensitic matrix. The thermal cycles consisted of fast heating and cooling rates without holding time at peak temperature. This allowed a limited time for phase transformation to proceed sufficiently to equilibrium phase fractions. AW 16 contained 5.1% delta ferrite, the highest Ae_1 temperature (817°C) of the Gleeble specimens, and the lowest peak temperature of 841°C. The small difference between the Ae_1 and Gleeble peak temperatures resulted in limited time for austenite nucleation and growth, which meant that no fresh martensite formed on cooling. The significant amount of delta ferrite present and the absence of untempered martensite resulted in the reported softening of weld AW 16 after Gleeble treatment.

Table 11.5 *Weld data for Gleeble samples thermally treated to 900°C peak temperature*

Weld ID	***Hardness Hv_{10} (as-welded)***	***Hardness Hv_{10} at 900°C Gleeble treatment***	***Actual Gleeble peak temp. (°C)***	***Ae_1 temp. (°C)***	***Delta ferrite (%)***
PH 5	380	360	880	803	2.2 ± 0.8
AW 9	401	395	891	810	1.5 ± 0.6
AW 16	395	338	841	817	5.1 ± 1.4
AW 18	421	418	936	784	0.0
AW 21	414	388	890	793	0.9 ± 0.2

The difference between Ae_1 and actual peak temperatures in the remaining four specimens was large enough to allow for austenite formation, which would transform to untempered martensite on cooling. This was evident in the hardness values remaining similar to that of specimens in the as-welded condition and in the reduction of delta ferrite after the Gleeble thermal treatment.

The hardness at 1100°C peak temperature ranged between 408 and 423 Hv_{10}, which is consistent with the untempered martensite microstructure. The 1100°C peak temperature is closer to the Ae_4 of the specimen within the austenite-only region. The 1350°C peak temperature is positioned in the region where both austenite and delta ferrite are stable. All Gleeble specimens from the 1350°C peak temperature comprised a fully untempered martensitic microstructure with hardness values ranging between 397 and 413 Hv_{10}. The delta ferrite that likely formed at 1350°C was allowed sufficient time, at the average cooling rate of 23°C/s, to transform to austenite. The fully martensitic microstructure at 1350°C peak temperature was similar to that of the uninterrupted dilatometry specimens cooled at 30°C/s (see Section 12.2).

Chapter 12

Dilatometry experimental results and analysis

Dilatometry was conducted to study the austenite/delta ferrite phase transformation thermodynamics in P91 and to determine the Ae_1 and Ae_3 critical transformation temperatures, simulating equilibrium conditions, and to compare the results with the transformation temperatures calculated using Thermo-Calc software. The Ae_1 and Ae_3 transformation temperatures were determined for AW 4, AW 6, and AW 22 weld metals. An experiment to examine the influence of cooling rate on delta ferrite/austenite phase transformation was conducted on P91 base metal.

12.1 Dilatometry (Ae_1/Ae_3) equilibrium transformation temperatures

The Ae_1 and Ae_3 transformation temperatures of AW 4, AW 6, and AW 22 welds were determined by application of thermal treatment in a Bahr dilatometer, as prescribed by the ASTM A1033-04 standard, up to 1000°C peak temperature. The Ae_1 and Ae_3 transformation temperatures of the three welds determined from the dilatometry curves, as shown in Figure 12.1 for AW 6, and from Thermo-Calc software are presented in Table 12.1.

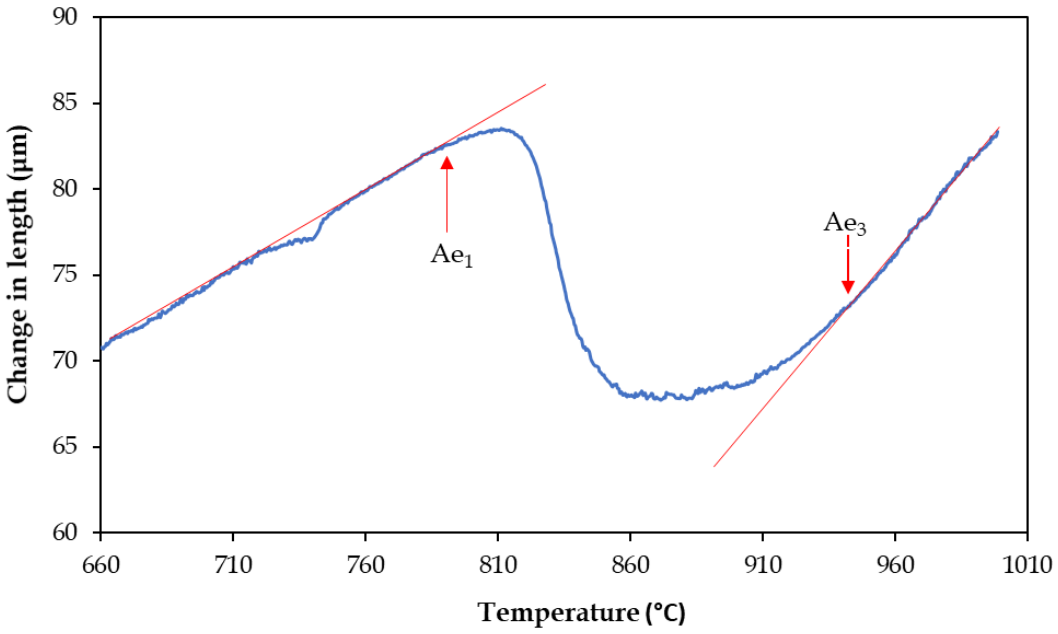

Fig. 12.1 Thermal curve plotted to determine the equilibrium transformation temperature of AW 6 weld. The red arrows indicate where the Ae_1 and Ae_3 transformation temperatures were determined.

Table 12.1 *Ae_1 and Ae_3 transformation temperatures of three selected welds*

Weld ID	***Dilatometry (°C)***		***Thermo-Calc (°C)***	
	Ae_1	Ae_3	Ae_1	Ae_3
AW 4	788	925	806	866
AW 6	790	930	791	850
AW 22	800	910	771	835

The Thermo-Calc transformation temperatures were plotted against the dilatometric-measured Ae_1 and Ae_3 temperatures, as shown in Fig. 12.2. The AW 4 and AW 22 dilatometric Ae_1 temperatures were 18°C below and 29°C above the Thermo-Calc values, respectively. There was inconsistency in the Ae_1 temperatures. There was some consistency in the Ae_3 values, in that all dilatometry Ae_3 temperatures were, on average, 70°C higher that the calculated Thermo-Calc values. Based on the ideal line plotted in Fig. 12.2, the calculated Ae_1 temperatures were reasonably accurate when compared with the over-estimated Ae_3 temperatures.

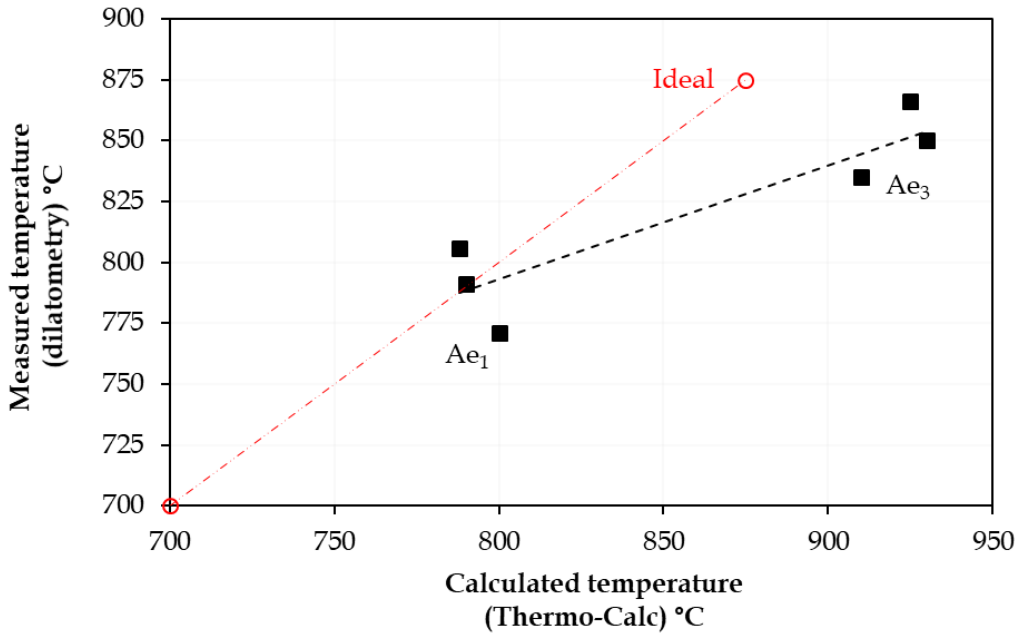

Fig. 12.2 Measured transformation temperatures plotted against calculated values. The ideal line is plotted for the same Thermo-Calc and dilatometry temperatures.

12.2 Microstructures of base metal dilatometry specimens

Results are presented for experiments performed on P91 base material. The specimens were heated at 200°C/s to 1350°C with no holding time. This peak temperature was chosen to achieve a starting microstructure that consisted of approximately equal volume fractions of austenite and delta ferrite phases, as per the P91 phase diagram in Section 5.2. Two thermal cycle routes were applied during cooling:

***Uninterrupted cooling*:** The specimens were cooled at cooling rates of 1, 10, 30, 50, 100, 200°C/s from 1350°C to ambient. The varying cooling rates were intended to simulate the different cooling rates that would be experienced in the various regions of the HAZ.

Interrupted cooling: The specimens were cooled at rates of 0.1, 1, 10, and 50°C/s from 1350 to 1270°C before quenching at 200°C/s.

Both dilatometry thermal cycles for specimens cooled at 1°C/s from 1350°C are shown in Fig. 12.3.

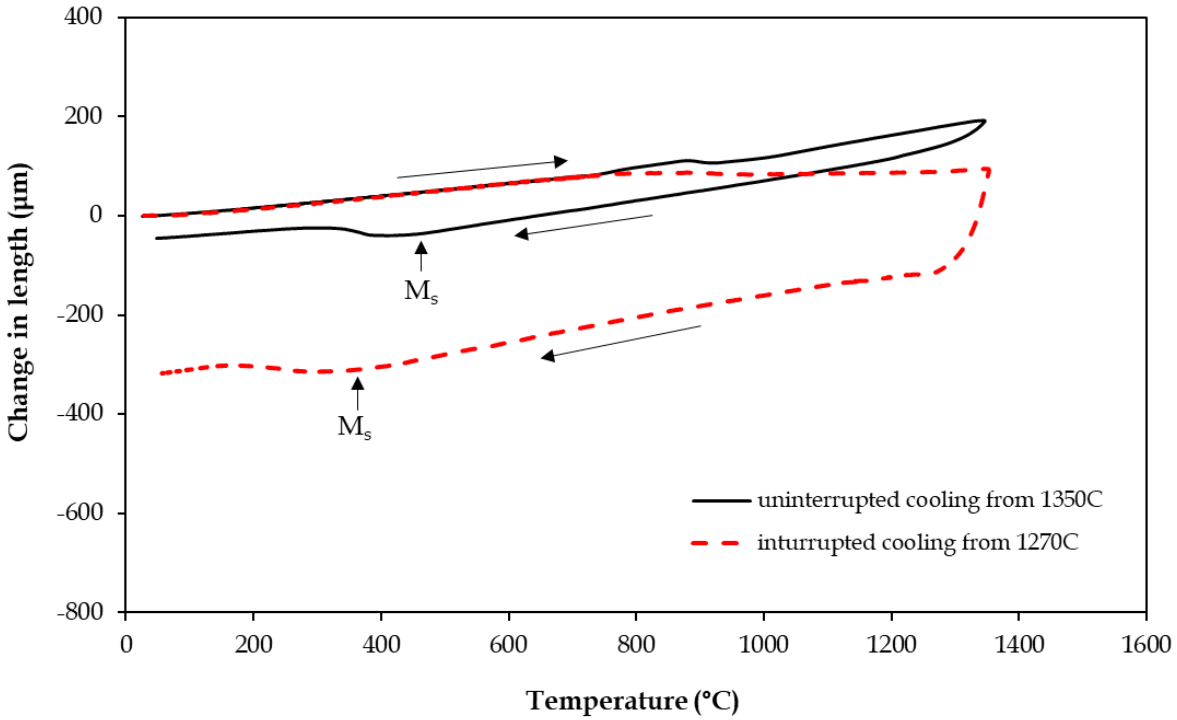

Fig. 12.3 Thermal cycles of the two cooling routes. The black curve was cooled from 1350°C to ambient temperature at 1°C/s. The dashed red curve was cooled from 1350 to 1270°C at 1°C/s before quenching at 200°C/s.

The Ac_4 temperature could not be identified during both dilatometry heating and cooling cycles. During dilatometry experiment, as the temperature reaches the austenite start temperature (Ac_1) during heating, the volume of the specimen contracts, due to the high packing density of the fcc structure. This can be observed in the deviation from the linear curve in Fig. 12.3. At the start of delta ferrite transformation (Ac_4) during heating, a dilation should be observed because of lower packing density of delta ferrite. As can be seen in Fig 12.3 such change in specimen length was not observed.

12.2.1 Microstructure of dilatometry specimens after uninterrupted cooling thermal treatment

Figure 12.4(i) shows a microstructure of the dilatometry specimen cooled at 200°C/s. This seemed to be fully martensitic, but at higher (200×) magnification (Fig. 12.4(ii)), there was evidence of small isolated delta ferrite grains on the outer surface of the specimen. With heating and cooling rates of 200°C and no holding time at peak temperature, the specimen spent less than 1 s above 1270°C (Ae_4 temperature), where delta ferrite is stable, it is therefore unlikely that appreciable delta ferrite was formed.

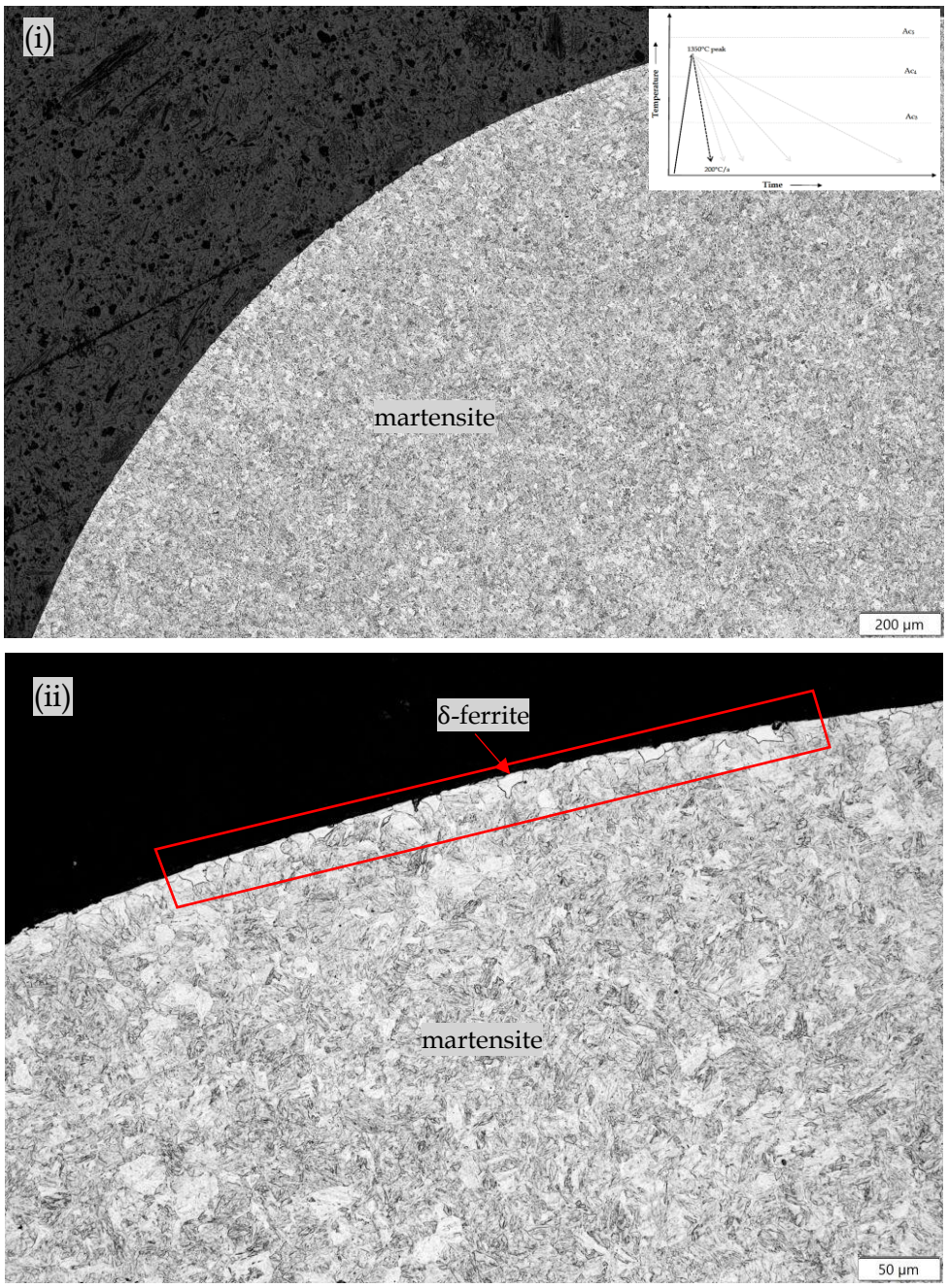

Fig. 12.4 Optical microstructure images (50× and 200× magnification) of dilatometry specimen cooled from 1350°C at 200°C/s. (i) Microstructure mainly consists of a fully martensitic phase except for fine delta ferrite grains on the outer surface, highlighted by the red box.

Figure 12.5 shows the microstructure of a specimen cooled at 1°C/s (200× magnification). The austenite → delta ferrite transformation occurred from the outer surface whilst the core region of the specimen remained fully austenitic during the thermal treatment. The microstructure of the core region was fully martensitic. The thickness of the transformed region on the outer surface was 300 µm and consisted of a martensitic matrix with 27% delta ferrite.

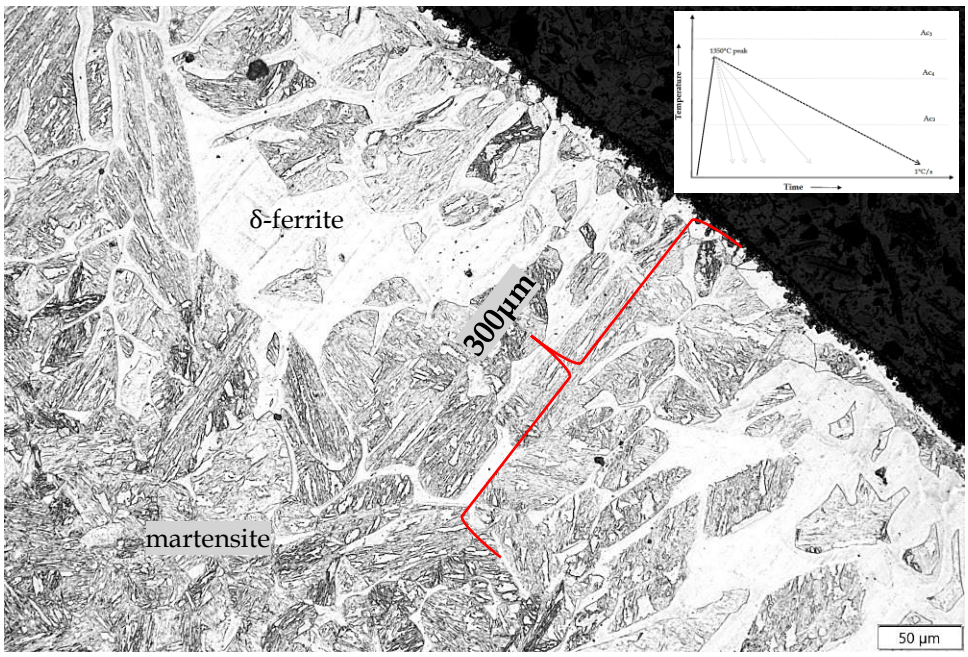

Fig. 12.5 Optical microstructure image of dilatometry specimen cooled at 1°C/s (200× magnification). The specimen's microstructure consists of a fully martensitic core with an outer surface region that contains 27% delta ferrite.

Figure 12.6 shows the microstructure of a specimen cooled at 10°C/s (200× magnification). This consisted of a martensitic matrix with isolated small delta ferrite grains amounting to 7% on the outer surface region of the specimen. The distance of the transformed region from the outer surface was approximately 50 µm.

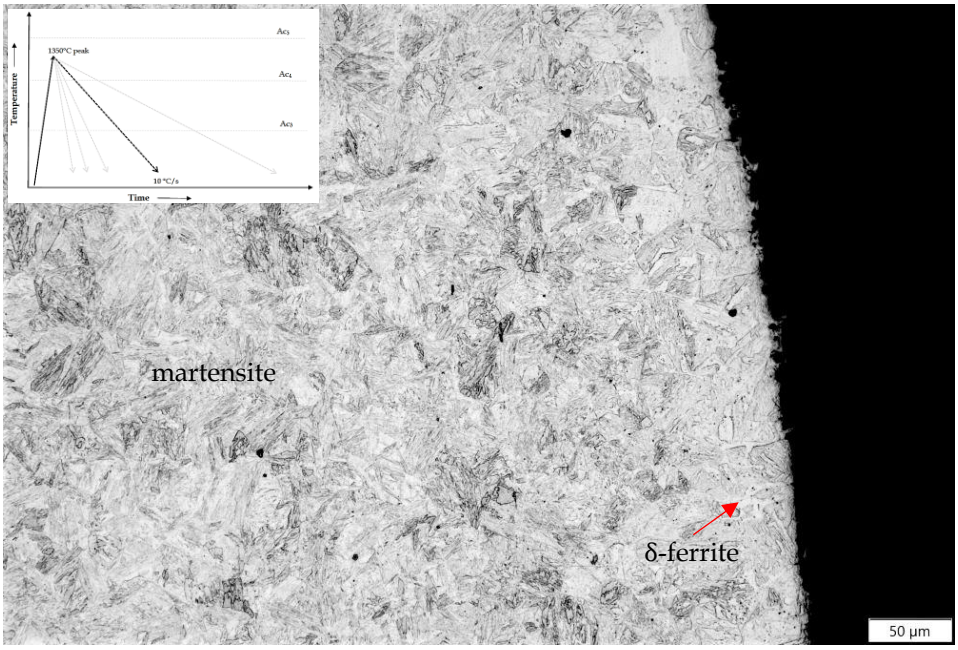

Fig. 12.6 Optical microstructure image of a specimen cooled at 10°C/s consisting of a martensitic matrix with isolated delta ferrite amounting to 7% on the outer surface region (200× magnification).

Figure 12.7 shows the microstructure of a specimen cooled at 30°C/s (200× magnification). This consisted of a fully martensitic matrix with no evidence of delta ferrite phase.

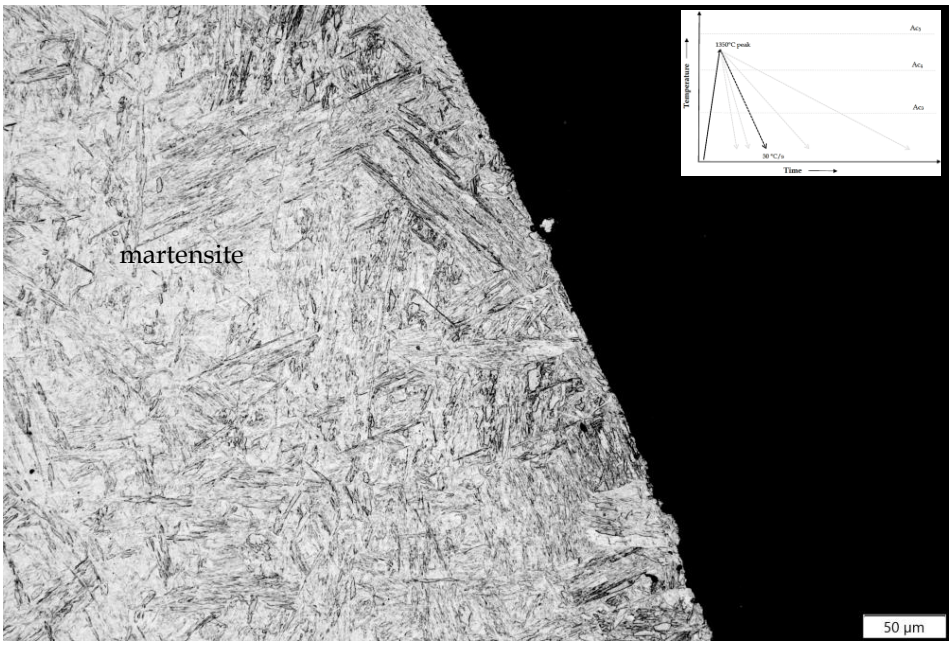

Fig. 12.7 Optical microstructure image consisting of a fully martensitic matrix cooled at 30°C/s (200× magnification).

Figure 12.8 shows the microstructure of a specimen cooled at 50°C/s (200× and 500× magnification). The martensitic matrix had polygonal grains of delta ferrite that formed a layer on the outer surface region. The depth of the layer from the outer surface was approximately 30 µm and it consisted of 43% delta ferrite.

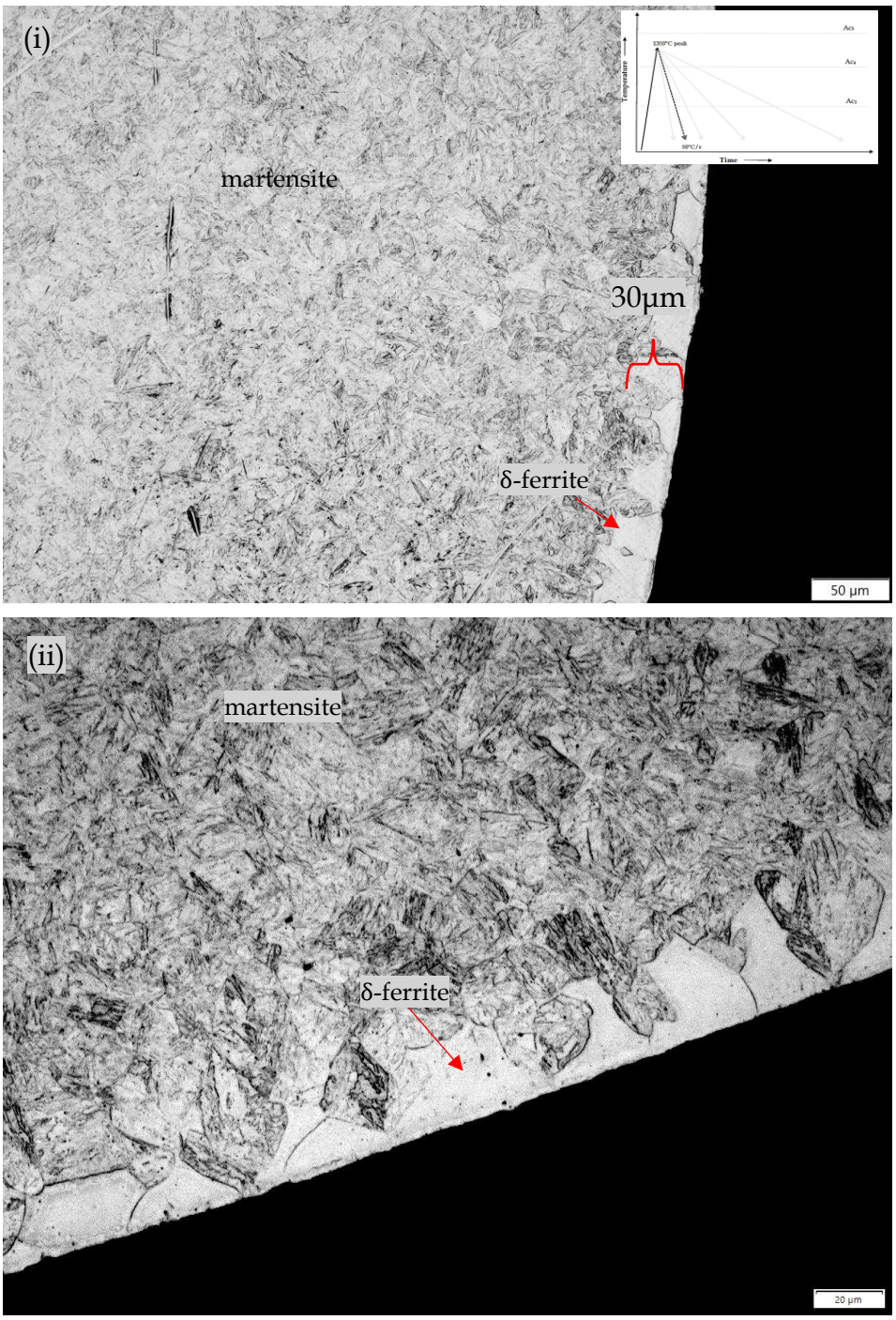

Fig. 12.8 Optical microstructure images of a martensitic matrix with fine polygonal grains of delta ferrite on the outer surface cooled at 50°C/s (200× and 500× magnification).

Figure 12.9 shows the microstructure of a specimen cooled at 100°C/s (200× magnification). It consisted of a martensitic matrix with isolated polygonal grains of delta ferrite that formed on the outer surface. The depth of the layer from the outer surface was approximately 20 µm and it contained 2.1% delta ferrite.

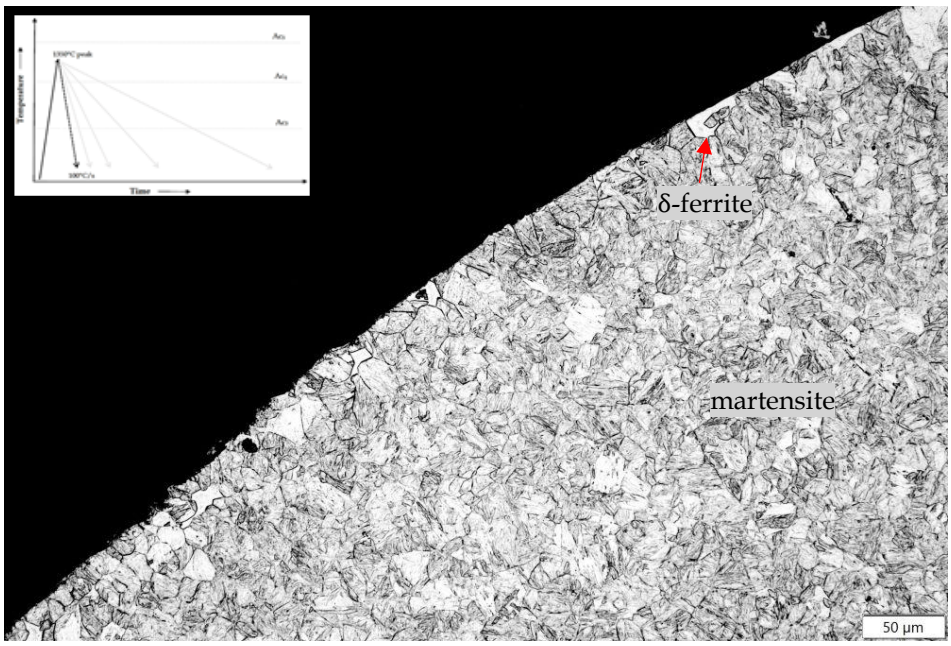

Fig. 12.9 Optical microstructure image of a martensitic matrix with fine polygonal grains of delta ferrite on the outer surface cooled at 100°C/s (200× magnification).

Table 12.2 summarises the results of the transformed outer surface region and amount of delta ferrite in this region. These results are graphically illustrated in Fig. 12.10. The outer region of the specimen that cooled at 30°C/s was not microstructurally distinguishable and no delta ferrite was observed.

Table 12.2 *Width of transformed outer surface region and amount delta ferrite formed during uninterrupted cooling thermal treatment*

Cooling rate (°C/s)	***Width of the outer region (µm)***	***Delta ferrite (%)***
1	300	27 ± 5.2
10	50	7 ± 3.1
30	0	0
50	30	43 ± 6.1
100	20	2 ± 1.2
200	10	11 ± 6.7

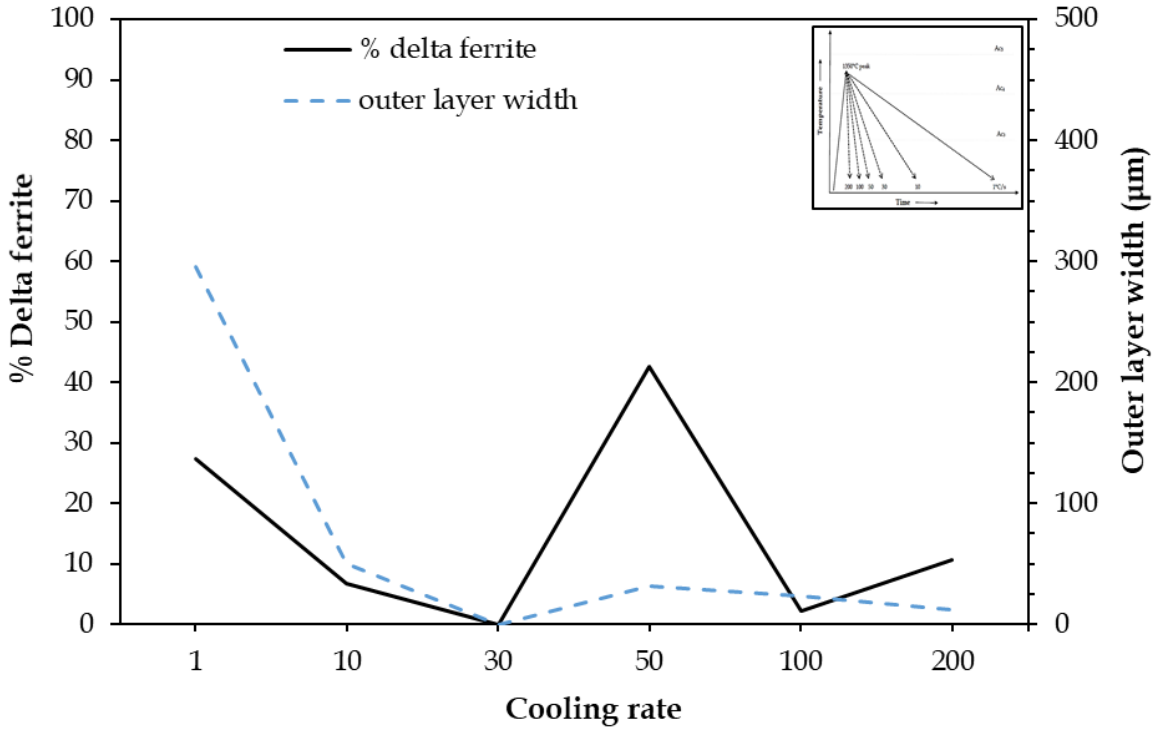

Fig. 12.10 Width of transformed outer surface region and amount delta ferrite, as influenced by the cooling rate. No transformed region or delta ferrite were observed at a cooling rate of 30°C/s.

12.2.2 Microstructure of dilatometry specimens after interrupted cooling thermal treatment.

The objective of this experiment was to confirm that during cooling from a peak temperature above the Ae_4, delta ferrite continues to transform from austenite because of non-equilibrium phase fraction distribution until the Ae_4 temperature (1270°C for the P91 base metal specimens). Quenching from 1270°C was also performed to observe the influence of the cooling rate on the phase distribution just above the Ae_4 temperature.

Figure 12.11 shows microstructure images of a specimen cooled at 0.1°C/s from 1350 to 1270°C followed by quenching. Figure 12.11(i) shows the outer region microstructure, consisting of a mixture of 45% delta ferrite with martensite. The core region consisted of a martensitic matrix with 0.2% delta ferrite, as shown in Fig. 12.11(ii). The difference between the core and outer surface regions was due to the temperature gradient that existed between the two regions during thermal treatment. The width of the outer surface region was an average of 1000 µm.

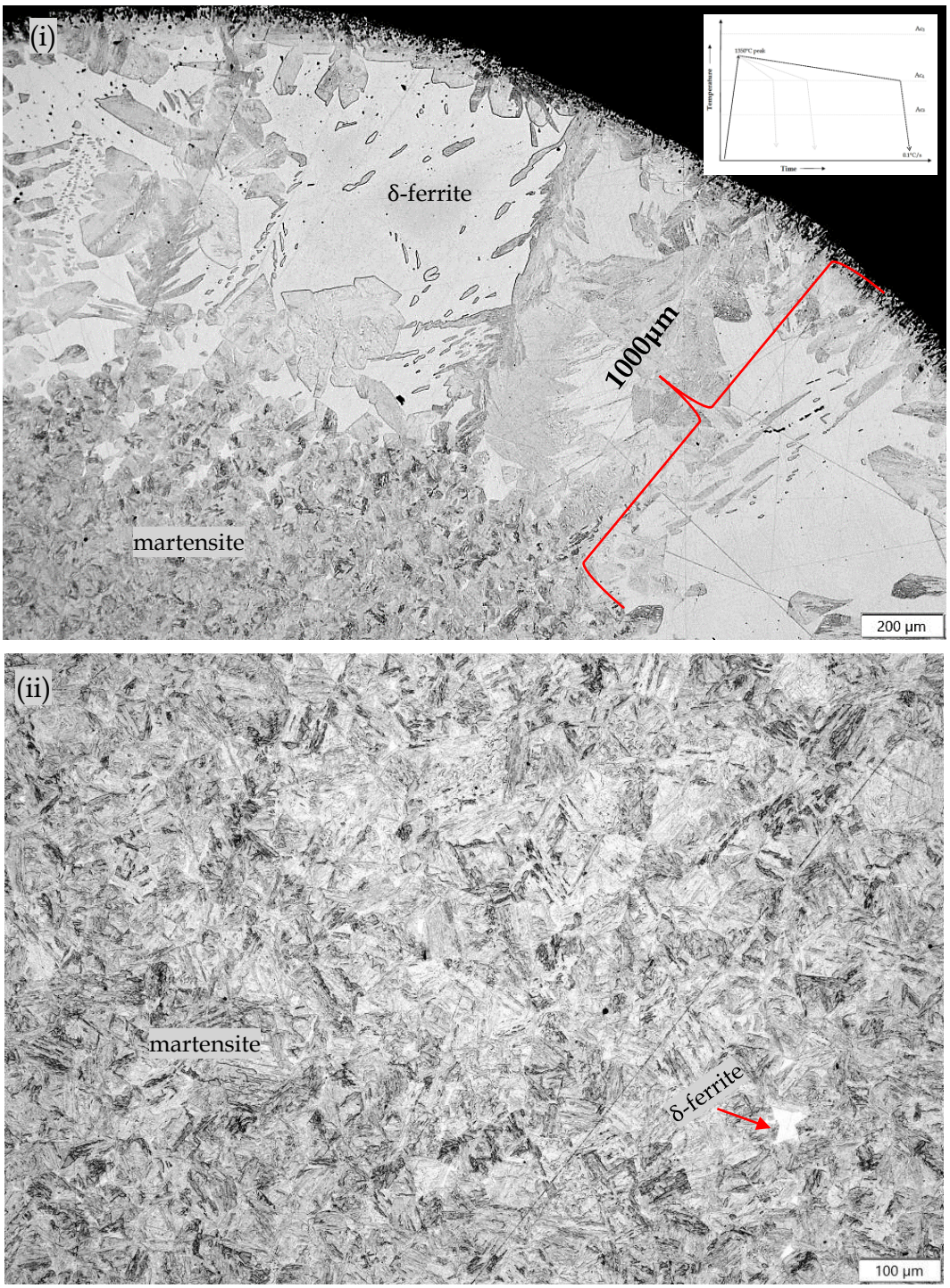

Fig. 12.11 Optical microstructure images of specimen cooled at 0.1°C/s. (i) Outer region consisting of a mixture of 45% delta ferrite with martensite (200× magnification). (ii) Core region consisting of martensitic matrix with 0.2% delta ferrite (100× magnification).

Figure 12.12 shows microstructure images of a specimen cooled at 1°C/s. The outer region consisted of 40% delta ferrite with martensite; the core region was fully martensitic. The width of the outer surface was approximately 170 µm on average.

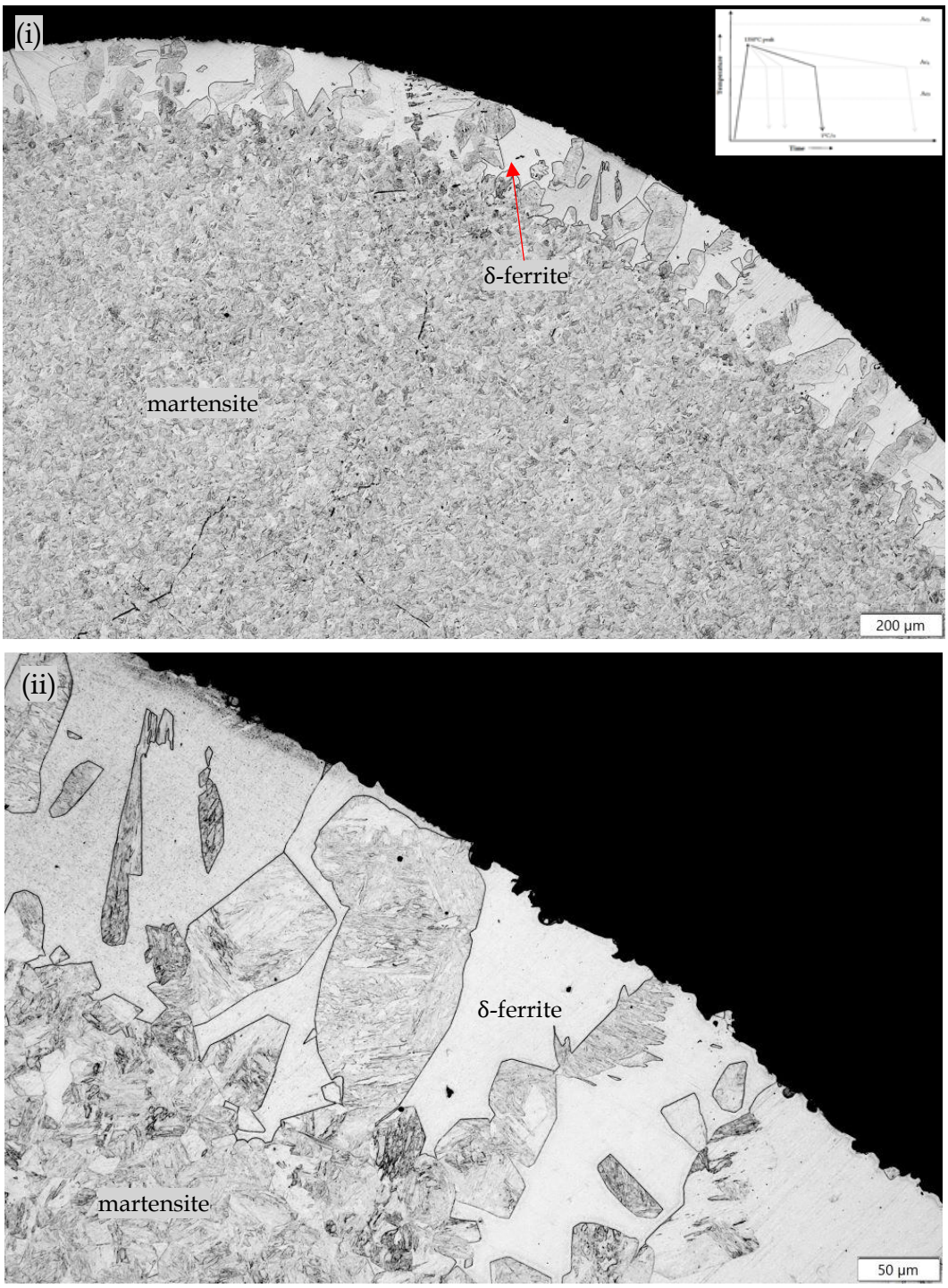

Fig. 12.12 Microstructure images of specimen cooled at 1°C/s. The core region is fully martensitic and the outer region consists of a mixture of delta ferrite and martensitic phase ((i) 50× and (ii) 200× magnification).

Figure 12.13 shows microstructure images of a specimen cooled at 10°C/s. The microstructure was largely fully martensitic, but did contain isolated small delta ferrite grains on the outer surface of the specimen, with a width of 40 µm. The microstructure contained approximately 8% delta ferrite.

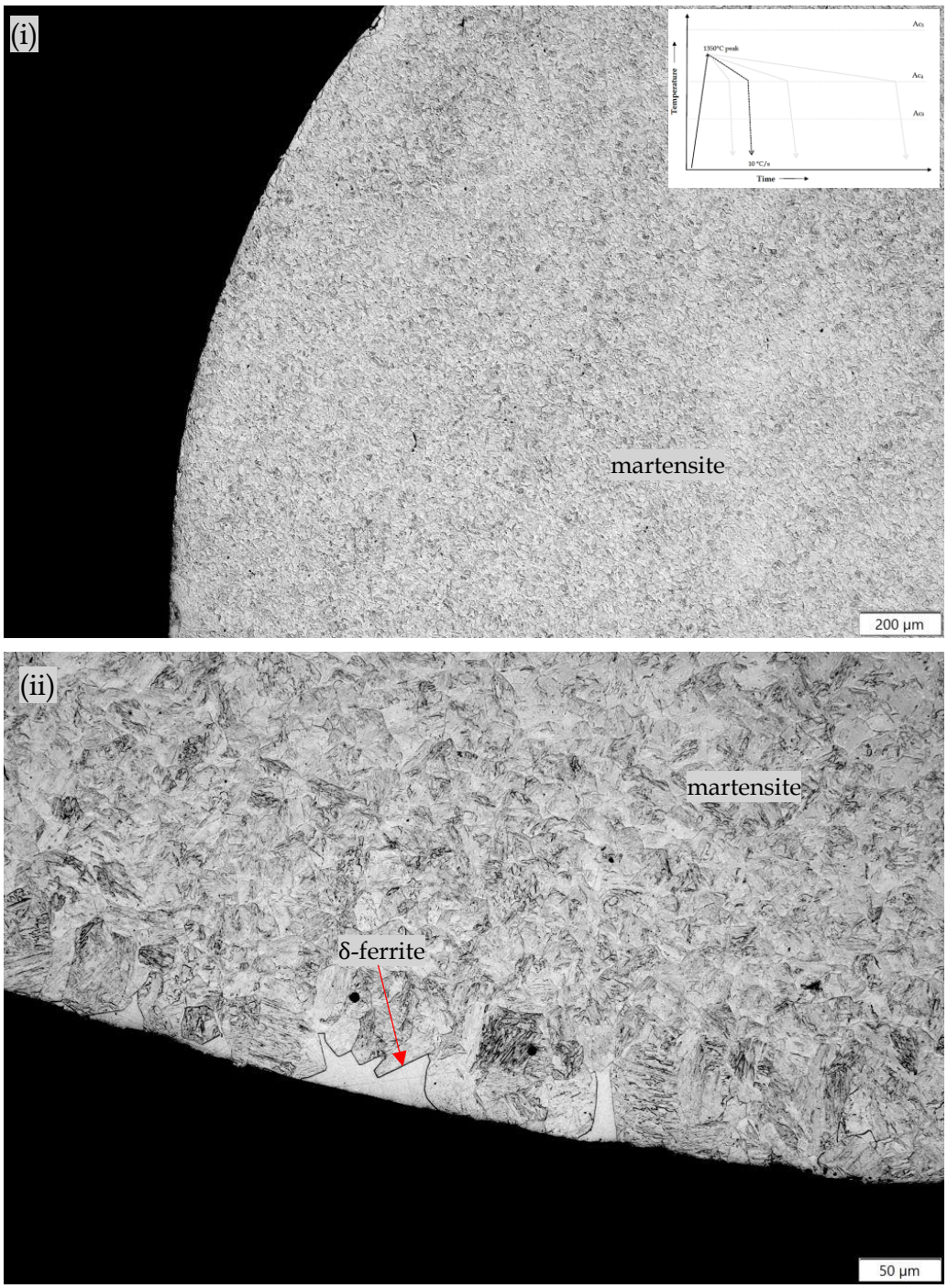

Fig. 12.13 Microstructure images of specimen cooled at 10°C/s. The microstructure was martensitic with fine isolated polygonal grains of delta ferrite on the outer surface ((i) 50× and (ii) 200× magnification).

Figure 12.14 shows analogous data for a specimen cooled at 50°C/s. The microstructure was fully martensitic, with no evidence of delta ferrite on the outer surface.

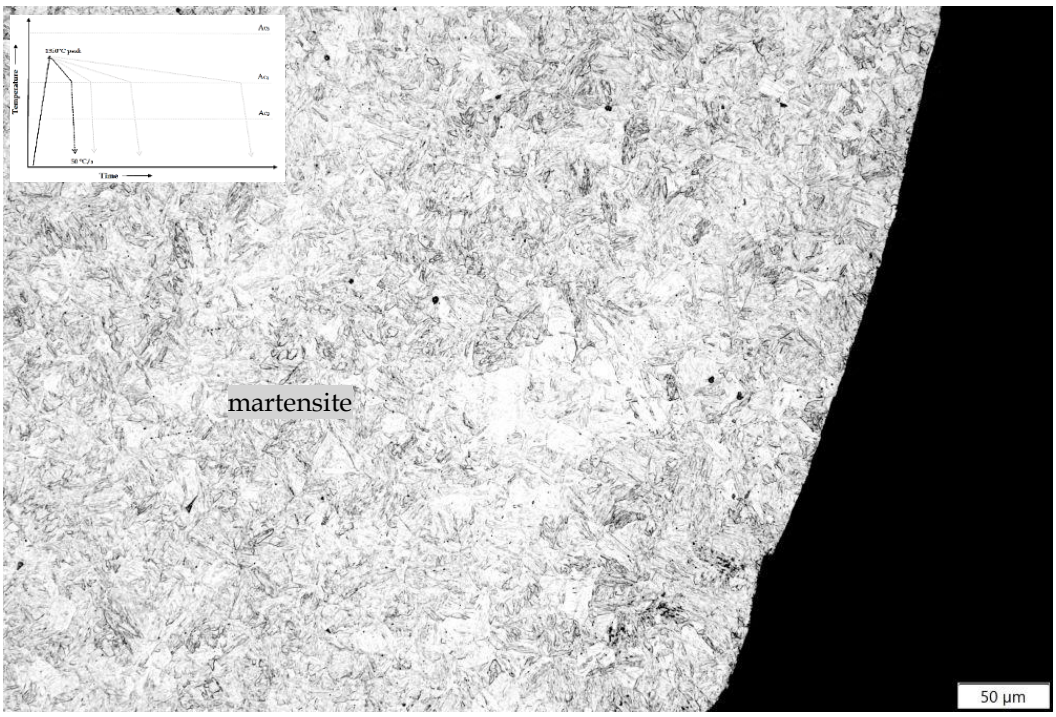

Fig. 12.14 Fully martensitic microstructure image of specimen cooled at 50°C/s (200× magnification).

Table 12.3 summarises the results of the transformed outer surface region and amount of delta ferrite phase in this region. The width of the transformed region and amount of delta ferrite decreased with faster cooling rate.

Table 12.3 *Width of transformed region and the amount of delta ferrite formed during interrupted cooling cycle*

Cooling rate (°C/s)	*Thickness of outer region (µm)*	*Delta ferrite (%)*
0.1	1000	45 ± 5.6
1	170	40 ± 4.3
10	40	8 ± 3.8
50	0	0

12.2.3 Comparison of differences in microstructures between interrupted and uninterrupted cooling thermal cycles

There were three common cooling rates between the two thermal cycles; namely, 1, 10, and 50°C/s. Table 12.4 compares the microstructures and thickness of the transformed outer region of the dilatometry specimens with cooling rate. These results are graphically illustrated in Fig. 12.15.

Table 12.4 *Comparison of cooling protocols in generating delta ferrite in the transformed outer region and its thickness*

Parameter	*Uninterrupted cooling*			*Interrupted cooling*		
	Cooling rate (°C/s)			*Cooling rate (°C/s)*		
	1	*10*	*50*	*1*	*10*	*50*
Delta ferrite (%)	27	7	43	40	8	0
Thickness of outer layer (μm)	300	50	30	170	40	0

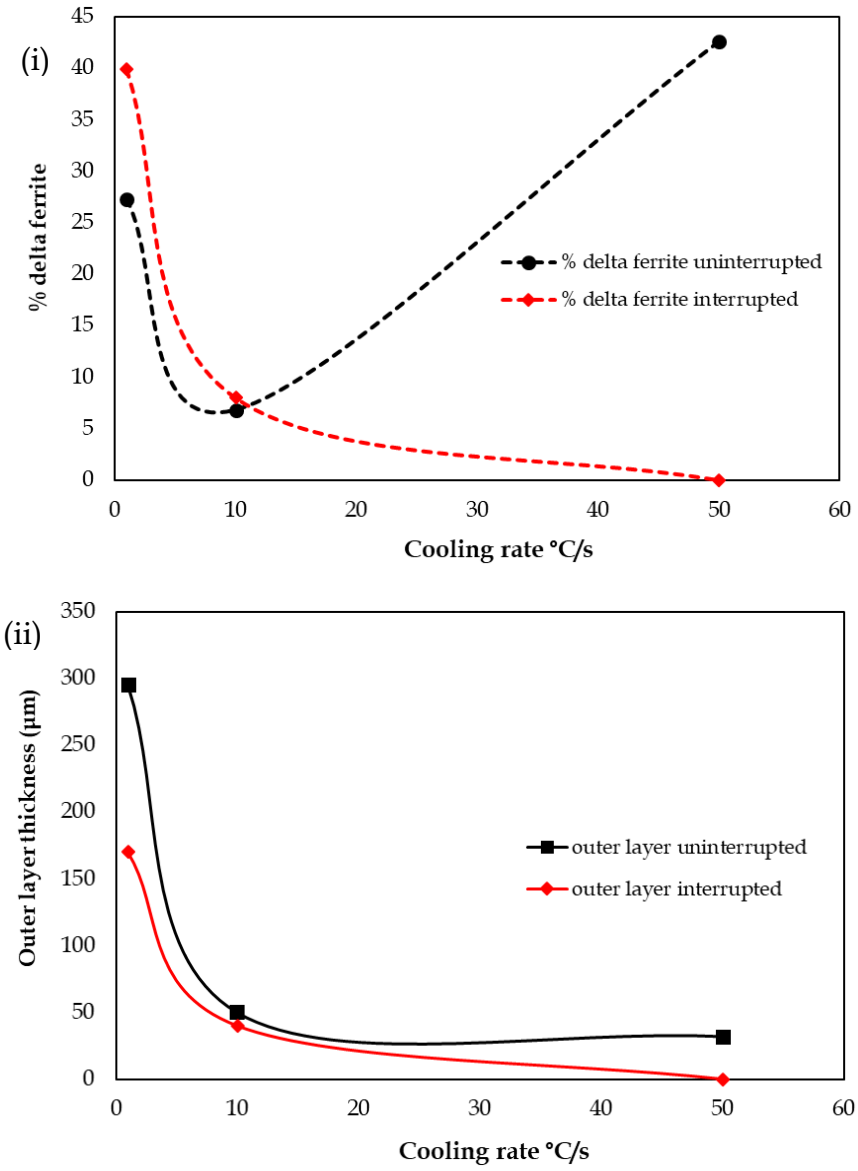

Fig. 12.15 Comparison of cooling rate influence on (i) delta ferrite content and (ii) thickness of the transformed outer region between the interrupted and uninterrupted thermal cycles.

Figure 12.16 shows microstructures of specimens cooled at 1, 10, and 50°C/s in the interrupted and uninterrupted cooling thermal cycles. In both cycles, faster cooling rates resulted in narrower width of the transformed outer region.

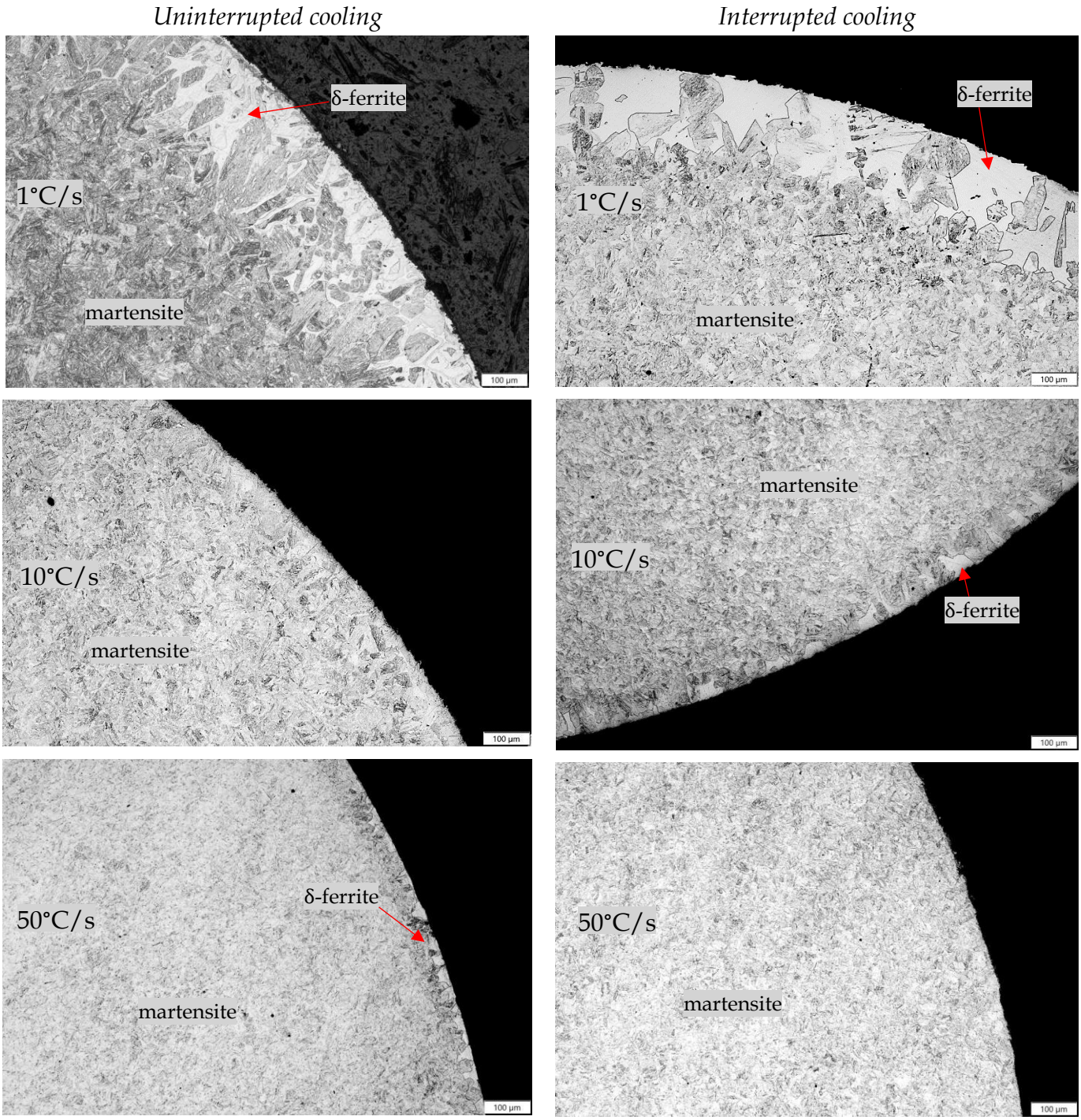

Fig. 12.16 Optical microstructure images of specimens cooled at 1, 10, and 50°C/s in the interrupted and uninterrupted cooling thermal cycles.

Effect of cooling rate on delta ferrite in the uninterrupted cycle initially decreased with faster cooling rate, but at 50°C/s the amount of delta ferrite increased significantly. In the interrupted cycle, higher cooling rate resulted in lower delta ferrite.

12.3 Hardness of dilatometry specimens

Vickers hardness measurements were performed on all dilatometry specimens with 300 gf load and 10 s dwell time. Ten measurements, 0.25 mm apart, were taken from the surface to the centre of the specimen to determine the change in hardness with distance. Figure 12.17(i) demonstrates how the hardness measurements were positioned on the specimen cross-section. Five additional measurements were taken 100 µm from the outer surface, as demonstrated in Fig. 12.17(ii), to determine the effect of cooling rate on the transformed outer region of the specimen.

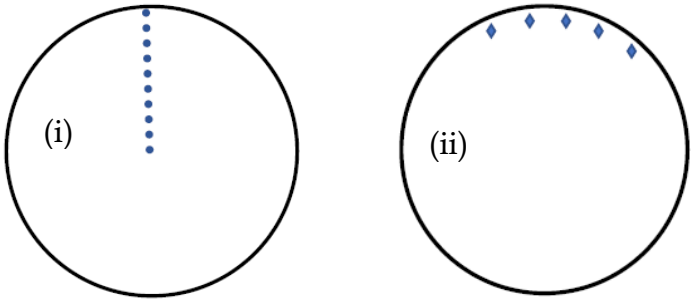

Fig. 12.17 Sketches of dilatometry specimens, demonstrating positions of hardness measurements.

Figure 12.18 shows the effect of cooling rate on hardness measurements taken from the outer surface to the centre for all dilatometry specimens. The Vickers hardness values shown in Table 12.5 were measured on the outer surfaces of the specimens.

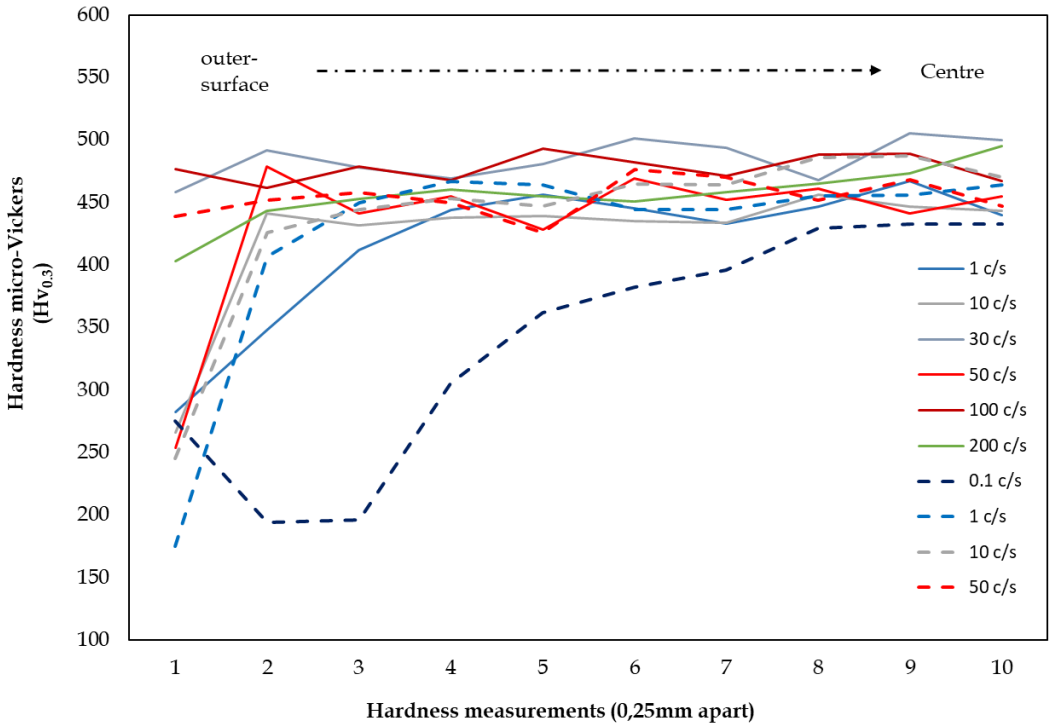

Fig. 12.18 Dilatometry samples showing the effect of cooling rate on hardness, expressed as the micro-Vickers hardness, determined using with 300 gf load. Graphs with dashed line are for specimens quenched from 1270°C.

Table 12.5 *Dilatometry average Vickers hardness values including the standard deviation and 95% confidence interval.*

Thermal cycle	*Cooling rate (°C/s)*	*Hardness ($HV_{0.3}$)*			*Std. deviation*	*95% CI*
		Min.	**Max.**	**Ave.**		
Cooled from 1350°C to room temp.	1	217	273	243	21	17
	10	315	359	346	18	16
	30	409	446	427	14	12
	50	364	446	410	27	19
	100	436	461	447	10	9
	200	415	453	435	15	12
Cooled from 1350°C to 1270°C	0.1	173	206	190	13	10
	1	167	199	186	12	10
	10	418	452	441	12	10
	50	443	457	452	6	5

Figure 12.19 shows the average hardness values plotted against the delta ferrite volume fraction. The hardness of the outer surface region decreased with lower cooling rate and increasing amount of delta ferrite.

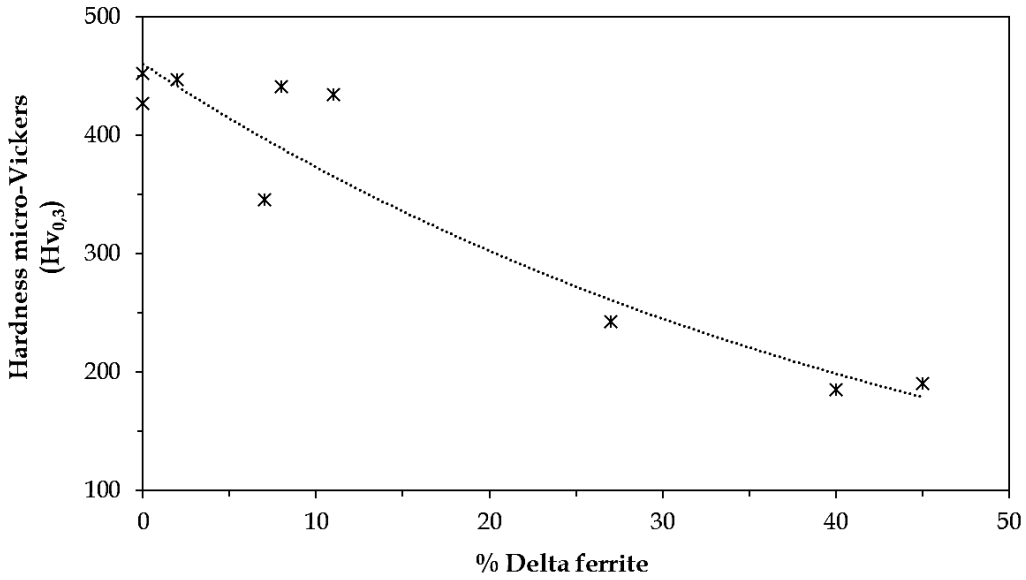

Fig. 12.19 Average hardness ($Hv_{0.3}$) as a function of the delta ferrite content.

A dilatometry experiment was also conducted on P91 base metal. The core of all specimens consisted of a fully martensitic structure with an average hardness range of 432 to 491 $Hv_{0.3}$. The martensite hardness increased with faster cooling rate.

12.3.1 Influence of cooling rate on hardness

The dilatometry specimens consisted of a transformed region on the outer surface that exhibited a martensitic matrix with delta ferrite phase. The thickness of the transformed region and volume fraction of delta ferrite increased with lower cooling rate. Figure 12.20 shows the effect of cooling rate on the hardness of the transformed outer surface region. Specimens cooled at < 10°C/s showed significant softening in the transformed outer region, with measured hardness of 167 $Hv_{0.3}$ for the 1°C/s interrupted cycle. The lower hardness values for lower cooling rates are attributed to the growing volume fraction of delta ferrite.

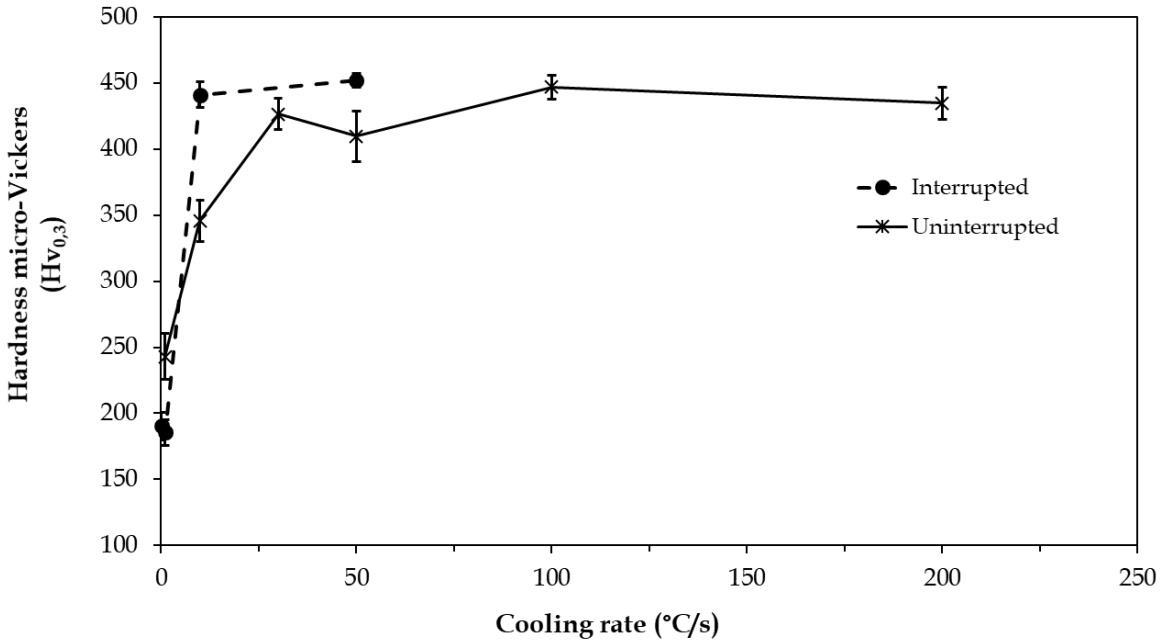

Fig. 12.20 Effect of cooling rate on hardness of dilatometry samples, expressed as the micro-Vickers hardness, determined using with 300 gf load.

12.4 Influence of cooling rate on phase transformation

The influence of cooling rate on delta ferrite/austenite transformation was studied using dilatometry on P91 base metal. Experiments were conducted using the *uninterrupted* and *interrupted* cooling cycles described in Section 4.9.

Two main observations were derived from microstructure analysis of the dilatometry specimens. The first was that delta ferrite was only observed on the outer region of the specimen whilst the core remained fully martensitic, as shown in Fig. 12.21. The difference in transformation products between the core and outer surface of specimen was an indication of a significant temperature gradient that persisted during the thermal treatment. Decarburisation was unlikely because dilatometry was performed under vacuum and helium gas was introduced in the chamber during cooling. During the dilatometry experiment, the specimen was heated by an induction coil in which heating occurred from the outer surface inwards. At the high applied heating rate with no holding time, to simulate a typical welding thermal cycle, cooling began before the

specimen core could reach the peak temperature. The observed outer region of the specimen is believed to have exceeded the Ae_4 temperature, where austenite-to-delta ferrite transformation occurs. In both the uninterrupted and interrupted cooling cycles, the width of the outer region increased with lower cooling rate due to more time spent above the Ae_4 temperature. A hollow dilatometry specimen would have been ideal to limit the thermal gradient.

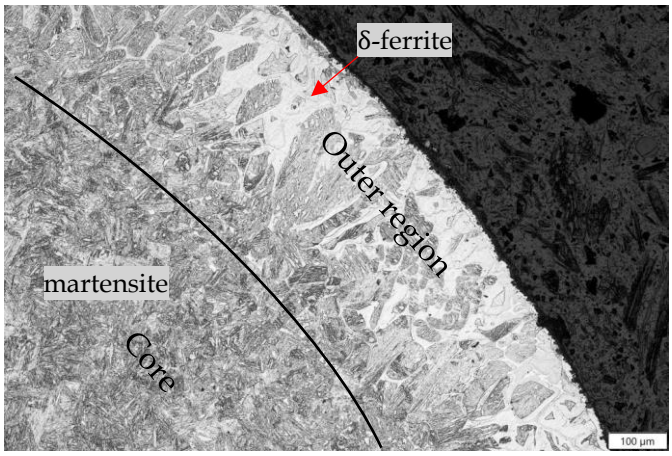

Fig. 12.21 Microstructure image of dilatometry specimen, showing the outer and core regions.

The second observation concerns the influence of cooling rate on the amount delta ferrite. The reported volume fraction of delta ferrite was only measured on the outer region. In the interrupted cycle, the observed amount of delta ferrite decreased with faster cooling rate, as shown in Fig. 12.22. In the interrupted cycle, the specimens were quenched at 1270°C, so the observed microstructures reflected the phase distribution of austenite and delta ferrite at temperatures just above Ae_4. The sample cooled at 50°C/s was fully martensitic. At 10°C/s cooling rate, the outer region microstructure contained 8% delta ferrite. At cooling rates ≤ 1°C/s, the amount of delta ferrite was 40%–45%. During cooling from 1350°C at low cooling rates, the austenite-to-delta ferrite transformation persisted because of the large proportion of austenite relative to the equilibrium volume fraction.

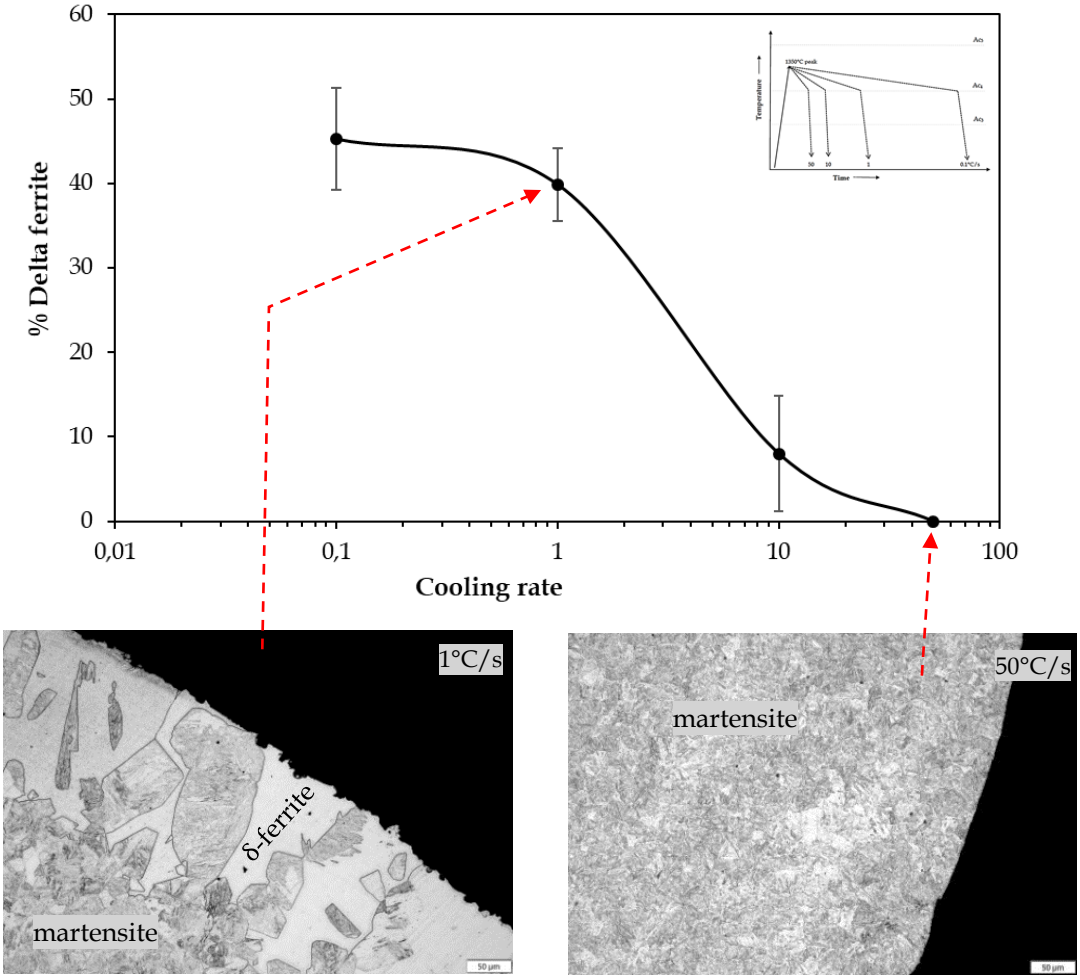

Fig. 12.22 Effect of cooling rate on delta ferrite content in the interrupted cycle. Microstructure images shown for indicated cooling rates (200× magnification).

In the uninterrupted cycle, the observed amount of delta ferrite generally decreased with faster cooling rate, except at 50°C/s, where the amount of delta ferrite increased significantly, as shown in Fig. 12.23.

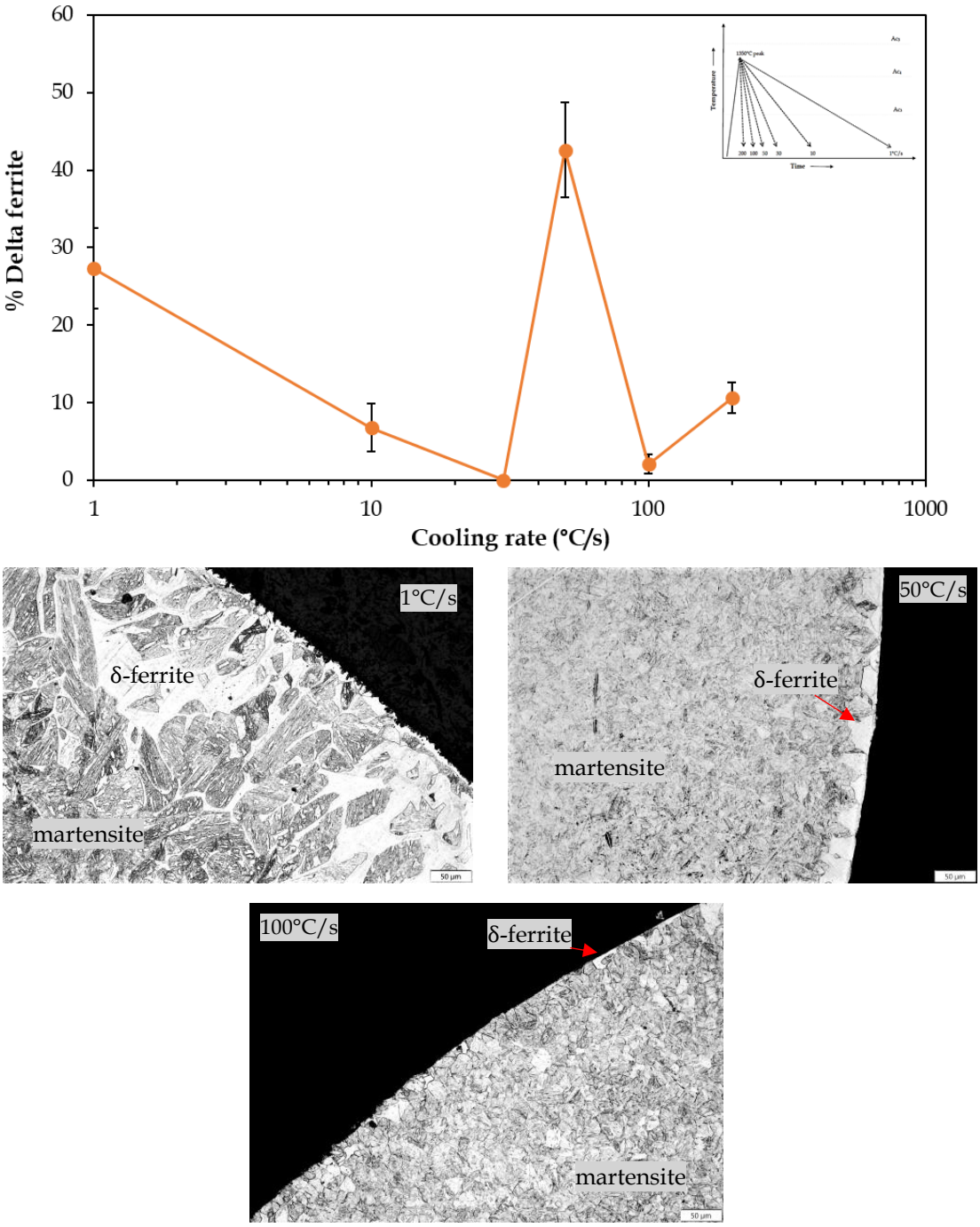

Fig. 12.23 Effect of cooling rate on delta ferrite in uninterrupted cycle. Microstructure images of specimens cooled at 1, 50, and 100°C/s. (200× magnification).

Considering the results of the interrupted cycle at 1°C/s, where delta ferrite content was 40%, the amount of delta ferrite was lower (27%) in the uninterrupted cycle for the same cooling rate. This implies that below the Ae_4 temperature, the cooling rate was sufficiently slow to allow the delta ferrite volume fraction to decrease by 13%. At a cooling rate of 30°C/s, no delta ferrite was observed. This cooling rate was fast enough to limit the austenite-to-delta ferrite transformation above the Ae_4 temperature, but sufficiently slow for the delta ferrite that formed above the Ae_4 temperature to

transform back into austenite during cooling. At 50°C/s, there was significant delta ferrite, which was against the observed trend. Above 100°C/s, the small amount of delta ferrite that formed on the outer surface of the specimen did not have time to transform back to austenite because of the high cooling rate.

The general observation from the dilatometry experiments is that delta ferrite decreased with higher cooling rate. The cooling rates during the dilatometry experiment were faster than the maximum cooling rate (0.06°C/s) required for austenite to form alpha ferrite during continuous cooling [4].

Chapter 13
Overview of results

The main results of the study are summarized and discussed in this chapter. In addition, the results of the study are considered in terms of their implications for practical welding of P91 steel.

13.1 Alloying technique to alter bead composition

DLD was applied as an alloying technique to alter the composition of GMAW beads. Considering the difficulty in accurately controlling the small quantities of the alloying powder required, the applied alloying technique was satisfactory in achieving the desired compositional changes. The composition was fairly uniform along the bead lengths of five analysed welds. Weld AW 17 showed the most inconsistency in all three added alloying elements (Cr, Mo, and Si). Limiting the bead size by reducing the laser spot size and number of beads deposited in each GMAW bead at a given time may improve composition consistency along the bead length. Some of the issues encountered during the DLD process, stated in Section 7.2.2.1, also contributed to composition inconsistency along the bead length. By optimising the DLD parameters and ensuring better control of the powder particle size, improved reliability and reproducibility in altering the weld metal composition should be achieved with this alloying technique.

13.2 Gas–metal arc weld and bead geometry

Despite applying similar GMAW parameters, there were differences in the weld metal geometry. The depth of penetration varied from 2.5 to 3.6 mm and the bead width varied from 14.1 to 17.5 mm. Weld dilution varied from 24% to 40%. Differences in weld bead geometry and dilution between the weld beads were attributed to the composition and number of laser bead. The weaving technique in GMAW was effective in increasing the weld width and heat input, but resulted in an uneven fusion line, which made accurate weld geometry calculation difficult. No significant effect of preheating was observed on the geometry of the weld bead.

13.3 Effect of equilibrium transformation temperatures on delta ferrite content

There were significant differences in the Ae_1 and Ae_3 transformation temperatures calculated from Thermo-Calc and from dilatometry measurements. There was some consistency in the Ae_3 values, in that all dilatometry Ae_3 temperatures were, on average, 70°C higher that the Thermo-Calc values. The measured Ae_1 temperatures were closer to the Thermo-Calc predicted values than the Ae_3 temperatures.

The relationship between the P91 calculated equilibrium transformation temperatures and the amount of delta ferrite in the final GMAW microstructure was analysed. Single-

parameter transformation temperatures (Ae_1, Ae_3, Ae_4, and Ae_5) were not observed to have significant predictive capability.

Correlations between the Ae_1, Ae_3, and Ae_4 calculated transformation temperatures of the welds were analysed to determine if they affect each other. The strongest relationship was observed between the ($Ae_4 - Ae_3$) temperature range and Ae_4, which gave a coefficient of determination (R^2) of 0.96. This implies that alloying elements like Cr, which have a strong influence on reducing the Ae_4 temperature, will also have a strong effect on the value of the ($Ae_4 - Ae_3$) temperature range. A larger ($Ae_4 - Ae_3$) value means that austenite is stable over a wider range of temperature and that delta ferrite has more time to transform to austenite during cooling of the weld bead after solidification.

The influence of ($Ae_4 - Ae_3$) value on the amount of delta ferrite in the as-welded beads was analysed. An increasing value of ($Ae_4 - Ae_3$) was consistently observed to decrease the amount of delta ferrite. This observation was also valid for previous work conducted on SMAW beads [18]. A value of ($Ae_4 - Ae_3$) > 415°C for welds that were not preheated seemed necessary to suppress delta ferrite in the as-welded microstructure; this value decreased to 385°C when 250°C preheating was applied. These results indicate that both the chemical composition, which determines the ($Ae_4 - Ae_3$) temperature range, and the cooling rate through this temperature range are important in suppressing delta ferrite in the final as-welded microstructure.

13.4 Effect of chemical composition on delta ferrite content

Composition of GMA welds: Thirteen of the 20 welds that complied with composition specification contained delta ferrite. These results clearly demonstrate that compliance of weld metal chemical composition to the AWS A5.28/A5.28 M:2020 (ER90S-B9) and EN ISO 21952-A CrMo91 specification ranges does not necessarily ensure a fully martensitic as-welded microstructure. The three welds that exceeded the maximum 1.5% (Mn + Ni) requirement had an Ae_1 temperature between 730 and 752°C, which is below the minimum recommended PWHT temperature of 760°C. Mn and Ni are effective in limiting delta ferrite, but their amounts should not exceed the recommend limits.

Microstructure of as-welded GMA beads: Eighteen of the 28 welds contained delta ferrite in their final as-welded microstructure, with amounts ranging from 0.3% to 6.2%. The delta ferrite morphology was a mixture of small to large polygonal grains and fine elongated grains.

Four of six welds that were welded using a preheat temperature of 250°C were fully martensitic. Welds PH 4 and PH 5 consisted of a martensitic matrix with 0.3% and 3.5% delta ferrite, respectively. Weld PH 5 contained additional Mo and Cr, which are both strong ferrite formers, and a single laser bead of Mn, which is an austenite stabiliser. The additional Mn in weld PH 4 was insufficient to ensure complete transformation of delta ferrite to austenite during cooling.

Only six of the 22 welds that were not preheated comprised a fully martensitic microstructure and contained additional Ni and Mn alloying. The addition of austenite-forming elements in the weld was effective in limiting the observed delta ferrite. The amount of delta ferrite increased with Cr_{eq}, which is based on ferrite-forming elements like Cr, Si, and Mo.

Prediction empirical formulae: Eighteen of the 28 welds (64%) were correctly predicted by all empirical formulae considered. The prediction accuracy improved in welds containing > 1% delta ferrite. In both the Schaeffler and Schneider prediction diagrams, several welds predicted to contain delta ferrite fell within the martensite-only region. The Cr_{eq} and Ni_{eq} formulae require modification to improve their predictive accuracy. The delta ferrite content was plotted against Cr_{eq} and FF in Section 9.3 (Fig. 9.3 and Fig. 9.4). FF is the difference between the Cr and Ni equivalents ($Cr_{eq} - Ni_{eq}$). A steep increase in delta ferrite content was observed above the recommended Schneider Cr_{eq} of 13.5. For the Schaeffler Cr_{eq}, a steep increase was observed from 11.5, which was below the 12.5 value recommended by Faulkner et al. [80]. Based on these results, the recommended Schaeffler Cr_{eq} value to limit the presence of delta ferrite in P91 GMA welds should be lowered to 11.5.

13.5 Post-weld heat treatment

PWHT was performed on five welds with different amounts of delta ferrite in the as-welded condition. No precipitates were observed in the as-welded condition, consistent with Pandey et al. [24], who observed no precipitates in P91 steel in the normalised condition before temper treatment. All PWHT welds comprised a tempered martensitic matrix with precipitates observed mainly along PAGB, sub-grain boundaries, and between martensite laths. No precipitates were observed in the delta ferrite phase. The precipitates experienced coarsening and growth in population density with increasing PWHT temperature.

PWHT did not change the amount of delta ferrite observed in as-welded condition, even when the PWHT temperatures exceeded the Ae_1 temperature calculated by Thermo-Calc. PWHT at 815°C exceeded the PH 4 Ae_1 temperature (773°C) by 42°C, yet the observed amount of delta ferrite remained the same as in the as-welded condition. Above the Ae_1 temperature, ferrite becomes stable and formation of alpha ferrite can occur. This would be expected to result in an increased amount of ferrite, but this was not observed in these experiments.

13.6 Sensitivity of delta ferrite to changes in weld thermal cycle

Influence of cooling rate on delta ferrite: There was a fundamental difference in analysing the effect of cooling rate between the weld metal and dilatometry specimens. Dilatometry specimens were cooled from a peak temperature of 1350°C. This peak temperature was chosen to achieve a starting microstructure that consisted of approximately equal volume fractions of austenite and delta ferrite phases. In real welds, cooling starts at the solidification temperature. The effect of cooling rate in welds was studied by the application of preheating. Four preheated welds had compositions

comparable with those of non-preheated welds. It was therefore not possible to provide a definite conclusion on the effect of cooling rate on delta ferrite in weld metal based on this preheating experiment because of limited and inconsistent results. The general observation from the dilatometry experiments performed on P91 base metal was that delta ferrite decreased with faster cooling rate. The absence of delta ferrite in the dilatometry specimens was observed at cooling rates from 30 to 50°C/s. A similar effect of cooling rate on retained delta ferrite was reported by Zhou et al. [36] from dilatometric experiments using P92 alloy.

Gleeble thermal treatment: The Gleeble thermal peak temperatures of 900°C and 1100°C were within the (Ae_3 – Ae_4) temperature range where only austenite phase is stable and no delta ferrite was expected. Significant reduction in delta ferrite was observed in Gleeble specimens treated at peak temperatures of 900°C and 1100°C. The degree by which the delta ferrite was reduced after 900°C Gleeble treatment was shown to be related to the Ae_3 temperature of the weld metal. The percentage reduction of delta ferrite increased with larger difference in (Gleeble – Ae_3) temperature. No delta ferrite was observed for 1350°C peak temperature. These results suggest that the amount of delta ferrite can be reduced by applying a subsequent bead or temper bead.

13.7 Hardness

Welds in the as-welded condition decreased in hardness from 421 to 394 Hv_{10} with increasing amount of delta ferrite (1%–6%). There was little influence on the hardness of P91 welds that contained < 1% delta ferrite. Increasing delta ferrite content decreased the average hardness in the Gleeble and dilatometry specimens, especially at > 2% delta ferrite.

For welds with < 1% delta ferrite, the weld chemical composition played a more determining role in the hardness values than the volume fraction of delta ferrite phase. In the as-welded condition, the hardness of delta ferrite phase increased with Cr content. Welds that received preheating showed lower hardness due to slower cooling rates. The hardness of PWHT specimens that consisted of tempered martensite softened to 203–253 Hv_{10}. Hardness values of the Gleeble specimens ranged from 340 to 423 Hv_{10}. The wide range in hardness is attributed to the different amounts of delta ferrite contained in the specimens and differences in the actual peak temperatures achieved. The cores of all dilatometry specimens consisted of a fully martensitic structure with an average hardness of 432 to 491 $Hv_{0.3}$. Generally, faster cooling rates increased the measured average martensite hardness. The hardness of delta ferrite in the dilatometry specimens at slow cooling rates averaged 167 $Hv_{0.3}$.

13.8 Phase transformation in P91 weld metal

Transformation between liquidus and solidus temperature: The phase-transformation sequence can take two slightly different routes during cooling, depending on the balance between austenite- and ferrite-forming elements in the composition of the P91 weld metal.

In the first transformation sequence, with higher amounts of ferrite-forming elements in P91 alloy, the liquid transforms to 100% delta ferrite during cooling:

$$\text{Liquid} \rightarrow \text{liquid} + \delta \rightarrow \delta \quad (13.1)$$

In the second transformation sequence, austenite begins forming before solidification is complete: this phase evolution is referred to as a peritectic transition [19, 20]. A peritectic reaction occurs when the liquid and delta ferrite phases transform to austenite and delta ferrite at the Ae_5 temperature:

$$\text{Liquid} \rightarrow \text{liquid} + \delta \rightarrow \delta + \gamma \quad (13.2)$$

Welds AW 1, AW 13, and AW 16 were analysed using Thermo-Calc software to determine the phase compositions below and above the solidus/peritectic temperature. Welds AW 1 and AW 16 followed the first transformation route (Equation 13.1); weld AW 13 followed the second route (Equation 13.2). Table 13.1 shows the average bead compositions, solidus/peritectic temperatures, and amount of delta ferrite observed in the as-welded beads.

Table 13.1 *Bead composition, amount of delta ferrite observed, and solidus/peritectic temperature of welds AW 1, AW 13, and AW 16*

	GMAW beads		
	AW 1	**AW 13**	**AW 16**
Alloying added (laser beads deposited)	No alloying	(2)Mn, (1)Si	(2)Cr, (1)Mo, (1)Si
Delta ferrite (%)	0.0	0.0	6.0 ± 1.1
Solidus temperature (°C)	1449	1413	1438
Phase transformation	(liquid + δ) → δ	(liquid + δ) → (δ + γ)	(liquid + δ) → δ
	Weld composition (mass %)		
	AW 1	**AW 13**	**AW 16**
C	0.09	0.09	0.08
Mn	0.48	1.12	0.46
Cr	8.60	8.40	9.80
Si	0.31	0.42	0.45
Mo	0.94	0.95	1.15
NI	0.35	0.36	0.35

Tables 13.2 to 13.4 show the Thermo-Calc phase compositions in the three welds below and above the solidus/peritectic temperature. The AW 1 and AW 16 austenite compositions just below the Ae_5 transformation temperature are also shown. The liquid just above the solidus temperature is enriched with alloying elements. The difference in ferrite composition below and above the solidus temperature is negligible. The

austenite composition is significantly different from the delta ferrite from which it nucleates, especially with respect to the austenite- and ferrite-forming elements.

Table 13.2 *Phase composition (mass%) of weld AW 1 above and below the solidus temperature. Austenite composition just below the Ae_5 temperature*

	Above solidus temp. (mass%)						**Below solidus temp. (mass%)**					
AW 1	C	Mn	Cr	Si	Mo	Ni	C	Mn	Cr	Si	Mo	Ni
Liquid	0.54	0.63	9.9	0.36	1.20	0.41	-	-	-	-	-	-
Delta ferrite	0.09	0.48	8.6	0.31	0.94	0.35	0.09	0.48	8.6	0.31	0.94	0.35
Austenite (below Ae_5)	0.20	0.52	8.2	0.29	0.76	0.40						

Table 13.3 *Phase composition (mass%) of weld AW 13 above and below the solidus temperature. A peritectic transformation is observed.*

	Above solidus temp. (mass%)						**Below solidus temp. (mass%)**					
AW 13	C	Mn	Cr	Si	Mo	Ni	C	Mn	Cr	Si	Mo	Ni
Liquid	0.48	1.56	9.5	0.49	1.26	0.44	-	-	-	-	-	-
Delta ferrite	0.07	1.10	8.3	0.42	0.93	0.36	0.07	1.10	8.4	0.43	0.98	0.35
Austenite	-	-	-	-	-	-	0.19	1.22	8.1	0.39	0.78	0.41

Table 13.4 *Phase composition (mass%) of weld AW 17 above and below the solidus temperature. Austenite composition just below the Ae_5 temperature.*

	Above solidus temp. (mass%)						**Below solidus temp. (mass%)**					
AW 16	C	Mn	Cr	Si	Mo	Ni	C	Mn	Cr	Si	Mo	Ni
Liquid	0.48	0.60	11.0	0.51	1.41	0.41	-	-	-	-	-	-
Delta ferrite	0.08	0.46	9.8	0.45	1.15	0.35	0.08	0.46	9.8	0.45	1.16	0.35
Austenite (Below Ae_5)	0.19	0.51	9.2	0.41	0.91	0.41						

Transformation below Ae_5 temperature: With further cooling below the Ae_5 temperature, austenite nucleates and grows from the delta ferrite ($\delta \rightarrow \delta + \gamma$) or the peritectic reaction occurs where the liquid and delta ferrite phases transform to austenite and delta ferrite (liquid + $\delta \rightarrow \delta + \gamma$). The growth of austenite during cooling is mainly controlled by diffusion. Villaret et al. [117] demonstrated that the nucleation of austenite is delayed to lower temperatures at fast cooling rates and grain growth rate is reduced because of slow diffusion of interstitial elements like C.

Transformation below Ae_4 temperature: The completion of austenite formation is expected to be achieved under equilibrium conditions, but higher cooling rate and delayed

nucleation of austenite to lower temperatures could mean that the presence of delta ferrite persists below the Ae_4 temperature and, as observed in this study, delta ferrite continues to persist to ambient temperature. A large (Ae_4 − Ae_3) value, which is dependent on the P91 composition, is beneficial in allowing more time for completion of the delta ferrite/austenite transformation above the Ae_3 temperature.

Transformation between Ae_3 and ambient temperature: Under equilibrium conditions, alpha ferrite begins to nucleate and grow from austenite. The austenite/α-ferrite transformation is complete at the Ae_1 temperature.

During cooling in non-equilibrium conditions, delta ferrite present below Ae_3 becomes stable and will be retained to ambient temperatures. Any retained austenite transforms to martensite below the M_s temperature when cooled above the 0.06°C/s critical cooling rate [4]. Eighteen of the 28 GMA welds in this study contained delta ferrite in their final as-welded microstructures. This implies that delta ferrite formed during solidification was not fully transformed to austenite below the Ae_4 temperature. The two possible transformation sequences under non-equilibrium cooling, where delta ferrite is retained to room temperature, are as follows:

$$\text{Liquid} \rightarrow \text{liquid} + \delta \rightarrow \delta \rightarrow \delta + \gamma \rightarrow \gamma + \delta \rightarrow \alpha' + \delta \quad (13.3)$$

(α′ is martensite)

or

$$\text{Liquid} \rightarrow \text{liquid} + \delta \rightarrow \delta + \gamma \rightarrow \gamma + \delta \rightarrow \alpha' + \delta \quad (13.4)$$

13.9 Implications for practical welding of P91

Weld composition:

(i) For the 28 GMA welds, dilution varied from 24% to 40%. The composition of the weld metal is dependent on the extent of dilution between the base and filler metal. The ASTM A335/A335M−21 base metal composition requirements are 0.30–0.60 Mn and 0.40 Ni maximum. AWS A5.28/A5.28 M:2020 (ER90S-B9) specifies 1.20% Mn and 0.8% Ni maximum for filler metal; minimum requirements are not specified. Both Mn and Ni are austenite formers, so sufficient amounts of both elements in the final weld metal are important in preventing delta ferrite. The specified base metal ASTM A335/A335M−21 upper composition limits for Mn and Ni are lower than those of the filler metal for AWS A5.28/A5.28 M:2020 (ER90S-B9). The risk for delta ferrite presence in weld metal is increased with higher dilution, especially because the latter standard does not specify minimum requirements of Mn and Ni in the filler metal.

(ii) In this study, 64% of welds that complied with the composition specification contained delta ferrite. The AWS A5.28/A5.28M:2020 (ER90S-B9) specification limits may need to be revised to ensure a fully martensitic microstructure. Table 13.5 shows the proposed changes to the current specification. Mo and Si are ferrite-formers so these limits are proposed to be lowered. Changes in Cr limits are not recommended, even though it is a strong ferrite former, because it is the

main alloying element in P91 steels, having an important role in elevated-temperature strength properties and improving resistance to oxidation and corrosion. Mn and Ni are strong austenite formers/stabilisers, so it is proposed that lower limits should be specified to ensure that they are present in sufficient quantities in the weld.

Table 13.5 *Proposed changes to chemical composition range limits of AWS A5.28/A5.28M:2020 (ER90S-B9) and ISO 21952:2007 (CrMo91) specifications*

Element	***P91 weld metal (%)***					
	AWS A5.28/A5.28M:2020 (ER90S-B9)		*ISO 21952:2007 (CrMo91)*		*Recommended changes**	
	Min	*Max*	*Min*	*Max*	*Min*	*Max*
C	0.07	0.13	0.07	0.15		
Mn	–	1.20	0.40	1.50	0.60	1.20
Cr	8.00	10.50	8.00	10.50		
Si	0.15	0.50	–	0.60	0.15	0.35
Mo	0.85	1.20	0.80	1.20	0.70	1.00
V	0.15	0.30	0.15	0.30		
Nb	0.02	0.10	0.03	0.10		
N	0.03	0.07	0.02	0.07		
Ni	–	0.80	0.40	1.00	0.40	0.80
Al	–	0.04				

* *Schaeffler* $Cr_{eq} \leq 11.5$ *is recommended*

(iii) Qualification of the filler material is recommended. Before using a batch of welding consumable, testing of the weld metal composition to ensure that Schaeffler $Cr_{eq} < 11.5$ and analysis of the as-welded microstructure to confirm the absence of delta ferrite are recommended.

Cooling rate:

(i) There are two main welding implications derived from this study. Firstly, in a single-pass welding process, lower cooling rate was observed to decrease delta ferrite in the final as-welded microstructure. This is because the diffusion-controlled transformation of delta ferrite to austenite is afforded time above the Ae_3 temperature to proceed to completion. Secondly, in multi-pass welds simulated by Gleeble and dilatometry experiments, low heat input, which results in fast cooling rates, decreased the delta ferrite content in the microstructure of previously deposited beads. This was because, in multi-pass weld, the amount of delta ferrite that forms from austenite during heating in the bead overlaid by subsequent passes depends on the time spent above the Ae_4 temperature. Low heat input in subsequent beads will limit the delta ferrite in previously laid beads.

(ii) Applying low heat input temper beads can be beneficial in decreasing delta ferrite in overlay beads.

Conclusions

The aim of this study was to examine the influence of alloying elements and cooling rate on the presence of delta ferrite in modified 9Cr–1Mo as-welded microstructure.

(i) The applied alloying technique was satisfactory in achieving the desired compositional changes. The nature of the DLD process limits this alloying technique to single-bead welds. Inhomogeneity observed along the weld bead length was attributed to the DLD process and not the alloying technique. By optimising the DLD parameters and ensuring better control of the powder particle size, reliability in altering the weld metal composition can be achieved with the DLD alloying technique.

(ii) GMAW bead microstructure results in the as-welded condition clearly demonstrate that compliance of the weld metal chemical composition to the AWS A5.28/A5.28 M:2020 (ER90S-B9) and EN ISO 21952-A CrMo91 specification ranges does not ensure a fully martensitic microstructure. Of the GMA welds that complied with the composition specification, 65% contained delta ferrite in their microstructure. To quote extreme examples, AW 9 and AW 16 contained 3.8% and 6% delta ferrite, respectively, yet their compositions were within the specification limits.

(iii) Alloy additions to alter the weld composition and PWHT did not change the morphology of the observed delta ferrite, which was a mixture of small to large polygonal grains and, in some welds, fine elongated grains. Cr, Mo, and Si increased the amount of delta ferrite and Ni and Mn limited the observed delta ferrite in as-welded P91 beads. The delta ferrite phase was not uniformly distributed throughout the cross-section of the bead in many welds; for example, AW 17 contained approximately 8% delta ferrite in the weld centre, whereas the microstructure was fully martensitic in areas close to the fusion line.

(iv) Empirical formulae cannot exclusively be relied upon to accurately predict weld microstructures with the current recommended limits, especially where small amounts of delta ferrite are probable. The prediction accuracy of the empirical formulae improved in welds containing > 1% delta ferrite. The data in Fig 9.1 and Fig. 9.2 indicate that the martensite regions of the Schaeffler and Schneider diagrams are inadequate to accurately predict the weld metal constituents.

(v) An ($Ae_4 - Ae_3$) temperature range > 415°C for P91 welds that were not preheated was necessary to suppress delta ferrite in the as-welded microstructure. This value decreased to 385°C when 250°C preheating was applied. These results indicate that both the chemical composition, which determines the ($Ae_4 - Ae_3$) temperature range, and the cooling rate through this temperature range are important in suppressing delta ferrite in the final as-welded microstructure.

(vi) PWHT did not change the amount of delta ferrite observed in as-welded condition even for PWHT temperatures that exceeded the weld Ae_1 temperature. For example, PWHT at 815°C exceeded the weld PH 4 Ae_1 temperature (773°C) by 42°C, yet the observed amount of delta ferrite remained the same as in the as-welded condition. Unless austenitisation is feasible after fabrication, delta ferrite formed in the weld and HAZ will remain during PWHT. The precipitate distribution within the tempered martensite at 815°C was random in nature and not aligned along any boundaries, unlike that at lower PWHT temperatures, where the precipitates were observed along PAGB and between martensite laths.

(vii) Gleeble results indicated that the amount of delta ferrite can be reduced by applying a subsequent bead or temper bead. Significant reduction in delta ferrite was observed in Gleeble specimens treated at peak temperatures of 900°C and 1100°C; no delta ferrite was observed for 1350°C peak temperature. The degree by which delta ferrite was reduced after 900°C Gleeble treatment was shown to be related to the Ae_3 temperature. The percentage reduction of delta ferrite increased with larger difference in (Gleeble – Ae_3) temperature.

(viii) In the dilatometry experiments, the austenite-to-delta ferrite transformation persisted, even during cooling from 1350°C to Ae_4. This was due to the large proportion of austenite relative to the equilibrium fraction at 1350°C. A decrease in cooling rate resulted in an increased amount of delta ferrite observed in the interrupted dilatometry experiment, which involved cooling specimens from 1350°C to 1270°C before quenching. For example, a sample cooled at 10°C/s contained of 8% delta ferrite; at cooling rates of 1°C/s and lower, the amount of delta ferrite was 40%–45%.

(ix) An increasing amount of delta ferrite, from 1% to 6%, in as-welded P91 beads resulted in a decrease in hardness from 421 to 394 Hv_{10}. Delta ferrite did not show much influence on hardness of P91 welds that contained < 1% delta ferrite. Increasing amount of delta ferrite was also observed to decrease average hardness in the Gleeble and dilatometry specimens, especially at > 2% delta ferrite. Welds that received preheating showed lower hardness due to slower cooling rates. A muted reduction in hardness from 250 to 212 Hv_{10} was observed on increasing PWHT temperature from 760 to 815°C.

Recommendations

(i) The AWS A5.28/A5.28M:2020 (ER90S-B9) specification limits need to be revised, especially with respect to the ferrite-forming elements, to ensure a fully martensitic microstructure. Mo and Si are ferrite formers: it is proposed that these ranges be revised to 0.7–1.0 mass% and 0.15–0.35 mass%, respectively. Mn and Ni are strong austenite formers/stabilisers: it is proposed that lower limits of 0.6 mass% and 0.4 mass%, respectively, should be specified to ensure that they are present in sufficient quantity in the weld. In addition, it is proposed that the Mn and Ni content of the weld metal should not exceed 1.2 mass% and 0.8 mass%, respectively. This is consistent with the current AWS A5.28/A5.28M:2020 (ER90S-B9) specifications.

(ii) The Schaeffler Cr_{eq} limit recommended by Faulkner [86] is 12.5. In this study, a steep increase in the amount of delta ferrite was observed at $Cr_{eq} > 11.5$. Based on these results, the recommended Schaeffler Cr_{eq} value to limit the presence of delta ferrite in P91 GMA welds should be lowered to 11.5.

(iii) Low heat input temper beads can be considered in P91 welds to decrease delta ferrite in the main weld.

Future work

(i) *Alloying technique:* Application of the DLD process was effective in making required small changes to bead composition. Experimental trials are proposed to focus on optimising the DLD parameters, ensuring better control of the powder particle size, and determining the maximum number of laser beads that can be added for each GMAW bead while ensuring uniform composition along the bead length.

(ii) *Effect of cooling rate:* It was a challenge to provide a clear conclusion on the effect of cooling rate on delta ferrite in weld metal based on these preheating experiments. Results of the dilatometry experiments showed that cooling rate does affect the observed amount of delta ferrite in P91 steel. A welding experiment that can examine the effect of cooling rate on the amount of delta ferrite in as-welded P91 is proposed using a bead-on-plate GMAW experiment with a thermocouple in the weld to record the thermal cycle. Cooling rate should be varied by applying different preheating temperatures and heat input:

a. The EN 12070: 1996; CrMo91 standard recommends a preheat/interpass temperature of 250 to 350°C. Preheating temperature limits for the suggested welding experiment are 150 to 350°C.
b. Heat input in this study ranged from 1.4 to 2.0 kJ/mm. This range can be extended to 0.6 to 2 kJ/mm by changing the welding speed.
c. Such a study may involve, in the first instance, only single-pass welds.

References

[1] C. Pandey, M. M. Mahapatra, P. Kumar, and N. Saini, "Some studies on P91 steel and their weldments," *Journal of Alloys and Compounds,* vol. 743, pp. 332-364, 2018.

[2] A. Czyrska-Filemonowicz, A. Zielińska-Lipiec, and P. J. Ennis, "Modified 9% Cr steels for advanced power generation microstructure and properties," *Achievements in Materials and Manufacturing Engineering,* vol. 19, no. 2, pp. 43-47, 2006.

[3] R. Viswanathan and W. Bakker, "Materials for ultrasupercritical coal power plants—Boiler materials: Part 1," *Journal of materials engineering and performance,* vol. 10, no. 1, pp. 81-95, 2001.

[4] K. Haarmann, J. Vaillant, and B. Vandenberghe, "Vallourec & Mannesmann Tubes," *The T91/P91 Book,* p. 62, 2002.

[5] R. W. Swindeman, M. L. Santella, P. J. Maziasz, B. W. Roberts, and K. Coleman, "Issues in replacing Cr-Mo steels and stainless steels with 9Cr-1Mo-V steel," *International Journal of Pressure Vessels and Piping,* vol. 81, no. 6, pp. 507-512, 2004.

[6] B. Arivazhagan and M. Kamaraj, "A study on influence of D-ferrite phase on toughness of P91 steel welds," *White Paper, Steel-Grips. Com,* pp. 19-24, 2013.

[7] B. Arivazhagan, G. Srinivasan, S. K. Albert, and A. K. Bhaduri, "A study on influence of heat input variation on microstructure of reduced activation ferritic martensitic steel weld metal produced by GTAW process," *Fusion Engineering and Design,* vol. 86, no. 2, pp. 192-197, 2011.

[8] J. DiStefano *et al.*, "Summary of modified 9Cr-1Mo steel development program, 1975-1985," Oak Ridge National Lab.(ORNL), Oak Ridge, TN (United States)1986.

[9] C. Pandey, M. Mohan Mahapatra, P. Kumar, and N. Saini, "Autogenous tungsten inert gas and gas tungsten arc with filler welding of dissimilar P91 and P92 steels," *Journal of Pressure Vessel Technology,* vol. 140, no. 2, 2018.

[10] A. Czyrska-Filemonowicz, P. J. Ennis, and A. Zielinska-Lipiec, "High chromium creep resistant steels for modern power plant applications," *Proc. of the metallurgy on the turn of 20th century. The Committee of Metallurgy of the Polish Academy of Sciences,* no. 193, 2002.

[11] D. J. Abson and J. S. Rothwell, "Review of type IV cracking of weldments in 9-12%Cr creep strength enhanced ferritic steels," *International Materials Reviews,* vol. 58, no. 8, pp. 437-473, 2013.

[12] H. Cerjak, P. Hofer, and B. Schaffernak, "The influence of microstructural aspects on the service behaviour of advanced power plant steels," *ISIJ international,* vol. 39, no. 9, pp. 874-888, 1999.

[13] L. Wang, "Development of predictive formulae for the A1 temperature in creep strength enhanced ferritic steels," The Ohio State University, 2010.

[14] H. K. D. H. Bhadeshia, "Design of ferritic creep-resistant steels," *ISIJ international,* vol. 41, no. 6, pp. 626-640, 2001.

[15] R. Viswanathan *et al.*, "US program on materials technology for ultra-supercritical coal power plants," *Journal of materials engineering and performance,* vol. 14, pp. 281-292, 2005.

[16] C. Pandey, M. M. Mahapatra, P. Kumar, and A. Giri, "Microstructure characterization and charpy toughness of P91 weldment for as-welded, post-weld heat treatment and normalizing & tempering heat treatment," *Metals and Materials International,* vol. 23, no. 5, pp. 900-914, 2017.

[17] V. Sikka, "Development of modified 9Cr-1Mo steel for elevated temperature service," *Oak Ridge National Lab,* ConferenceOak Ridge National Lab vol. (No. CONF-830659--16), 1983.

[18] S. S. Mahlalela and P. G. H. Pistorius, "Investigation of δ-ferrite content in weld metal of modified 9Cr–1Mo electrodes using thermodynamic modelling and quenching experiments," *Welding in the World,* vol. 66, no. 6, pp. 1191-1198, 2022/06/01 2022.

[19] D. Phelan, M. Reid, and R. Dippenaar, "Kinetics of the peritectic phase transformation: In-situ measurements and phase field modeling," *Metallurgical and Materials Transactions A,* vol. 37, pp. 985-994, 2006.

[20] S.-C. Moon, D. Phelan, and R. Dippenaar, "New insights of the peritectic phase transition in steel through in-situ measurement of thermal response in a high-temperature confocal microscope," *Materials Characterization,* vol. 172, p. 110841, 2021.

[21] H. W. Kerr, J. Cisse, and G. Bolling, "On equilibrium and non-equilibrium peritectic transformations," *Acta Metallurgica,* vol. 22, no. 6, pp. 677-686, 1974.

[22] D. M. Stefanescu, "Microstructure evolution during the solidification of steel," *ISIJ international,* vol. 46, no. 6, pp. 786-794, 2006.

[23] P. Mayr, T. A. Palmer, J. W. Elmer, E. D. Specht, and S. M. Allen, "Formation of Delta Ferrite in 9 Wt Pct Cr Steel Investigated by In-Situ X-Ray Diffraction Using Synchrotron Radiation," *Metallurgical and Materials Transactions A,* vol. 41, no. 10, pp. 2462-2465, 2010.

[24] C. Pandey, A. Giri, and M. M. Mahapatra, "Evolution of phases in P91 steel in various heat treatment conditions and their effect on microstructure stability and mechanical properties," *Materials Science & Engineering A,* vol. 664, pp. 58-74, 2016.

[25] J. Hald, "Microstructure and long-term creep properties of 9–12% Cr steels," *International Journal of Pressure Vessels and Piping,* vol. 85, no. 1-2, pp. 30-37, 2008.

[26] C. Pandey, M. M. Mahapatra, P. Kumar, and N. Saini, "Homogenization of P91 weldments using varying normalizing and tempering treatment," *Materials Science & Engineering A,* vol. 710, pp. 86-101, 2018.

[27] N. Z. Gutiérrez, J. V. Alvarado, H. n. de Cicco, and A. Danón, "Microstructural Study of Welded Joints in a High Temperature Martensitic-ferritic ASTM A335 P91 Steel," *Procedia Materials Science,* vol. 8, pp. 1140-1149, 2015.

[28] P. Ennis and A. Czyrska-Filemonowicz, "Recent advances in creep-resistant steels for power plant applications," *Sadhana,* vol. 28, no. 3-4, pp. 709-730, 2003.

[29] R. Klueh, "Elevated temperature ferritic and martensitic steels and their application to future nuclear reactors," *International Materials Reviews,* vol. 50, no. 5, pp. 287-310, 2005.

[30] K. Maruyama, K. Sawada, and J. Koike, "Strengthening mechanisms of creep resistant tempered martensitic steel (Review)," *ISIJ INTERNATIONAL,* vol. 41, no. Part 6, pp. 641-653, 2001.

[31] C. Panait, W. Bendick, A. Fuchsmann, A.-F. o. Gourgues-Lorenzon, and J. Besson, "Study of the microstructure of the grade 91 steel after more than 100.000h of creep exposure at 600°C," *International Journal of Pressure Vessels and Piping*. doi: 10.1016/j.ijpvp.2010.03.017

[32] H. K. Danielsen and J. Hald, "A thermodynamic model of the Z-phase Cr(V, Nb)N," *CALPHAD,* vol. 31, no. 4, 2007.

[33] W. B. Jones, C. R. Hills, and D. H. Polonis, "Microstructural evolution of modified 9Cr-1Mo steel," *Metallurgical Transactions A,* vol. 22, no. 5, pp. 1049-1058, 1991.

[34] A. A335/A335M-21, "Standard specification for seamless ferritic alloy-steel pipe for high-temperature service," ed, 2021.

[35] V. K. Sikka, P. Patriarca, T. N. O. R. N. L. Oak Ridge, and A. Not, "Analysis of weldment mechanical properties of modified 9 Cr-1 Mo steel," 1984.

[36] X. Zhou *et al.*, "Effects of cooling rates on δ-ferrite/γ-austenite formation and martensitic transformation in modified ferritic heat resistant steel," *Fusion Engineering and Design,* vol. 125, pp. 354-360, 2017.

[37] A. Di Gianfrancesco, L. Cipolla, F. Cirilli, G. Cumino, and S. Caminada, "Microstructural stability and creep data assessment of Tenaris Grades 91 and 911," in *Proceedings of 1 th International Conference Super-High Strength Steels*, 2005, pp. 2-4.

[38] D. A. Carrizo, J. I. Besoky, M. Luppo, C. Danon, and C. P. Ramos, "Characterization of an ASTM A335 P91 ferritic-martensitic steel after continuous cooling cycles at moderate rates," *Journal of Materials Research and Technology,* vol. 8, no. 1, pp. 923-934, 2019.

[39] D. R. Bush, "An introduction to the 9Cr-1Mo-V alloys," *Valve magazine,* vol. 13, no. 1, pp. 10-17, 2001.

[40] R. L. Klueh and D. R. Harries, "High-chromium ferritic and martensitic steels for nuclear applications," 2001: AsTM West Conshohocken, PA.

[41] F. Abe, "Precipitate design for creep strengthening of 9% Cr tempered martensitic steel for ultra-supercritical power plants," *Science and technology of advanced materials,* vol. 9, no. 1, p. 013002, 2008.

[42] B. Arivazhagan, R. Prabhu, S. K. Albert, M. Kamaraj, and S. Sundaresan, "Microstructure and Mechanical Properties of 9Cr-1Mo Steel Weld Fusion Zones as a Function of Weld Metal Composition," *Journal of Materials Engineering and Performance,* vol. 18, no. 8, pp. 999-1004, 2009.

[43] S. Merchant, "A review of effect of welding and thermal treatment processes on microstructure and mechanical properties of grade 91 steel," *International Journal of Research in Engineering and Technology,* vol. 4, no. 3, pp. 574-580, 2015.

[44] M. E. Abd El-Azim, O. H. Ibrahim, and O. E. El-Desoky, "Long term creep behaviour of welded joints of P91 steel at 650 °C," *Materials Science & Engineering A,* vol. 560, pp. 678-684, 2013.

[45] M. Sireesha, S. Sundaresan, and S. K. Albert, "Microstructure and mechanical properties of weld fusion zones in modified 9Cr-1Mo steel," *Journal of materials engineering and performance,* vol. 10, no. 3, pp. 320-330, 2001.

[46] Z. Zhang, A. Marshall, and J. Farrar, "Recent developments in welding consumables for P (T) 91 creep-resisting steels," in *Conference Proceedings, International Conference on Integrity of High-Temperature Welds*, 1998, pp. 77-91.

[47] K. Anderko, L. Schäfer, and E. Materna-Morris, "Effect of the δ-ferrite phase on the impact properties of martensitic chromium steels," *Journal of Nuclear Materials: Part 1,* vol. 179, no. Part 1, pp. 492-495, 1991.
[48] X. Y. Liu and T. Fujita, "Effect of chromium content on creep rupture properties of a high chromium ferritic heat resisting steel," *ISIJ International,* vol. 29, no. 8, pp. 680-686, 1989.
[49] Y. Wang *et al.*, "Development of new 11%Cr heat resistant ferritic steels with enhanced creep resistance for steam power plants with operating steam temperatures up to 650 C," *Materials Science and Engineering A,* vol. 510-511, no. C, pp. 180-184, 2009.
[50] B. Arivazhagan and M. Vasudevan, "A comparative study on the effect of GTAW processes on the microstructure and mechanical properties of P91 steel weld joints," *Journal of Manufacturing Processes,* vol. 16, no. 2, pp. 305-311, 2014.
[51] K. Kimura, K. Sawada, H. Kushima, and Y. Toda, "Influence of chemical composition and heat treatment on long-term creep strength of grade 91 steel," *Procedia Engineering,* vol. 55, pp. 2-9, 2013.
[52] J. C. Lippold and D. J. Kotecki, *Welding metallurgy and weldability of stainless steels*. 2005.
[53] S. Chen and L. Rong, "Effect of silicon on the microstructure and mechanical properties of reduced activation ferritic/martensitic steel," *Journal of Nuclear Materials,* vol. 459, pp. 13-19, 2015.
[54] T. Fujita, "Current progress in advanced high Cr ferritic steels for high-temperature applications," *ISIJ international,* vol. 32, no. 2, pp. 175-181, 1992.
[55] M. Basirat, T. Shrestha, L. L. Barannyk, G. P. Potirniche, and I. Charit, "A creep damage model for high-temperature deformation and failure of 9Cr-1Mo steel weldments," *Metals,* vol. 5, no. 3, pp. 1487-1506, 2015.
[56] G. Golanski, "Effect of the heat treatment on the structure and properties of GX12CrMoVNbN9-1 cast steel," *Archives of Materials Science and Engineering,* vol. 46, no. 2, pp. 88-97, 2010.
[57] G. George, H. Shaikh, N. Parvathavarthini, R. George, and H. Khatak, "On the microstructure-polarization behavior correlation of a 9Cr-1Mo steel weld joint," *Journal of materials engineering and performance,* vol. 10, no. 4, pp. 460-467, 2001.
[58] K. Easterling, *Introduction to the physical metallurgy of welding*. Elsevier, 2013.
[59] X. Li, M. Cabrillat, and Y. Lejeail, "Study of modified 9Cr-1Mo welds," 2006.
[60] B. Arivazhagan and M. Kamaraj, "Metal-cored arc welding process for joining of modified 9Cr-1Mo (P91) steel," *Journal of Manufacturing Processes,* vol. 15, no. 4, pp. 542-548, 2013.
[61] S. A. David, Z. Feng, and J. A. Siefert, "Welding and weldability of candidate ferritic alloys for future advanced ultrasupercritical fossil power plants," *Science and Technology of Welding and Joining,* vol. 18, no. 8, pp. 631-651, 2013.
[62] M. Sireesha, S. Albert, and S. Sundaresan, "Importance of filler material chemistry for optimising weld metal mechanical properties in modified 9Cr–1Mo steel," *Science and technology of welding and joining,* vol. 6, no. 4, pp. 247-254, 2001.
[63] G. Chakraborty, J. Ganesh Kumar, P. Vasantharaja, C. R. Das, S. K. Albert, and K. Laha, "Effect of Delta Ferrite on Microstructure and Mechanical Properties of

High-Chromium Martensitic Steel," *Journal of Materials Engineering and Performance,* vol. 28, no. 2, pp. 876-885, 2019.

[64] C. Pandey, A. Giri, M. M. Mahapatra, and P. Kumar, "Characterization of microstructure of HAZs in as-welded and service condition of P91 pipe weldments," *Metals and Materials International,* vol. 23, no. 1, pp. 148-162, 2017.

[65] L. Schafer, "Influence of delta ferrite and dendritic carbides on the impact and tensile properties of a martensitic chromium steel," *Journal of nuclear materials. Journal des matériaux nucléaires.,* vol. 258, no. A, p. 1336, 1998.

[66] F. Abe, H. Araki, T. Noda, and M. Okada, "Microstructure and toughness of Cr-W and Cr-V ferritic steels," *Journal of nuclear materials,* vol. 155, pp. 656-661, 1988.

[67] F. Abe, T. Noda, H. Araki, and S. Nakazawa, "Alloy composition selection for improving strength and toughness of reduced activation 9Cr-W steels," *Journal of Nuclear Materials: Part 1,* vol. 179, no. Part 1, pp. 663-666, 1991.

[68] E. Materna-Morris, "The Development of Dendritic Carbides in a Dual-Phase martensitic/Ferritic Steel," *Scanning Microscopy,* vol. 4, no. 2, p. 7, 1990.

[69] D. Carrouge, H. Bhadeshia, and P. Woollin, "Effect of δ-ferrite on impact properties of supermartensitic stainless steel heat affected zones," *Science and Technology of Welding and Joining,* vol. 9, no. 5, pp. 377-389, 2004.

[70] P. Wang, S. Lu, N. Xiao, D. Li, and Y. Li, "Effect of delta ferrite on impact properties of low carbon 13Cr–4Ni martensitic stainless steel," *Materials Science and Engineering: A,* vol. 527, no. 13-14, pp. 3210-3216, 2010.

[71] K. Sawada, H. Kushima, and K. Kimura, "Z-phase formation during creep and aging in 9–12% Cr heat resistant steels," *ISIJ international,* vol. 46, no. 5, pp. 769-775, 2006.

[72] P. Mayr, *Evolution of microstructure and mechanical properties of the heat affected zone in B-containing 9% chromium steels*. na, 2007.

[73] M. Yoshizawa and M. Igarashi, "Long-term creep deformation characteristics of advanced ferritic steels for USC power plants," *International Journal of Pressure Vessels and Piping,* vol. 84, no. 1, pp. 37-43, 2007.

[74] S. Kobayashi, K. Sawada, T. Hara, H. Kushima, and K. Kimura, "The formation and dissolution of residual δ ferrite in ASME Grade 91 steel plates," *Materials Science & Engineering: A,* vol. 592, 2014.

[75] K. Laha, K. Chandravathi, K. B. S. Rao, and S. Mannan, "Hot tensile properties of simulated heat-affected zone microstructures of 9Cr・1Mo weldment," *International journal of pressure vessels and piping,* vol. 62, no. 3, pp. 303-311, 1995.

[76] K. S. Chandravathi, K. Laha, K. Bhanu Sankara Rao, and S. L. Mannan, "Microstructure and tensile properties of modified 9Cr–1Mo steel (grade 91)," *Materials Science and Technology,* vol. 17, no. 5, pp. 559-565, 2001.

[77] A. Kumar, K. Laha, T. Jayakumar, K. B. S. Rao, and B. Raj, "Comprehensive microstructural characterization in modified 9Cr-1Mo ferritic steel by ultrasonic measurements," *Metallurgical and Materials Transactions A,* vol. 33, no. 6, pp. 1617-1626, 2002.

[78] A. Zala, N. Jamnapara, V. Badheka, C. Sasmal, S. Sam, and M. Ranjan, "Delta (δ) ferrite formation in the welds of aluminized 9Cr-1Mo steels," *Metallography, Microstructure, and Analysis,* vol. 8, no. 2, pp. 256-262, 2019.

[79] D. Olson, "Prediction of austenitic weld metal microstructure and properties," *Welding journal,* vol. 64, no. 10, pp. 281s-295s, 1985.

[80] E. Folkhard and G. n. Rabensteiner, *Welding metallurgy of stainless steels*. Wien: Springer-Verlag, 1988.
[81] A. Feild, F. Bloom, G. Linnert, R. IRON, and S. C. B. MD, "Development of Armor Welding Electrodes: Relation of the Composition of Austenitic (20 Cr-10 Ni) Electroded to the Physical and Ballistic Properties of Armor Weldments (OD-36-2)," 1943.
[82] D. Olson and T. H. North, "Ferrous alloy weldments," 1992.
[83] D. Kotecki and T. Siewert, "WRC-1992 constitution diagram for stainless steel weld metals: a modification of the WRC-1988 diagram," *Welding Journal,* vol. 71, no. 5, pp. 171-178, 1992.
[84] T. Siewert, C. McCowan, and D. Olson, "Ferrite number prediction to 100 FN in stainless steel weld metal," *Welding Journal,* vol. 67, no. 12, pp. 289-298, 1988.
[85] M. Balmforth and J. Lippold, "A preliminary ferritic-martensitic stainless steel constitution diagram," *WELDING JOURNAL-NEW YORK-,* vol. 77, pp. 1-s, 1998.
[86] R. Faulkner, J. Williams, E. G. Sanchez, and A. Marshall, "Influence of Co, Cu and W on microstructure of 9% Cr steel weld metals," *Materials science and technology,* vol. 19, no. 3, pp. 347-354, 2003.
[87] E. Ayala, M. Roman, J. Vega, X. Gomez, T. Gomez-Acebo, and J. Echeberria, "Delta ferrite formation in 9-12% chromium steel weldments," in *Advanced heat resistant steels for power generation. Conference*, 1998.
[88] A. Barnes, "The effect of composition and heat treatment on the microstructure and mechanical properties of modified 9Cr 1Mo weld metal," TWI Members Report1995.
[89] J. Onoro, "Martensite microstructure of 9–12% Cr steels weld metals," *Journal of Materials Processing Technology,* vol. 180, no. 1-3, pp. 137-142, 2006.
[90] S. Sam *et al.*, "Delta ferrite in the weld metal of reduced activation ferritic martensitic steel," *Journal of Nuclear Materials,* vol. 455, no. 1-3, pp. 343-348, 2014.
[91] C. Pandey and M. M. Mahapatra, "Effect of Heat Treatment on Microstructure and Hot Impact Toughness of Various Zones of P91 Welded Pipes," *Journal of Materials Engineering and Performance,* vol. 25, no. 6, pp. 2195-2210, 2016.
[92] V. T. Paul, S. Saroja, P. Hariharan, A. Rajadurai, and M. Vijayalakshmi, "Identification of microstructural zones and thermal cycles in a weldment of modified 9Cr-1Mo steel," *Journal of materials science,* vol. 42, no. 14, pp. 5700-5713, 2007.
[93] B. Arivazhagan, M. Vasudevan, and M. Kamaraj, "Influence of low nickel (0.09 wt%) content on microstructure and toughness of P91 steel welds," *Metals and Materials International,* vol. 21, no. 3, pp. 538-542, 2015.
[94] M. Abd El-Rahman Abd El-Salam, I. El-Mahallawi, and M. El-Koussy, "Influence of heat input and post-weld heat treatment on boiler steel P91 (9Cr–1Mo–V–Nb) weld joints Part 1–Microstructure," *International Heat Treatment and Surface Engineering,* vol. 7, no. 1, pp. 23-31, 2013.
[95] C. Pandey, M. M. Mahapatra, P. Kumar, and N. Saini, "Dissimilar joining of CSEF steels using autogenous tungsten-inert gas welding and gas tungsten arc welding and their effect on δ-ferrite evolution and mechanical properties," *Journal of Manufacturing Processes,* vol. 31, pp. 247-259, 2018.

[96] B. Shanmugarajan, G. Padmanabham, H. Kumar, S. K. Albert, and A. K. Bhaduri, "Autogenous laser welding investigations on modified 9Cr-1Mo (P91) steel," *Science and Technology of Welding and Joining,* vol. 16, no. 6, pp. 528-534, 2011.

[97] Q. Gao, Y. Liu, X. Di, Z. Dong, and Z. Yan, "The isochronal δ→ γ transformation of high Cr ferritic heat-resistant steel during cooling," *Journal of materials science,* vol. 46, no. 21, pp. 6910-6915, 2011.

[98] S. Mahlalela and P. Pistorius, "Influence of alloying elements and cooling rate on the presence of delta ferrite in modified 9Cr–1Mo as-welded microstructure produced by gas–metal arc welding," *Welding in the World,* pp. 1-12, 2023.

[99] J. A. Francis, W. Mazur, and H. K. D. H. Bhadeshia, "Review Type IV cracking in ferritic power plant steels," *Materials Science & Technology,* vol. 22, no. 12, 2006.

[100] B. Alexandrov, L. Wang, J. Siefert, J. Tatman, and J. Lippold, "Phase transformation in creep strength enhanced ferritic steel welds, machines, technologies," *Materials,* vol. 4, pp. 33-36, 2012.

[101] S. Paddea, *Stress and creep damage evolution in materials for ultra-supercritical power plants*. Open University (United Kingdom), 2014.

[102] J. Dutta Majumdar and I. Manna, "Laser material processing," *International materials reviews,* vol. 56, no. 5-6, pp. 341-388, 2011.

[103] K. Weman, "Welding processes handbook, Woodhead Publishing Limited," 2003.

[104] K. Weman, *Welding processes handbook*. Elsevier, 2011.

[105] J. Hilkes and V. Gross, "Welding CrMo steels for Power Generation and Petrochemical applications," *Past, Present & future,* 2009.

[106] K. P. Ngwenya, "Development and Characterization of 9% Cr Shielded Metal Arc Welding Electrodes," University of Pretoria, 2019.

[107] L. Chen and K. Yamashita, "Effects of PWHT temperature on mechanical properties of high-Cr ferritic heat-resistant steel weld metals," *Welding in the World,* vol. 56, no. 1-2, pp. 81-91, 2012.

[108] Z. Zhang, J. Farrar, and A. Barnes, "Weld Metal for P91-Tough Enough; IIW Doc II-A-073-00," II-1428-012000.

[109] R. Nikhil, S. Krishnan, A. Moitra, and M. Vasudevan, "Tensile Deformation Study on Heat Affected Zone of Mod. 9Cr-1Mo Steel Weld," *Journal of Materials Engineering and Performance,* pp. 1-10, 2022.

[110] Y. Chen, Y. He, H. Chen, H. Zhang, and S. Chen, "Effect of weave frequency and amplitude on temperature field in weaving welding process," *The International Journal of Advanced Manufacturing Technology,* vol. 75, pp. 803-813, 2014.

[111] H. Lu *et al.*, "Towards a Uniform Welding Quality: A Novel Weaving Welding Control Algorithm Based on Constant Heat Input," *Materials,* vol. 15, no. 11, p. 3796, 2022.

[112] J. C. Lippold, *Welding metallurgy and weldability*. John Wiley & Sons, 2014.

[113] J. N. Dupont and A. R. Marder, "Thermal efficiency of arc welding processes," *Welding Journal-Including Welding Research Supplement,* vol. 74, no. 12, p. 406s, 1995.

[114] D. Rosenthal, "The theory of moving sources of heat and its application to metal treatments," *Transactions of the American Society of Mechanical Engineers,* vol. 68, no. 8, pp. 849-865, 1946.

[115] S. J. Reed, "Optimization of wavelength dispersive X-ray spectrometry analysis conditions," *Journal of research of the National Institute of Standards and Technology,* vol. 107, no. 6, p. 497, 2002.

[116] M. Loretto and M. Loretto, "Introduction to Electron Beam Instruments," *Electron Beam Analysis of Materials,* pp. 1-18, 1984.

[117] F. Villaret, X. Boulnat, P. Aubry, J. Zollinger, D. Fabrègue, and Y. de Carlan, "Modelling of delta ferrite to austenite phase transformation kinetics in martensitic steels: application to rapid cooling in additive manufacturing," *Materialia,* vol. 18, p. 101157, 2021.

Appendix A

A.1 Additional laser welding variables

Table B *Essential welding variables used to produce all laser welds*

ASME IX paragraph		Process variable	Parameter
QW-402 Joints	.1	Groove design	Bead on plate
QW-403 Base metals	.3	Penetration	Normal weld penetration
QW-408 gas	.2	Single, mixture, or %	Argon
	.12	Flow rate	1.2 l pm
QW-409 Electrical characteristics	.20	Mode, energy	Continuous mode
	.21	Power, speed	Max 3 kW, 0.5 and 1.2 m/min (see ***Table 4.6***)
QW-410 Technique	.17	Type/model of equipment	IPG YLR 3000 - ST fibre laser
	.37	Single to multiple pass	Single-pass
	.77	Wavelength	1.07 µm
	.80	Spot size	2 and 4mm

A.2 Phase diagrams (constructed from Thermo-Calc software)

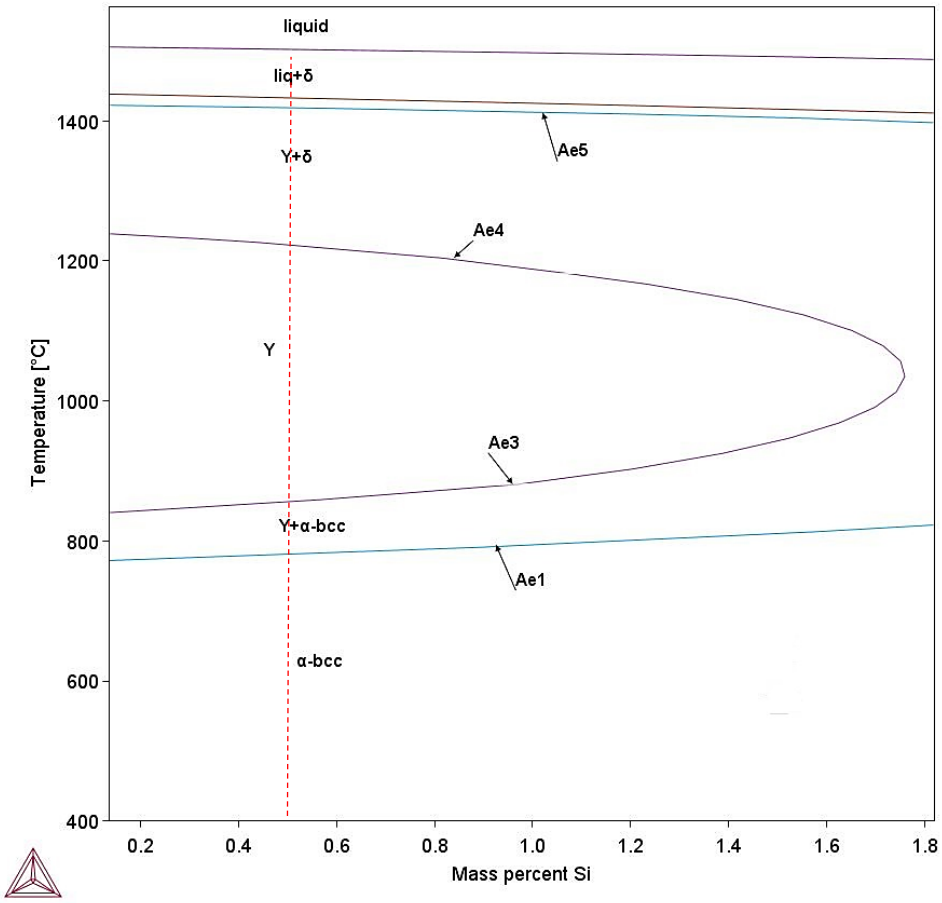

Fig A.1 P91 compositional phase diagram showing 0.2 to 1.8 mass% Si. P91 Si range is specified to be 0.5 mass% max., indicated by the red dash lines.

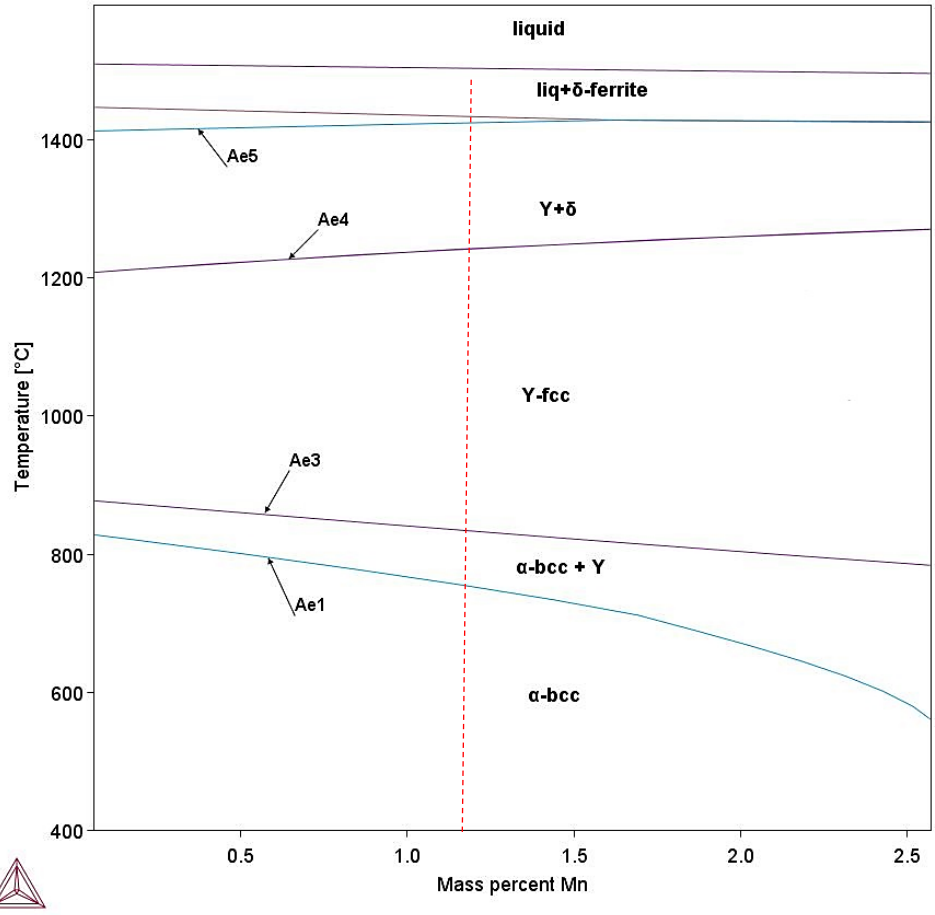

Fig. A.2 P91 compositional phase diagram showing 0.0 to 2.5 mass% Mn. P91 Mn range is specified to be 1.2 mass% max., indicated by the red dash lines.

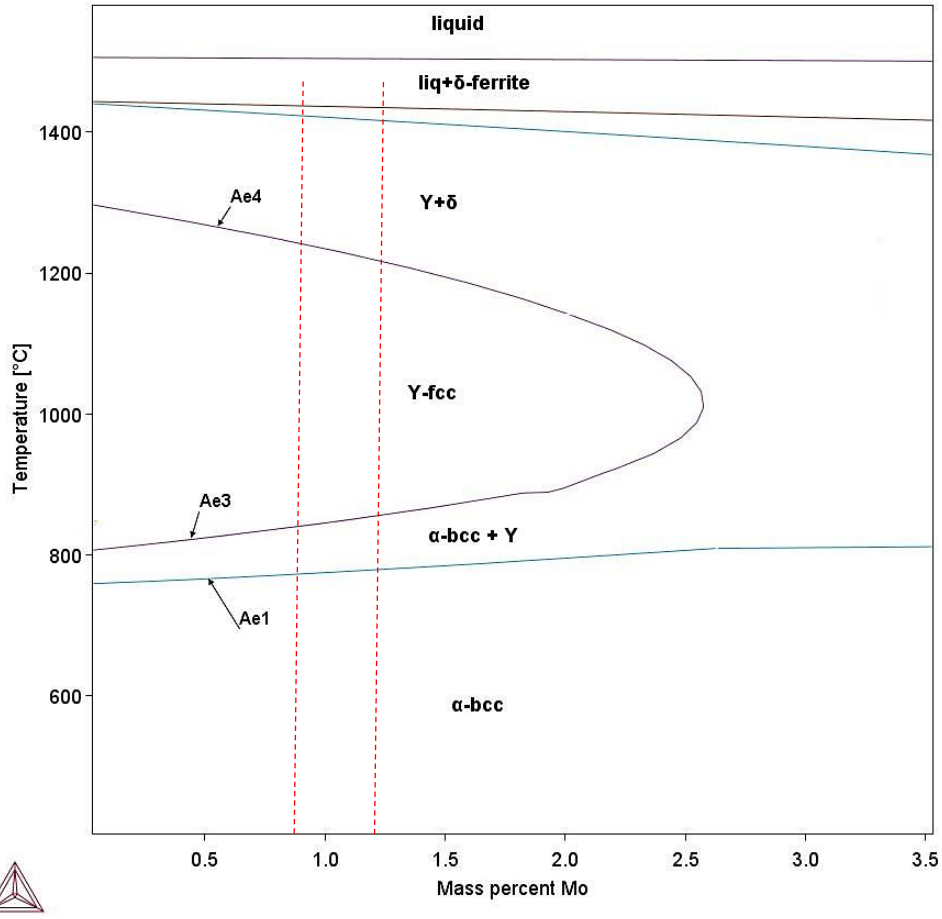

Fig. A.3 P91 compositional phase diagram showing 0.0 to 3.5 mass% Mo. P91 Mo range is specified to be 0.85 to 1.2 mass%, indicated by the red dash lines.

A.3 Calculation demonstration of confidence interval

Below is an example of a 95% CI calculation for welding PH 1 hardness values:

Five hardness values:	400, 410, 405, 410, 413
Average hardness value ($\bar{X}$):	408
Standard deviation (σ):	6
Sample size:	5
Z value:	1.960
95% CI:	$\bar{X} \pm Z \times (\sigma/\sqrt{n})$
95% CI:	5

Below is an example of a 95% CI calculation of the amount of delta ferrite in weld PH 4. Twenty-six microstructure images were analysed with % delta ferrite ranging between 0.0 to 1.7.

Average % delta ferrite ($\bar{X}$):	0.31
Standard deviation (σ):	0.28
Sample size:	26
Z value:	1.96
95% CI:	$\bar{X} \pm Z \times (\sigma/\sqrt{n})$
95% CI:	0.11